Theory and Phenomenology of Classical Scale Invariance, Dark Matter and Ultralight Axions

PLASCENCIA-CONTRERAS, ALEXIS,DAVID

Theory and Phenomenology of Classical Scale Invariance, Dark Matter and Ultralight Axions

Alexis David Plascencia

A Thesis presented for the degree of
Doctor of Philosophy

Institute for Particle Physics Phenomenology
Department of Physics
University of Durham
United Kingdom

September 2018

Dedicated to

my mother and my sister

Theory and Phenomenology of Classical Scale Invariance, Dark Matter and Ultralight Axions

Alexis David Plascencia

Submitted for the degree of Doctor of Philosophy, September 2018

Abstract

The Standard Model of particle physics does not provide a complete description of nature, there are many questions that remain unsolved. In this work, we study the theory and phenomenology of different models beyond the Standard Model that address some of its shortcomings. Motivated by naturalness arguments, we discuss the idea of classical scale invariance where all the fundamental scales are generated dynamically via quantum effects. We apply this approach to an extension of the inert doublet model and present a model that addresses the dark matter, neutrino masses and the baryon asymmetry of the Universe simultaneously.

We then study a set of simplified models of dark matter to address the effects of three-point interactions between the dark matter particle, its dark coannihilation partner, and the Standard Model degree of freedom, which we take to be the tau lepton. In these models, the contributions from dark matter coannihilation channels are highly relevant for a determination of the correct relic abundance. Firstly, we investigate these effects as well as the discovery potential for dark matter coannihilation partners at the LHC by searches for long-lived electrically charged particles. Secondly, we study the sensitivity that future linear electron-positron colliders will have to these models for the region in the parameter space where the coannihilation partner decays promptly.

Lastly, we discuss an observable for the detection of ultralight axions. In the presence of an ultralight axion, a cloud of these particles will form surrounding a rotating black hole through the mechanism of superradiance. This inhomogeneous pseudoscalar field configuration behaves like an optically active medium. Consequently, as light passes through the axion cloud it experiences polarisation-dependent bending, we argue that for some regions in the parameter space of axion-like particles this effect can be observed by current radio telescope arrays.

Declaration

The work in this thesis is based on research carried out at the Institute for Particle Physics Phenomenology, Department of Physics, University of Durham, England, United Kingdom. No part of this thesis has been submitted elsewhere for any other degree or qualification and it is all my own work unless referenced to the contrary in the text. The following chapters in this work are based on articles that have been published,

- Chapter **2** is based on Refs. [1] and [2].

  A. D. Plascencia, *Classical scale invariance in the inert doublet model, JHEP* **09** (2015) 026, [arXiv:1507.04996].

  V. V. Khoze and A. D. Plascencia, *Dark Matter and Leptogenesis Linked by Classical Scale Invariance, JHEP* **11** (2016) 025, [arXiv:1605.06834].

- Chapter **3** is based on Ref. [3].

  V. V. Khoze, A. D. Plascencia, and K. Sakurai, *Simplified models of dark matter with a long-lived co-annihilation partner, JHEP* **06** (2017) 041, [arXiv:1702.00750].

- Chapter **4** is based on Ref. [4].

  A. D. Plascencia and A. Urbano, *Black hole superradiance and polarization-dependent bending of light, JCAP* **1804** (2018), no. 04 059, [arXiv:1711.08298].

Acknowledgements

I am grateful to have had the opportunity to pursue my doctoral studies at the IPPP in Durham, United Kingdom. First and foremost, I would like to thank my PhD supervisor Valentin (Valya) Khoze for his encouragement and insightful discussions on a wide range of topics. I gratefully acknowledge financial support from CONACyT (Mexican National Council for Science and Technology) throughout the whole period of my doctoral studies.

I would like to thank all my collaborators for their insights and useful conversations, including Seyda Ipek, Alberto Salvio, Francesco Sannino and Juri Smirnov. I am especially thankful to David Cerdeño, Kazuki Sakurai, Carlos Tamarit and Alfredo Urbano for always having time to discuss physics with me and for providing their guidance throughout my studies.

I am also grateful to Silvia Pascoli and the Elusives network for their financial support to do a research secondment at IPMU in Kashiwa, Japan. I thank Alessandro Strumia for supporting me to visit the theory department at CERN and his collaboration. I am also indebted to Alexander Lenz and Michael Spannowsky for useful discussions and motivation during my studies. In addition, I would like to thank my internal and external examiners for taking time to read and provide feedback on this thesis.

Thanks to all my friends from Ustinov College and my housemates that brought joy to my time in Durham. Especial thanks to Andrew Cheek, Matheus Hostert, Matthew Kirk, Kristian Moffat, Oscar Ochoa, Andres Olivares, Maura Ramirez, Darren Scott, Gilberto Tetlalmatzi, Jessica Turner and Ye-Ling Zhou for also providing comments on this thesis.

Last but not least, I would like to thank my family. My parents Alejandro and Elizabeth, my brother Ricardo and my sister Tanya for all their support and encouragement to pursue my doctoral studies. I am grateful to have you in my life and I know that I can always count on you.

Contents

List of Figures

List of Tables

Chapter 1

Introduction

The formulation of the Standard Model (SM) of particle physics has been one of the greatest triumphs of science in the past century. It represents the best attempt made by physicists to describe the fundamental laws of nature, and it has been in remarkable agreement with experimental data. Nevertheless, we know that the SM cannot comprehensively describe all the phenomena we observe in nature.

In Section **1.1**, we present a brief overview of the SM and the great success it has garnered in making predictions that agree with experimental results. However, despite its success, there are outstanding problems that the SM fails to address, these are discussed in Sections **1.2**−**1.7**. The latter provide motivation for the existence of new physics beyond the SM (BSM) that can address these issues and at the same time make predictions that can be tested by current or future experiments. In Section **1.8**, we present the outline of the thesis.

1.1 The Standard Model of Particle Physics

The Standard Model (SM) is constructed upon the theoretical framework of quantum field theory (QFT). After the development of quantum mechanics during the early decades of the 20th century, the task to make this theory compatible with the special theory of relativity developed by Einstein in 1905 still remained. The efforts to achieve this were in part led by Dirac, and resulted in the development of QFT over the next few decades.

The first step in the formation of the SM lay in the development of quantum electrodynamics (QED) in the 1940s as a framework to describe electromagnetic phenomena. The latter is based on a local Abelian gauge theory. This further inspired physicists to apply a similar approach to describe the weak interactions; that are responsible for the radioactive decay observed in certain nuclei. However, it was not until 1954 that Yang and Mills [5] developed a non-Abelian gauge theory based on the SU(2) symmetry group. Later on, Glashow [6] showed that the weak and the electromagnetic interactions could be described within a single framework by the symmetry group $\mathrm{SU}(2)_L \otimes \mathrm{U}(1)_Y$.

A crucial step came in the late 1960s when Weinberg [7] and Salam [8] implemented the mechanism of spontaneous symmetry breaking (SSB) to the electroweak unified model by Glashow. However, the question still remained whether theories with a local non-Abelian symmetry and SSB were renormalisable. This was demonstrated to be true by t'Hooft and Veltman [9, 10], and after this, the framework attracted the attention from many physicists in the field. Its predictions were confirmed experimentally soon after this. In 1973 neutral currents were discovered in the Gargamelle bubble chamber at CERN [11], in 1974 the charm quark was discovered by a group at BNL [12] and one at SLAC [13], and in 1983 the $W^{\pm}$ [14, 15] and Z^0 [16, 17] gauge bosons were discovered by the UA1 and UA2 collaborations at CERN. Since its birth until present, the predictions of the SM have been more and more successful.

Gauge symmetries play a crucial role in the description of the fundamental interactions between particles. They also provide the guiding principle to construct the SM Lagrangian as we shall see below. The SM is described by the following gauge group,

$$G_{\mathrm{SM}} = \mathrm{SU}(3)_c \otimes \mathrm{SU}(2)_L \otimes \mathrm{U}(1)_Y, \tag{1.1.1}$$

the first group corresponds to the strong force, the second one describes weak interactions and the third corresponds to the hypercharge. From experimental evidence we know that the weak interactions only act at very short distances implying that the mediators of this force are massive. However, by introducing mass terms for

the vector bosons in the Lagrangian, gauge invariance is broken, which is crucial for renormalisability of the theory. Moreover, these terms lead to the violation of unitarity in $W_L W_L$ scattering, where the subscript L stands for the longitudinal polarisation.

The solution to this problem came in the mid-1960s, when Higgs [18], Englert and Brout [19], and Guralnik, Hagen and Kibble [20] found independently a mechanism to give masses to the gauge bosons and at the same time preserve gauge invariance of the underlying theory. By achieving this, two crucial properties of the theory are kept, unitarity and renormalisability. In this mechanism a scalar charged under the gauge group is introduced. Its potential is minimized for a non-zero value of the scalar field and this non-zero vacuum expectation value is responsible for providing masses to the gauge bosons. This mechanism is referred to as spontaneous symmetry breaking or Higgs mechanism.

The symmetry breaking pattern in the SM, for which the Higgs mechanism is responsible, is the following,

$$\mathrm{SU}(3)_c \otimes \mathrm{SU}(2)_L \otimes \mathrm{U}(1)_Y \longrightarrow \mathrm{SU}(3)_c \otimes \mathrm{U}(1)_{\mathrm{EM}}, \tag{1.1.2}$$

this gives rise to the masses for the $W^{\pm}$ and Z^0 gauge bosons, thus the latter are short range. The $\mathrm{U}(1)_{\mathrm{EM}}$ gauge group describes electromagnetism and its gauge boson, which remains massless, corresponds to the photon.

The discovery of the Higgs boson at the LHC by the ATLAS [21] and CMS [22] collaborations in 2012 provided the final missing piece to complete the picture of the SM. This discovery gives strong experimental support to the Higgs mechanism responsible for giving mass to the electroweak gauge bosons and all the fermions, the latter acquire their mass through the Yukawa terms. Nonetheless, some of its properties still need to be measured to assert whether this scalar particle corresponds to the Higgs boson predicted in the SM or deviates from it.

We proceed to describe the particle content of the SM. Fermions, that correspond to spin-$\frac{1}{2}$ particles, can be divided into leptons and quarks. Leptons consist of the electron e^-, muon μ^-, tau τ^- and the corresponding neutrinos ν_e, ν_μ and ν_τ. Quarks

come in three colours each and are the constituents of the proton and the neutron in atoms. Gauge bosons, which are spin-1 particles, correspond to the force mediators between particles. Additionally, there is a single spin-0 scalar particle in the SM, the Higgs boson.

The vector fields belong to the adjoint representation of the corresponding gauge groups,

$$\mathrm{SU}(3)_c:\ G^a_\mu = (\mathbf{8},\mathbf{1},0), \qquad \mathrm{SU}(2)_L:\ W^i_\mu = (\mathbf{1},\mathbf{3},0), \qquad \mathrm{U}(1)_Y:\ B_\mu = (\mathbf{1},\mathbf{1},0),$$

where the first entry in the parenthesis gives the representation under $\mathrm{SU}(3)_c$, the second one gives the representation under $\mathrm{SU}(2)_L$, and the third one gives the hypercharge, related to the Abelian group $\mathrm{U}(1)_Y$.

The SM is a chiral theory, in the sense that left-handed fermions possess quantum numbers different from their right-handed counterparts. As has been mentioned previously, there are three families of leptons and quarks. Each family consists of the following set of fields,

$$\begin{aligned} Q_L &= \begin{pmatrix} u_L \\ d_L \end{pmatrix} = \left(\mathbf{3},\mathbf{2},\tfrac{1}{6}\right), \quad u_R = \left(\mathbf{3},\mathbf{1},\tfrac{2}{3}\right), \quad d_R = \left(\mathbf{3},\mathbf{1},-\tfrac{1}{3}\right), \\ L_L &= \begin{pmatrix} \nu_L \\ l_L \end{pmatrix} = \left(\mathbf{1},\mathbf{2},-\tfrac{1}{2}\right), \quad e_R = (\mathbf{1},\mathbf{1},-1). \end{aligned} \tag{1.1.3}$$

Then, there is the scalar sector which consists of an $\mathrm{SU}(2)_L$ doublet that contains the Higgs boson h,

$$H = \begin{pmatrix} -iG^+ \\ \frac{1}{\sqrt{2}}\left(v + h + iG^0\right) \end{pmatrix} = \left(\mathbf{1},\mathbf{2},\tfrac{1}{2}\right),$$

where $v = 246.22$ GeV corresponds to the Higgs vacuum expectation value and, G^0 and G^+ are the would-be Goldstone bosons that provide the longitudinal degree of freedom to the weak bosons.

The SM Lagrangian consists of all renormalisable (operators with dimension less

than or equal to four) and gauge invariant operators that can be written with the fields above described, it can be written in simple form as follows,

$$\mathcal{L}_{\rm SM} = -\frac{1}{4}F^{\mu\nu}F_{\mu\nu} - \bar{\psi}\gamma^{\mu}D_{\mu}\psi - y\,\bar{\psi}H\psi - D^{\mu}H^{\dagger}D_{\mu}H - V(H), \tag{1.1.4}$$

the first term corresponds to the Yang-Mills action for the vector fields and is given by,

$$F^{a}_{\mu\nu} = \partial_{\mu}A^{a}_{\nu} - \partial_{\nu}A^{a}_{\mu} + g\,f^{abc}A^{b}_{\mu}A^{c}_{\nu}, \tag{1.1.5}$$

where A^{a}_{μ} describes the spin-1 fields, g is the gauge coupling and f^{abc} corresponds to the group structure constant, which vanishes for an Abelian group. The second and third term in Eq. (1.1.4) describe the fermionic fields, they include the covariant derivative defined as,

$$D_{\mu} = \partial_{\mu} - ig\,\tau^{a}A^{a}_{\mu}, \tag{1.1.6}$$

this term gives the kinetic term for fermions and their interaction with vector fields. τ^{a} correspond to the group generators. The third term is the Yukawa interaction that gives rise to the mass of the fermions, once the Higgs field acquires a non-zero vev. The last two terms describe the Higgs field. The Higgs potential $V(H)$ will be discussed in Section **1.5**.

In Fig. 1.1 we present a summary of the cross-sections of SM processes that take place at the LHC. The coloured boxes show the measurements performed by the CMS collaboration for different centre-of-mass energies and integrated luminosities, while the theoretical predictions are shown by the bands shaded in gray. It is remarkable to see the high level of agreement between the two, across many orders of magnitude.

Despite the high level of success of the SM, there are several pieces of information that motivate new fundamental physics beyond the SM. These correspond to: baryon asymmetry of the Universe, CP violation in QCD, cosmological inflation, dark energy, dark matter, naturalness of the Higgs mass, neutrino masses and vacuum stability of the Higgs potential. In the remainder of the present chapter, we will discuss each of these points in more detail, including a discussion of the obser-

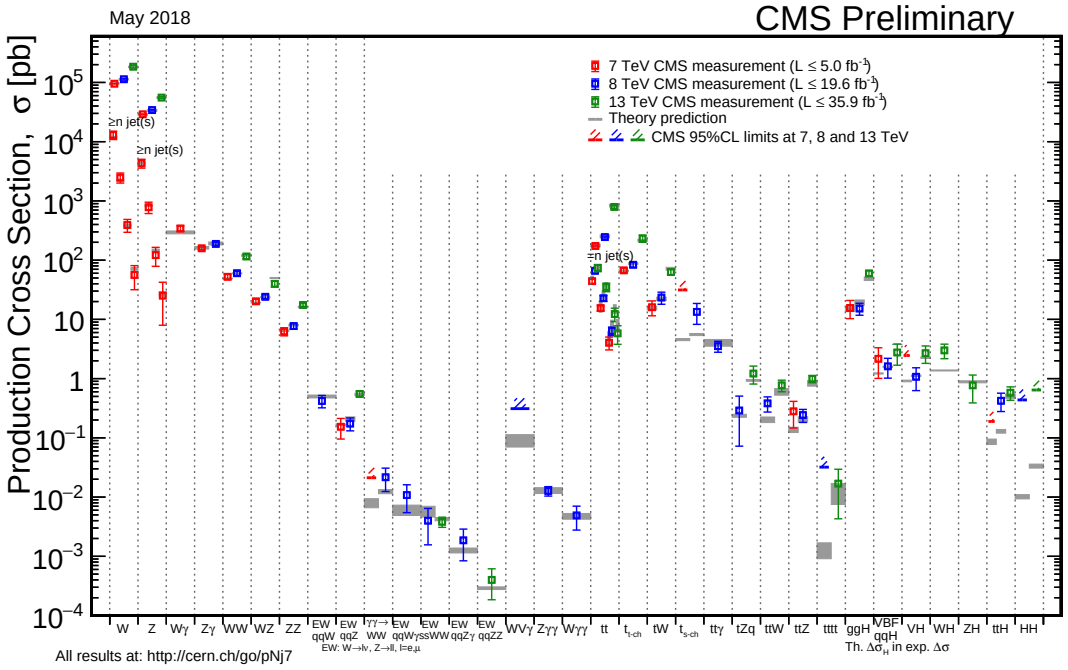

Figure 1.1: Summary of the cross-section measurements of Standard Model processes performed by the CMS collaboration [23].

vational evidence supporting them, with the exception of inflation and dark energy that are topics not covered in this thesis[1].

1.2 Neutrino Masses

Neutrinos appear in the SM only as part of an $SU(2)_L$ doublet, see Eq.(1.1.3), and hence a Yukawa term cannot be written for them without violating gauge invariance. This implies that neutrinos in the SM are predicted to be massless. As we have discussed earlier, neutrinos in the SM appear in three flavours: ν_e, ν_μ and ν_τ. If neutrinos were not massless then the mass eigenstates: ν_1, ν_2 and ν_3, could differ from the flavour eigenstates and the possibility arises to observe neutrinos oscillating among each other $v_\alpha \leftrightarrow v_\beta$. Therefore, if experiments observe neutrino oscillations this would provide evidence that neutrinos have non-zero masses and that the SM

[1]There is also the problem of making the general theory of relativity compatible with quantum mechanics which is also not discussed in this work.

must be extended in order to account for them.

The first experiment to observe hints of neutrino oscillations was the Homestake experiment in the late 1960s by observing a deficit in the flux of neutrinos emitted from the sun [24, 25], this lead to the solar neutrino problem. Many years later, the Super-Kamiokande (SK) collaboration presented conclusive evidence for neutrino oscillations from atmospheric neutrinos in 1998 [26] and the Sudbury Neutrino Observatory (SNO) found evidence of neutrino flavour transitions from solar neutrinos in 2002 [27].

Neutrino oscillations were first discussed by Pontecorvo [28] and by Maki, Nakagawa and Sakata [29] hence the neutrino mixing matrix is referred to as the PMNS matrix. The probability of a neutrino oscillation is proportional to the $\Delta m_{ij}^2 = m_j^2 - m_i^2$. For example, the probability of a ν_μ appearance from a ν_e goes as

$$P(\nu_e \to \nu_\mu) \propto \sin^2\left(\frac{\Delta m_{21}^2 L}{4E}\right), \tag{1.2.7}$$

where E and L correspond to the energy of the initial neutrino and the distance travelled respectively. From experimental data one can infer that

$$|\Delta m_{31}^2| \approx |\Delta m_{32}^2| = \Delta m_{\text{atm}}^2 \approx 10^{-3}\,\text{eV}^2,$$
$$\Delta m_{21}^2 = \Delta m_{\text{sun}}^2 \approx 10^{-4}\,\text{eV}^2,$$

the former comes from data on atmospheric neutrinos, while the latter is obtained from data on solar neutrinos. Since this data provides information about the squared mass differences rather than the individual masses, it can be explained even if the lightest neutrino is massless.

The current experimental central values for the parameters in the PMNS matrix: the active neutrino masses, m_{ν_i}, the mixing angles, θ_{ij}, and the Dirac CP-phase, δ, are the following [30]

$$\theta_{13} = 8.52^\circ, \quad \theta_{12} = 33.63^\circ, \quad \theta_{23} = 48.7^\circ, \quad \delta = 228^\circ,$$
$$\Delta m_{21}^2 = 7.40 \times 10^{-5}\,\text{eV}^2, \quad \Delta m_{31}^2 = 2.515 \times 10^{-3}\,\text{eV}^2,$$

for a normally ordered mass spectrum. Moreover, there are two Majorana phases that are currently completely unconstrained.

The mechanism via which neutrinos acquire mass is crucially related to whether they are Dirac or Majorana fermions. Although there has been impressive progress in understanding neutrino physics in the last decades, it still remains unknown whether they are Dirac or Majorana.

If neutrinos are Dirac fermions, then by adding three right-handed singlets to the SM it becomes possible to write a Dirac mass as it is done for the other fermions in the SM, see Eq. (1.1.4). However, the measured neutrino masses seem to be too small to be directly connected to the electroweak scale, requiring very small Yukawa couplings $y_\nu \approx 10^{-13}$, this motivates models beyond the SM that can explain the origin of neutrino masses without requiring such a small parameter.

If neutrinos are Majorana fermions, then there is need for physics beyond the SM to generate their masses. One of the most economical possibilities to generate Majorana masses is via the type-I seesaw mechanism [31–34]. The latter consists of adding three heavy right-handed Majorana neutrinos N_i and the following terms to the SM Lagrangian,

$$\mathcal{L} = \mathcal{L}_{\rm SM} + i\overline{N_i}\partial\!\!\!/ N_i - Y_{N\alpha i}\overline{L_\alpha}\tilde{H}N_i - \frac{1}{2}M_i\overline{N_i^c}N_i + \text{h.c.}\,, \tag{1.2.8}$$

where $\alpha = e, \mu, \tau$, $i = 1, 2, 3$, M_N is the Majorana mass term for the right-handed neutrinos and Y_N is the Yukawa matrix that once the Higgs gets a vev gives rise to the Dirac mass term. H corresponds to the Higgs $\mathrm{SU}(2)_L$ doublet, $\tilde{H} = i\sigma_2 H^*$ and $L^T = \left(\nu_L^T, l_L^T\right)$ is the leptonic $\mathrm{SU}(2)_L$ doublet.

The mass matrix has to be diagonalised in order to obtain the Majorana mass terms. Once this is performed and assuming $M_N \gg Y_N v$, then one obtains the following mass matrix for the active neutrinos,

$$m_\nu = -\frac{Y_N^T v^2 Y_N}{2M_N}, \tag{1.2.9}$$

where $v = 246.22$ GeV is the vacuum expectation value of the Higgs scalar and

M_N is the diagonal mass matrix of the heavy neutrinos. In this manner, if we take M_N to be large, then the active neutrino masses can be explained without requiring very small Yukawa couplings. For example, if we assume that $Y_N \sim \mathcal{O}(1)$ and $m_\nu \sim \sqrt{\Delta m_{\rm atm}} \sim 0.05$ eV then this mechanism predicts $M_N \sim 10^{15}$ GeV.

1.3 Baryon Asymmetry of the Universe

The SM predicts the existence of an antiparticle for each particle we observe[2]. This is confirmed at particle colliders where antiparticles are produced in large amounts. However, the vast majority of the matter we observe around us, from microscopic to extragalactic scales, consists of particles rather than antiparticles. Therefore, our description of nature should provide a mechanism that explains this baryon asymmetry of the Universe (BAU). When studying the cosmological history of the Universe, the measured matter asymmetry cannot be generated relying only on the SM and hence this represents evidence for new physics beyond the SM.

The matter asymmetry can be characterised by the baryon-to-photon ratio defined as follows,

$$\eta_B \equiv \frac{n_B - n_{\overline{B}}}{n_\gamma}, \tag{1.3.10}$$

where n_B, $n_{\overline{B}}$ and n_γ are the number densities of baryons, antibaryons and photons respectively. In view that η_B is a ratio of number densities, it remains constant with the expansion of the Universe. There are two different techniques to measure η_B. On the first hand, this quantity can be determined using Big-Bang nucleosynthesis (BBN) measurements. The abundance of light elements in the Universe, such as D, ^{3}He, ^{4}He, ^{6}Li, and ^{7}Li provides information about the baryonic matter in the Universe [35,36]. On the second hand, this quantity can be determined from Cosmic Microwave Background (CMB) radiation data [37]. These measurements provide the following values,

$$\eta_{B\rm BBN} = (5.80 - 6.60) \times 10^{-10},$$
$$\eta_{B\rm CMB} = (6.02 - 6.18) \times 10^{-10},$$

[2]Some particles have the property of being their own antiparticle, e.g. the photon.

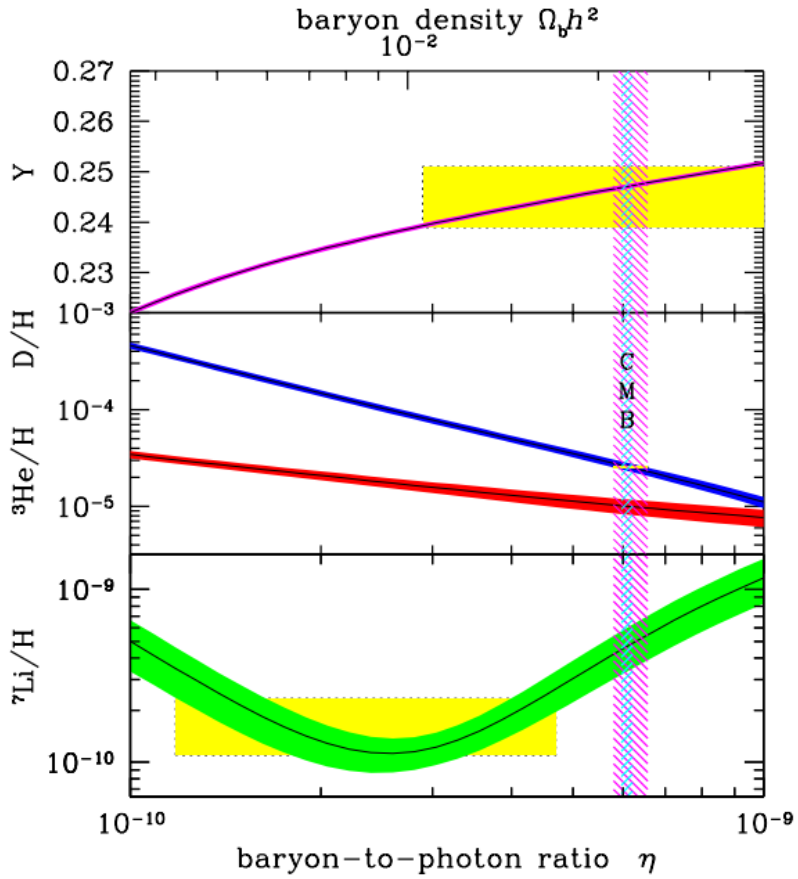

Figure 1.2: Different curves giving the primordial abundances of light elements as a function of the baryon-to-photon ratio η_b. The narrow vertical blue band corresponds to the CMB measurement, while the wider red band corresponds to BBN measurements. The yellow boxes correspond to measurement of the abundance of the light elements. Figure taken from Ref. [36].

at 95% CL, respectively.

In Fig. 1.2 we present a comparison between the CMB measurement and observations for the abundances of different light elements. As can be seen, the baryon-to-photon ratio obtained from measurements of D and ^{3}He are in agreement with the one obtained from the CMB spectrum. Although, at present the lithium measurement has preference for a lower baryon-to-photon ratio.

In order to produce a baryon asymmetry in the early Universe, there are three conditions that must be satisfied. These are also known as Sakharov conditions, named after the first author to discuss them [38]: baryon number violation, CP

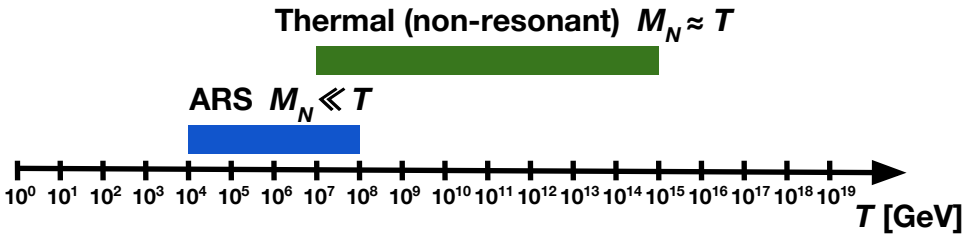

Figure 1.3: Temperature ranges for which leptogenesis can generate the observed baryon asymmetry in the Universe. The green (blue) shaded region corresponds to non-resonant thermal (ARS) leptogenesis. Thermal leptogenesis works at high temperatures and for very heavy right-handed neutrinos $M_N \approx T$, while the ARS mechanism works for much lighter masses $M_N \approx \mathcal{O}(\text{GeV})$.

violating processes and departure from thermodynamical equilibrium. To satisfy these conditions and generate the observed baryon number asymmetry it is necessary to introduce new physics beyond the SM. Most of the proposals that address the BAU can be divided into two main categories,

- **Electroweak baryogenesis:** In this approach the baryon asymmetry is produced during the electroweak phase transition (EWPT). For this mechanism to be successful it requires a first order phase transition and an extra source of CP violation to the one present in the SM. For reviews on this topic see [39,40].

- **Leptogenesis:** In addition to providing an explanation for small but non-zero neutrino masses, the type-I seesaw mechanism also provides a solution to the BAU, due to a new source of CP violation present in the out-of-equilibrium decays of the heavy Majorana neutrinos in the early Universe [41].

An alternative mechanism to produce a baryon asymmetry, which also involves the type-I seesaw, is the Akhmedov-Rubakov-Smirnov (ARS) mechanism [42], in this framework a lepton flavour asymmetry is produced during CP violating oscillations of the GeV-scale right-handed neutrinos and converted to the baryon asymmetry by the electroweak sphalerons. In contrast to high-scale thermal leptogenesis, this mechanism can be probed experimentally [43–45]. Due to the mixing between the left-handed and right-handed neutrinos, it becomes possible to produce the latter

at fixed target experiments such as the proposed SHiP facility [46]. In Fig. 1.3 we show the temperature ranges required to generate the correct baryon asymmetry for the two mechanisms of leptogenesis previously discussed. The scale for thermal leptogenesis can be lowered if one also considers resonant effects [47].

1.4 Dark Matter

The first evidence of dark matter came in 1933 when Zwicky showed that the velocity dispersion of galaxies in the Coma cluster is much larger than what was expected from the luminous matter [48]. Later on, in the 1970s Freeman [49] and, independently, Rubin and Ford [50] observed that the velocity of stars in the galactic spiral arms also seem to point to a large missing component of matter. For a recent historical account of the dark matter problem see [51–53].

In Fig. 1.4 we present an example of a rotation curve for the galaxy NGC 6503, where the circular velocity of different components of the galaxy is shown as a function of the distance to the galactic centre. As can be seen in the plot, the circular velocity of gas and stars flattens at large radius, contrary to the expectation from Newtonian dynamics that far from the galactic centre the circular velocity should decrease as the distance increases, $v_c(r) \propto 1/\sqrt{r}$.

In addition to the modification of galactic dynamics, dark matter plays a crucial role in the structure formation of the Universe. DM provides the gravitational potential wells in the early Universe by means of which baryonic matter starts to cluster. Measurements of the cosmic microwave background (CMB) allow us to determine the fraction of baryonic (Ω_b) and dark matter ($\Omega_{\rm DM}$) in the Universe with high precision. The Planck satellite mission has measured the DM relic density to be $\Omega_{\rm DM}h^2 = 0.1197 \pm 0.0022$ [37], which corresponds to $\Omega_{\rm DM} = 0.265$ and hence 26.5% of the total energy in the Universe is in the form of DM.

From the general theory of relativity we know that a large and heavy mass distribution, such as galaxy or galaxy clusters, will act as a gravitational lens. The dark matter hypothesis is also supported by observations from weak and strong

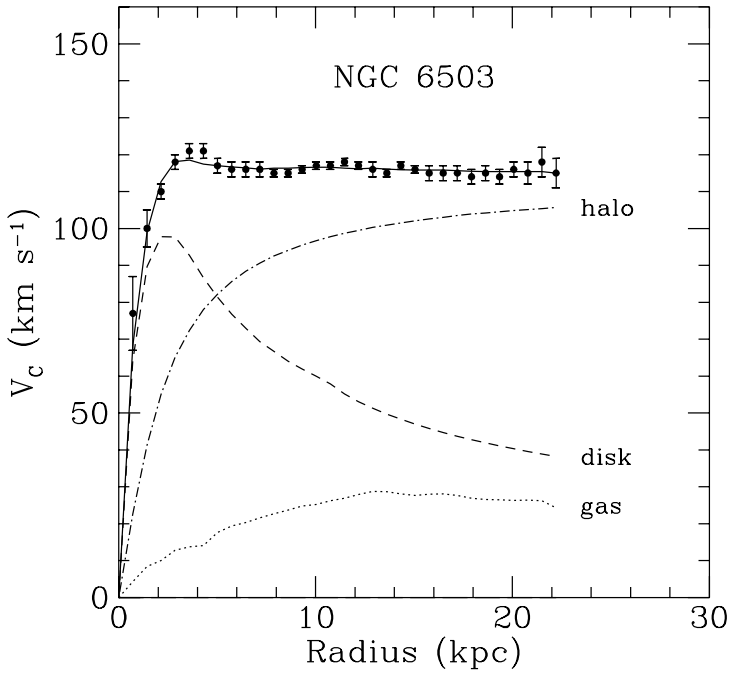

Figure 1.4: Rotation curve for the NGC 6503 galaxy. Circular velocity of gas and stars as a function of the radial distance to the galactic centre. The dashed (dotted) correspond to the predictions from disk (gas). The dot-dashed line is the contribution from the dark matter halo. Figure taken from Ref. [54] which at the same time was adapted from Ref. [55].

gravitational lensing, which show that the ratio of dark matter to luminous matter in galaxy clusters is much larger than one. For reviews on this topic see Refs. [56,57].

A particularly striking piece of evidence comes from the system 1E0657-56 of colliding clusters of galaxies [58]. The hot gas in the clusters interacts and it is slowed down by the collision; a shape in the form of a bow-shaped shock wave can be seen on the right side in Fig. 1.6, for this reason the system is known as the "bullet cluster". Using gravitational lensing one can infer that the dominant component in the system is dark matter, this is showed by green contours in the same figure. Dark matter passes through without interaction during the collision, and therefore, this observation provides evidence that a large matter component in the clusters is made of non-baryonic and almost collisionless matter.

One more piece of evidence comes from Big Bang nucleosynthesis (BBN), the

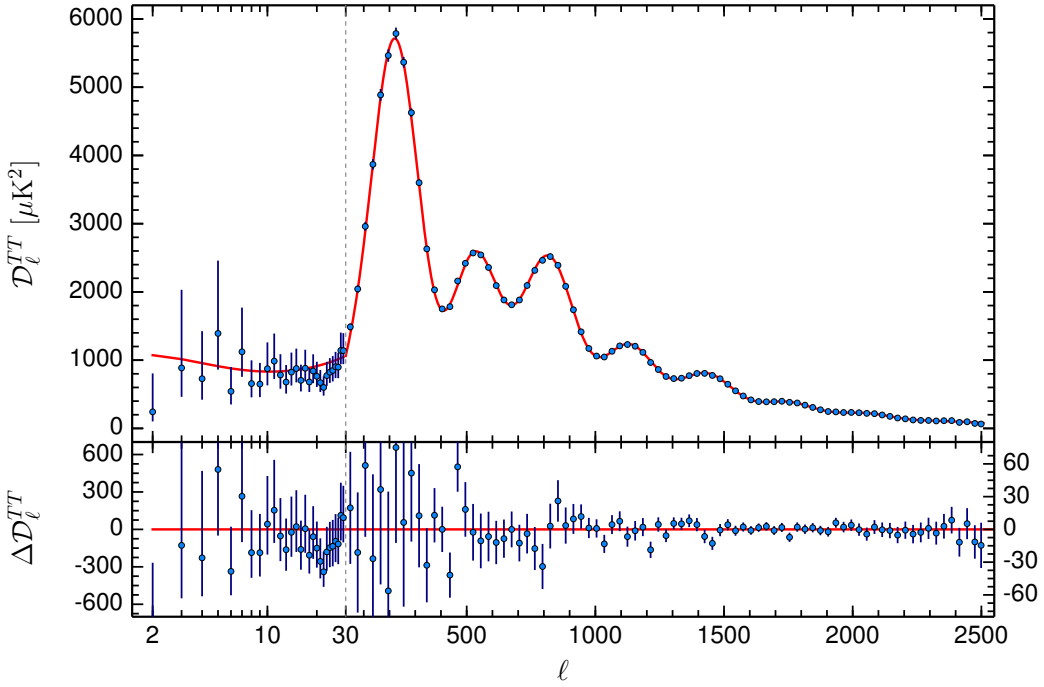

Figure 1.5: The power spectrum of the CMB as measured by the Planck satellite mission [37]. The vertical axis shows the temperature fluctuations in units of μK^2 and the horizontal axis shows the multipole moment, l. The red solid line shows the best fit based in the ΛCDM model. Figure taken from [37].

epoch of the early Universe during which light nuclei were synthesized. The primordial abundance of the light elements D, ^{3}He, ^{4}He and ^{7}Li can be inferred from observations, and these measurements are in good agreement with the predictions from BBN in the SM[3]. These measurements indicate that the baryonic density in the Universe is $\Omega_{\rm b} = 0.0487$ [35, 36], consistent with the value inferred from the CMB. This number is much smaller than the inferred value for $\Omega_{\rm DM}$ and hence the dark matter cannot consist of ordinary baryons.

[3]Although, at present there is a discrepancy between the measurement and the prediction for the abundance of lithium.

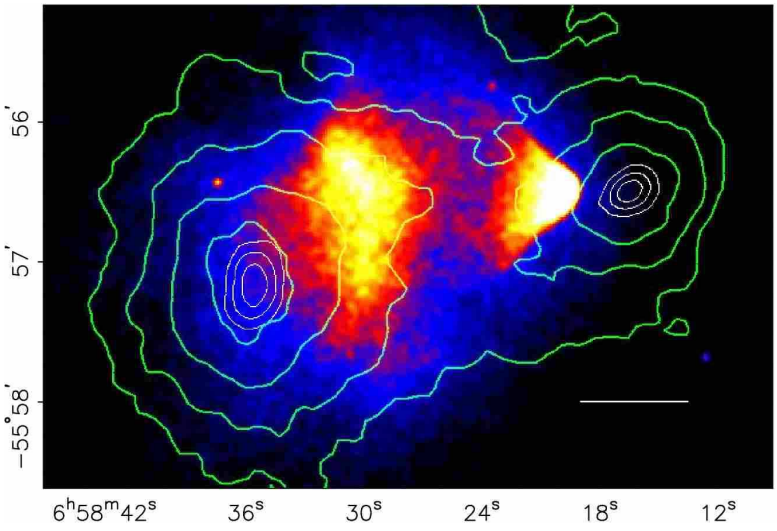

Figure 1.6: Collision of two galaxy clusters. The green contours represent the matter inferred from gravitational lensing. The colours show the distribution of the hot baryonic gas from X-ray observations. As can be seen, most of the matter in the clusters is in the form of dark matter and remains unaffected by the collision. Figure taken from Ref. [58].

1.4.1 Dark Matter Candidates

From the observations that have been previously discussed, we can deduce the following properties for any good dark matter candidate. We know that the dark matter does not emit or absorb electromagnetic radiation and hence it is either electrically neutral or its interactions with photons are highly suppressed, such as in the scenario of milli-charged DM [59–61]. DM needs to be present in the early Universe for the formation of structure to take place, we also observe it at present time in the halos that surround galaxies. Therefore, the dark matter particle needs to have a lifetime larger than the present age of the Universe.

Moreover, due to the observation of small scale structure dark matter cannot be relativistic at the time of structure formation. This is because hot dark matter has a large free-streaming length that suppresses the formation of small structures. Therefore, the DM population needs to be either warm or cold. Finally, there should be a production mechanism leading to the observed value of the relic density.

There have been many proposed candidates that satisfy all these properties and can also account for the observed relic density. We briefly review some of them. The following list is far from being complete, since there is a plethora of DM candidates and the list never stops growing.

- **ALPs:** Axion-like particles. The QCD axion provides a solution to the strong CP puzzle as discussed in Section **1.6**. The QCD axion is very weakly interacting and can have a long lifetime on cosmological scales; hence, it represents a good dark matter candidate. More generally, one can treat the axion independently from the strong CP problem giving rise to ALPs, for reviews on this topic see [62, 63]. We will further discuss these particles in Chapter **5**. Dark matter ALPs are produced non-thermally and are usually light ($m_{\rm DM} < \text{eV}$).

- **Asymmetric DM:** In this setup the DM population is asymmetric. Therefore, one needs to produce an initial asymmetry between particle and antiparticle DM in a similar fashion as for baryons. In these scenarios the dark matter mass is usually a few GeV [64].

- **Dark photon:** Similar to ALPs, very light spin-1 bosons can also form a condensate that behaves as cold dark matter. The production is also non-thermal [65, 66]. Although, a heavier gauge boson could also be a WIMP and be produced through the freeze-out mechanism [67].

- **FIMP:** Feebly interacting massive particle. The production mechanism is via freeze-in; namely, the interactions with the SM are highly suppressed and they cannot thermalise the DM candidate [68, 69]. Requires very small interactions $g \lesssim 10^{-10}$ with the SM particles. The relic density can be independent of FIMP mass, allowing for a large range of masses. This is a non-thermal candidate.

- **Primordial black holes:** These consist of a hidden population of black holes created in the early stages of the Universe, e.g. they could have been produced during inflation. The main observational technique to search for primordial black holes is using gravitational lensing. For a recent review on this topic see [70].

- **SIDM:** Self-interacting dark matter. In these models dark matter has large self-interactions which impact the small scale structure in the Universe [71]. An example is the strongly interacting massive particle (SIMP). In this scenario the DM relic density is set by $3 \to 2$ processes, i.e. three DM particles annihilating into two of them, instead of the usual $2 \to 2$ where DM pairs annihilate into SM states. The dark matter candidate is strongly interacting with mass at the MeV scale [72]. The production mechanism for this candidate is thermal.

- **SuperWIMPs:** Super weakly interacting massive particle. The relic abundance is obtained from the late decay of a metastable WIMP [73]. Most common examples are the gravitino in supersymmetric theories and Kaluza-Klein gravitons in theories with extra dimensions. These candidates are hard to detect experimentally. The production mechanism for this candidate is non-thermal.

- **Warm dark matter:** This corresponds to a light DM particle, with mass around the keV scale, and velocity dispersions between that of hot DM and cold DM. The most common example is the sterile neutrino [74, 75]. This candidate has larger free-streaming length compared with cold DM, which reduces the formation of small scale structures.

- **WIMP:** Cold dark matter as a weakly interacting massive particle. This is a thermal candidate. In the early Universe the WIMP is in thermal equilibrium with the SM plasma. The relic abundance is obtained via the freeze-out mechanism, described in Section **3.1**. Typical values for its mass are around the electroweak scale $m_{\rm DM} \sim \mathcal{O}(100)$ GeV. This is one of the most studied DM candidates, since it leads to detectable predictions at different types of experiments. The dark matter population in this scenario is symmetric. For recent reviews see [54, 76].

- **WIMPzilla:** This corresponds to a superheavy dark matter candidate with mass $m_{\rm DM} \sim 10^{10}$ GeV or larger values. In some scenarios it can be detected

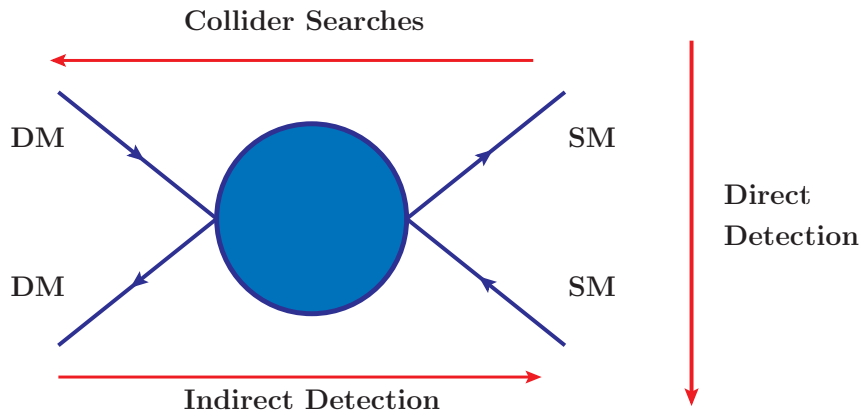

Figure 1.7: Schematic diagram of the three main experimental searches for particle dark matter. For each type of experiment, time goes in the direction of the corresponding arrow.

through its decays by using indirect detection. The WIMPzilla is a non-thermal candidate, one of the most studied mechanisms to generate its relic density is gravitational production at the end of inflation [77].

1.4.2 Experimental Searches for Dark Matter

In many models of dark matter, its production in the early Universe requires couplings to Standard Model states. These interactions can be exploited to experimentally search for the dark matter particle. The three main three avenues for the detection of DM are the following,

- **Direct detection:** The aim of this type of experiment is to measure the energy deposited when dark matter scatters off nuclei in ground-based detectors. This process is depicted in Fig. 1.7 if we follow the vertical arrow from top to bottom. In order to avoid large backgrounds, e.g. from cosmic rays, these detectors are placed underground. Examples include CRESST [78], Lux-Zeplin [79], PandaX [80], SuperCDMS [81] and XENON 1T [82].

- **Indirect detection:** Dark matter particles in the halo surrounding our galaxy can annihilate into visible states $\chi\,\chi \rightarrow \mathrm{SM}\,\overline{\mathrm{SM}}$, e.g. charged particles or photons. Satellite or ground-based telescopes can then look for a signal excess

after removing known astrophysical backgrounds. This process is depicted in Fig. 1.7 if we follow the horizontal arrow from left to right. Examples include AMS [83], CTA [84], Fermi-LAT [85], HAWC [86], HESS [87], IceCube [88] and PAMELA [89].

- **Collider searches:** Pair-production of the dark matter particle can be studied at colliders. The DM particle will leave no signature in the detectors, so in order to tag this process a visible emission needs to be considered, e.g. one channel that can be studied is the mono-jet plus missing transverse energy. We will further discuss these searches in Section **3.2**. This approach is depicted in Fig. 1.7 if we follow the horizontal arrow from right to left. Examples include the LHC and future collider proposals such as the International Linear Collider (ILC) [90], the Compact Linear Collider (CLIC) [91] and the Future Circular Collider (FCC) [92].

For literature reviews covering different dark matter candidates and experimental search strategies we refer the reader to [54, 93, 94].

1.5 Vacuum Stability of the Higgs Potential

In the Standard Model, the Higgs potential at tree-level is given by,

$$V\left(|H|^2\right) = -\mu^2|H|^2 + \lambda|H|^4, \tag{1.5.11}$$

where λ is the Higgs quartic coupling, $\mu^2 = M_h^2/2$ and M_h corresponds to the Higgs mass. In the unitary gauge we can write the Higgs doublet as $H = (0\,,\, h/\sqrt{2})^T$. If we take $\mu^2 > 0$ then the potential has a minimum at $|H|^2 = \mu^2/2\lambda = v^2$. This minimum gives the vacuum expectation value to the Higgs field $\langle 0|h|0\rangle = v$.

Radiative corrections have a twofold impact on the tree-level potential given in Eq. (1.5.11). Firstly, there are loop corrections to the potential itself that lead to the effective potential. The calculation of these corrections will be discussed in detail in Sec. **2.3**. The effective Higgs quartic coupling is defined in terms of higher order

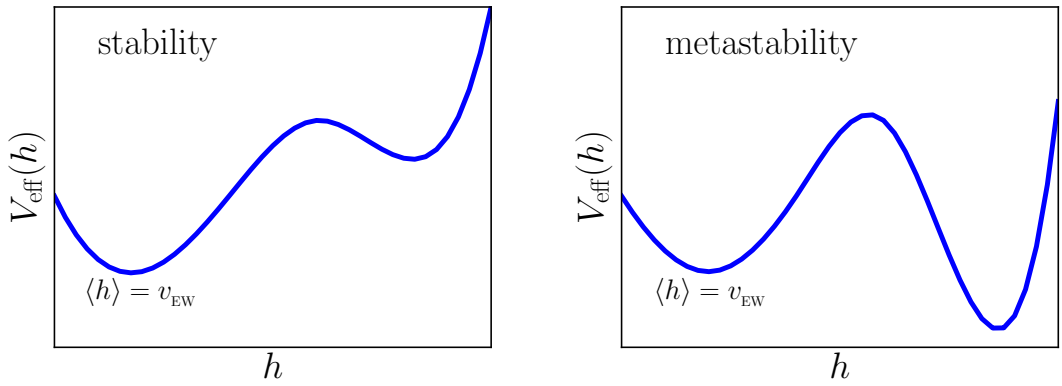

Figure 1.8: The left (right) panel shows a schematic depiction of a scalar potential where the minimum is absolutely stable (metastable).

corrections to the Higgs potential and at one-loop is given as follows [95, 96],

$$\lambda_{\text{eff}} = \lambda_H + \frac{1}{16\pi^2}\left[\frac{3}{16}\left(g_Y^2 + g_2^2\right)^2\left(\ln\frac{g_Y^2+g_2^2}{4} - \frac{5}{6}\right) + \frac{3}{8}g_2^4\left(\ln\frac{g_2^2}{4} - \frac{5}{6}\right) - 3y_t^4\left(\ln\frac{y_t^2}{2} - \frac{3}{2}\right) + 3\lambda_H^4\left(4\ln\lambda_H - 6 + 3\ln 3\right)\right]. \tag{1.5.12}$$

Secondly, each coupling in the Lagrangian has a renormalisation scale dependence. In order to compute the latter, one has to solve the RG group equations, a set of coupled differential equations, also referred to as β-functions. After being included in the computation of the potential, one refers to the latter as the RG-improved Higgs effective potential.

Once the inclusion of quantum corrections to the potential has been taken into account, three different scenarios can arise regarding the stability of the electroweak (EW) vacuum:

1. **Stability**: The electroweak vacuum is stable if no other minima appear in the effective potential or the other minima that appear lie above the current EW vacuum. See left plot of Fig. 1.8.

2. **Metastability**: If the new minimum lies deeper than the electroweak vacuum, then the Higgs field can tunnel into the new vacuum. If the lifetime of the

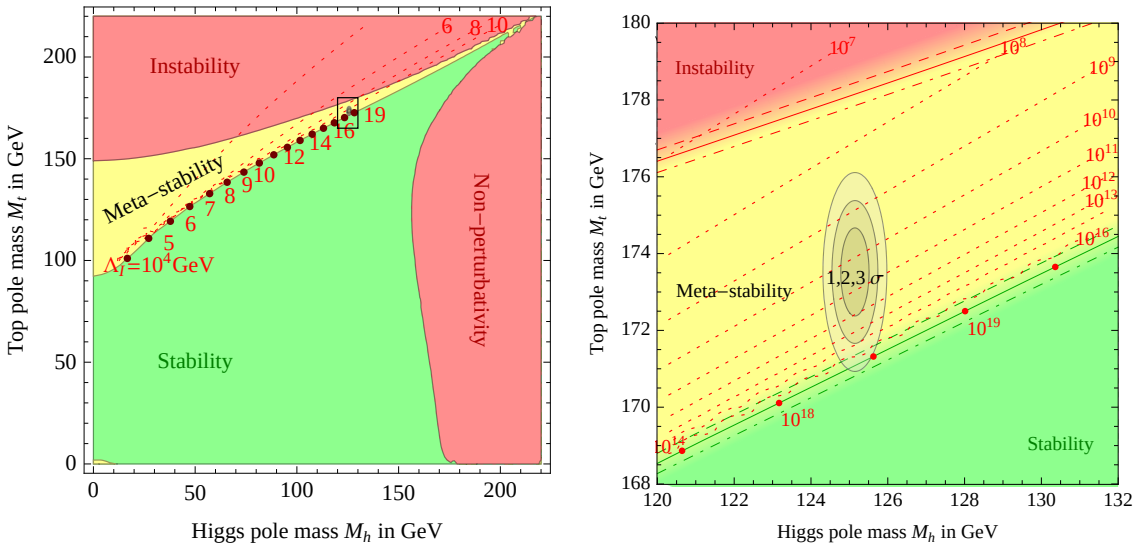

Figure 1.9: Left panel: Different regions characterising the stability of the electroweak vacuum in the top versus Higgs mass plane. Right panel: Zoom in into the region preferred by experimental measurements of the top and Higgs mass. Figure taken from [96].

current vacuum is larger than the age of the Universe, then the EW vacuum is said to be metastable. See right plot of Fig. 1.8.

3. **Instability**: The electroweak vacuum is unstable, if the new minimum is deeper and the lifetime of the current minimum is smaller than the age of the Universe. If this happens then there should be regions of our Universe in which the potential energy associated to the Higgs is much smaller and this would lead to a very fast expansion eventually modifying the vacuum expectation value throughout the Universe [97].

A detailed RG study of the Higgs potential in the SM has shown that at high scales the quartic coupling turns negative and the potential develops a new minimum [96, 97], for earlier related work on this topic see [98, 99]. Taking the central values for measurements of the Higgs and the top mass, this secondary vacuum is deeper than the electroweak vacuum and hence, given sufficient time, there is a chance the Higgs field will tunnel into it.

Requiring the age of the Universe to be larger than the lifetime of the electroweak

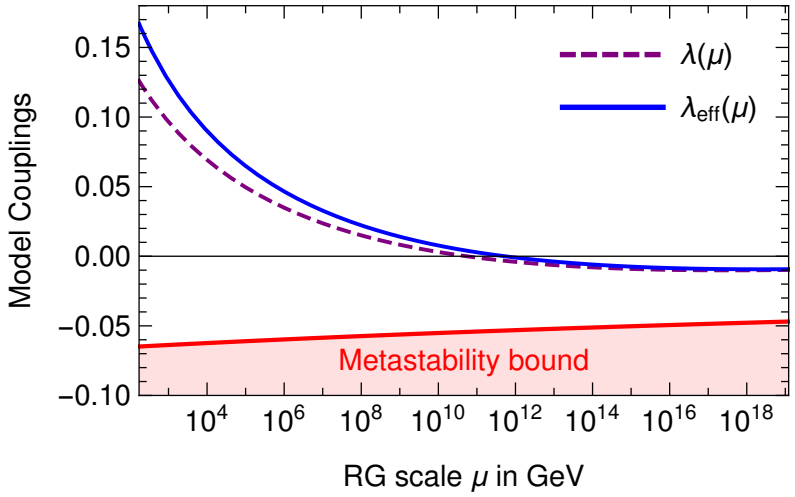

Figure 1.10: RG running of the Higgs scalar quartic. The dashed purple line corresponds to the tree-level coupling. The solid blue line is the one-loop effective scalar coupling. The red shaded region corresponds to the region where the lifetime of the electroweak vacuum is smaller than the age of the Universe.

vacuum implies a lower bound for negative values of $\lambda_{\rm eff}(\mu)$ [96]

$$|\lambda_{\rm eff}(\mu)| > \frac{2\pi^2}{3}\frac{1}{\ln(\tau\mu)}, \tag{1.5.13}$$

where $\tau = 4.35 \times 10^{17}$ s is the age of the Universe [37]. Fig. 1.9 shows the SM phase diagram that characterises the stability of the EW vacuum as a function of the top and the Higgs mass. As we can see, the experimental central values of the latter set the SM to be in the small metastability region very close to the region with absolute stability.

In Fig. 1.10 we present our result for the RG running of the effective Higgs quartic coupling taking the most up to date measurements of the Higgs and the top quark mass. Namely, $M_h = 125.09$ GeV [36] and $M_t = 172.5$ GeV [100, 101]. We have solved the two-loop β-functions and worked with the one-loop RG-improved effective potential. In addition we have taken the next-to-next-to-leading order initial conditions for the couplings as given in [96]. We find that $\lambda_{\rm eff}$ becomes negative at $\mu_{\rm inst} \approx 5.2 \times 10^{11}$ GeV. As we can see, despite the fact that the effective

Higgs quartic coupling becomes negative it remains above the metastability bound.

Although non-perturbatively it is possible to show the gauge-independence of tunnelling rates by applying Nielsen identities [102] to the false-vacuum effective action [103], in perturbative calculations the lifetime of the electroweak vacuum does show gauge-dependence [104–106]. There has been recent progress in performing a perturbative calculation of the decay rate that is gauge invariant [107, 108]. In this work, we use the Landau gauge; however, our conclusions do not change for a different choice of gauge-fixing.

1.6 CP Violation in Quantum Chromodynamics

Previously, we discussed the structure of the SM Lagrangian which is dictated by renormalisability and gauge invariance. There exists one more term that satisfies this criteria and can be added to the Lagrangian,

$$+\frac{\theta}{32\pi^2}\mathrm{Tr}[G_{\mu\nu}\widetilde{G}^{\mu\nu}] \subset \mathcal{L}_{\mathrm{SM}}, \tag{1.6.14}$$

where θ is a dimensionless quantity and $G_{\mu\nu}$ corresponds to the field strength of quantum chromodynamics (QCD) and $\widetilde{G}_{\mu\nu} \equiv \varepsilon^{\mu\nu\alpha\beta}G_{\alpha\beta}/2$ is the dual to it. The term above breaks CP (charge conjugation and parity) and P (parity) symmetries. From the conservation of CPT, this implies that T (time) symmetry is also broken. The parameter leading to an observable is the sum of θ and the overall phase of the quark mass matrix,

$$\bar{\theta} = \theta + \arg\left(\det M_q\right), \tag{1.6.15}$$

which induces an electric dipole moment (edm) for the neutron [109],

$$d_n \approx 3.6 \times 10^{-16}\,\bar{\theta}\; e\,\mathrm{cm}, \tag{1.6.16}$$

where e is the electron's electric charge. The current experimental upper limit on the edm of the neutron is $|d_n| < 2.9 \times 10^{-26}\, e\,\mathrm{cm}$ [110] which implies the following

upper bound,

$$\bar{\theta} \lesssim 10^{-10}, \tag{1.6.17}$$

explaining such a small quantity requires a fine-tuning, demanding both terms in Eq. (1.6.15) to cancel to a high level of accuracy[4]. In other words, if $\bar{\theta} \sim 1$ then the edm of the neutron should be ten orders of magnitude above current experimental limits.

The most compelling solution to this problem was proposed by Peccei and Quinn [111]. They argued that by introducing a new global chiral symmetry one could rotate away the $\bar{\theta}$ term. One possibility to implement this new symmetry is for the up-quark to be massless. However, the latter is strongly disfavoured by lattice calculations [112–114], see [36] for a review of these calculations. The second possibility is for the SM to have a global $\mathrm{U}(1)_{\mathrm{PQ}}$ chiral symmetry, this is the solution that we will discuss in the remainder of this section. As we shall see, this solution leads to the axion particle.

Soon after the work by Peccei and Quinn was published, Weinberg [115] and Wilczek [116] pointed out that since the global $\mathrm{U}(1)_{\mathrm{PQ}}$ symmetry is spontaneously broken, a massless Goldstone boson would appear in the spectrum. Due to strong dynamics in QCD at low energies, non-perturbative effects explicitly break this symmetry and the particle receives a non-zero mass from this effect, becoming then a pseudo-Goldstone boson. The latter has been named the axion particle. For a historical account of the QCD axion see [117] and for recent reviews we refer the reader to [63, 118].

In brief, the idea is to promote the $\bar{\theta}$ parameter to a dynamical field, the QCD axion $a(x)$, and provide a dynamical explanation for why the term in Eq. (1.6.14) vanishes. Due to the shift symmetry of the axion at high energies, the $\bar{\theta}$ parameter can be absorbed by setting $a \to a - \bar{\theta}$. Once non-perturbative QCD effects become

[4]We would like to mention in passing that no new symmetry is recovered in the SM Lagrangian as we set $\bar{\theta} \to 0$, this is because we already know that CP symmetry is violated in the quark sector and possibly also in the neutrino sector.

active they induce the following potential (at zero temperature),

$$V(a) \approx m_u \Lambda_{\rm QCD}^3 \left[1 - \cos\left(\frac{N_{\rm DW}\ a}{f_a}\right)\right], \tag{1.6.18}$$

where $N_{\rm DW}$ is the colour anomaly also known as the domain wall number. This potential is minimized at $a = 0$ corresponding to the CP conserving value. These non-perturbative effects also give rise to a non-zero mass to the axion of order $\Lambda_{\rm QCD}^2/f_a$. At leading order the mass of the QCD axion is given by,

$$m_a = \frac{\sqrt{m_u m_d}}{m_u + m_d}\ \frac{m_\pi f_\pi}{f_a}, \tag{1.6.19}$$

where m_π is the pion mass and f_π is the pion constant.

At low energies, after PQ symmetry breaking and QCD non-perturbative effects become active, we can write the following interaction terms for the axion,

$$\mathcal{L}_{\rm int} = -\frac{g_{a\gamma}}{4}\, a\, F_{\mu\nu}\widetilde{F}^{\mu\nu} + \frac{g_{aN}}{2m_N}\partial_\mu a(\overline{N}\gamma^\mu\gamma^5 N) + \frac{g_{ae}}{2m_e}\,\partial_\mu a\,(\overline{e}\gamma^\mu\gamma^5 e) - \frac{i}{2}g_d\, a\,\overline{N}\sigma_{\mu\nu}\gamma^5 N F^{\mu\nu}, \tag{1.6.20}$$

where $\sigma^{\mu\nu} = \frac{i}{2}\left[\gamma^\mu, \gamma^\nu\right]$, e stands for the electron field, $F_{\mu\nu}$ stands for the electromagnetic field strength and N for a nucleon that can be the proton or the neutron. All the g_i couplings in the above relation are proportional to $1/f_a$, where f_a has dimensions of energy and is referred to as the axion decay constant.

The axion decay constant is proportional to the symmetry breaking scale of the $\mathrm{U(1)_{PQ}}$ symmetry and it is usually large, $f_a \gg$ GeV, thus the axion is very weakly coupled to SM particles. The specific values of the couplings depend on the details of the ultraviolet (UV) completion, two of the most studied ones are the KSVZ [119, 120] and the DFSZ [121, 122] models. At present, values of the decay constant $f_a < 4 \times 10^8$ GeV in the KSVZ completion of the QCD axion have already been ruled out by astrophysical observations [123]. This corresponds to the exclusion of $m_a \gtrsim 0.02$ eV.

One more attractive feature of the axion is that it represents a good candidate for dark matter. Whenever the f_a scale is large, the QCD axion is very weakly

interacting and long-lived on cosmological scales. Cosmologically, once the Hubble parameter becomes smaller than the axion mass, $H < m_a$, the axion field oscillates and its energy density scales as $\rho \propto a^{-3}$ and hence it behaves as matter.

More generic axion-like particles (ALPs) can arise independently of the strong CP violation problem. For these generic ALPs, the couplings to SM particles are independent of its mass and a much larger parameter space becomes available. These particles can be motivated from different perspectives, axions as a mediator between dark matter and the visible sector [124], axion dark matter [125–127], axions from the compactifications of extra-dimensions [128] or more generic situations with multiple axions [129].

Owing to its interactions with SM particles given in Eq. (1.6.20), it is possible perform experimental searches for the axion particle. There are many ongoing experimental efforts to search for the QCD axion and ALPs, some of them include ABRACADABRA [130], ADMX [131], ALPS [132, 133], CASPEr [134, 135], CAST [136,137], IAXO [138,139] and MADMAX [140]. Axions can also be searched for at particles colliders and fixed target experiments [141, 142].

Let us now briefly discuss an example of an astrophysical constraint. Due to their coupling with photons, axions can be produced at the interior of stars and then escape, this contributes to the energy loss of the star. The lack of an observation of anomalous energy loss of Horizontal Branch (HB) stars sets the following constraint on the axion-to-photon coupling [143],

$$g_{a\gamma} < 6.6 \times 10^{-11}\ \text{GeV}^{-1}, \tag{1.6.21}$$

for axion masses $m_a \lesssim 100$ keV.

The relation between m_a, m_π and f_π in Eq.(1.6.19) does not apply to generic axion-like particles and their masses can be treated as a free parameter. Ultralight axions are commonly defined to lie in the following mass range,

$$\text{Ultralight axions}: \qquad 10^{-24}\,\text{eV} \leq m_a \leq 10^{-12}\,\text{eV}, \tag{1.6.22}$$

this mass range is difficult to test experimentally. However, there is an astrophysical effect that arises solely from gravitational effects. A cloud of ultralight axions with an astrophysical size can form surrounding rotating black holes via the mechanism of superradiance [144, 145]. This axionic cloud can produce observable signatures, such as gravitational waves [146, 147]. Astrophysical black holes have a wide range of masses, from a few solar masses to supermassive ones with $M \sim 10^6$ $M_\odot$, and therefore this mechanism can probe a large range of axion masses; namely, $10^{-18}\,\text{eV} \leq m_a \leq 10^{-12}\,\text{eV}$.

1.7 Higgs Mass and Naturalness

The mass of the Higgs boson receives quantum corrections through diagrams like the ones shown in Fig. 1.11. These diagrams give rise to two types of corrections:

- **Cutoff sensitivity:** The diagrams are quadratically divergent, and hence the Higgs mass squared receives a loop contribution proportional to the square of the cutoff scale of the SM. Namely,

$$\delta M_h^2 = \frac{1}{32\pi^2}\left[6\lambda + \frac{1}{4}(9g^2 + 3g'^2) - y_t^2\right]\Lambda^2, \tag{1.7.23}$$

  where Λ represents the cutoff scale up to which the SM remains a valid theory. However, there are regularisation schemes in which the quadratic sensitivity to the cutoff scale disappears, e.g. dimensional regularisation.

- **Mass thresholds:** If there exist heavier states coupled to the Higgs, then the Higgs mass squared will receive corrections that go quadratically as the mass of these heavier states. This contribution is not regularisation scheme dependent. Let us take as an example a new scalar ϕ with mass $M_\phi \gg M_h$ and portal coupling to the Higgs $\lambda_{h\phi}|H|^2\phi^2$. Then, the Higgs mass will receive the following contribution,

$$\delta M_h^2 \approx -\frac{1}{16\pi^2}\,\lambda_{h\phi}\,M_\phi^2, \tag{1.7.24}$$

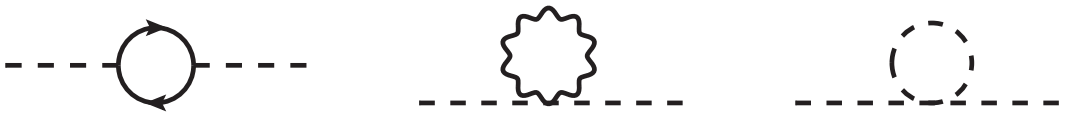

Figure 1.11: Feynman diagrams for the one-loop contributions to the Higgs mass. From left to right we show fermions, gauge and scalar loops respectively.

if we have that $\delta M_h^2 \gg M_h^2$, a large cancellation needs to take place between the tree-level mass term and this contribution in order to obtain the observed value for M_h. This high level of fine tuning is what we shall refer to as the Higgs mass naturalness problem or gauge hierarchy problem.

This issue is not present for fermions and gauge bosons, this is because as we set $m_F, m_V \to 0$ a new symmetry appears in the Lagrangian, chiral symmetry for fermions and gauge symmetry for gauge bosons. This ensures quantum corrections to be proportional to the mass itself,

$$\delta m_F^2 \propto m_F^2 \ln\left(\frac{\Lambda}{m_F}\right), \tag{1.7.25}$$

$$\delta m_V^2 \propto m_V^2 \ln\left(\frac{\Lambda}{m_V}\right), \tag{1.7.26}$$

and thus, quantum corrections to the masses cannot be too large.

In the SM the condition $\delta M_h^2 < M_h^2$ is satisfied, and therefore, there is no fine-tuning of the Higgs mass if we remain purely within the SM. However, the SM cannot be extrapolated to arbitrarily high energies since the hypercharge coupling develops a Landau pole at $\mu \approx 10^{40}$ GeV and gravitational effects might become relevant above the Planck scale. The issue of large corrections to the Higgs mass appears only when new heavy states that are directly or indirectly coupled to the Higgs boson are introduced. For a detailed discussion of the Higgs naturalness problem and different approaches to solve it we refer the reader to [148, 149].

Stating it briefly, this problem has to do with explaining the lightness of the Higgs boson. Some of the most studied solutions to this problem include supersymmetric theories (SUSY), theories with extra spacetime dimensions and theories

with a composite Higgs boson. Generally, these theories predict many new states charged under the SM gauge group with masses around the electroweak scale in order to solve this problem. Nevertheless, the absence of experimental evidence for these new states is pointing to alternative directions in model building.

An alternative path to explain the origin of the electroweak scale is the approach of classical scale invariance, in which only dimensionless couplings appear in the Lagrangian. In these models, the EW scale is dynamically generated through quantum corrections via the Coleman-Weinberg mechanism. In Section **2.3.1**, we will discuss an example where this approach can also explain why the EW scale is much smaller than the cutoff scale of the theory [150–152], although this is not the case in general.

Moreover, the approach of CSI does not provide a mechanism to protect the Higgs mass from large threshold corrections. However, when provided with a UV completion, this approach can solve this problem. In [152] it was emphasised that CSI could make the electroweak scale compatible with a high scale of new physics without requiring a large fine-tuning. This model could then be embedded in a UV theory where large threshold corrections vanish.

A possible UV completion is to embed the model in an asymptotically safe theory, in which all dimensionless couplings in the Lagrangian reach an ultraviolet fixed point. In dimensional regularisation the mass terms are multiplicatively renormalisable, and therefore, in a model with CSI the mass terms vanish at all scales. A theory with this properties is fundamental in the Wilsonian sense, since it is well-defined at arbitrarily high energies, and hence the cutoff scale is absent. Recent progress has been made in this direction [153–155].

Since the sensitivity to the cutoff scale is regularisation scheme dependent and also relies on the top Yukawa coupling, rather than the coupling of the new states to the Higgs boson, one more take on this issue is the approach of finite naturalness [156, 157]. In the latter, one ensures threshold corrections to be small by requiring BSM models to satisfy $\delta M_h^2 \leq M_h^2$. This means that even if there are new heavy states, they could be very weakly coupled to the Higgs particle and induce small quantum corrections without requiring a large cancellation to obtain M_h. Due to

the common origin of mass scales, in the CSI framework it is difficult to generate vastly different scales. Therefore, CSI provides a natural setting for models that satisfy finite naturalness.

1.8 Motivation and Outline of this Thesis

Essentially, every attempt to solve the aforementioned issues, cf. Sections **1.2**−**1.7**, includes the addition of new particles, new symmetries and (or) new forces to the SM. Namely, the fact that the SM fails to explain all aspects of the Universe, motivates theoretical and experimental efforts to go beyond it. In this thesis, we will propose concrete BSM models that provide solutions to some of these problems and study their phenomenological implications. In addition, we will discuss a new observable that can serve to detect ultralight axions beyond the SM.

Chapter **2** is based on Refs. [1, 2]. Motivated by arguments of naturalness, we discuss an approach to explain the origin of the electroweak scale. We briefly review the approach of classical scale invariance, in which all the scales in the theory are dynamically generated via the Coleman-Weinberg mechanism [150]. We perform an RG study of the inert doublet model [158, 159], a minimal extension of the SM that introduces a second scalar doublet and can account for dark matter. We also construct an extension of the IDM that has CSI. In both scenarios we find the regions in parameter space that satisfy perturbativity, unitarity and absolute vacuum stability up to the Planck scale. We also discuss a CSI extension of the SM in which neutrino masses are generated via the type-I seesaw [31–34] with GeV right-handed neutrinos. We apply the mechanism of ARS leptogenesis [42] in order to generate the baryon asymmetry of the Universe. The model also contains a good dark matter candidate and its phenomenology is studied.

Chapter **3** is partially based on Ref. [3]. We begin by presenting a brief overview of searches for WIMP dark matter at the LHC. We then introduce a new set of simplified models of dark matter to address the effects of 3-point interactions between the dark matter particle, its dark co-annihilation partner, and the Standard Model degree of freedom, which we take to be the τ-lepton. Some of these models are

manifestly gauge invariant and renormalisable. The contributions from dark matter co-annihilation channels are highly relevant for a determination of the correct relic abundance. We investigate these effects as well as the discovery potential for dark matter co-annihilation partners at the LHC and at the future e^-e^+ linear colliders, such as the ILC and CLIC. Since the DM candidate is coupled directly only to the τ-lepton in the SM, strong constraints from direct detection experiments can be avoided. In fact, as we show, the most promising search technique is using particle colliders.

Chapter **4** is based on Ref. [4]. We discuss a new observable to detect ultralight axions, the latter can be motivated by the strong CP problem [111, 115, 116], axion dark matter [125–127] or axion as a mediator between DM and the visible sector [124]. In the presence of an ultralight scalar, a cloud of these particles will form around a rotating black hole by the mechanism of superradiance [145–147]. This effect can be seen as the wave analogue of the Penrose process, in which a particle extracts angular momentum from a rotating black hole [144]. We show that as light passes through an axion cloud that surrounds a black hole, it may experience polarization-dependent bending. Consequently, a highly polarised source will be split into two images once it reaches the observer. We argue that this effect can be observed at a VLBI array of radio telescopes. The conclusions of this thesis are presented in Chapter **5**.

Chapter 2

Classically Scale Invariant Extensions of the Standard Model

The discovery of the Higgs boson [21, 22], the last undiscovered particle in the SM, has provided us an insight into how fundamental particles in the SM acquire their mass. However, the origin of the electroweak scale and why its value is many orders of magnitude smaller than the Planck scale still remains unexplained. Motivated by this, in this chapter we explore the idea of classical scale invariance (CSI) which states that there should be no mass scales in the Lagrangian at the classical level and hence all the mass scales must be generated by the dynamics of the theory. Based on Refs. [1, 2], we will discuss how this approach can be applied as a guiding principle for models beyond the SM that aim to explain its shortcomings, such as the baryon asymmetry of the Universe, the existence of dark matter and neutrino masses.

2.1 Preamble

The idea of generating a scale radiatively was originally proposed by Coleman and Weinberg in Ref. [150], where they calculated the one-loop quantum corrections to the effective potential in the $\lambda|\phi|^4$ scalar theory. In that work it was realised that if the complex scalar ϕ is charged under a local U(1) group with gauge coupling g and its quartic coupling was small, of order $\lambda \sim g^4$ (e.g. due to the RG running), then the

tree-level term and the one-loop contribution to the effective potential have the same order of magnitude and a cancellation could take place. This leads to a minimum of the potential away from zero and hence a non-zero vacuum expectation for ϕ, as illustrated in Fig. 2.1. In Section **2.2**, we briefly review scale transformations in QFT, and in Section **2.3**, we discuss the Coleman-Weinberg mechanism in further detail and provide a derivation of the one-loop effective potential in the $\lambda\phi^4$ theory.

Due to the condition $\lambda \sim g^4$, which shall be explained in Section **2.3**, one expects the scalar to be much lighter than the gauge bosons in the theory, $M_\phi \ll M_Z$. In the SM, the Higgs is actually heavier than the Z and the $W^\pm$ gauge bosons. Moreover, the RG-improved Higgs effective potential receives a large negative contribution from the top Yukawa coupling and the effective potential becomes unbounded from below up to the Planck scale.

Consequently, the Coleman-Weinberg mechanism within the SM cannot reproduce the observed value for the Higgs mass. However, it is possible to introduce a hidden Coleman-Weinberg sector and then transmit the scale to the SM via a Higgs portal interaction [160]. One of the motivations for the present chapter is to address whether classical scale invariance implemented through a Higgs portal has implications for other extensions of the Standard Model. These ideas have attracted a lot of attention recently [150–152, 160–180].

In Section **2.4**, we investigate how the dynamical generation of the electroweak scale through the Coleman-Weinberg mechanism in the hidden sector can be achieved in a model with a non-minimal Higgs sector, focusing in particular in a minimal realization of the two Higgs doublet model (2HDM) [181], which is the inert doublet model (IDM) [158, 159]. The latter was first introduced in Ref. [158], where the authors give different possibilities to achieve EWSB in the 2HDM. The IDM has become particularly attractive because it provides a natural candidate for cosmologically stable dark matter [159, 182]; namely, the lightest inert neutral scalar.

In Section **2.5**, we study a classically scale invariant extension of the Standard Model that can explain simultaneously dark matter and the baryon asymmetry in the Universe. In our set-up we introduce a dark sector, namely a non-Abelian

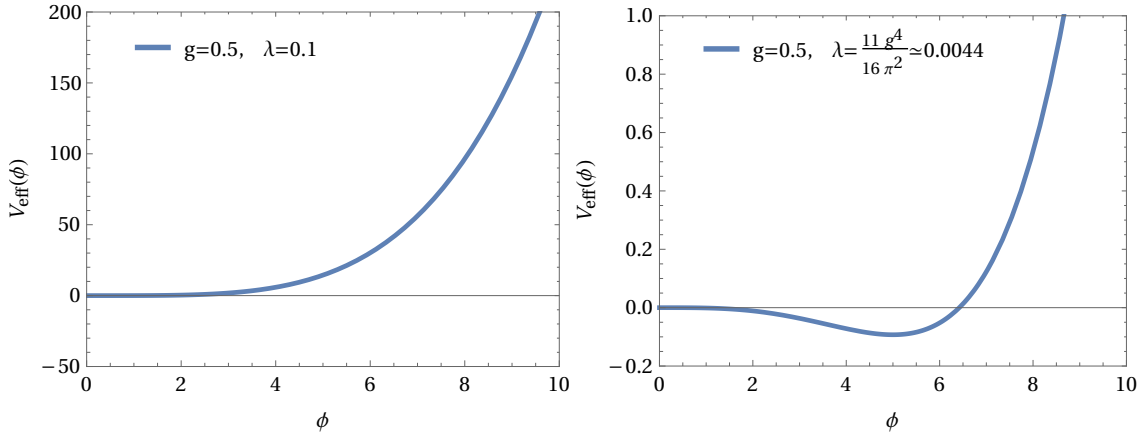

Figure 2.1: The one-loop Coleman-Weinberg effective potential for massless scalar QED, as given in Eq. (2.3.29). Left panel: The gauge and scalar quartic do not satisfy the CW condition Eq. (2.3.30) and the effective potential does not develop a new minimum. Right panel: The couplings on the right plot satisfy the CW condition and hence the effective potential develops a new minimum.

SU(2) hidden sector coupled to the SM via the Higgs portal, and a singlet sector responsible for generating Majorana masses for three right-handed sterile neutrinos. Due to a remnant SO(3) global symmetry, the gauge bosons of the dark sector are mass-degenerate and stable, and this makes them suitable as dark matter candidates. This model also accounts for the matter-anti-matter asymmetry. The lepton flavour asymmetry is produced during CP-violating oscillations of the GeV-scale right-handed neutrinos, and converted to the baryon asymmetry by the electroweak sphalerons. In Section **2.6**, we present our concluding remarks.

2.2 Scale Transformations

A scale transformation or dilatation acts on the spacetime coordinates x^μ and operators $\hat{\mathcal{O}}$ as follows,

$$x^\mu \to e^{-\varepsilon a} x^\mu, \tag{2.2.1}$$

$$\hat{\mathcal{O}} \to e^{\varepsilon \Delta} \hat{\mathcal{O}}, \tag{2.2.2}$$

where ε is a scaling parameter and Δ corresponds to the scaling dimension of the operator. In four space-time dimensions $\Delta = 1$ for a scalar field and $\Delta = 3/2$ for a fermion field. In order to study the implications of scale transformations and apply the formalism of Noether's theorem we need to consider the infinitesimal transformations corresponding to Eqs. (2.2.1) and (2.2.2). The latter are given by,

$$\delta x^\mu = -\varepsilon x^\mu, \tag{2.2.3}$$

$$\delta\phi(x^\mu) = \varepsilon(\Delta + x^\mu\partial_\mu)\,\phi(x^\mu). \tag{2.2.4}$$

We aim to find which class of theories remain invariant under these transformations. Noether's theorem implies that a given continuous transformation is a symmetry if the Lagrangian changes by a total derivative $\delta\mathcal{L} = \partial_\mu F^\mu$. Henceforth, we shall refer to the Noether current associated to scale symmetry as scale or dilatation current S^μ.

We proceed to study how scale transformations act on a Lagrangian with a fermionic field ψ and a real scalar field ϕ. We write down all renormalisable interactions as $\mathcal{L} = \mathcal{L}_1 + \mathcal{L}_2$,

$$\mathcal{L}_1 = \frac{1}{2}\partial_\mu\phi\,\partial^\mu\phi + i\overline{\psi}\gamma^\mu\partial_\mu\psi + y\,\phi\,\overline{\psi}\psi - \frac{\lambda}{4!}\phi^4, \tag{2.2.5}$$

$$\mathcal{L}_2 = -m_\psi\overline{\psi}\psi - \frac{1}{2}m_\phi\phi^2 - \frac{M}{3!}\phi^3, \tag{2.2.6}$$

we will see below the reason for writing $\mathcal{L}_1$ and $\mathcal{L}_2$ separately. Since all the operators in $\mathcal{L}_1$ have dimension four, then it follows that

$$\delta\mathcal{L}_1 = (4 + x_\mu\partial^\mu)\mathcal{L}_1 = \partial_\mu(x^\mu\mathcal{L}_1), \tag{2.2.7}$$

this means that the scale transformation is a symmetry of $\mathcal{L}_1$. On the other hand, the operators in $\mathcal{L}_2$ have dimension different than four and we find,

$$\delta\mathcal{L}_2 = -(3 + x_\mu\partial^\mu)m_\psi\overline{\psi}\psi - \frac{1}{2}(2 + x_\mu\partial^\mu)m_\phi^2\phi^2 - (3 + x_\mu\partial^\mu)\frac{M}{3!}\phi^3 \tag{2.2.8}$$

$$= \partial_\mu(x^\mu\mathcal{L}_2) + m_\psi\overline{\psi}\psi + m_\phi^2\phi^2 + \frac{M}{3!}\phi^3, \tag{2.2.9}$$

since we cannot write $\delta\mathcal{L}_2$ as a total divergence, the scale current is not conserved for these terms and we have that

$$\partial_\mu S^\mu = m_\psi \overline{\psi}\psi + m_\phi^2\phi^2 + \frac{M}{3!}\phi^3. \tag{2.2.10}$$

The important point we would like to stress here is that a theory with classical scale invariance cannot have a mass term or any scale as input in the Lagrangian, the latter must only contain dimensionless couplings as in $\mathcal{L}_1$.

More generally, if we define the symmetric energy-momentum tensor as follows

$$T^{\mu\nu} = 2\frac{\delta}{\delta g_{\mu\nu}(x)}\int d^4x\mathcal{L}, \tag{2.2.11}$$

it then becomes possible to write the scale current as

$$S^\mu = T^{\mu\nu}x_\nu, \tag{2.2.12}$$

for a detailed discussion on how to arrive to the above relation we refer the reader to section 19.5 in [183]. This is somewhat expected since we know that transformations involving spacetime coordinates are related to the energy-momentum tensor [1]. From Eq. (2.2.12) we see that

$$\partial_\mu S^\mu = T^\mu_\mu, \tag{2.2.13}$$

and hence the scale current is conserved when the energy-momentum tensor is traceless. At the classical level, the trace contains the mass terms and interactions terms with dimensionful couplings in the theory, as can be seen in Eq. (2.2.10).

As we have seen, if a theory contains only dimensionless couplings the scale current is conserved at tree-level. However, the scale symmetry can be broken by quantum corrections. Once quantum effects are taken into account, the RG running of the couplings breaks scale invariance logarithmically. For a massless non-Abelian

[1] Take for example spacetime translations $x^\mu \to x^\mu - a^\mu$ which lead to the conservation of the energy-momentum tensor $\partial_\mu T^{\mu\nu} = 0$.

gauge theory we have that [184–186]

$$\partial_\mu S^\mu = \beta(g)\mathrm{Tr}(G_{\mu\nu}G^{\mu\nu}), \tag{2.2.14}$$

where $\beta(g)$ corresponds to the renormalisation group equation for the coupling g and $G_{\mu\nu}$ is the field strength. Eq. (2.2.13) encodes the fact that quantum corrections can break the scale symmetry and is referred to as scale anomaly.

For a theory to possess exact quantum scale invariance, then quantum effects should also preserve this symmetry which means that the β-functions must vanish to all orders in perturbations theory. Theories with a large number of symmetries can have this property such as $N = 4$ super Yang-Mills theory. Also, trivial theories with no interactions such as a free massless scalar field or Abelian gauge theory have exact quantum scale invariance, while a massless non-Abelian gauge theory does not. This is due to the fact that non-Abelian gauge bosons have self-interactions and $\beta(g) \neq 0$. A theory that is described by a scale invariant Lagrangian, but has quantum corrections that break this symmetry, for example by having $\beta(g) \neq 0$, is classically scale invariant (CSI).

We know that our Universe is not scale invariant, if it were, physical processes would remain the same as we zoom in or zoom out. We know that this is not true, e.g. the physics is very different as we zoom in from galaxies to the inside of stars where thermonuclear reactions take place. Therefore, any physical theory that is based on scale invariance should also provide a mechanism to break such a symmetry. For example, the SM could be embedded in a UV theory where exact scale symmetry is restored at very large energies.

2.3 The Coleman-Weinberg Mechanism

In this section, we review the Coleman-Weinberg [150] mechanism, cf. [187], in which radiative corrections generate a non-zero vacuum expectation value (vev) in a theory that has no scales to begin with. First, we will consider the case of a single massless scalar and show that the regime where this mechanism works lies outside

the perturbative regime. We will then consider a massless complex scalar field charged under a U(1) gauge symmetry and give the condition for the mechanism to work. The latter will be the main focus of this chapter. We will follow the original work [150] and present a derivation based on calculating Feynman diagrams with vev insertions.

First, we will study a theory with a single massless scalar field. The Lagrangian of this theory is given by

$$\mathcal{L} = \frac{1}{2}\partial_\mu\phi\,\partial^\mu\phi - \frac{\lambda}{4!}\phi^4 + \left[\frac{1}{2}\delta_\phi\,\partial_\mu\phi\,\partial^\mu\phi - \frac{1}{2}\delta_m\phi^2 - \frac{1}{4!}\delta_\lambda\phi^4\right], \tag{2.3.15}$$

where ϕ is a real scalar and the counterterms δ_ϕ, δ_m and δ_λ absorb the divergences in the loop contributions to the scalar self-energy, the mass and the four-point scalar vertex respectively.

The diagrams that contribute to the one-loop effective potential take the form of a single loop with an arbitrary number of ϕ_c^2 insertions, the latter correspond to the vacuum expectation value of ϕ. The diagrams are shown in Fig. 2.2 and give the following contribution

$$\Delta V = i\int \frac{d^4k}{(2\pi)^4}\sum_{n=1}^{\infty}\frac{1}{2n}\left(\frac{\lambda\phi_c^2}{2(k^2+i\varepsilon)}\right)^n, \tag{2.3.16}$$

the factor of i comes from the path integral, the factor $1/2n$ comes from $1/n$ rotations and $1/2$ reflections of the loop that do not change the diagram and hence the $1/n!$ in Dyson's formula is not completely cancelled.

Applying a Wick rotation and and making use of the following identity

$$\sum_{n=1}^{\infty}\frac{1}{n}(-1)^{n+1}x^n = \ln(1+x) \qquad \text{for} \quad |x|<1, \tag{2.3.17}$$

we can rewrite the integral in Eq. (2.3.16) as

$$\Delta V = -\int \frac{d^4k_E}{(2\pi)^4}\sum_{n=1}^{\infty}\frac{(-1)^n}{2n}\left(\frac{\lambda\phi_c^2}{2(k_E^2+i\varepsilon)}\right)^n = \frac{1}{2}\int\frac{d^4k_E}{(2\pi)^4}\ln\left(1+\frac{\lambda\phi_c^2}{2k_E^2}\right), \tag{2.3.18}$$

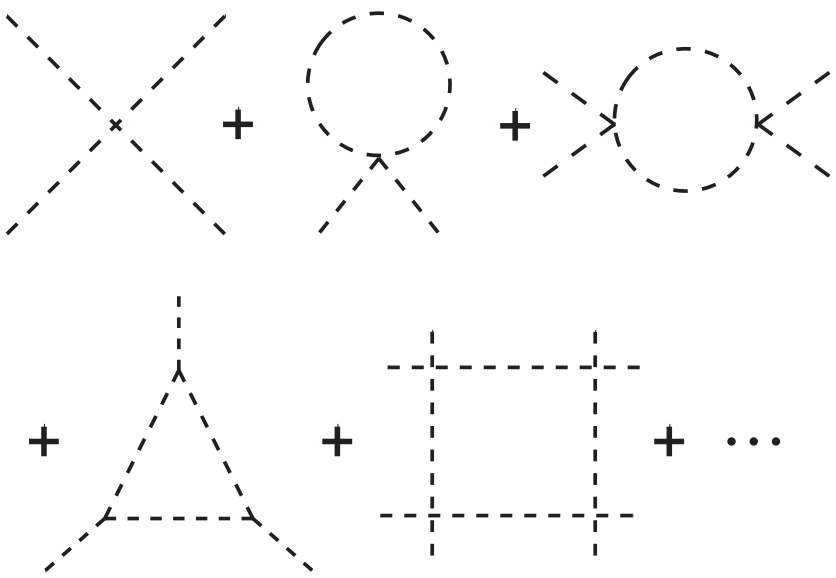

Figure 2.2: Feynman diagrams that contribute to the one-loop effective potential in the $\lambda\phi^4/4!$ theory.

although each term in the sum has an IR divergence summing over all diagrams makes it IR finite. The integral still has a UV divergence and in order to evaluate it we will apply the cutoff regularisation method. Namely, we will evaluate the integral up to a cutoff scale $k_E = \Lambda$, in Section **2.4.1** we will see that the same final result is obtained in the $\overline{\text{MS}}$ scheme,

$$\int_0^\Lambda d^4k_E \ln\left(\frac{k_E^2+a^2}{k_E^2}\right) = \frac{\pi^2}{4}\Lambda^4\left[1-2\ln(\Lambda^2)\right] + 2\pi^2\left[\frac{1}{4}a^4\ln(a^2)+\frac{1}{4}a^2\Lambda^2-\frac{1}{8}\Lambda^4-\frac{1}{4}(a^4-\Lambda^4)\ln(a^2+\Lambda^2)\right],$$

the term on the first line just adds a constant term to the potential and can be ignored. Regarding the term on the second line, we can also ignore the constant terms, then we expand in powers of a^2/Λ^2 take the limit $\Lambda \to \infty$ and keep only the non-vanishing terms. The one-loop contribution to the potential then takes the form

$$\Delta V = \frac{1}{16\pi^2}\left[\frac{1}{4}\lambda\phi^2\Lambda^2 - \frac{1}{32}\lambda^2\phi^4 + \frac{1}{16}\lambda^2\phi^4\ln\left(\frac{\lambda\phi^2}{2\Lambda^2}\right)\right]. \tag{2.3.19}$$

To find the value of the counterterms we need to impose renormalisation con-

ditions, the renormalised mass should vanish at the origin and the renormalised quartic coupling can be defined at an arbitrary scale μ,

$$\frac{d^2V(\phi)}{d\phi^2}\Big|_{\phi=0} = 0, \qquad \frac{d^4V(\phi)}{d\phi^4}\Big|_{\phi=\mu} = \lambda, \tag{2.3.20}$$

from these two conditions we find that

$$\delta_m = -\frac{\lambda\Lambda^2}{32\pi^2}, \qquad \delta_\lambda = -\frac{3\lambda^2}{32\pi^2}\left[\ln\left(\frac{\lambda\mu^2}{2\Lambda^2}\right) + \frac{11}{3}\right]. \tag{2.3.21}$$

After substituting back the value of the counterterms we find the final expression for the one-loop effective potential

$$V_1(\phi) = \frac{\lambda}{4!}\phi^4 + \frac{\lambda^2\phi^4}{256\pi^2}\left[\ln\left(\frac{\phi^2}{\mu^2}\right) - \frac{25}{6}\right], \tag{2.3.22}$$

requiring a new minimum to appear away from $\phi = 0$ gives the following condition

$$\lambda\ln\left(\frac{\phi^2}{\mu^2}\right) = -\frac{32}{3}\pi^2 + \frac{11}{3}\lambda, \tag{2.3.23}$$

the first term on the right hand side is quite large. From Eq. (2.3.30) we are required to have $\lambda\ln(\phi^2/\mu^2) \approx -105$ which is far outside the validity of the one-loop approximation, since higher order corrections will introduce higher powers of $\lambda\ln(\phi^2/\mu^2)$. Therefore, for a single massless scalar field it is not possible to generate a non-zero vev from quantum corrections to the effective potential. This mechanism was generalised and shown to work for a theory with multiple scalars in Ref. [188], we will review this approach in Section **2.5.1**.

Now we turn to study the case where a complex scalar $\Phi = (\phi + i\chi)/\sqrt{2}$ is charged under a local U(1) gauge symmetry. The Lagrangian density is given by

$$\mathcal{L} = D^\mu\Phi^\dagger D_\mu\Phi - \lambda(\Phi^\dagger\Phi)^2 - \frac{1}{4}F_{\mu\nu}F^{\mu\nu}, \tag{2.3.24}$$

the covariant derivative acts on the scalar field as follows

$$D_\mu\Phi = (\partial_\mu - igA_\mu)\Phi, \tag{2.3.25}$$

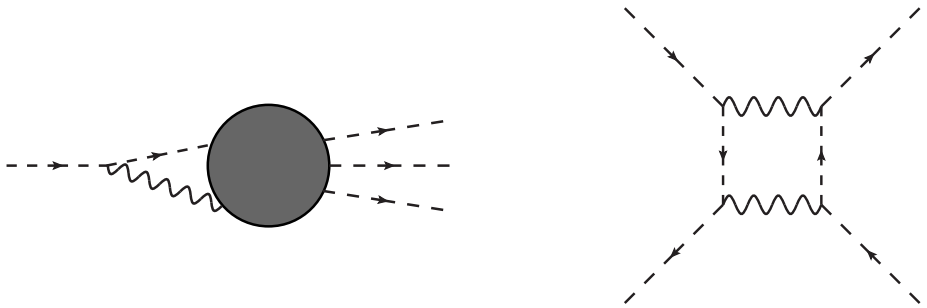

Figure 2.3: Left panel: Class of diagrams with vanishing contribution to the effective potential. Right panel: One example of a diagram that does not contribute to effective potential.

and $F_{\mu\nu} = \partial_\mu A_\nu - \partial_\nu A_\mu$ corresponds to the gauge field strength.

In the Landau gauge the gauge field propagator $D_{\mu\nu}(k)$ at tree-level is given by

$$D_{\mu\nu}(k) = \frac{-iP_{\mu\nu}(k)}{k^2 + i\varepsilon}, \qquad P_{\mu\nu}(k) = \eta_{\mu\nu} - \frac{k_\mu k_\nu}{k^2 + i\varepsilon}, \tag{2.3.26}$$

and satisfies the following identities

$$k^\mu D_{\mu\nu}(k) = k^\nu D_{\mu\nu}(k) = 0. \tag{2.3.27}$$

Since the computation of the effective potential involves external scalar legs with vanishing external momenta, by means of the identity in Eq. (2.3.27) all the diagrams of the type shown in Fig. 2.3 will not contribute to the effective potential. This is because the momentum of the internal scalar is equal to the one of the gauge boson, therefore when contracted with the gauge boson propagator it vanishes (the vertex is proportional to the momentum of the scalar field).

The diagrams that contribute to the effective potential are those shown in Fig. 2.2 and also those involving gauge bosons in the loop. Following the same procedure as before, the one-loop potential is given by

$$V_1(\phi) = \frac{\lambda}{4}\phi^4 + \left(\frac{5\lambda^2}{32\pi^2} + \frac{3g^4}{64\pi^2}\right)\phi^4\left[\ln\left(\frac{\phi^2}{\mu^2}\right) - \frac{25}{6}\right], \tag{2.3.28}$$

when compared to Eq. (2.3.22) this potential has a new term that goes as g^4. If we take λ to be order g^4 this new term competes with the tree-level term and the

potential could develop a new minimum within perturbative values of the couplings.

Following our previous discussion, by taking $\lambda \sim g^4$ we can ignore the λ^2 term in Eq. (2.3.28) and write the one-loop potential as

$$V_1(\phi) = \frac{\lambda}{4}\phi^4 + \frac{3g^4\phi^4}{64\pi^2}\left[\ln\left(\frac{\phi^2}{\mu^2}\right) - \frac{25}{6}\right], \tag{2.3.29}$$

this potential might develop a new minimum at a non-zero field value $\phi = \langle\phi\rangle$. We can set the RG scale at the value of this minimum $\mu = \langle\phi\rangle$, and then, by imposing the condition that a new minimum appears $V'(\langle\phi\rangle) = 0$ we find the Coleman-Weinberg relation between the scalar and the gauge coupling,

$$\lambda = \frac{11}{16\pi^2}g^4 \qquad \text{at} \quad \mu = \langle\phi\rangle. \tag{2.3.30}$$

On the left panel in Fig. 2.1 we show the one-loop effective potential for arbitrary values of the couplings that do not satisfy the above relation. On the right panel the above relation is satisfied and one can see how the potential develops a new minimum.

This non-zero vacuum expectation value $\langle\phi\rangle$ leads to spontaneous symmetry breaking breaking of the U(1) gauge symmetry. This implies that the scalar and the gauge boson acquire the following masses,

$$m_S^2 = V''(\langle\phi\rangle) = \frac{3g^4}{8\pi^2}\langle\phi\rangle^2, \qquad m_V^2 = g^2\langle\phi\rangle^2, \tag{2.3.31}$$

since the g coupling is perturbative, one of the implications of the CW mechanism is that the scalar is much lighter than the gauge boson, $m_S \ll m_V$.

It is interesting to note that due to the common origin of the scalar and the gauge boson mass, the ratio of their masses is independent of $\langle\phi\rangle$,

$$\frac{m_S^2}{m_V^2} = \frac{3g^2}{8\pi^2}. \tag{2.3.32}$$

In fact, all dimensionless quantities depend only on the gauge coupling g. The dimensionless coupling λ has been replaced by the mass parameter $\langle\phi\rangle$. This is

the mechanism of dimensional transmutation, in which a dimensionless quantity is converted into a physical scale $\langle\phi\rangle \neq 0$. Quoting the original paper [150]:

> The surprising thing is that we have traded a dimensionless parameter, λ, on which physical quantities can depend in a complicated way, for a dimensional one, $\langle\phi\rangle$, on which physical quantities must depend in a trivial way, governed by dimensional analysis.

2.3.1 Naturalness

In the Introduction we discussed the issue of naturalness of the Higgs mass. Naively, the Higgs mass will receive corrections proportional to the energy cutoff of the theory. More concretely, if there is a new heavier scalar with mass M_S and portal coupling to the Higgs λ_P, then the Higgs mass will receive corrections proportional to that value $\delta M_h^2 \propto \lambda_P\, M^2$.

It can be shown that the vev generated from the Coleman-Weinberg mechanism is exponentially smaller than the UV cutoff. As an example let us consider a scalar charged under a local U(1) gauge symmetry, the latter having coupling g. Due to the RG running, g develops a Landau pole at some scale $\Lambda_{\rm UV}$ which characterizes the cutoff scale of the theory. This can be seen by solving the RG equation for the gauge coupling g [152],

$$\frac{dg}{dt} = \frac{g^3}{48\pi^2}, \qquad \text{where} \quad t = \ln\left(\frac{M}{\Lambda_{\rm UV}}\right), \tag{2.3.33}$$

from this equation we see that the gauge coupling will grow as the RG scale increases, eventually reaching a Landau pole. After integrating Eq. (2.4.64) and setting the RG scale to $\mu = \langle\phi\rangle$ we find that

$$\langle\phi\rangle = \Lambda_{\rm UV} \exp\left[-24\pi^2\left(\frac{1}{g^2(\langle\phi\rangle)} - \frac{1}{g^2(\Lambda_{\rm UV})}\right)\right] \approx \Lambda_{\rm UV} \exp\left[\frac{-24\pi^2}{g^2(\langle\phi\rangle)}\right], \tag{2.3.34}$$

and hence the generated vev $\langle\phi\rangle$ is exponentially smaller than the cutoff scale of the theory. This explains the smallness of the scalar mass when compared to the UV cutoff scale.

Moreover, from a naturalness perspective the approach of CSI is attractive, since all scales have a common origin and hence it is difficult to generate vastly different scales in the theory. However, this mechanism does not provide a full solution to the hierarchy problem since it is unable to protect the CW scalar from large threshold corrections, e.g. if there exists a much heavier particle coupled to it.

2.3.2 Asymptotic Freedom and Safety

There has been recent progress in constructing UV-complete models where all the couplings reach a fixed point in the UV, the fixed points can either be be non-interacting, where the coupling goes to zero (asymptotic freedom), or interacting, where the coupling goes to a finite value (asymptotic safety). These fixed points g_i^* correspond to the zeros of the β-function $\beta_i(g_i^*) = 0$. Asymptotic safety was recently shown to exist for gauge-Yukawa theories in a perturbative manner [153] and has attracted recent attention [189–196]. Theorems for weakly interacting theories with asymptotic safety have been established in [197, 198]. In [154], the authors provide a prescription for constructing extensions of the SM in which the weak and strong coupling constants reach perturbative fixed points in the UV, but the hypercharge still suffers from a Landau pole.

An alternative approach to achieve an interacting UV-fixed point for a gauge coupling, associated to the gauge group G, is to add a large number (N_F) of fermions charged under G and perform a $1/N_F$ expansion in the computation of the β-functions [199–201][2]. Recently, the large-N_F resummed contributions to the RG equations were computed in [203] for generic semi-simple groups. In [204], a large number of vector-like fermions were added to the SM in order to ensure the asymptotic safety of the gauge couplings; nevertheless, this calculation was completed without the inclusion of the large-N_F resummation for the Yukawa and the Higgs quartic.

The large-N_F resummation was performed for a Yukawa coupling in [155,205]. In

[2]For a different proposal to achieve asymptotic safety due to an energy cutoff in the theory above which there are no quantum fluctuations see [202].

the latter work, the resummation was also computed for a scalar quartic coupling. These results were applied in [155] to extensions of the SM by a large number N_F of charged fermions in order to make the strong or the weak gauge coupling asymptotically safe in the UV. Nonetheless, in that study it was shown that when one makes the hypercharge coupling safe in the UV, the Higgs quartic is driven to large non-perturbative values. This is because the location of the pole in the resummed functions for the Yukawa and the scalar quartic has the same location as the one in the Abelian case.

This class of theories represent a natural completion to models with CSI where all mass parameters are set to zero, and remain zero at all scales due to the multiplicative renormalisability of the mass parameters in dimensional regularisation. A theory with classical scale invariance in which all the dimensionless couplings reach an ultraviolet fixed point is fundamental according to the Wilsonian definition and hence it is sheltered from any UV cutoff.

2.4 Classical Scale Invariance in the Inert Doublet Model

The inert doublet model (IDM) is a minimal extension of the SM that can explain dark matter, it introduces a second complex doublet H_2 and a discrete Z_2 symmetry such that

$$H_1 \to H_1, \qquad H_2 \to -H_2,$$

where H_1 stands for the Standard Model Higgs doublet and all the fields in the SM are even under this Z_2 symmetry, meaning that H_2 has no tree-level couplings to the SM fermions. The potential in this model is given by

$$\begin{aligned} V_{\text{IDM}} &= \mu_1^2|H_1|^2 + \mu_2^2|H_2|^2 + \lambda_1|H_1|^4 + \lambda_2|H_2|^4 + \lambda_3|H_1|^2|H_2|^2 + \lambda_4|H_1^\dagger H_2|^2 \\ &\quad + \frac{1}{2}\lambda_5[(H_1^\dagger H_2)^2 + (H_2^\dagger H_1)^2], \end{aligned} \tag{2.4.35}$$

expanding the two doublets in their components we have

$$H_1 = \begin{pmatrix} G^+ \\ \frac{1}{\sqrt{2}}(v+h+iG) \end{pmatrix}, \qquad H_2 = \begin{pmatrix} H^+ \\ \frac{1}{\sqrt{2}}(H+iA) \end{pmatrix},$$

the inert doublet consists of a neutral CP-even scalar H, a neutral CP-odd scalar A and a pair of charged scalars $H^\pm$.

Imposing the requirement of an exact Z_2 symmetry means that the inert H_2 does not acquire a vacuum expectation value (vev), so the lightest particle in the inert doublet is stable and if it is one of the neutral scalars it can be studied as a dark matter candidate. For the rest of this work we consider $M_H < M_A,\ M_{H^+}$, and hence we take H to be the dark matter candidate, similar results apply if one takes A to be the lightest. The vevs for the doublets then read

$$\langle H_1 \rangle = \frac{v}{\sqrt{2}}, \qquad \langle H_2 \rangle = 0, \tag{2.4.36}$$

where $v = 246$ GeV, and the mass of the SM Higgs boson is given by the usual relation $M_h^2 = -2\mu_1^2 = 2\lambda_1 v^2$ which we fix to 125 GeV. The masses of the two neutral scalars, H and A, and the charged, $H^\pm$, are given by

$$M_H^2 = \mu_2^2 + \frac{1}{2}(\lambda_3+\lambda_4+\lambda_5)v^2, \tag{2.4.37}$$

$$M_A^2 = \mu_2^2 + \frac{1}{2}(\lambda_3+\lambda_4-\lambda_5)v^2, \tag{2.4.38}$$

$$M_{H^\pm}^2 = \mu_2^2 + \frac{1}{2}\lambda_3 v^2. \tag{2.4.39}$$

We define the mass splittings $\Delta M_A = M_A - M_H$ and $\Delta M_{H^\pm} = M_{H^\pm} - M_H$, where the mass splitting between A and H is determined by λ_5 and since we consider $M_H < M_A$ we take λ_5 to be negative. It is convenient to work with the coupling

$$\lambda_L \equiv \frac{\lambda_3+\lambda_4+\lambda_5}{2},$$

which determines the interaction between inert scalars and the SM Higgs boson.

This section is structured as follows, in Section **2.4.1**, we start by showing how

the CW mechanism can be applied to the inert doublet model with the addition of a hidden sector and then perform a scan on the free parameters of the theory. In Section **2.4.1**, we measure the impact of introducing this hidden sector on the calculation of the relic density, and in Section **2.4.1**, we calculate the spin-independent nucleon cross-section and compare with current and future limits from direct detection experiments. In Section **2.4.2**, we perform the RG analysis on the model and show that some points satisfy vacuum stability, perturbativity, and unitarity up to the Planck scale.

2.4.1 Dark Matter Phenomenology

In our approach there are no mass scales in the classical Lagrangian and all masses need to be generated dynamically via dimensional transmutation. We cannot directly apply the Coleman-Weinberg mechanism to the Standard Model because the Higgs mass is larger than the mass of the gauge bosons and also the large negative contribution from the top quark makes the effective potential unbounded from below. Nevertheless, it has been shown [152, 160] that we can still have classical scale invariance in the SM if we introduce a hidden sector with a complex scalar Φ and a $\mathrm{U}(1)_{\mathrm{CW}}$ gauge symmetry in which the symmetry is broken via the CW mechanism and the vev is communicated to the SM Higgs boson via a portal coupling.

One possibility to account for the dark matter in the Universe in CSI models with a hidden sector is to extend the $\mathrm{U}(1)_{\mathrm{CW}}$ to a larger group, e.g. it has been shown that for $\mathrm{SU}(2)_{\mathrm{CW}}$ the vector bosons can account for a portion of dark matter and a scalar gauge singlet can be introduced to account for the rest of dark matter [177]. In this section, we adhere to the minimal case of having a $\mathrm{U}(1)_{\mathrm{CW}}$ symmetry and a single complex scalar Φ in the hidden sector and in order to account for dark matter we extend the SM by adding an $\mathrm{SU}(2)_L$ vevless doublet.

Since the second doublet in the IDM does not acquire a vev we will apply a similar mechanism as in Ref. [152]. In this case we introduce a second portal coupling between the CW scalar and the inert doublet, $\lambda_{\mathrm{P}2}$, in order to generate the quadratic term for H_2 after the CW scalar acquires a vev. The idea of classical scale invariance

has been applied before to the IDM [206], but in that case the authors consider the Coleman-Weinberg mechanism within the IDM, they found this gives a small DM mass $M_{\rm DM} < M_W$ and large quartic couplings $\mathcal{O}(1)$ meaning that this model cannot remain perturbative at high energies. Recently, the authors of [207] introduced heavy right-handed neutrinos with a Majorana mass to the IDM in order to generate the mass scale parameters via radiative corrections, while in order to generate the Majorana mass they outline a mechanism in which there is some strong dynamics in a hidden sector with vanishing couplings to the Higgs doublets.

In the inert doublet model with CSI the potential is given by

$$\begin{aligned} V_{\rm CSI} &= \lambda_1|H_1|^4 + \lambda_2|H_2|^4 + \lambda_3|H_1|^2|H_2|^2 + \lambda_4|H_1^\dagger H_2|^2 + \frac{1}{2}\lambda_5[(H_1^\dagger H_2)^2 + (H_2^\dagger H_1)^2] \\ &\quad +\lambda_\phi|\Phi|^4 - \lambda_{\rm P1}|\Phi|^2|H_1|^2 + \lambda_{\rm P2}|\Phi|^2|H_2|^2, \end{aligned} \tag{2.4.40}$$

where $\Phi = (\phi + i\chi)/\sqrt{2}$, so ϕ is the CW scalar that will induce the breaking of the symmetries and χ is the would-be Goldstone boson of the broken $\mathrm{U}(1)_{\rm CW}$ in the hidden sector. Focusing only on the CW sector and working with the one-loop contributions proportional to $e_{\rm CW}^4$, where $e_{\rm CW}$ denotes the gauge coupling in the hidden sector, the effective potential for ϕ in the $\overline{\rm MS}$ scheme reads

$$V_1(\phi;\mu) = \frac{\lambda_\phi(\mu)\phi^4}{4} + \frac{3e_{\rm CW}(\mu)^4}{64\pi^2}\phi^4\left(\ln\left(\frac{\phi^2}{\mu^2}\right) - \frac{25}{6}\right). \tag{2.4.41}$$

This potential will develop a non-zero vev, $\langle\phi\rangle \neq 0$ if the following relation between the scalar and gauge coupling is satisfied[3]

$$\lambda_\phi = \frac{11}{16\pi^2}e_{\rm CW}^4. \tag{2.4.42}$$

After symmetry breaking takes place in the hidden sector, we obtain the following

[3]For more details on the CW symmetry breaking in the hidden sector we refer the reader to Ref. [177].

masses

$$M_\phi = \sqrt{\frac{3}{8}}\frac{e_{\rm CW}^2}{\pi}\langle\phi\rangle, \tag{2.4.43}$$

$$M_{Z'} = e_{\rm CW}\langle\phi\rangle, \tag{2.4.44}$$

the mass of the Coleman-Weinberg scalar is much lower than the mass of the vector boson Z', $M_\phi \ll M_{Z'}$. The value of M_ϕ is usually obtained around the weak scale, but it can take values from a few MeVs to a few TeVs. Once we take into account the portal couplings (2.4.40), the CW condition for λ_ϕ (2.4.42) and the mass of the CW scalar (2.4.43) are modified as follows

$$\lambda_\phi = \frac{11}{16\pi^2}e_{\rm CW}^4 + \lambda_{\rm P1}\frac{v^2}{2\langle\phi\rangle^2}, \tag{2.4.45}$$

$$M_\phi^2 = \frac{3e_{\rm CW}^4}{8\pi^2}\langle\phi\rangle^2 + \lambda_{\rm P1}\,v^2. \tag{2.4.46}$$

Once the CW scalar ϕ acquires a vev, the mass parameters for the Higgs doublets will be generated through the portal couplings

$$\mu_1^2 = -\lambda_{\rm P1}\frac{\langle\phi\rangle^2}{2}, \tag{2.4.47}$$

$$\mu_2^2 = +\lambda_{\rm P2}\frac{\langle\phi\rangle^2}{2}, \tag{2.4.48}$$

to trigger electroweak symmetry breaking (EWSB) we need $\mu_1 < 0$. This was our motivation to choose a negative sign for $\lambda_{\rm P1}$ in the potential, so that we can work with $\lambda_{\rm P1} > 0$. Once EWSB occurs the two vevs in the model are connected via the relation

$$\langle\phi\rangle = \sqrt{\frac{2\lambda_1}{\lambda_{\rm P1}}}\,v, \tag{2.4.49}$$

and the portal couplings also obey the relation

$$\lambda_{\rm P2} = \frac{2\mu_2^2}{\langle\phi\rangle^2} = \frac{\lambda_{\rm P1}\mu_2^2}{\lambda_1 v^2}. \tag{2.4.50}$$

Since the CW scalar acquires a vev, due to the portal coupling $\lambda_{\rm P1}$, ϕ will mix with the SM Higgs boson. The mass eigenstates $h_{\rm SM}$ and $h_{\rm CW}$ are linear combinations of

the fields h and ϕ

$$h_{\rm SM} = h\cos\theta - \phi\sin\theta, \tag{2.4.51}$$

$$h_{\rm CW} = \phi\cos\theta + h\sin\theta, \tag{2.4.52}$$

where θ is the mixing angle and we fix the mass of $h_{\rm SM}$ to $M_{h_{\rm SM}} = 125$ GeV hereafter. There have been many studies to constrain this mixing angle [208–210]. For CW scalar masses in the range 130 GeV to 1 TeV we impose the constraint $\sin^2\theta < 0.15$; for masses $M_{h_{\rm CW}} < M_{h_{\rm SM}}/2$ we use the bounds from [152]; and in the intermediate region $62.5 < M_{h_{\rm CW}} < 120$ GeV we impose $\sin\theta < 0.44$.

Dark matter relic density

In this work we consider H to be the lightest inert particle, which due to the Z_2 symmetry is stable and is a good dark matter candidate. For the calculation of the relic density and the direct detection cross-section we implement our model in `MicrOMEGAs 4.1.5` [211]. Previous studies of the IDM [212, 213] have shown that there are two mass regions in which H can play the role of DM:

1. $50 < M_H < 80$ GeV

   In this region the annihilation is mainly into $b\bar{b}$ and three body final states WW^* and requires small values for λ_L, otherwise the $b\bar{b}$ dominates and the relic density obtained is too small. Once we have $M_H \geq M_W$ the $HH \to VV$ channel opens up and we obtain smaller values for the relic density. Due to a careful cancellation between diagrams that contribute to the annihilation into gauge bosons [214], this region can be extended to 110 GeV, however, this new viable region has already been excluded by XENON100 [215]. Constraints from colliders already exclude $M_H < 55$ GeV in some cases [216, 217] and Run 2 of the LHC could be able to probe the Higgs funnel region $M_H \approx M_{h_{\rm SM}}/2$.

2. $M_H > 500$ GeV

   In this region, the dominant annihilation is into W^+W^-, ZZ and hh. The values obtained for the relic density are usually too small. Nonetheless, by taking

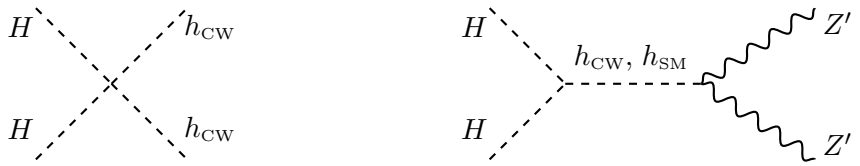

Figure 2.4: Feynman diagrams for two of the new annihilation channels from adding a $\mathrm{U}(1)_{\rm CW}$ hidden sector to the inert doublet model. These contributions reduce the relic abundance in the classically scale invariant version of the IDM. Similar diagrams are also taken into account for coannihilations.

small mass splittings and an appropriate value for λ_L the correct relic abundance can be obtained. The largest contribution to $HH \to VV$ comes from longitudinal gauge boson components and when H and A or $H^\pm$ are nearly mass-degenerate there is a cancellation among the t/u channel contributions and the four-vertex diagram [213] and hence the correct relic abundance can be obtained. General perturbativity bounds translate into an upper limit $M_H < 58$ TeV [218], while a more conservative bound $\lambda_i \leq 2$ gives an upper limit $M_H < 5$ TeV [219].

For intermediate masses 130 GeV $< M_H <$ 500 GeV the annihilation into gauge bosons is no longer suppressed and generates too small relic abundances. In region 1, annihilation into a final state which contains the CW scalar $h_{\rm CW}$ will only have impact on the relic density if $M_{h_{\rm CW}}$ is also small, but for masses $M_{h_{\rm CW}} < M_{h_{\rm SM}}/2$ current LHC constraints give a strong bound $\lambda_{\rm P1} \lesssim 2 \times 10^{-5}$ [152]. In this region $\lambda_{\rm P2} \approx \lambda_{\rm P1}$ and hence $h_{\rm CW}$ will have no impact on DM annihilation, if we want to study the impact of the CW hidden sector in the dark matter phenomenology and the RG analysis, then we must focus on the large mass region $M_H > 500$ GeV.

The parameter λ_2, being the quartic coupling between inert scalars, has no impact on the computation of the relic density at leading order. Nonetheless, this parameter will have an impact on the RG analysis, so we scan over the whole perturbative regime. In the heavy mass region due to the destructive interference of diagrams, as we decrease the mass splittings of the inert scalars the cross-section decreases and hence we have an increase in the relic density. Moreover, the mass splittings cannot be too large due to the perturbativity of the scalar couplings, com-

bining this with the DM relic abundance it has been shown [213] that they cannot be larger than ≈ 20 GeV. In summary, one can select the value of λ_L and ΔM_i in order to get the correct relic density for different values of M_H.

We proceed to perform the calculation of the dark matter relic abundance for region 2, the high mass regime. In Fig. 2.4 we show two of the new annihilations channels that we need to study in the CSI IDM compared to the ordinary IDM. To exemplify the impact of adding a CW hidden sector we focus on the case $\lambda_L = 0$, in this scenario the interactions between the inert particles and the Higgs boson are highly suppressed, they only occur through mixing of h with ϕ and hence it is possible to avoid constraints coming from direct detection experiments.

In Fig. 2.5 we show the effect of adding the new annihilation channels on the calculation of the relic density for different values of the portal coupling. The values for the relic density are smaller and the dark matter mass giving the correct relic density goes up. It is interesting to note that for $\lambda_{\rm P1} = 0.005$ there is a whole region for $M_H \approx [900, 1300]$ GeV in which the correct relic abundance is obtained to 2σ. It is important to remark that due to CSI the parameters of the theory need to satisfy certain relations, Eqs.(2.4.45 - 2.4.50), which distinguishes our model from a singlet extension of the IDM [220].

Annihilation into the hidden gauge boson Z' (diagram on the right in Fig. 2.4) is also possible, but since $\langle\phi\rangle \gg v$ in most cases we get $M_{Z'} > M_H$, where this annihilation channel is closed. Nonetheless, this effect can be visualized in the third case (brown line) of Fig. 2.5, where the relic density has a sudden drop near the threshold $M_{Z'} \approx 1.6$ TeV. By introducing annihilation of H into the CW scalar $h_{\rm CW}$ and the hidden gauge boson Z', we open a small new region in the parameter space of the IDM that can lead to the correct relic abundance. Nevertheless, later we will show that the RG analysis enforces the CSI IDM to be more constrained than the traditional IDM. Also, due to the CSI conditions, Eqs.(2.4.45 - 2.4.50), our model is more predictive than simply adding a hidden sector with a local U(1) gauge symmetry to the IDM. Once we fix the mass M_H and the mass splittings, the parameter μ_2^2 gets fixed; on the other hand the portal coupling $\lambda_{\rm P1}$ is constrained from LHC data and hence we can use Eq. (2.4.50) to also fix the value of $\lambda_{\rm P2}$.

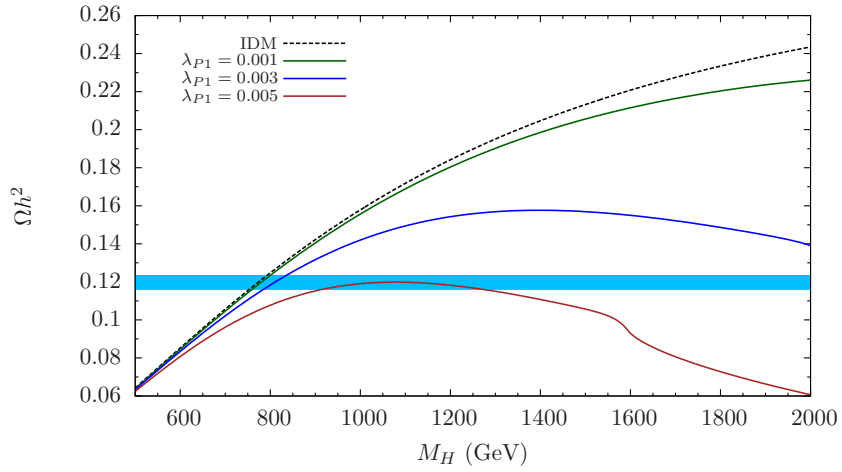

Figure 2.5: Impact of adding a CW scalar in the calculation of the relic density, the introduction of a new annihilation into $h_{\rm CW}$ means that the values for the relic density will be smaller, the effect becomes more relevant as we go to larger values of the DM mass M_H. The parameters we take are $\lambda_L = 0$, $\lambda_2 = 0.15$, $e_{\rm CW} = 0.9$ and mass splittings $\Delta M_A = 4$ GeV, $\Delta M_{H^\pm} = 6$ GeV. We study three cases $\lambda_{\rm P1} = 0.001, 0.003$ and 0.005, which correspond to $M_{h_{\rm CW}} = 624, 360$ and 280 GeV, respectively. The light blue band corresponds to the measured dark matter relic abundance by the Planck collaboration to 2σ [37].

Constraints from direct detection

One of the most promising ways to look for dark matter is through its scattering with heavy nuclei on underground detectors, by studying the dark matter-nucleon scattering cross-section we can make predictions for this kind of experiments. The inert Higgs H can interact with quarks in the nucleon via exchange of a Z boson if the mass splitting between A and H is less than a few 100 keV [212], giving cross-sections orders of magnitude above current experimental limits and for this reason we impose $\Delta M_i > 1$ MeV in our scan. The other mechanism in which the inert Higgs H interacts with quarks is through exchange of a Higgs boson. In our model due to the addition of the CW scalar, H can also interact with quarks through the exchange of this scalar meaning that the spin-independent cross-section between H and a nucleon is modified to

$$\sigma_{\rm SI} = \frac{1}{\pi} \frac{f^2 M_N^4}{(M_H + M_N)^2} \left(\frac{\lambda_{h_{\rm SM} HH} \cos\theta}{M^2_{h_{\rm SM}}} + \frac{\lambda_{h_{\rm CW} HH} \sin\theta}{M^2_{h_{\rm CW}}} \right)^2 , \tag{2.4.53}$$

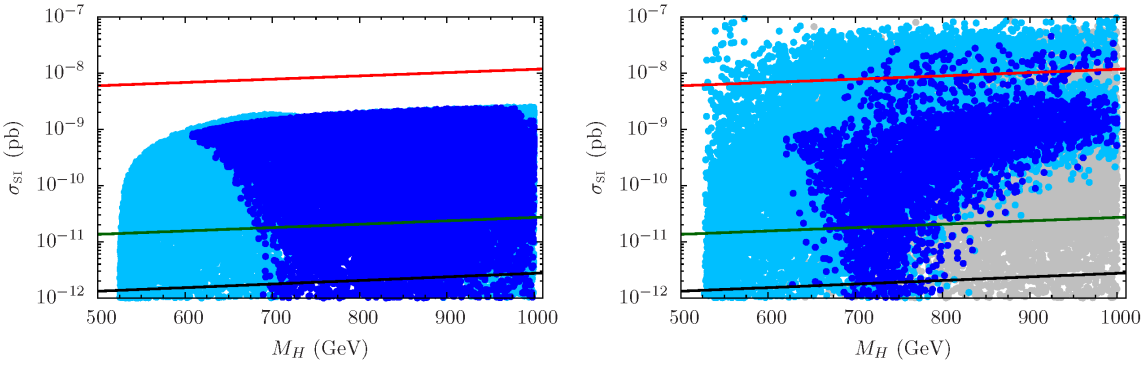

Figure 2.6: Spin-independent DM-nucleon cross-section as a function of the DM candidate mass M_H. All points give the correct DM relic abundance from the latest Planck result to 2σ. Left panel: Results for the ordinary IDM. Colour coding corresponds to the RG analysis, points in light blue satisfy vacuum stability, perturbativity, and unitarity at the scale $\mu = m_t$. Right panel: Results for the for the CSI IDM, points in light blue satisfy all constraints up to the scale $\mu = \langle\phi\rangle$. In gray we show the points that do not satisfy condition (2.4.67). In both plots points in dark blue are those that survive up to the Planck scale. We show current experimental limits from LUX [221] (red line), future limits from LZ [79] (green line) and the neutrino coherent scattering limit [222] (black line).

where $f \approx 3$ is a nuclear form factor, M_N is the nucleon mass, θ is the scalar mixing angle and the scalar couplings for the vertices $h_{\rm SM}HH$ and $h_{\rm CW}HH$ are given by

$$\lambda_{h_{\rm SM}HH} = \lambda_L \cos\theta - \frac{\langle\phi\rangle}{2v}\lambda_{\rm P2}\ \sin\theta, \tag{2.4.54}$$

$$\lambda_{h_{\rm CW}HH} = \lambda_L \sin\theta + \frac{\langle\phi\rangle}{2v}\lambda_{\rm P2}\ \cos\theta. \tag{2.4.55}$$

We now perform a random scan in parameter space and keep those points that satisfy the latest Planck measurement for DM relic abundance, $\Omega h^2 = 0.1197 \pm 0.0022$ [37]. We show the results in Fig. 2.15 where the colour coding refers to the RG analysis explained in the following section. In this model it is possible to have a lighter scalar mediator, and in the region where $M_{h_{\rm SM}}/2 < M_{h_{\rm CW}} < M_{h_{\rm SM}}$ it is also possible to get large mixing angles $|\sin\theta| \gtrsim 0.2$. For this reason we can get cross-sections that are larger than the ones obtained in the ordinary IDM. This means that a larger region in parameter space will be tested by future experiments, such as SuperCDMS [223], XENON1T [224] and LZ [79].

Since we focus our analysis in the region $500 < M_H < 1000$ GeV for this DM masses the current strongest constraints come from LUX [221], which we show as a red line in Fig. 2.15. As we can see from the plot in the right some points in the CSI case even exceed this limit, we do not consider these points for the rest of our analysis. The points in gray are not physical due to the RG running of the portal couplings and also a lesser number of points survive to the Planck scale compared to the traditional IDM. It has been argued by [225, 226] that taking into account loop corrections can have some impact on the direct detection cross-section in certain regions of parameter space, these calculations are beyond the scope of the present work.

2.4.2 Renormalisation Group Analysis

It is well known that in the SM λ_1 develops an instability around the scale $\approx 10^{10}$ GeV [96–99]. Apart from providing a good DM candidate, the IDM can also make the SM Higgs potential absolutely stable. In this section, we present the RG equations for our model and impose absolute vacuum stability, perturbativity and unitarity to study its validity all the way up to the Planck scale $= 2.435 \times 10^{18}$ GeV.

In Ref. [213, 227] the authors studied the high scale validity of the IDM. In region 1 where $50 < M_H < 80$ GeV they found only a few points can evade the direct detection experimental limits (those in the Higgs funnel region survive) and from these only a smaller fraction satisfy all the imposed constraints up to the Planck scale. For our model, we have argued that since $\lambda_{P2} \approx \lambda_{P1}$ in the small mass region there are no modifications coming from new annihilation channels. Moreover, in this region the RG analysis has almost no impact, and hence this mass region remains valid in the CSI IDM. From now on we focus our work on the large mass region

$M_H > 500$ GeV. In our model the running of the scalar couplings is given by

$$\begin{aligned}
(4\pi)^2\frac{d\lambda_1}{d\ln\mu} &= 24\lambda_1^2 + 2\lambda_3^2 + 2\lambda_3\lambda_4 + \lambda_4^2 + \lambda_5^2 + \frac{3}{8}(3g_2^4 + g'^4 + 2g_2^2g'^2) \\
&\quad -\lambda_1(9g_2^2 + 3g'^2 - 12y_t^2) - 6y_t^2 + \lambda_{\mathrm{P1}}^2, \qquad (2.4.56)\\
(4\pi)^2\frac{d\lambda_2}{d\ln\mu} &= 24\lambda_2^2 + 2\lambda_3^2 + 2\lambda_3\lambda_4 + \lambda_4^2 + \lambda_5^2 + \frac{3}{8}(3g_2^4 + g'^4 + 2g_2^2g'^2) \\
&\quad -3\lambda_2(3g_2^2 + g'^2) + \lambda_{\mathrm{P2}}^2, \qquad (2.4.57)\\
(4\pi)^2\frac{d\lambda_3}{d\ln\mu} &= 4(\lambda_1+\lambda_2)(3\lambda_3+\lambda_4) + 4\lambda_3^2 + 2\lambda_4^2 + 2\lambda_5^2 + \frac{3}{4}(3g_2^4 + g'^4 - 2g_2^2g'^2) \\
&\quad -3\lambda_3(3g_2^2 + g'^2 - 2y_t^2) - 2\lambda_{\mathrm{P1}}\lambda_{\mathrm{P2}}, \qquad (2.4.58)\\
(4\pi)^2\frac{d\lambda_4}{d\ln\mu} &= 4\lambda_4(\lambda_1+\lambda_2+2\lambda_3+\lambda_4) + 8\lambda_5^2 + 3g_2^2g'^2 \\
&\quad -3\lambda_4(3g_2^2 + g'^2 - 2y_t^2), \qquad (2.4.59)\\
(4\pi)^2\frac{d\lambda_5}{d\ln\mu} &= 4\lambda_5(\lambda_1+\lambda_2+2\lambda_3+3\lambda_4) - 3\lambda_5(3g_2^2 + g'^2) + 6\lambda_5 y_t^2, \qquad (2.4.60)\\
(4\pi)^2\frac{d\lambda_\phi}{d\ln\mu} &= 20\lambda_\phi^2 + 2\lambda_{\mathrm{P1}}^2 + 2\lambda_{\mathrm{P2}}^2 - 12\lambda_\phi e_{\mathrm{CW}}^2 + 6e_{\mathrm{CW}}^4. \qquad (2.4.61)
\end{aligned}$$

For the portal couplings that couple the Coleman-Weinberg scalar with the Higgs doublets we have

$$\begin{aligned}
(4\pi)^2\frac{d\lambda_{\mathrm{P1}}}{d\ln\mu} &= \lambda_{\mathrm{P1}}\left(6y_t^2 + 12\lambda_1 + 8\lambda_\phi - 4\lambda_{\mathrm{P1}} - 6e_{\mathrm{CW}}^2 - \frac{3}{2}g'^2 - \frac{9}{2}g_2^2\right) \\
&\quad -2\lambda_{\mathrm{P2}}(2\lambda_3+\lambda_4), \qquad (2.4.62)\\
(4\pi)^2\frac{d\lambda_{\mathrm{P2}}}{d\ln\mu} &= \lambda_{\mathrm{P2}}\left(12\lambda_2 + 8\lambda_\phi + 4\lambda_{\mathrm{P2}} - 6e_{\mathrm{CW}}^2 - \frac{3}{2}g'^2 - \frac{9}{2}g_2^2\right) \\
&\quad -2\lambda_{\mathrm{P1}}(2\lambda_3+\lambda_4). \qquad (2.4.63)
\end{aligned}$$

For the gauge couplings

$$(4\pi)^2\frac{dg'}{d\ln\mu} = 7g'^3, \qquad (4\pi)^2\frac{dg_2}{d\ln\mu} = -3g_2^3, \qquad (2.4.64)$$

$$(4\pi)^2\frac{dg_3}{d\ln\mu} = -7g_3^3, \qquad (4\pi)^2\frac{de_{\mathrm{CW}}}{d\ln\mu} = \frac{1}{3}e_{\mathrm{CW}}^3. \qquad (2.4.65)$$

For the top Yukawa coupling y_t

$$(4\pi)^2 \frac{dy_t}{d\ln\mu} = y_t\left(\frac{9}{2}y_t^2 - \frac{17}{12}g'^2 - \frac{9}{4}g_2^2 - 8g_3^2\right). \tag{2.4.66}$$

All the RG equations have been checked with `SARAH` [228]. The gauge boson in the hidden sector will develop a kinetic mixing with hypercharge from radiative corrections, for this reason it cannot be a good DM candidate; nevertheless, the impact of this mixing on the RG analysis has been shown to be very small [177]. In our analysis we do not take this effect into account. Due to the introduction of a second portal coupling, the running of $\lambda_{\rm P1}$, Eq. (2.4.62), receives a negative contribution $-2\lambda_{\rm P2}(2\lambda_3+\lambda_4)$ which might be dangerous since in the large mass region we have $\lambda_{\rm P2} \gg \lambda_{\rm P1}$ and hence this contribution can change the sign of $\lambda_{\rm P1}$ before reaching the scale $\mu = \langle\phi\rangle$. Thus, in order to ensure EWSB occurs we need to check the condition

$$\lambda_{\rm P1} > 0 \quad \text{for} \quad \mu \leq \langle\phi\rangle. \tag{2.4.67}$$

We ensure the model remains perturbative by requiring all the scalar couplings to be bounded up to the Planck scale. To do so we impose a conservative constraint

$$|\lambda_i(\mu)| < \text{const}\ \mathcal{O}(1) = 3, \tag{2.4.68}$$

and also we check that all the unitarity constraints are satisfied [229–231]. To ensure absolute vacuum stability we impose the following constraints

$$\begin{aligned} \lambda_1(\mu), \lambda_2(\mu), \lambda_\phi(\mu) &> 0, \\ \lambda_3(\mu) &> -2\sqrt{\lambda_1(\mu)\lambda_2(\mu)}, \\ \lambda_3(\mu) + \lambda_4(\mu) - |\lambda_5(\mu)| &> -2\sqrt{\lambda_1(\mu)\lambda_2(\mu)}, \end{aligned} \tag{2.4.69}$$

and for the portal couplings the conditions are given by

$$\lambda_{\rm P1}(\mu) < 2\sqrt{\lambda_1(\mu)\lambda_\phi(\mu)}, \tag{2.4.70}$$

$$\lambda_{\rm P2}(\mu) > -2\sqrt{\lambda_2(\mu)\lambda_\phi(\mu)}. \tag{2.4.71}$$

When studying the potential in the direction of the three fields H_1, H_2 and Φ we get two more conditions for absolute stability, these are lengthy expressions that can be found in [1].

We start the RG running from $\mu = M_t$, we take $M_W = 80.384$ GeV, $\alpha_3 = 0.1184$ and for the top quark mass we take the combined result of ATLAS, CDF, CMS and D0, $M_t = 173.34$ GeV [232]. We work with the NNLO initial values for the SM gauge couplings and the top Yukawa from Ref. [96]

$$\begin{aligned}
y_t(\mu = M_t) &= 0.93558 + 0.00550\left(\frac{M_t}{\text{GeV}} - 173.1\right) + \\
&\quad -0.00042\frac{\alpha_3(M_Z) - 0.1184}{0.0007} - 0.00042\frac{M_W - 80.384}{0.014\ \text{GeV}} \pm 0.00050_{\text{th}}, \\
g_3(\mu = M_t) &= 1.1666 + 0.00314\frac{\alpha_3(M_Z) - 0.1184}{0.0007} - 0.00046\left(\frac{M_t}{\text{GeV}} - 173.1\right), \\
g_2(\mu = M_t) &= 0.64822 + 0.00004\left(\frac{M_t}{\text{GeV}} - 173.1\right) + 0.00011\frac{M_W - 80.384\ \text{GeV}}{0.014\ \text{GeV}}, \\
g'(\mu = M_t) &= 0.35761 + 0.00011\left(\frac{M_t}{\text{GeV}} - 173.1\right) - 0.00021\frac{M_W - 80.384\ \text{GeV}}{0.014\ \text{GeV}}.
\end{aligned}$$

In the right panel of Fig. 2.7 we show our results for the RG analysis in the CSI IDM and to serve as a comparison we show in the left panel the same plot for the IDM without CSI. In the CSI case there are less points that survive to the Planck scale. This is mainly because as we increase λ_{P1}, the second portal coupling, λ_{P2}, also increases and hence there is more annihilation into the CW scalar, therefore the values of λ_3, λ_4 and λ_5 that give the correct relic density are smaller compared to the IDM and not able to provide absolute stability for λ_1. Also, for large masses M_H the coupling λ_{P2} can be two orders of magnitude larger than λ_{P1} and condition (2.4.67) is not satisfied. The gray points are those that do not work below the scale $\mu = \langle\phi\rangle$, mainly because of this condition and hence they do not correspond to physical points in the CSI IDM. Therefore, as we can see from comparing both plots the CSI case is more restrictive.

In Fig. 2.8 we show on the left the values of λ_{P1} that give the correct relic abundance as a function of M_H. The upper bound in this plot comes from the

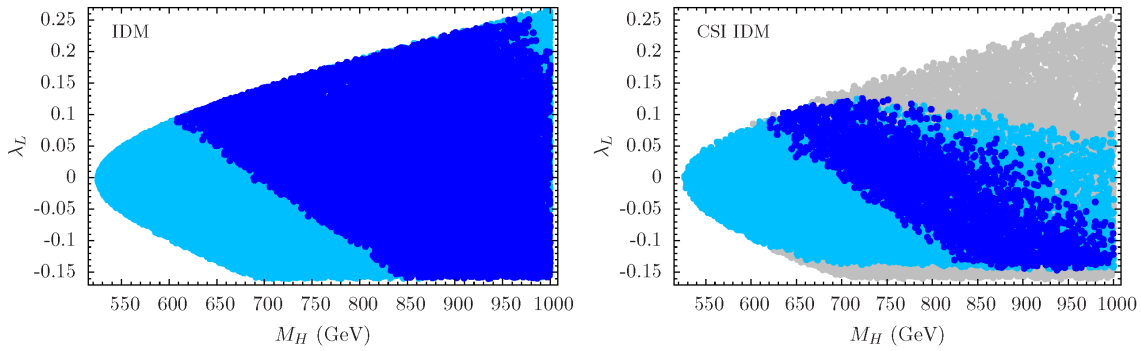

Figure 2.7: Left panel: Points in the IDM (high mass regime) that give the correct DM relic abundance from the latest Planck result to 2σ, points in dark blue work well up to the Planck scale. Right panel: Points in the CSI IDM (high mass regime) that give the correct DM relic abundance from the latest Planck result to 2σ, points in light blue satisfy all the constraints up to the scale $\mu = \langle\phi\rangle$ but develop a vacuum instability or a Landau pole before the Planck scale, points in dark blue satisfy all the constraints up to the Planck scale. In gray we show the unphysical points that do not survive up to $\mu = \langle\phi\rangle$, mainly due to condition (2.4.67). We show in the x-axis the mass of the DM candidate H and in the y-axis the quartic coupling λ_L.

experimental constraints on the scalar mixing angle θ between the SM Higgs and the CW scalar, which means the region with $\lambda_{P1} \approx 0.01$ can be tested at Run 2 of the LHC. The plot in the right shows the values of λ_{P2} that give the correct relic abundance, since this second portal coupling controls the annihilation into the CW scalar it has a similar behaviour as λ_L.

In summary, the main impact of having CSI in the inert doublet model is that in the large mass region, where $\lambda_{P2} \gg \lambda_{P1}$, due to the negative contribution of λ_{P2} to the running of λ_{P1} condition (2.4.67) excludes a large region in parameter space, we have found that in our model $|\lambda_L| < 0.13$. Moreover, experimental constraints on the mixing angle in conjunction with obtaining the correct DM relic density constrain $\lambda_{P1} \in [0, 0.012]$. If we restrict to the regions in parameter space viable up to the Planck scale, then we find an upper bound on the DM mass of $M_H < 1.1$ TeV.

The IDM is a minimal scenario in which the dark matter candidate possesses a symmetry of the Standard Model and hence its properties and interactions can be studied in detail. Apart from explaining dark matter, there are other issues that should be addressed by models beyond the Standard Model such as neutrino

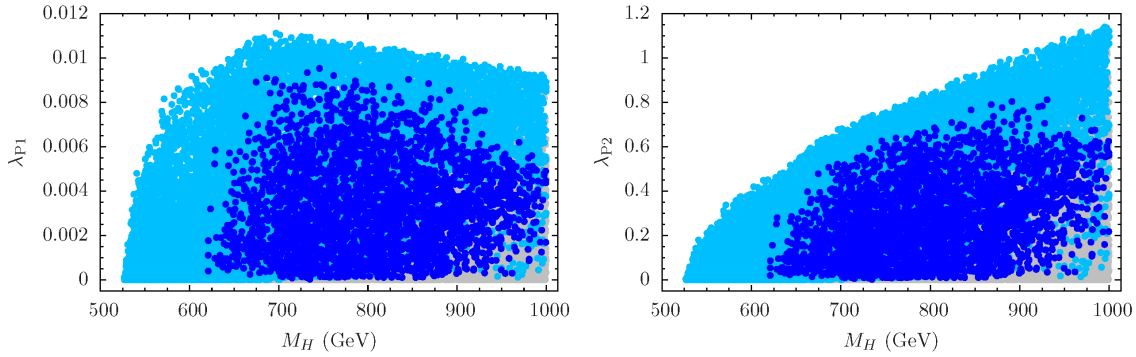

Figure 2.8: Plot of the portal couplings versus the DM mass M_H for the same points as in Fig. 2.7, same colour coding. The upper limit on λ_{P1} comes mainly from the experimental upper limit on the scalar mixing angle.

masses and the baryon asymmetry of the Universe; in order to address these issues with the present model we envision two possibilities. On the one side, the IDM can be extended with inert right-handed neutrinos and then SM neutrino masses can be generated through radiative corrections [182]. A second possibility is to extend the $\mathrm{U}(1)_{\mathrm{CW}}$ symmetry to the $\mathrm{U}(1)_{B-L}$ and then the results of Ref. [233] could be applied to generate the baryon asymmetry of the Universe through leptogenesis while preserving classical scale invariance.

2.5 Dark Matter and Leptogenesis Linked by Classical Scale Invariance

In this section, we present and study a model that addresses three of the shortcomings of the SM that were discussed in the Introduction of this thesis. The model has a good dark matter candidate, provides masses for the neutrinos and also solves the baryon asymmetry in the Universe. All the characteristic scales in the model: the electroweak, dark matter and the leptogenesis/neutrino mass scales, are generated radiatively, have a common origin and related to each other via scalar field couplings in perturbation theory. Our specific approach is motivated by the earlier work in Refs. [152, 170, 177, 233–236] and [42, 237]. The idea of generating the electroweak scale and various scales of new physics via quantum corrections,

by starting from a classically scale-invariant theory, has generated a lot of interest. For related studies on this subject we refer the reader to recent papers including Refs. [1, 162–169, 171–174, 178, 179, 238–240].

In our set-up we extend the Standard Model by a dark sector, namely a non-Abelian $\mathrm{SU}(2)_{\mathrm{DM}}$ hidden sector that is coupled to the Standard Model via the Higgs portal, and a singlet sector that includes a real singlet σ and three right-handed Majorana neutrinos N_i. Due to an SO(3) custodial symmetry all three gauge bosons Z'^a have the same mass and are absolutely stable, making them suitable dark matter candidates [67] (this also applies to larger gauge groups $\mathrm{SU(N)}_{\mathrm{DM}}$ [180, 241] and to scalar fields in higher representations [242], albeit symmetry breaking patterns get more complicated).

The tree-level scalar potential of our model is given by

$$V_0 = \lambda_\phi |\Phi|^4 + \lambda_h |H|^4 + \frac{\lambda_\sigma}{4}\sigma^4 - \lambda_{h\phi}|H|^2|\Phi|^2 - \frac{\lambda_{\phi\sigma}}{2}|\Phi|^2\sigma^2 + \frac{\lambda_{h\sigma}}{2}|H|^2\sigma^2, \quad (2.5.72)$$

where Φ denotes the $\mathrm{SU}(2)_{\mathrm{DM}}$ doublet, H is the SM Higgs doublet, and σ is a gauge-singlet introduced in order to generate the Majorana masses for the sterile neutrinos, and hence the visible neutrinos masses and mixings via the see-saw mechanism. The portal couplings $\lambda_{h\phi}$, $\lambda_{\phi\sigma}$ and $\lambda_{h\sigma}$ will play a role in order to induce non-trivial vacuum expectation values for all three scalar. As will become clear from Table 2.1 we will scan over positive as well as negative values of the portal couplings $\lambda_{h\phi}$ and $\lambda_{h\sigma}$. As we are working with multiple scalars we will adopt the Gildener-Weinberg approach [188], which is a generalisation of the Coleman-Weinberg mechanism to multiple scalar states and will be briefly reviewed in Section **2.5.1**. Later on we shall see that the most interesting region in parameter space leading to both the correct dark matter abundance and the correct baryon asymmetry is for $\langle\sigma\rangle \gg \langle\phi\rangle$ and hence one can think of σ as a Coleman-Weinberg scalar that once it acquires a non-zero vev it will be communicated to ϕ and h through the portal couplings $\lambda_{\phi\sigma}$ and $\lambda_{h\sigma}$.

The interactions for the right-handed neutrinos in the Lagrangian are given by

$$\mathcal{L}_N = -\frac{1}{2}\left(Y^M_{ij}\sigma\overline{N_i}^c N_j + Y^{M\dagger}_{ij}\sigma\overline{N_i}N^c_j\right) - Y^D_{ia}\,\overline{N_i}(\varepsilon H)l_{La} - Y^{D\dagger}_{ai}\,\overline{l_{La}}(\varepsilon H)^\dagger N_i, \quad (2.5.73)$$

where the first two term give rise to the Majorana mass once σ acquires a vev, while the last two terms are responsible for the CP-violating oscillations of N_i.

Since we do not wish to break the lepton-number symmetry explicitly, it follows from (2.5.73) that our new singlet scalar field σ should have the lepton number $L = -2$. We can think of it as the real part of a complex scalar $\Sigma = (\sigma + i\pi)/\sqrt{2}$ where S transforms under a $\mathrm{U}(1)_L$ symmetry associated with the lepton number, which is broken spontaneously by $\langle\sigma\rangle \neq 0$. If this is a global $\mathrm{U}(1)$ symmetry then there must exist a massless (or very light) (pseudo)-Goldstone boson. Since the Higgs can pair-produce them and decay, this would severely constrain the portal coupling of Σ with the Higgs, $\lambda_{h\sigma} < 10^{-5}$, see e.g. Ref. [152]. If we wish to avoid such fine-tuning, a much more appealing option would be to gauge the lepton number. A compelling scenario is the $B-L$ theory with the anomaly free $\mathrm{U}(1)_{B-L}$ factor. The generation of matter-anti-matter asymmetry via a leptogenesis mechanism through sterile neutrino oscillations in a classically scale invariant $\mathrm{U}(1)_{B-L}\times\mathrm{SM}$ theory was considered in Ref. [233], and their results will also apply to our model. The main difference with the set-up followed in this work is that here we allow for a separate non-Abelian Coleman-Weinberg sector (i.e. it remains distinct from the $\mathrm{U}(1)_{B-L}$ gauge sector) and as a result we have a non-Abelian vector DM candidate.

Finally, it should also be possible to restrict the complex singlet Σ back to the real singlet σ, just as we have in (2.5.72). In this case the continuous lepton number $\mathrm{U}(1)$ symmetry is reduced to a discrete sub-group:

$$\sigma \to -\sigma\,, \quad (N, \overline{N}^c, l_L) \to e^{i\pi/2}(N, \overline{N}^c, l_L)\,, \quad (\overline{N}, N^c, \overline{l_L}) \to e^{-i\pi/2}(\overline{N}, N^c, \overline{l_L})\,. \quad (2.5.74)$$

In general all three possibilities corresponding to global, local and discrete lepton-number symmetries can be accommodated and considered simultaneously in the context of Eqs. (2.5.72)-(2.5.73) by either working with the real scalar σ or the

complex one by promoting $\sigma \to \sqrt{2}\Sigma$ (or $\sqrt{2}\Sigma^\dagger$ in the second term in the brackets on the r.h.s. of (2.5.73)). In this work we consider σ to be a real scalar singlet.

2.5.1 From Coleman-Weinberg to the Gildener-Weinberg Mechanism

The scalar field content of our model consists of an $\mathrm{SU}(2)_L$ doublet H, an $\mathrm{SU}(2)_{\mathrm{DM}}$ doublet Φ and a real scalar σ; the latter giving mass to the sterile neutrinos after acquiring a vev in similar fashion to Ref. [236]. Working in the unitary gauge of the $\mathrm{SU}(2)_L \times \mathrm{SU}(2)_{\mathrm{DM}}$, the two scalar doublets in the theory are reduced to,

$$H = \frac{1}{\sqrt{2}} \begin{pmatrix} 0 \\ h \end{pmatrix}, \qquad \Phi = \frac{1}{\sqrt{2}} \begin{pmatrix} 0 \\ \phi \end{pmatrix},$$

and the tree-level potential becomes,

$$V_0 = \frac{\lambda_h}{4} h^4 + \frac{\lambda_\phi}{4} \phi^4 + \frac{\lambda_\sigma}{4} \sigma^4 - \frac{\lambda_{h\phi}}{4} h^2 \phi^2 - \frac{\lambda_{\phi\sigma}}{4} \phi^2 \sigma^2 + \frac{\lambda_{h\sigma}}{4} h^2 \sigma^2 . \tag{2.5.75}$$

There are no mass scales appearing in the classical theory, and at the origin in the field space, all scalar vevs are zero, in agreement with classical scale invariance. We impose a conservative constraint on all the scalar couplings for the model to be perturbative $|\lambda_i| < 3$, we also impose $g_{\mathrm{DM}} < 3$ and in order to ensure vacuum stability the following set of constraints need to be satisfied,

$$\lambda_h \geq 0, \qquad \lambda_\phi \geq 0, \qquad \lambda_\sigma \geq 0, \tag{2.5.76}$$

$$\frac{\lambda_{h\phi}}{2\sqrt{\lambda_h \lambda_\phi}} \leq 1, \quad -\frac{\lambda_{h\sigma}}{2\sqrt{\lambda_h \lambda_\sigma}} \leq 1, \quad \frac{\lambda_{\phi\sigma}}{2\sqrt{\lambda_\phi \lambda_\sigma}} \leq 1, \tag{2.5.77}$$

$$\frac{\lambda_{h\phi}}{2\sqrt{\lambda_h \lambda_\phi}} - \frac{\lambda_{h\sigma}}{2\sqrt{\lambda_h \lambda_\sigma}} + \frac{\lambda_{\phi\sigma}}{2\sqrt{\lambda_\phi \lambda_\sigma}} \leq 1. \tag{2.5.78}$$

For more detail we refer to Table 2.1.

The Coleman-Weinberg approximation

For simplicity, let us temporarily ignore the singlet σ and concentrate on the theory with two scalars, ϕ and h. We will further refer to the hidden $\mathrm{SU}(2)_{\mathrm{DM}}$ sector with ϕ as the Coleman-Weinberg (CW) sector. In the near-decoupling limit, $\lambda_{h\phi} \ll 1$, between the CW and the SM sectors, we can view electroweak symmetry breaking effectively as a two-step process [152].

First, the CW mechanism [150] generates $\langle\phi\rangle$ in the hidden sector through running couplings (or more precisely the dimensional transmutation). To make this work, the scalar self-coupling λ_ϕ at the relevant scale $\mu = \langle\phi\rangle$ should be small – of the order of $g^4_{\mathrm{DM}} \ll 1$, as we will see momentarily. This has the following interpretation: in a theory where λ_ϕ has a positive slope, we start at a relatively high scale where λ_ϕ is positive and move toward the infrared until approach the value of the μ where $\lambda_\phi(\mu)$ becomes small and is about to cross zero. This is the Coleman-Weinberg scale where the potential develops a non-trivial minimum and ϕ generates a non-vanishing vev.

To see this, consider the 1-loop effective potential evaluated at the scale μ (*cf.* [177]):

$$V(\phi, h) = \frac{\lambda_\phi(\mu)}{4}\phi^4 + \frac{9}{1024\,\pi^2}\, g^4_{\mathrm{DM}}(\mu)\,\phi^4 \left(\ln\frac{\phi^2}{\mu^2} - \frac{25}{6}\right) - \frac{\lambda_{h\phi}(\mu)}{4} h^2\phi^2\,, \qquad (2.5.79)$$

Here we are keeping 1-loop corrections arising from interactions of ϕ with the SU(2) gauge bosons in the hidden sector, but neglecting the loops of ϕ (since λ_ϕ is close to zero) and the radiative corrections from the Standard Model sector. The latter would produce only subleading corrections to the vevs. Minimising at $\mu = \langle\phi\rangle$ gives:

$$\lambda_\phi \;=\; \frac{33}{256\,\pi^2}\, g^4_{\mathrm{DM}} + \lambda_{h\phi}\frac{v^2}{2\langle\phi\rangle^2} \qquad \text{at} \quad \mu = \langle\phi\rangle\,. \qquad (2.5.80)$$

For small portal coupling $\lambda_{h\phi}$, this is a small deformation of the original CW condition, $\lambda_\phi(\langle\phi\rangle) = \frac{33}{256\,\pi^2}\, g^4_{\mathrm{DM}}(\langle\phi\rangle)$.

The second step of the process is the transmission of the vev $\langle\phi\rangle$ to the Standard Model via the Higgs portal, generating a negative mass squared parameter for the

Higgs $= -\lambda_{h\phi}\langle\phi^2\rangle$ which generates the electroweak scale v,

$$v = \langle h\rangle \;=\; \sqrt{\frac{2\lambda_{h\phi}}{\lambda_h}}\,\langle\phi\rangle\,, \quad m_h \;=\; \sqrt{2\lambda_h}v\,. \tag{2.5.81}$$

The fact that for $\lambda_{h\phi} \ll 1$ the generated electroweak scale is much smaller than $\langle\phi\rangle$, guarantees that any back reaction on the hidden sector vev $\langle\phi\rangle$ is negligible. Finally, the mass of the CW scalar is obtained from the 1-loop potential and reads:

$$m_\phi^2 \;=\; \frac{9}{128\,\pi^2}\,g_{\rm DM}^4\,\langle\phi\rangle^2 + \lambda_{h\phi}v^2\,. \tag{2.5.82}$$

As already stated, this approach is valid in the near-decoupling approximation where all the portal couplings are small. The dynamical generation of all scales is visualised here as first the generation of the CW scalar vev $\langle\phi\rangle$, which then induces the vevs of other scalars proportional to the square root of the corresponding portal couplings $\ll 1$, as in (2.5.81). This implies the hierarchy of the vevs.

For multiple scalars, ϕ, h and σ, it is not a priori obvious why the portal couplings should be small and which of the scalar vevs should be dominant. For example on one part of the parameter space we can find $\langle\phi\rangle > \langle\sigma\rangle$ and on a different part one has $\langle\sigma\rangle > \langle\phi\rangle$ (so that σ rather than ϕ effectively plays the role of the CW scalar). To consider all such cases and not be constrained by the near-decoupling limits we will utilise the Gildener-Weinberg set-up [188], which is a generalization of the Coleman-Weinberg method.

The Gildener-Weinberg approach

We now return to the general case with the three scalars in the model are described by the tree-level massless scalar potential (2.5.75). The Gildener-Weinberg mechanism was recently worked out for this case in Ref. [236], which we will follow. All three vevs can be generated dynamically but neither of the original scalars is solely responsible for the intrinsic scale generation; this instead is a collective effect generated by a linear combination of all three scalars φ.

Following [188], we change variables and reparametrise the scalar fields via,

$$h = N_1\varphi, \qquad \phi = N_2\varphi, \qquad \sigma = N_3\varphi. \tag{2.5.83}$$

where each N_i is a unit vector in three-dimensions. The Gildener-Weinberg mechanism tells us that a non-zero vacuum expectation value will be generated in some direction in scalar field space $N_i = n_i$, so this direction must satisfy the condition,

$$\left.\frac{\partial V_0}{\partial N_i}\right|_{\mathbf{n}} = 0, \tag{2.5.84}$$

and furthermore the value of the tree-level potential in this vacuum is independent of φ,

$$V_0(n_1\varphi, n_2\varphi, n_3\varphi) = 0\,. \tag{2.5.85}$$

The latter condition is simply the statement that the potential restricted to the single degree of freedom φ, is of the form $\frac{1}{4}\lambda_\varphi\,\varphi^4$ with the corresponding coupling constant vanishing $\lambda_\varphi = 0$. This is nothing but the definition of scale $\mu_{\rm GW}$ where $\lambda_\varphi(\mu_{\rm GW})$ vanishes, and is a reflection of a similar statement in the Coleman-Weinberg case for the single scalar that its self-coupling was about to cross zero, but was stabilised at the small positive value by the gauge coupling at the Coleman-Weinberg scale $\mu_{\rm CW}$, see Eq. (2.5.80).

Being a unit vector in three-dimensions, n_i's can be parametrised in terms of two independent angles, α and γ and we will call the φ vev, w, so that,

$$n_1 = \sin\alpha\,, \quad n_2 = \cos\alpha\cos\gamma \quad n_3 = \cos\alpha\sin\gamma\,, \tag{2.5.86}$$

$$\langle h\rangle = wn_1\,, \quad \langle\phi\rangle = wn_2\,, \qquad \langle\sigma\rangle = wn_3. \tag{2.5.87}$$

The three linearly-independent conditions arising from the Gildener-Weinberg min-

imisation (2.5.84) of the tree-level potential amount to the following set of relations,

$$2\lambda_h n_1^2 = \lambda_{h\phi} n_2^2 - \lambda_{h\sigma} n_3^2, \tag{2.5.88}$$

$$2\lambda_\phi n_2^2 = \lambda_{h\phi} n_1^2 + \lambda_{\phi\sigma} n_3^2, \tag{2.5.89}$$

$$2\lambda_\sigma n_3^2 = \lambda_{\phi\sigma} n_2^2 - \lambda_{h\sigma} n_1^2. \tag{2.5.90}$$

These conditions hold at the scale $\mu_{\rm GW}$ where the scalar fields develop the vev $\langle\varphi\rangle = w$ (2.5.87). Due to the three scalars acquiring non-zero vacuum expectation values, the three states will mix among each other. The mass matrix M^2 is diagonalised for h_1, h_2 and h_3 eigenstates via the rotation matrix O,

$$\text{diag}\left(M_{h_1}^2, M_{h_2}^2, M_{h_3}^2\right) = O^{(-1)}\, M^2\, O\,, \qquad \begin{pmatrix} h \\ \phi \\ \sigma \end{pmatrix} = O_{ij} \begin{pmatrix} h_1 \\ h_2 \\ h_3 \end{pmatrix}, \tag{2.5.91}$$

and we further identify the state h_1 with the SM 125 GeV Higgs boson. Following [236] we parametrise the rotation matrix in terms of three mixing angles α, β and γ,

$$O = \begin{pmatrix} \cos\alpha\cos\beta & \sin\alpha & \cos\alpha\sin\beta \\ -\cos\beta\cos\gamma\sin\alpha + \sin\beta\sin\gamma & \cos\alpha\cos\gamma & -\cos\gamma\sin\alpha\sin\beta - \cos\beta\sin\gamma \\ -\cos\gamma\sin\beta - \cos\beta\sin\alpha\sin\gamma & \cos\alpha\sin\gamma & \cos\beta\cos\gamma - \sin\alpha\sin\beta\sin\gamma \end{pmatrix}, \tag{2.5.92}$$

and use it to compute the scalar mass eigenstates (2.5.91) at tree-level. The resulting expressions for the scalar masses can be found in Ref. [236]. There is one classically flat direction in the model – along φ – in which the potential develops the vacuum expectation value. Our choice of parametrisation in (2.5.87) and in the second row of (2.5.92) in terms of the same two angles α and γ, selects this direction to be identified with h_2. Hence, at tree level, $M_{h_2} = 0$, but it will become non-zero, see Eq. (2.5.96) below, when one-loop effects are included.

At the scale $\mu_{\rm GW}$ the one-loop effective potential along the minimum flat direction

can be written as [188],

$$V(\varphi\mathbf{n}) = A\varphi^4 + B\varphi^4 \ln\left(\frac{\varphi^2}{\mu_{\rm GW}^2}\right), \tag{2.5.93}$$

where the A and B coefficients are computed in the $\overline{\rm MS}$ [243] scheme and given by,

$$\begin{aligned} A &= \frac{1}{64\pi^2 w^4}\left[\sum_{i=1,3} M_{h_i}^4\left(-\frac{3}{2}+\ln\frac{M_{h_i}^2}{w^2}\right)+6M_W^4\left(-\frac{5}{6}+\ln\frac{M_W^2}{w^2}\right)\right. \\ &\quad +3M_Z^4\left(-\frac{5}{6}+\ln\frac{M_Z^2}{w^2}\right)+9M_{Z'}^4\left(-\frac{5}{6}+\ln\frac{M_{Z'}^2}{w^2}\right)-12M_t^4\left(-1+\ln\frac{M_t^2}{w^2}\right) \\ &\quad \left.-2\sum_{i=1}^{3} M_{N_i}^4\left(-1+\ln\frac{M_{N_i}^2}{w^2}\right)\right], \\ B &= \frac{1}{64\pi^2 w^4}\left(\sum_{i=1,3} M_{h_i}^4+6M_W^4+3M_Z^4+9M_{Z'}^4-12M_t^4-2\sum_{i=1}^{3} M_{N_i}^4\right), \end{aligned}$$

where M_{h_i} are the tree-level masses of the three scalar eigenstates, h_1, h_2 and h_3, and the rest are the masses of the SM and the hidden sector vector bosons as well as the top quark and the right-handed Majorana neutrinos. We can now see that at the RG scale $\mu_{\rm GW}$ the 1-loop corrected effective potential has a fixed vacuum expectation value w that satisfies,

$$\ln\left(\frac{w}{\mu_{\rm GW}}\right) = -\frac{1}{4}-\frac{A}{2B}, \tag{2.5.94}$$

and using this relation we can rewrite the one-loop effective potential as,

$$V = B\varphi^4\left(\ln\frac{\varphi^2}{w^2}-\frac{1}{2}\right), \tag{2.5.95}$$

and we can also evaluate the potential at the minimum to be $V(\varphi=w)=-Bw^4/2$, which gives the requirement $B>0$ for this to be a lower minimum than the one at the origin. The mass of the pseudo-dilaton h_2 is then given by,

$$M_{h_2}^2 = \left.\frac{\partial^2 V}{\partial\varphi^2}\right|_{\mathbf{n}} = \frac{1}{8\pi w^2}\left(M_{h_1}^4+M_{h_3}^4+6M_W^4+3M_Z^4+9M_{Z'}^4-12M_t^4-2\sum_{i=1}^{3} M_{N_i}^4\right). \tag{2.5.96}$$

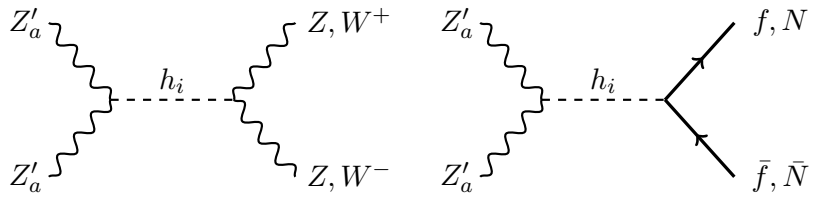

Figure 2.9: Dark matter annihilation diagrams into Standard Model gauge bosons and fermions, we also include annihilation into right-handed neutrinos.

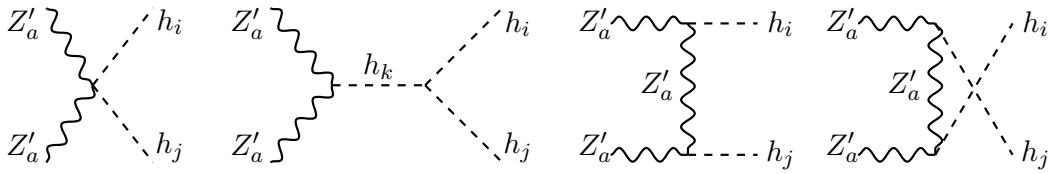

Figure 2.10: Dark matter annihilation diagrams into scalar states.

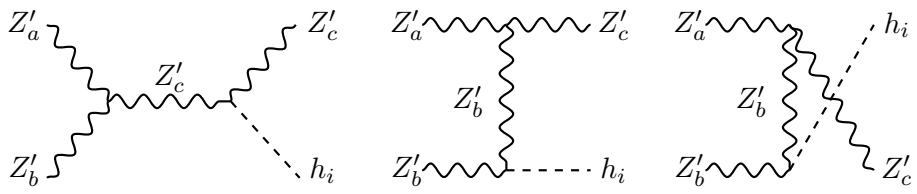

Figure 2.11: Vector dark matter semi-annihilation diagrams. In contrast to some other models of dark matter, Z'_a is stable due to an remnant global symmetry.

In summary, at the scale $\mu_{\rm GW}$ the conditions Eqs. (2.5.88)–(2.5.90) will be satisfied and the scalar potential will develop a non-trivial vev w giving rise to non-zero vacuum expectation values $\langle h\rangle$, $\langle\phi\rangle$, and $\langle\sigma\rangle$. For one scalar field, the Coleman-Weinberg mechanism requires the scalar quartic coupling to take very small values $\lambda_\phi \sim g_{\rm DM}^4$, in the Gildener-Weinberg scenario it is a combination of the quartic couplings that needs to vanish, so these couplings can take larger values individually.

The formulae for the mixing angles in terms of the coupling constants and the vevs follow from the diagonalisation of the tree-level mass matrix,

$$\tan^2\alpha = \frac{\langle h\rangle^2}{\langle\phi\rangle^2+\langle\sigma\rangle^2} = \frac{4\lambda_\phi\lambda_\sigma-\lambda_{\phi\sigma}^2}{2(\lambda_\sigma\lambda_{h\phi}-\lambda_\phi\lambda_{h\sigma})+\lambda_{\phi\sigma}(\lambda_{h\phi}-\lambda_{h\sigma})}\,, \quad (2.5.97)$$

$$\tan^2\gamma = \frac{\langle\sigma\rangle^2}{\langle\phi\rangle^2} = \frac{2\lambda_h\lambda_{\phi\sigma}-\lambda_{h\phi}\lambda_{h\sigma}}{4\lambda_h\lambda_\sigma-\lambda_{h\sigma}^2}\,, \quad (2.5.98)$$

$$\tan 2\beta = \frac{\langle h\rangle\langle\phi\rangle\langle\sigma\rangle w(\lambda_{h\sigma}+\lambda_{h\phi})}{(\lambda_\phi+\lambda_\sigma+\lambda_{\phi\sigma})\langle\phi\rangle^2\langle\sigma\rangle^2-\lambda_h\langle h\rangle^2 w^2}\,. \quad (2.5.99)$$

Experimental searches of a scalar singlet mixing with the SM Higgs provide constraints on the mixing angles [208–210]. In our case, these translate as,

$$\cos^2\alpha\,\cos^2\beta > 0.85. \quad (2.5.100)$$

In the region where the decay $h_1 \to h_2 h_2$ is allowed we impose the stronger constraint $\cos^2\alpha\,\cos^2\beta > 0.96$. Nonetheless, due to the Gildener-Weinberg conditions the decay $h_1 \to h_2 h_2$ is highly suppressed. In the scan we perform M_{h_3} is always greater than M_{h_1}, so there is no need to worry about the SM Higgs decaying into two h_3 scalars. At the same time, strong constraints could come when the decays $h_1 \to Z'^a Z'^a$ are allowed, we set $M_{Z'} > M_{h_1}/2$ so that these decays are kinematically forbidden.

For the study of dark matter the Lagrangian contains ten dimensionless free parameters, which are reduced to eight after fixing $\langle h\rangle = 246$ GeV and $M_{h_1} = 125$ GeV. We perform a random scan on the remaining eight parameters in the ranges given in Table 2.1.

Parameter	Scan range
$\lambda_{\phi\sigma}$	(0, 0.5)
$\lambda_{h\phi}$	(-0.5, 0.5)
$\lambda_{h\sigma}$	(-0.25, 0.25)
λ_{ϕ}	(0, 3)
$g_{\rm DM}$	(0, 3)
M_{N_i}	(0, 100) GeV

Table 2.1: Ranges for the input parameters in the scan.

The matrix Y^D has no impact on the dark matter phenomenology, but it is crucial for leptogenesis and it will be parametrised by three complex angles ω_{ij} using the Casas-Ibarra parametrisation [244]. Therefore, once we set all the parameters for the active neutrinos to their best experimental fit, there are twelve free parameters in the model.

2.5.2 Dark Matter Phenomenology

Evidence from astrophysics suggests that most of the matter in the Universe is made out of cosmologically stable dark matter that interacts very weakly with ordinary matter. Being able to identify what constitutes this dark matter is one of the deepest mysteries in both particle physics and astrophysics. In this work we consider the possibility of dark matter being a spin-1 particle from a hidden sector with non-Abelian $\mathrm{SU}(2)_{\rm DM}$ gauged symmetry. The idea of vector dark matter was first introduced in Ref. [67] and later studied in Refs. [170,177,241,245]. Note that if the hidden sector had been U(1), the kinetic mixing among the hidden sector and the hypercharge will have made our dark matter candidate unstable.

After radiative symmetry breaking breaking of $\mathrm{SU}(2)_{\rm DM}$ by Φ, which is in the fundamental representation of the group, there is a remnant SO(3) symmetry that ensures the three gauge bosons Z'^a acquire the same mass $M_{Z'} = \frac{1}{2}\, g_{\rm DM}\langle\phi\rangle$, and are stable. In contrast to models where the DM is odd under a $\mathbb{Z}_2$ discrete symmetry, in the present scenario we can have dark matter semi-annihilation processes where a DM particle is also present in the final state. The DM annihilation diagrams are shown in Figs. 2.9 and 2.10, while the semi-annihilation ones are shown in Fig. 2.11.

Also, due to the radiative generation of $\langle\phi\rangle$ in most region of parameter space the

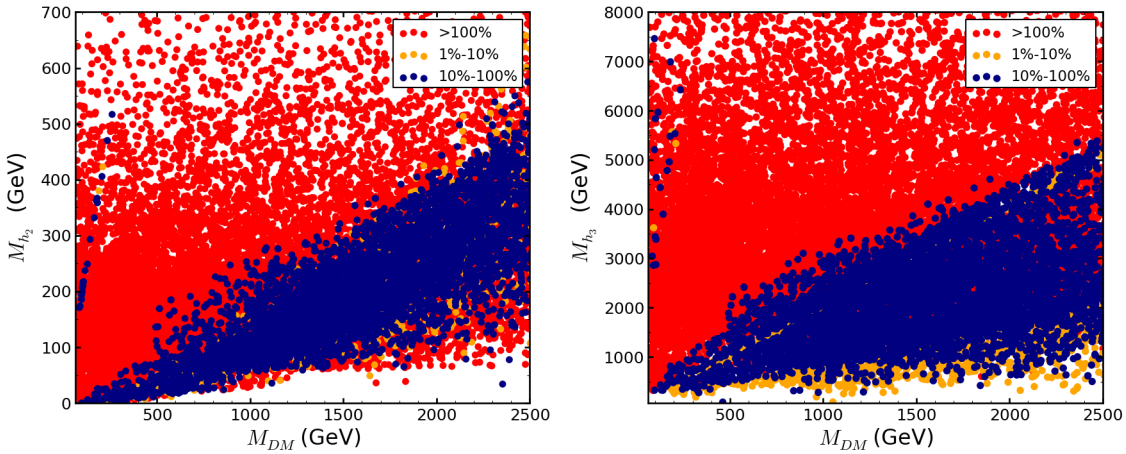

Figure 2.12: Left panel shows scatter plot of the dark matter mass $M_{\rm DM} = M_{Z'}$ versus the scalar mass M_{h_2}. Right panel gives scatter plot of the dark matter mass versus the mass of the heavier scalar h_3. Different colours indicate whether the vector gauge triplet accounts for more or less than 100%, 10% and 1% of the observed dark matter abundance.

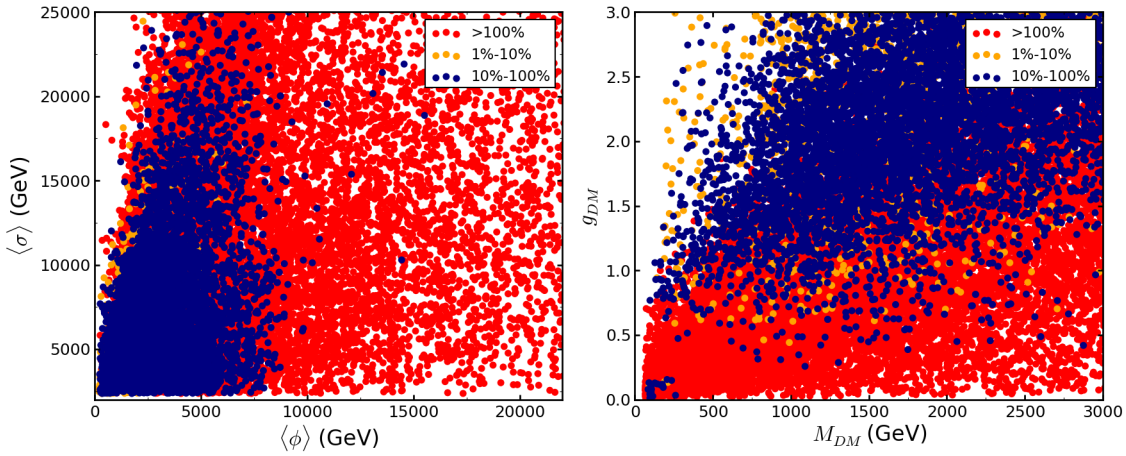

Figure 2.13: Left panel: Scatter plot of the vev $\langle\phi\rangle$ versus the vev of the scalar singlet $\langle\sigma\rangle$. Due to the small mixing angles, we can see that the dark matter relic density is almost independent of $\langle\sigma\rangle$. Right panel: Scatter plot of the dark matter mass $M_{Z'}$ versus the gauge coupling $g_{\rm DM}$. Different colours indicate whether the vector gauge triplet accounts for more or less than 100%, 10% and 1% of the observed dark matter abundance.

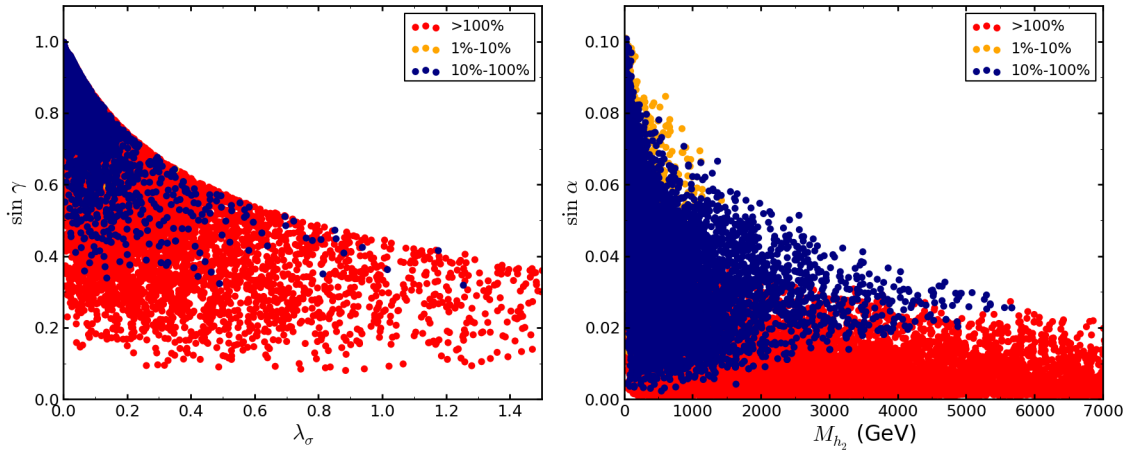

Figure 2.14: Left panel: Scatter plot of $\sin\gamma$ against the quartic coupling λ_σ. Larger values of $\sin\gamma$ are preferred. Right panel: Scatter plot of $\sin\alpha$ versus the scalar mass M_{h_2}. Due to $\langle\sigma\rangle \gg \langle h\rangle$ we get small values for the mixing angle α. Different colours indicate whether the vector gauge triplet accounts for more or less than 100%, 10% and 1% of the observed dark matter abundance.

scalar mass will be smaller than the gauge boson mass, $M_{h_2} < M_{Z'}$. This means that semi-annihilation processes $Z'^a Z'^b \to Z'^c h_i$ will be dominant over annihilation ones in most of the parameter space. To leading order the non-relativistic cross-section from the semi-annihilation diagrams is given by (*cf.* [177]),

$$\langle\sigma_{abc} v\rangle = \frac{3 g_{\rm DM}^4}{128\pi} \frac{(O_{2i})^2}{M_{Z'}^2} \left(1 - \frac{M_{h_i}^2}{3M_{Z'}^2}\right)^{-2} \left(1 - \frac{10 M_{h_i}^2}{9M_{Z'}^2} + \frac{M_{h_i}^4}{9M_{Z'}^4}\right)^{3/2} . \qquad (2.5.101)$$

In order to take into account all annihilation channels into SM particles and properly take into account thresholds and resonances we have implemented the model in `MicrOMEGAs 4.1.5` [211]. We fix the dark matter relic abundance from the latest Planck satellite measurement $\Omega h^2 = 0.1197 \pm 0.0022$ [37]. Figure 2.12 shows the dark matter fraction as a function of $M_{Z'}$ and the scalar mass M_{h_2}; the isolated strip of points on the left side of the plots corresponds to the resonance $M_{h_2} \approx 2M_{Z'}$.

On the left plot in Fig. 2.12 there is a large red coloured region on the left side (producing too much dark matter), in this region M_{h_2} has a close value to $M_{Z'}$ (note that this region does not exist in the Coleman-Weinberg limit). This region exists

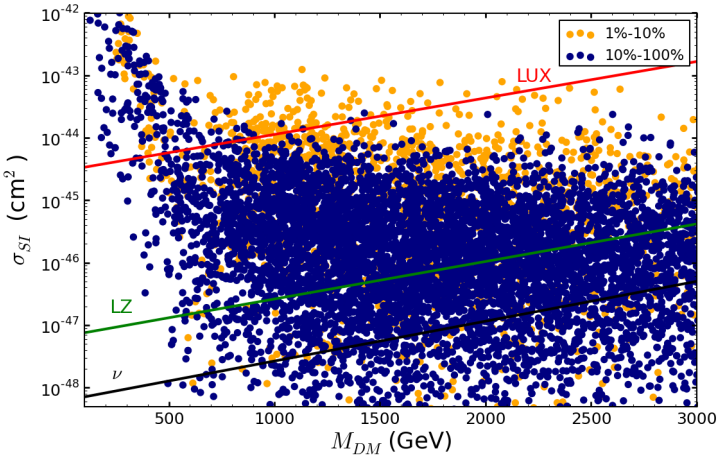

Figure 2.15: Spin-independent DM-nucleon cross-section as a function of the DM candidate mass $M_{Z'}$. We show current experimental limits from LUX [221] (red line), future limits from LZ [79] (green line) and the neutrino coherent scattering limit [246] (black line).

thanks to very large values of M_{h_3} and $\langle\phi\rangle \gg M_{Z'}$. In the left panel of Fig. 2.13 we show the dark matter fraction as a function of both vevs, $\langle\phi\rangle$ and $\langle\sigma\rangle$, from this plot we see there is an upper bound on $\langle\phi\rangle$ in order not to overproduce dark matter, $\langle\phi\rangle < 17$ TeV. Later on we shall see that there is a lower bound on $\langle\sigma\rangle$ coming from leptogenesis, $\langle\sigma\rangle > 2.5$ TeV, we have already imposed this bound on all the scatter plots we show.

In the right panel of Fig. 2.13 we show the dark matter fraction as a function of $M_{Z'}$ and the gauge coupling $g_{\rm DM}$. In this plot it becomes clear that as we increase the gauge coupling, the relic density decreases. The left panel of Fig. 2.14 shows the same analysis for the mixing angle $\sin\gamma$ and the quartic coupling λ_σ. Here we can already notice a preference for the region $\sin\gamma \approx 1$, where λ_σ takes on small values and $\langle\sigma\rangle \gg \langle\phi\rangle$. Due to the lower bound on $\langle\sigma\rangle$ the mixing angle α takes on very small values, this is shown in the right panel of Fig. 2.14.

The spin-independent cross-section between Z'^a and a nucleon is given by,

$$\sigma_{\rm SI} = \frac{f_N^2\, m_N^4\, M_{Z'}^2}{\pi\, \langle h\rangle^2\, \langle\phi\rangle^2} \left(\sum_{i=1}^{3} \frac{O_{2i} O_{1i}}{M_{h_i}^2}\right)^2 , \tag{2.5.102}$$

where m_N is the nucleon mass, $f_N = 0.303$ [180] is the nucleon form-factor, and

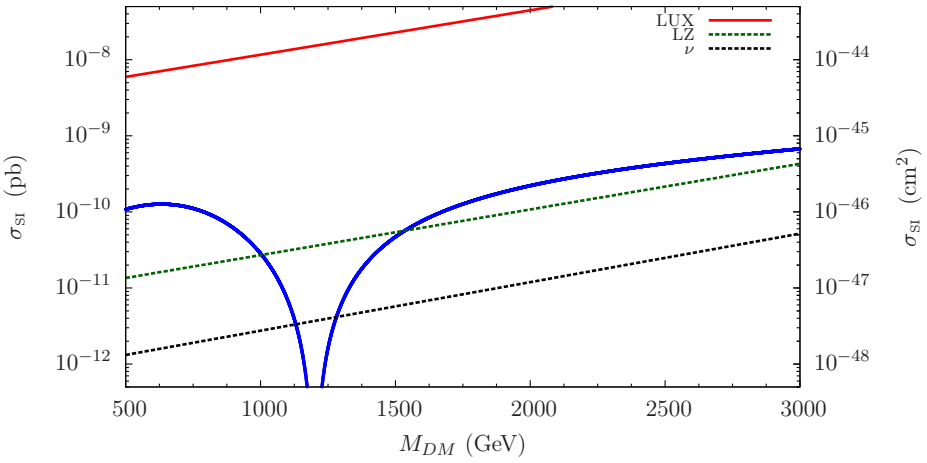

Figure 2.16: Spin-independent DM-nucleon cross-section as a function of the vector DM candidate mass $M_{Z'}$, for benchmark point BP 1. We show current experimental limits from LUX [221] (red line), future limits from LZ [79] (green line) and the neutrino coherent scattering limit [246] (black line). To generate this plot we fix all the scalar couplings and vary only $g_{\rm DM}$, which means that $M_{Z'}$ and M_{h_2} are also varied while all other parameters remain fixed.

O_{ij} are the elements of the rotation matrix Eq. (2.5.92) that relates the scalar mass eigenstates states to the ones in the Lagrangian. This orthogonal matrix O is the one that diagonalises the mass matrix. Due to the form of this matrix, the direct detection diagrams have a destructive interference when the scalar state with a large ϕ component has a mass very close to M_{h_1}, this has been previously noted in [170, 247]; while the scalar state with a large σ component has no direct couplings either to dark matter or to Standard Model particles and hence gives only a small contribution to $\sigma_{\rm SI}$. Figure 2.15 shows that except for resonances, the region with $M_{Z'} < 250$ GeV has been already excluded by the existing experiments, while a large region of parameter space will be tested by future underground experiments such as LZ [79] and XENON1T [82]. In Fig. 2.16 we show the direct-detection cross-section as a function of the dark matter mass for benchmark point BP 1, we fix all the scalar couplings and vary only $g_{\rm DM}$, the dip corresponds to $M_{h_2} \approx M_{h_1}$.

The hidden vector DM we have considered is stable due to the accidental non-Abelian global symmetry SO(3). This accidental symmetry could be broken by non-renormalisable operators leading to the decay of Z'^a, for example $D_\mu \Phi^\dagger \Phi D^\mu H^\dagger H/\Lambda^2$ leads to the decay $Z'^a \to \phi\phi^*$, requiring the lifetime to be longer than the age of the

Universe implies that $\Lambda \gtrsim 10^{13}$ GeV for a dark matter mass of $M_{Z'} \approx 1$ TeV [67]. The decay of the DM particle via higher-dimensional operators can produce an intense gamma-ray line that could be detected in future experiments [248]

2.5.3 Leptogenesis via Oscillations of Right-handed Neutrinos

Leptogenesis is an attractive and minimal mechanism to solve the baryon asymmetry of the Universe (BAU). This means being able to produce the observed value of

$$\frac{n_{b_{\rm obs}}}{s} = (8.75 \pm 0.23) \times 10^{-11}. \tag{2.5.103}$$

In the type-I seesaw mechanism, leptogenesis can take place through CP-violating out-of-equilibrium decays of the heavy Majorana neutrinos in the early Universe with $M_N > 10^9$ GeV [249]. In this scenario, the violation of lepton number goes as

$$\text{LNV} \propto \frac{M_i\, M_j}{\Delta M_{ij}^2}, \tag{2.5.104}$$

and hence it is possible to achieve large lepton asymmetries for smaller values of M_N than the previously quoted lower bound, if one fine-tunes the mass splittings ΔM_{ij} to be very small, this corresponds to resonant leptogenesis [47].

An alternative mechanism is the Akhmedov-Rubakov-Smirnov [42] in which a lepton flavour asymmetry is produced during oscillations of the right-handed Majorana neutrinos N_i with masses around the electroweak scale or below, which makes this approach compatible with classical scale invariance.[4] This mechanism works thanks to an enhancement of the flavour asymmetries at high temperatures $T \gg M_N$ [42, 237],

$$\text{LFV} \propto \frac{T^2}{\Delta M_{ij}^2}. \tag{2.5.105}$$

From Big Bang nucleosynthesis one obtains the lower bound $M_N > 200$ MeV, in

[4] In the sense that no additional very large scales are required to be introduced in the model to make this type of leptogenesis work.

order not to spoil primordial nucleosynthesis. For our calculations we make use of the Casas-Ibarra parametrisation [244] for the matrix Y^D,

$$Y^{D\,\dagger} = U_\nu \cdot \sqrt{m_\nu} \cdot \mathcal{R} \cdot \sqrt{M_N} \times \frac{\sqrt{2}}{\langle h \rangle}\,, \tag{2.5.106}$$

where m_ν and M_N are diagonal mass matrices of active and Majorana neutrinos respectively. The active-neutrino-mixing matrix U_ν is the PMNS matrix which contains six real parameters, including three measured mixing angles and three CP-phases. The matrix $\mathcal{R}$ is parametrised by three complex angles ω_{ij}. Using this framework with three right-handed neutrinos one can generate the correct baryon asymmetry without requiring tuning the N_i mass splittings, but rather enhancing the entries in the Dirac Yukawa matrix through the imaginary parts of the complex angles ω_{ij} [250].

The sterile neutrinos do not participate in Standard Model gauge interactions and for masses in the GeV regime the Majorana Yukawa couplings are small $Y^M \approx 10^{-5}$. Consequently, the initial abundances for the N_i are zero[5]

$$\rho_{N_i}(T_0) = 0. \tag{2.5.107}$$

The characteristic temperature at which oscillations start to occur, and the lepton asymmetry is generated, is usually much larger than the mass of the right-handed neutrinos, $T_{\rm osc} \gg M_{N_i}$. Consequently, lepton number violation is highly suppressed and the total lepton number is approximately conserved,

$$L_{\rm TOT} = L_e + L_\mu + L_\tau + N_1 + N_2 + N_3, \quad \Delta L_{\rm TOT} \approx 0. \tag{2.5.108}$$

Eventually, the sterile neutrinos will start to be produced due to their small Dirac Yukawa couplings at order $\mathcal{O}(|Y_D|^2)$, this production mechanism conserves CP, meaning that the same number of particles and anti-particles is produced. In the limit $T/M \gg 1$, one can define particle and anti-particle states for Majorana

[5] Also one has to assume there is no direct coupling of N_i to the inflaton.

states in terms of their helicity. Once the N_i's start to be produced, the CP-violating oscillations among them will produce an asymmetry $\Delta N_1 \neq 0$, $\Delta N_2 \neq 0$ and $\Delta N_3 \neq 0$, and due to the Dirac Yukawa couplings these asymmetries will be communicated to the active leptons.

In order to generate a baryon asymmetry we require that one of the flavours (N_1 in our case) does not get into thermal equilibrium before the electroweak phase transition[6]. N_2 and N_3 equilibrate with the SM thermal plasma and their asymmetry is communicated to the leptons. But the asymmetry in N_1 will not be communicated to the active leptons and hence N_1 will act as a reservoir for the asymmetry,

$$\Delta L(T_{\rm EW}) \approx -\Delta N_1(T_{\rm EW}), \tag{2.5.109}$$

where ΔL stands for the sum of the three SM flavours asymmetries $\Delta L = \Delta L_e + \Delta L_\mu + \Delta L_\tau$. The SM lepton asymmetry is stored in the least interacting right-handed neutrino and it will be transferred to the baryons via sphaleron processes. Once all three right-handed neutrinos reach thermal equilibrium all the lepton flavour asymmetries are washed out, this is why the condition that N_1 does not get into thermal equilibrium before the electroweak phase transition is a crucial requirement for this mechanism to work.

Applying the naive see-saw relation one finds for the active-sterile mixing angle $|U_{ai}| \sim m_i/M_{N_i}$, for GeV sterile neutrinos this mixing is highly suppressed; nevertheless, it can be enhanced with large imaginary parts of ω_{ij}. For the case of two sterile neutrinos we have the following relation

$$U^2 = \frac{\sum m_i}{2M_N}\left[\exp(\mathrm{Im}\omega)^2 + \exp(\mathrm{Im}\omega)^{-2}\right]. \tag{2.5.110}$$

Therefore, taking large imaginary parts of ω_{ij} one can achieve detectable signal in experiments like SHiP [46], this also leads to large cancellations in the matrix $Y_D M_N^{-1} Y_D^T$ in order to obtain the small masses for the active neutrinos which can

[6]In reality, the requirement is that at least one N_i does not get into thermal equilibrium, it may also be the case that two sterile neutrinos do not equilibrate before the EWPT.

be considered fine-tuning.

The ability to perform experimental searches for the $\mathcal{O}$(GeV) sterile neutrinos is an attractive feature of this mechanism. Allowing for large fine-tuning in the mass splittings opens the region $M_{N_i} \in [10-100]$ GeV. In Ref. [45] it was shown that near future experiments can probe $M_{N_i} = 0.1-10$ GeV for normal ordering and between $M_{N_i} = 0.1-22$ GeV for inverted ordering in the ARS mechanism. However, having experimental access to the heavy mass region is a difficult task.

Due to the non-trivial topological structure of the vacuum in $\mathrm{SU}(2)_L$ there exist electroweak sphaleron processes which violate $B+L$ quantum number, and these will transfer the lepton flavour asymmetry n_{Le} into a baryon asymmetry n_b, with the conversion factor given by,

$$\frac{n_b}{s} \simeq -\frac{3}{14} \times 0.35 \times \frac{n_{Le}}{s}. \tag{2.5.111}$$

As has been discussed previously, a critical condition for the mechanism of [42] to work is that two of three neutrino flavours, N_2 and N_3, should come into thermal equilibrium with their Standard Model counterparts before the Universe cools down to T_{EW} (when electroweak sphaleron processes freeze out), while the remaining flavour does not. In other words, the present mechanism consists of different time scales $T_{\mathrm{osc}} \gg T_{eq_3} \sim T_{eq_2} > T_{\mathrm{EW}} > T_{eq_1}$, where T_{eq_i} represents the temperature at which N_i equilibrates with the thermal plasma and T_{osc} is the temperature at which the oscillations start to occur. In terms of the decay rates for the three sterile neutrino flavours this implies,

$$\Gamma_2(T_{\mathrm{EW}}) > H(T_{\mathrm{EW}}) \,, \quad \Gamma_3(T_{\mathrm{EW}}) > H(T_{\mathrm{EW}}) \,, \quad \Gamma_1(T_{\mathrm{EW}}) < H(T_{\mathrm{EW}}), \tag{2.5.112}$$

where H is the Hubble constant,

$$H(T) = \frac{T^2}{M_{\mathrm{P}}^*}, \qquad M_{\mathrm{P}}^* \equiv \frac{M_{\mathrm{P}}}{\sqrt{g_*}\sqrt{4\pi^3/45}} \simeq 10^{18}\,\mathrm{GeV}, \tag{2.5.113}$$

and $M_{\rm P}^*$ is the reduced Planck mass. Therefore, we require,

$$\Gamma_1(T_{\rm EW}) \,=\, \frac{1}{2}\sum_i Y^{\rm D\,\dagger}_{ei} Y^{\rm D}_{ie}\,\gamma_{av}\,T_{\rm EW} \,<\, H(T_{\rm EW})\,. \tag{2.5.114}$$

Here the dimensionless quantities $\gamma_{av} \approx 3 \times 10^{-3}$ are derived from the decay rates of the right-handed neutrino N_e of the 'electron flavour' tabulated in Ref. [251]. These right-handed neutrino decay (or equivalently production) rates were computed in [251] using $1 \leftrightarrow 2$ and $2 \leftrightarrow 2$ processes[7] involving the neutrino vertices $Y^{D\dagger}_{ai}\,\overline{l_{La}}(\varepsilon H)^\dagger N_i$ and $Y^{D}_{ia}\,\overline{N_i}(\varepsilon H) l_{La}$ with the Dirac Yukawas.

The lepton flavour asymmetry is proportional to the Dirac Yukawa couplings, namely $(Y_D)^4$. Nevertheless, too large Dirac Yukawa couplings also lead to a washout of all the lepton asymmetry before the electroweak phase transition, if the criterion Eq. (2.5.114) is not satisfied any more. This also gives an upper bound on the masses M_{N_i}, which turns out to be around 100 GeV. Thanks to an inefficient washout, Eq. (2.5.114) an asymmetry is created in the individual flavours L_α. For example there might be a larger number of electrons than positrons but this is compensated by a larger number of anti-muons than muons and larger number of anti-taus than taus.

One can also ask if the new interactions present in our model, those involving the Majorana Yukawas, $\frac{1}{2}\,Y^M_{ij}\sigma\overline{N_i}^c N_j$ and $\frac{1}{2}\,Y^{M\dagger}_{ij}\sigma\overline{N_i}N^c_j$, could affect the dynamics. These interactions always contain a pair of right-handed neutrinos and do not change the right-handed neutrino number (the singlet σ carries the N-number -2 but above the electroweak phase transition temperature, the vev of σ vanishes). Hence these processes could contribute to the N production or decay into the Standard Model particles only in combination with other interactions. As the Majorana Yukawa couplings are small $Y^M \approx 10^{-5}$ on the part of the parameter space relevant for us (see Table 2.3) and the cross-section being proportional to $(Y^M)^2$ means that these interactions will give subleading effects to all the processes considered in [251]. Therefore, we can follow [237] and make the assumption that the number density

[7] These processes are shown in Figs. 1 and 2 in Ref. [251] and contain a single external N leg – as relevant for the N-production or decay processes of interest.

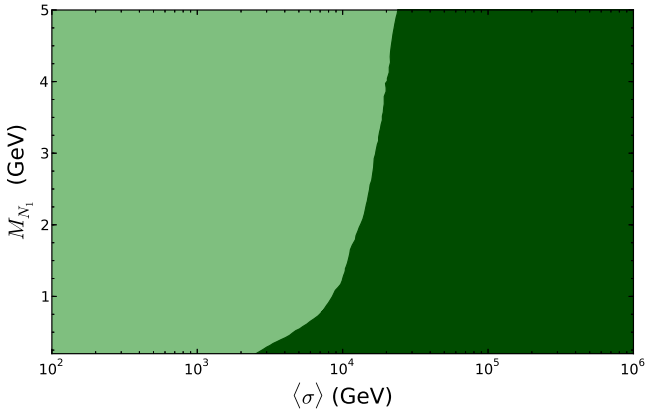

Figure 2.17: The region in dark green can explain the baryon asymmetry through leptogenesis; we have fixed the mass splittings to be $\Delta M_{N_i} \geq M_{N_1}/10$. This plot shows that there is a lower bound $\langle\sigma\rangle > 2.5$ TeV in order to produce the correct amount of baryon asymmetry. The region in light green cannot produce enough baryon symmetry and/or does not satisfy the wash-out criterion Eq. (2.5.114).

of sterile neutrinos is very small compared to their equilibrium density at high temperatures, $T_{\rm osc} \approx 10^6$ GeV, around which the main contributions to the lepton-flavour asymmetry are generated.

It was already shown in [233] that flavoured leptogenesis can work in a classically scale invariant framework. In their set-up three right-handed neutrinos are coupled to a scalar field that acquires a vev, as in the present model. The main difference being that in the present scenario we have not gauged the $B-L$ quantum number. We quote the final result for the lepton flavour asymmetry (of ath flavour) obtained in [233] from extending the results of Ref. [237] to the classically scale invariant case,

$$\frac{n_{La}}{s} = -\gamma_{av}^2 \times 7.3 \times 10^{-4} \sum_c \sum_{i\neq j} i \left(Y_{ai}^{\rm D\,\dagger} Y_{ic}^{\rm D} Y_{cj}^{\rm D\,\dagger} Y_{ja}^{\rm D} - Y_{ai}^{\rm D\,t} Y_{ic}^{\rm D\,*} Y_{cj}^{\rm D\,t} Y_{ja}^{\rm D\,*} \right) \times \mathcal{I}_{ij} \,, \tag{2.5.115}$$

where the quantity $\mathcal{I}_{ij}$ is given by,

$$\mathcal{I}_{ij} = \frac{16}{\sum_k (Y_{ik}^{\rm M\,\dagger} Y_{ki}^{\rm M} - Y_{jk}^{\rm M\,\dagger} Y_{kj}^{\rm M})} \frac{M_{\rm P}}{\langle\sigma\rangle} \left(1 - \frac{\langle\sigma\rangle}{T_{\rm osc}} + \frac{1}{4}\tan^{-1}\left(\frac{4\langle\sigma\rangle}{T_{\rm EW}}\right) - \frac{1}{4}\tan^{-1}(4) \right) , \tag{2.5.116}$$

for $\langle\sigma\rangle < T_{\rm osc}$. For the case $\langle\sigma\rangle \geq T_{\rm osc}$ and further details on the derivation of

Eq. (2.5.115) we refer the reader to Ref. [233]. It follows from (2.5.116) that the amount of the lepton flavour asymmetry is proportional to $\langle\sigma\rangle\, M_P/\Delta M^2_{N_i}$. Hence if we want to avoid any excessive fine-tuning of the mass splittings between different flavours of Majorana neutrinos, the relatively large values of $\langle\sigma\rangle \gtrsim 10^4$ GeV are preferred. From Fig. 2.17 we can see that there is a lower bound on $\langle\sigma\rangle$ if we impose some restriction on the mass splittings of the right-handed neutrinos. In view that we would like to stay far away from the fine-tuning region, we impose $\Delta M_{N_i} \geq M_{N_1}/10$ which gives the limit $\langle\sigma\rangle > 2.5$ TeV in order for leptogenesis to explain the baryon asymmetry. Imposing this condition removes the points with very small mixing angle γ, as can be seen in the left panel of Fig. 2.14.

As we can see from Fig. 2.17 there is also an upper bound on M_{N_i} for each value of $\langle\sigma\rangle$, this bound is mainly due to the wash-out criterion Eq. (2.5.114) not being satisfied any more. This upper bound becomes weaker once we reach $\langle\sigma\rangle \geq 10^4$ GeV. This sits well with our approach based on the common dynamical origin of all vevs: once an explanation for dark matter is included, $\langle\sigma\rangle$ cannot be too large compared to $\langle\phi\rangle$.

The procedure to obtain the plot in Fig. 2.17 is as follows. We fix the complex phases ω_{12} and ω_{13} to the benchmark values given in [237] ($\omega_{12} = 1 + 2.6i$ and $\omega_{13} = 0.9 + 2.7i$), and for each point we scan over ω_{23}, if we find at least one point that works well then we label it as a good point (dark green) otherwise it is a bad point (light green). In further scans we have found that varying ω_{12} and ω_{13} has a negligible impact on the final results.

The generated total lepton asymmetry is proportional to $\langle\sigma\rangle$, (*cf.* (2.5.115), (2.5.116))

$$n_L \sim (Y^D)^4\, \frac{\langle\sigma\rangle\, M_P}{\Delta M^2_{N_i}} \sim \langle\sigma\rangle\, M_P\, \frac{m_\nu^2}{v^4}\,, \tag{2.5.117}$$

where we used the see-saw mechanism for the masses m_ν of visible neutrinos, and v is the SM Higgs vev. Hence n_L vanishes as $\langle\sigma\rangle$ approaches zero. This also explains why in Fig. 2.17, there is a stronger dependence on $\langle\sigma\rangle$ than on the masses M_{N_i}.

We carried out a scan over all free parameters in our model to determine the region of the parameter space where the leptogenesis mechanism outlined above can

generate the observed baryon asymmetry. At the same time we require that the model provides a viable candidate for cosmological dark matter. We would like to mention in passing that all the present results on leptogenesis also hold when a generic scalar generates a mass for the sterile neutrinos (i.e with no reference to classical scale invariance).

The results of the scan and the connection between the leptogenesis and dark matter scales are reviewed in the following section. Furthermore, in Tables 2.2 and 2.3 we present four benchmark points to illustrate the viable model parameters. In the remainder of this section we would like to comment on the choice of parameters for the leptogenesis part of the story.

We first note that our leptogenesis realisation does not require any sizeable fine-tuning of the mass splittings ΔM_{N_i}. For example our first benchmark point BP 1 has (*cf.* Table 2.3),

$$M_N = (0.225\,,\, 0.25\,,\, 0.275)\,\text{GeV}. \tag{2.5.118}$$

At the same time, the masses of active neutrinos are set to agree with the observed mass splittings; for BP 1 we have,

$$m_\nu = (0\,,\, 8.7\,,\, 49.0)\,\text{meV}. \tag{2.5.119}$$

The lepton asymmetry (2.5.115) also depends on the matrix of Dirac Yukawa couplings Y^D. We compute Y^D in the Casas-Ibarra parametrisation Eq. (2.5.106) using (2.5.118) and (2.5.119) along with the PMNS matrix and the $\mathcal{R}$ matrix. We have carried out a general scan on the complex angles ω_{ij} of the $\mathcal{R}$ matrix and found that having non-vanishing $\text{Im}[\omega_{ij}]$ is important in order to obtain the required amount of lepton asymmetry.[8] At the same time this does not lead to any excessive fine-tuning. We have checked this for the numerical values of $\mathcal{R}$ matrix elements in our scan.

[8]Note that positive values of $\text{Im}[\omega_{ij}]$ enhance the elements of the Dirac Yukawa matrix Y^D.

For example, for BP 1 we have (using the ω_{ij} values in Table 2.3),

$$\mathcal{R} = \begin{pmatrix} -36.52 - 33.80i & 34.11 - 36.97i & 5.854 + 4.604i \\ 84.43 + 100.0i & -101.0 + 85.98i & -16.63 - 14.20i \\ -105.4 + 91.81i & -93.42 - 106.4i & 14.94 - 17.61i \end{pmatrix}, \tag{2.5.120}$$

and the resulting matrix of Dirac Yukawa couplings,

$$Y^D = \begin{pmatrix} 17.87 - 2.12i & -73.37 - 125.6i & -210.9 - 127.3i \\ -2.168 - 19.11i & -134.4 + 77.79i & -136.9 + 224.6i \\ -3.395 - 0.2434i & 9.677 + 24.56i & 34.69 + 28.93i \end{pmatrix} \times 10^{-8}. \tag{2.5.121}$$

These matrices do not exhibit a high degree of tuning, and we have checked that this is also the case for generic points of our scan.

2.5.4 Connection among the Scales

After having performed a scan over all free parameters in our model, we find that:
(1) $\langle\phi\rangle < 17$ TeV in order for dark matter not to overclose the Universe, and
(2) $\langle\sigma\rangle > 2.5$ TeV in order in order for leptogenesis to explain the baryon asymmetry.

From the left plot of Fig. 2.14 we can see that the interesting region in parameter space has large values of $\sin\gamma$, and with this in mind we can separate the interesting regime into two regions:

1. $\langle\sigma\rangle \approx \langle\phi\rangle \sim$ TeV

   In this region[9] we have $\sin\gamma \approx \cos\gamma$ ($\gamma \approx \pi/4$) so there is a strong mixing between the scalar states ϕ and σ, and due to the Gildener-Weinberg conditions $\lambda_\phi \approx \lambda_\sigma$. To avoid overproducing DM, both $\langle\sigma\rangle$ and $\langle\phi\rangle$ have to be less than 10 TeV. Due to the not so large values of $\langle\sigma\rangle$, a large part of this region requires some amount of fine-tuning of the right-handed neutrino mass splittings in

[9] Recall that $\tan^2\gamma = \langle\sigma\rangle^2/\langle\phi\rangle^2$.

	BP 1	BP 2	BP 3	BP 4
Ωh^2	0.122	0.12	0.12	0.118
$\sigma_{\rm SI}$ (cm^2)	1.90×10^{-46}	3.32×10^{-46}	1.06×10^{-46}	3.11×10^{-47}
$\langle h \rangle$ (GeV)	246	246	246	246
$\langle \phi \rangle$ (GeV)	2260	1260	1020	4590
$\langle \sigma \rangle$ (GeV)	3080	5930	2830	11790
$\lambda_{h\phi}$	0.035	0.406	-0.335	0.017
$\lambda_{\phi\sigma}$	0.164	0.122	0.40	0.141
$\lambda_{h\sigma}$	0.0185	0.018	-0.045	0.003
λ_h	0.131	0.159	0.147	0.130
λ_σ	0.044	0.003	0.027	0.011
λ_ϕ	0.152	1.352	1.527	0.464
$g_{\rm DM}$	0.61	1.39	0.96	2.41
M_{h_1} (GeV)	125	125	125	125
M_{h_2} (GeV)	81.6	94.1	137.3	839.1
M_{h_3} (GeV)	1544	2124	1900	4745
$M_{Z'}$ (GeV)	690	880	490	5527
$\sin\alpha$	0.06	0.04	0.08	0.02
$\sin\beta$	0.01	0.03	-0.025	0.001
$\sin\gamma$	0.80	0.98	0.94	0.93
$\mu_{\rm GW}$ (GeV)	829	1149	1110	4550

Table 2.2: Four benchmark points for the model presented in this work. All four points give the correct dark matter abundance within 2σ.

order for leptogenesis to work. The use of the Gildener-Weinberg mechanism is crucial in this region.

2. $\langle \sigma \rangle \gg \langle \phi \rangle \sim$ TeV

   In this region we have $\sin\gamma \approx 1$, so it can be seen as the Coleman-Weinberg limit of the more general Gildener-Weinberg mechanism. The scalar σ overlaps maximally with h_2 and can be thought of as the Coleman-Weinberg scalar. In this region the radiative symmetry breaking is induced by $\lambda_\sigma \ll 1$ and we get $M_{h_2} \ll M_{h_3}$. This region also corresponds to the majority of good (blue) points in Figs. 2.12-2.14. Most points have $M_{\rm DM} > M_{h_2}$. This is the region of most interest since the large values of $\langle \sigma \rangle$ require almost no fine-tuning in ΔM_{N_i} in order for leptogenesis to work.

In Table 2.2 we give a set of benchmark points that satisfy all experimental constraints and give the correct dark matter abundance within 2σ. The benchmark points BP1, BP2 and BP3 are within reach of future direct detection dark matter

	BP 1	BP 2	BP 3	BP 4
$\langle\sigma\rangle$ (GeV)	3080	5930	2830	11790
M_{N_1} (GeV)	0.225	0.30	0.20	0.9
M_{N_2} (GeV)	0.25	0.33	0.22	1.0
M_{N_3} (GeV)	0.275	0.36	0.24	1.1
m_1 (meV)	0.0	0.0	0.0	0.0
m_2 (meV)	8.7	8.7	8.7	8.7
m_3 (meV)	49.0	49.0	49.0	49.0
$\sin\theta_{12}$	0.55	0.55	0.55	0.55
$\sin\theta_{23}$	0.67	0.67	0.67	0.67
$\sin\theta_{13}$	0.15	0.15	0.15	0.15
δ	$-\pi/4$	-0.6	$-\pi/4$	π
α_1	0	0.3	0	$-\pi$
α_2	$-\pi/2$	-1.1	$-\pi/2$	π
ω_{12}	$1.5+2.6i$	$1.5+2.6i$	$1.0+2.6i$	$1.5+2.6i$
ω_{13}	$0.9+2.7i$	$0.9+2.7i$	$0.9+2.7i$	$0.9+2.7i$
ω_{23}	$0.03-1.8i$	$-0.30-1.4i$	$0.05-1.85i$	$-1.4i$
$n_{Le}/(s\times 2.5\times 10^{-10})$	-4.71	-5.75	-5.36	-6.43
$n_{L\mu}/(s\times 2.5\times 10^{-10})$	-1.66	-44.18	19.03	-75.82
$n_{L\tau}/(s\times 2.5\times 10^{-10})$	6.37	49.93	-13.67	82.25
$\Gamma_e/H(T_{\rm EW})$	0.90	0.82	0.91	0.98
$\Gamma_\mu/H(T_{\rm EW})$	58.43	42.29	56.61	315.5
$\Gamma_\tau/H(T_{\rm EW})$	167.63	99.03	163.07	115.56
$T_{\rm osc}$ (GeV)	4.43×10^6	1.90×10^6	3.71×10^6	4.84×10^6
$Y_1^{\rm M}$	7.3×10^{-5}	5.1×10^{-5}	7.1×10^{-5}	7.6×10^{-5}
$Y_2^{\rm M}$	8.1×10^{-5}	5.6×10^{-5}	7.8×10^{-5}	8.5×10^{-5}
$Y_3^{\rm M}$	8.9×10^{-5}	6.1×10^{-5}	8.5×10^{-5}	9.4×10^{-5}
$\langle Y^{\rm D}\rangle$	1.26×10^{-8}	1.45×10^{-8}	1.18×10^{-8}	2.5×10^{-8}

Table 2.3: Parameters for leptogenesis, same benchmark points as in Table 2.2.

experiments. For these same points we provide in Table 2.3 numerical values that generate the correct amount of baryon asymmetry via leptogenesis. We work with the current experimental central values for the neutrino sector taken from [252], we assume normal ordering for the active neutrino masses. The values for $\langle Y^D\rangle$ are computed as the average of $\sqrt{2M_N m_\nu}/\langle h\rangle$. This estimate corresponds to the naive see-saw relation and it is smaller than the actual entries in the matrix Y^D due to the enhancement by the imaginary parts of ω_{ij} in the $\mathcal{R}$ matrix. Nevertheless, for our benchmark points these enhancement factors are always less than 1.5×10^2.

Finding a connection between the scale $\langle\phi\rangle$, responsible for dark matter, and the scale $\langle\sigma\rangle$, responsible for leptogenesis, would be of high interest. From Eq. (2.5.115)

and applying the conversion factor (2.5.111), we can approximate the baryon relic abundance as,

$$\Omega_b h^2 \approx 2.045\, M_{\rm P} \frac{\Delta(Y_D^4)\,\langle\sigma\rangle}{\Delta(M_N^2)}\,. \tag{2.5.122}$$

Regarding the dark matter relic density, in a large portion of our parameter scan semi-annihilations are dominant over annihilations, and hence we can approximate by,

$$\Omega_{\rm DM} h^2 \approx \frac{1.07\times 10^9\, x_f}{\sqrt{g_\star}\, M_{\rm P}\, 2\langle\sigma_{abc} v\rangle/3} \times {\rm GeV}^{-1}\,, \tag{2.5.123}$$

where $x_f = M_{Z'}/T_f$, T_f is the freeze-out temperature for dark matter, and $g_\star$ is the effective number of relativistic degrees of freedom. A good approximation for the mixing angles is to take $\alpha \approx \beta \approx 0$ and $\sin\gamma \approx 0.9$, substituting these values into Eq. (2.5.101) leads to,

$$\Omega_{\rm DM} h^2 \approx \frac{7.76\times 10^{11}}{M_{\rm P}} \frac{\langle\phi\rangle^2}{g_{\rm DM}^2} \times {\rm GeV}^{-1}\,. \tag{2.5.124}$$

Using Eqs. (2.5.122) and (2.5.124) we can find the ratio

$$\frac{\Omega_{\rm DM} h^2}{\Omega_b h^2} \approx \frac{3.79\times 10^{11}\,\Delta(M_N^2)}{M_{\rm P}^2\, g_{\rm DM}^2\, \Delta(Y_D^4)} \frac{\langle\phi\rangle^2}{\langle\sigma\rangle} \times {\rm GeV}^{-1} = 5\,, \tag{2.5.125}$$

where the last equality comes from the observed relic densities [37]. After imposing this relation we find a connection among the scales in the model,

$$\langle\sigma\rangle \;\approx\; \varepsilon\,\langle\phi\rangle^2 \times {\rm GeV}^{-1}\,, \tag{2.5.126}$$

where the parameter ε is defined as,

$$\varepsilon \;=\; \frac{7.59\times 10^{10}\,\Delta(M_N^2)}{M_{\rm P}^2\, g_{\rm DM}^2\, \Delta(Y_D^4)}\,. \tag{2.5.127}$$

The parameter M_N has a dependence on $\langle\sigma\rangle$, but from a physical perspective it is more relevant to fix the mass splittings rather than the Majorana Yukawa couplings. The parameter ε gives the connection between both scales, typical values for this parameter are around 10^{-4}. Figure 2.18 illustrates this connection between the scales keeping the parameter ε fixed to different values.

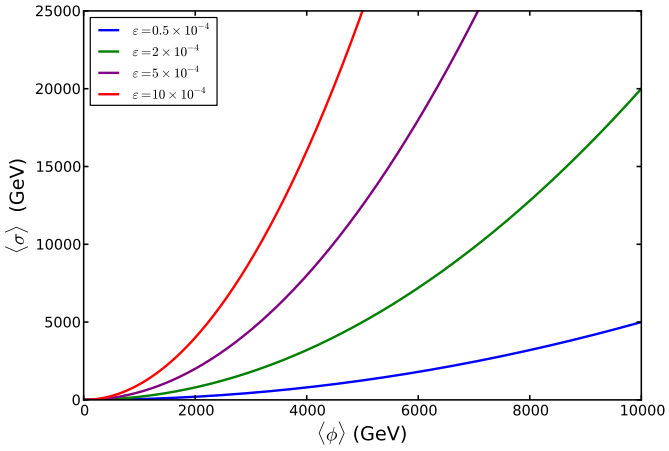

Figure 2.18: Relation among the two vacuum expectation values, $\langle\phi\rangle$ and $\langle\sigma\rangle$, that yields the observed value of $\Omega_{\rm DM}h^2/\Omega_b h^2 = 5$. Different colours correspond to different values of the parameter ε defined in Eq. (2.5.127).

2.6 Summary

In this chapter we discussed the concept of classical scale invariance as theoretical guide for models beyond the SM. In Section **2.2**, we discussed the role of scale invariance in QFT, and in Section **2.3**, we derived the one-loop Coleman-Weinberg effective potential.

In Section **2.4**, we constructed a classically scale invariant version of the inert doublet model that provides the correct dark matter relic abundance and can satisfy vacuum stability, perturbativity, and unitarity constraints all the way up to the Planck scale. We found that after imposing classical scale invariance the small mass region $50 < M_H < 80$ GeV remains unchanged, meaning that some points survive to the Planck scale for $M_H \approx 70$ GeV [213,227]. In the high mass region $M_H > 500$ GeV, CSI can have some relevant impact on the calculation of the relic density and one has to be careful to consider the interactions with the hidden sector to compute the correct value for the relic density. CSI also has an impact on the direct detection cross-section, the latter being enhanced by a light CW scalar and a large scalar mixing angle, giving in some cases cross-sections above current experimental limits. Regarding the RG analysis, we found that the regions in parameter space viable up to the Planck scale are significantly smaller in the CSI scenario.

Moreover, we showed that due to the dynamical origin of the scales, our model differs from an IDM plus a scalar singlet. The introduction of new annihilation channels for the H opens a small new region in parameter space where the correct relic density can be achieved. Nevertheless, after performing the RG analysis we showed that the parameter space in our model is more restrictive than in the ordinary IDM.

Similar extensions of the IDM to the one we constructed include [253] where a complex singlet was added to the IDM with complex quartic couplings mainly to trigger baryogenesis and in [254] the authors considered an extra U(1) symmetry in the IDM and study the production of dark matter from decaying cosmic strings. The authors in [255] promoted the Z_2 symmetry to a local U(1) symmetry and add two complex scalars charged under this U(1), this is different from our setup where the inert doublet has no charge under $\mathrm{U}(1)_{\mathrm{CW}}$ and the CW mechanism generates all the vevs. In [256] the authors studied dark matter candidates in the $\mathrm{U}(1)_{B-L}$ classically scale invariant theory, but they focused on a gauge singlet and a complex scalar which has a $B-L$ charge as dark matter.

As the inert scalars in H_2 couple to the electroweak gauge bosons and the SM Higgs, these particles may be searched for using leptons or jets plus missing energy at the LHC and future colliders [216, 257–260]. Nevertheless, the search for inert Higgses above 300 GeV seems difficult at the LHC. In our scenario, future searches for a new scalar that mix with the SM Higgs could provide some tighter bounds on the portal coupling λ_{P1} which then would have an impact on the parameters in the model presented herein.

In Section **2.5**, we presented a model that simultaneously explains the dark matter and the baryon asymmetry of the Universe, where all the scales in the theory are dynamically generated and therefore have a common origin. In order to ensure the stability of the dark matter candidate, one usually needs to introduce a discrete symmetry by hand. One of the attractive features of the present model is that it leads to a stable DM candidate without the need of introducing an extra discrete symmetry. We already know that in the Standard Model lepton number and baryon number are accidental symmetries, the latter being responsible for the stability of

the proton. In our framework, the hidden vector DM is stable due to the accidental non-Abelian global symmetry SO(3). This accidental symmetry could be broken by non-renormalisable operators leading to the decay of Z'^a and producing an intense gamma-ray line that could be detected in future experiments [248].

This model also predicts two extra scalar states that have a Higgs-like behaviour and masses around the electroweak scale. From the relation for $\tan^2\alpha$, Eq. (2.5.97), the interesting region $\langle\sigma\rangle \gg \langle h\rangle$ already requires a small mixing angle α with the SM Higgs boson, due to the small mixing angles we obtain values of $\cos^2\alpha\cos^2\beta > 0.95$, so their detection would only be feasible at future colliders. Nevertheless, the LHC at high luminosity will improve the current constraints on the mixing angles α and β.

From dark matter considerations the value of $\langle\phi\rangle$ is required to be around the TeV scale and due to the common origin of all the vevs, $\langle\sigma\rangle$ cannot be too large, compared to $\langle\phi\rangle$. This implies that sterile neutrinos should have small masses of order $\mathcal{O}(1)$ GeV in order for leptogenesis to work without severe tuning of the mass splittings ΔM_{N_i}. Under some mild assumptions, we found a connection among the scales $\langle\phi\rangle$ (responsible for dark matter) and $\langle\sigma\rangle$ (responsible for leptogenesis) Eq. (2.5.126), in order to match the observed ratio $\Omega_{\rm DM}h^2/\Omega_b h^2 = 5$. Assuming classical scale invariance as an underlying symmetry, we constructed a minimal extension of the SM that addresses dark matter, the baryon asymmetry of the Universe and the origin of the electroweak scale.

The issue of naturalness has been at the core of theories beyond the Standard Model. However, the so far negative results for searches of supersymmetric particles and other popular solutions to the naturalness problem are pointing to a different approach to explain the origin of the electroweak scale. In the models presented in this section, the electroweak scale and the dark matter scale have a common origin from the breaking of classical scale invariance. We hope that upcoming direct and indirect detection experiments along with the second run of the LHC will provide an insight into our understanding of the nature of dark matter.

Chapter 3

Dark Matter Searches at Particle Colliders

The nature of roughly 80% of the matter in the Universe remains a mystery. This missing matter is referred to as dark matter (DM). The evidence for its existence, that we have discussed in the Introduction, cf. Section **1.4**, presents strong motivation for new physics beyond the SM. In the present chapter, we will focus on the weakly interacting massive particle (WIMP) as a dark matter candidate.

In Section **3.1**, we discuss thermal freeze-out as a production mechanism for the DM relic density. In Section **3.2**, we provide a short review of dark matter searches at the Large Hadron Collider (LHC). In Section **3.3**, based on [3], we present and study simplified models of DM where the DM candidate and the coannihilation partner are added to the SM, we study current and future constraints. In Section **3.4**, we study the sensitivity that future e^+e^- linear colliders, such as the Compact Linear Collider (CLIC) and the International Linear Collider (ILC), will have to these models. We present our conclusions in Section **3.5**.

3.1 WIMP Dark Matter

In this section, we discuss the thermal freeze-out mechanism to generate the DM relic abundance for WIMPs. Assuming that the dark matter particle is its own anti-particle, the time evolution of the number density of this particle species is governed

by the Boltzmann equation

$$\frac{dn}{dt} = -3Hn - \langle\sigma v\rangle_{\rm ann}\left(n^2 - n_{\rm eq}^2\right), \tag{3.1.1}$$

where $\langle\sigma v\rangle_{\rm ann}$ is the thermally averaged annihilation cross-section and n ($n_{\rm eq}$) is the DM number density (at thermal equilibrium). $H \equiv \dot{a}/a$ is the Hubble expansion rate and a represents the scale factor. Writing the interaction rate as $\Gamma \equiv n\langle\sigma v\rangle_{\rm ann}$, the freeze-out temperature, T_F, is the temperature at which the interaction cross-section is at the same order as the Hubble expansion rate $\Gamma(T_F) \sim H(T_F)$. Important features can be captured by the factor Γ/H. When $\Gamma \gg H$ the interactions between dark matter and the SM particles keep DM in thermal equilibrium. Later on, when $\Gamma \ll H$, dark matter particles have become diluted and the interactions are not enough to keep thermal equilibrium. The annihilations freeze out and the DM population goes out of thermal equilibrium.

The number density decreases as the Universe expands. Consequently, in order to work with a quantity that factors out the expansion of the Universe we use the yield or comoving number density $Y \equiv n/s$, where s is the total entropy density of the Universe and the product sa^3 remains constant. The quantity Y represents the actual number of dark matter particles per comoving volume. Defining the paramater $x \equiv m/T$, for the radiation dominated epoch we have $H(T) = \sqrt{g_*}\sqrt{4\pi^3/45}\,T^2/M_P^2 = x^{-2}H(m)$, where g_* is the effective number of relativistic degrees of freedom. We can then write Eq. (3.1.1) as

$$\frac{dY}{dx} = \frac{-x\langle\sigma v\rangle_{\rm ann}s}{H(m)}\left(Y^2 - Y_{\rm eq}^2\right). \tag{3.1.2}$$

It is convenient to define the dimensionless quantity $\Omega_\chi \equiv \rho_\chi/\rho_c$ where ρ_c is the critical density of the Universe (for which the spatial geometry of the Universe is flat) and the χ subscript denotes quantities associated to the dark matter,

$$\rho_c = \frac{3H_0^2}{8\pi G} = 3H_0^2M_P^2, \tag{3.1.3}$$

the subscript 0 denotes the present values for the parameters. The DM relic density

is then given by,

$$\Omega_\chi = \frac{\rho_\chi}{\rho_c} = \frac{m_\chi n_0}{\rho_c} = \frac{m_\chi Y_0\, s_0}{\rho_c}, \tag{3.1.4}$$

where the current entropy density of the Universe is $s_0 = 2889.2\,\mathrm{cm}^{-3}$. At the time of freeze-out, the dark matter velocity is already small $\langle v^2\rangle \approx 0.3$ and therefore we can perform a non-relativistic expansion in powers of v^2 for the annihilation cross-section,

$$\langle \sigma v\rangle_{\rm ann} = a + b\langle v^2\rangle + \mathcal{O}(\langle v^4\rangle) \approx a + 6b/x, \tag{3.1.5}$$

where a and b are constant terms. This allows us to arrive to the solution of Eq. (3.1.2), cf. [261],

$$Y_0 = \sqrt{\frac{45}{\pi g_*}}\frac{x_F}{M_P\, m_\chi (a + 3b/x_F)}, \tag{3.1.6}$$

and the DM relic density can be expressed as follows,

$$\Omega_\chi h^2 \approx \frac{1.07\times 10^9\,\mathrm{GeV}^{-1}}{M_P}\frac{x_F}{\sqrt{g_*}(a + 3b/x_F)}, \tag{3.1.7}$$

where we have written in terms of the Hubble parameter $h = (H_0/100)\,\mathrm{km\,s^{-1}\,Mpc^{-1}}$.

A good estimate for the freeze-out temperature is $x_F = m/T_F \approx 25$ and at this temperature we have $g_* \approx 80$. Then, by taking $\langle \sigma v\rangle_{\rm ann} \sim \alpha^2/m_X^2$ where $\alpha = g^2/(4\pi)$ is the coupling between DM and the SM sector, we can write

$$\Omega_\chi h^2 \approx \frac{3\times 10^{-27}\,\mathrm{cm}^3/\mathrm{s}}{\langle \sigma v\rangle_{\rm ann}} \approx 0.1\left(\frac{0.01}{\alpha}\right)^2\left(\frac{m_\chi}{200\,\mathrm{GeV}}\right)^2. \tag{3.1.8}$$

Therefore, in order to reproduce the correct relic abundance $\Omega_\chi h^2 \approx 0.12$ the dark matter mass should be close to the electroweak scale $m_\chi \sim \mathcal{O}(100)$ GeV and the coupling between the DM and the visible sector should be close to the weak coupling in the SM $g \sim 0.4$. In the literature, this numerical coincidence is sometimes referred to as the WIMP miracle; however, as we have discussed in Section **1.4.1** there are many alternative proposals to the WIMP that can also naturally explain the observed relic density.

When examining the cosmological history of the Universe, it is not hard for a BSM particle to reach thermal equilibrium with the SM plasma in the early epochs,

even a small coupling $g \sim 10^{-6}$ to the visible sector will bring this new state into thermal equilibrium. WIMP candidates are also present in many models beyond the Standard Model. Moreover, due to its mass around the electroweak scale and a coupling similar to the weak coupling in the SM, this is an ideal DM candidate to be probed at particle colliders which is going to be the focus of the present chapter. All these reasons combined make the WIMP a very attractive DM candidate to study.

3.2 Dark Matter Searches at the LHC

An alternative and complementary search to direct and indirect detection is being able to produce the dark matter particle itself. This could be achieved at particle colliders by studying the pair production of dark matter recoiling against any visible particle X. At the LHC one can study the process,

$$pp\,(p\bar{p}) \to \chi\chi + X, \tag{3.2.9}$$

where χ corresponds to the DM candidate. The visible object needs to be hard, i.e. it must possess large transverse momentum p_T, for example the CMS mono-jet search requires a transverse momentum of at least 110 GeV [262]. The largest background for this process is when a Z boson decays into neutrinos in associated production of jets.

Ideally, one would like to find experimental constraints that are as model-independent as possible, rather than studying them model-by-model. Using effective field theory (EFT), where one integrates out all the new degrees of freedom except for the dark matter particle, is a powerful and model-independent approach [263–276]. For example, one could set out to study the following dimension six operator,

$$\mathcal{O}_{\mathrm{EFT}} = \frac{(\bar{\chi}\chi)(q\bar{q})}{\Lambda^2}, \tag{3.2.10}$$

where χ stands for the DM fermion candidate, q for a SM quark and Λ is a parameter with dimensions of energy. An EFT is non-renormalisable and it will break down at a scale connected to the masses of the heavier particles that have been integrated out,

$\Lambda \sim M_{\rm med}$. Therefore, this is a valid approach only when the mediator masses are much larger that the typical energy scale of the process being studied [262, 277, 278].

More concretely, the EFT is reliable as long as $Q_{\rm tr} < M_{\rm med}$, where $M_{\rm med}$ is the mass of the mediator and $Q_{\rm tr}$ is the momentum transfer in the process. At the LHC with centre of mass energy of 8 TeV, the momentum transfer $\langle Q_{\rm tr}^2 \rangle^{1/2}$ is always larger than 500 GeV. Therefore, $M_{\rm med}$ should be TeV scale in order for the EFT to be valid [262]. In the context of models of dark matter there is no reason to expect the mediator to be much heavier than the DM candidate, i.e. $M_{\rm med} \gg m_{\rm DM}$, and thus the community has proposed the study of simplified models of dark matter where the mediator particle is explicitly written in the model.

In the approach of simplified models one introduces to the SM the dark matter candidate and the mediator particle that couples to DM and quarks. The following simplified models of dark matter have been studied in the literature

$$\mathcal{L}_{\rm vector} \supset g_q V^\mu \sum_q \bar{q}\gamma_\mu q + g_{\rm DM} V^\mu \bar{\chi}\gamma_\mu \chi, \tag{3.2.11}$$

$$\mathcal{L}_{\rm axial-vector} \supset g_q V'^\mu \sum_q \bar{q}\gamma_\mu \gamma^5 q + g_{\rm DM} V'^\mu \bar{\chi}\gamma_\mu \gamma^5 \chi, \tag{3.2.12}$$

$$\mathcal{L}_{\rm scalar} \supset g_q \, \phi \sum_q \frac{y_q}{\sqrt{2}} \, \bar{q} q + g_{\rm DM} \phi \bar{\chi} \chi, \tag{3.2.13}$$

$$\mathcal{L}_{\rm pseudoscalar} \supset g_q \, a \sum_q \frac{y_q}{\sqrt{2}} \, \bar{q}\gamma^5 q + g_{\rm DM} a \bar{\chi}\gamma^5 \chi, \tag{3.2.14}$$

where the sum is over all quarks and χ stands for the DM particle which can be either a Majorana or a Dirac fermion. The first two models correspond to spin-1 mediators, where the coupling can be either vector or axial-vector. The last two lines correspond to spin-0 mediators, where the possibilities are scalar or pseudoscalar mediator. These couplings are taken proportional to the SM Yukawas y_q since they usually arise from Higgs mixing with a new scalar; in addition, flavour-changing neutral current are naturally suppressed in this manner.

The simplified models described above consist of four free parameters: the coupling of the mediator to DM $g_{\rm DM}$, the coupling of the mediator to the SM quarks g_q, the dark matter mass $m_{\rm DM}$, the mediator mass $M_{\rm med}$ and the width of the mediator

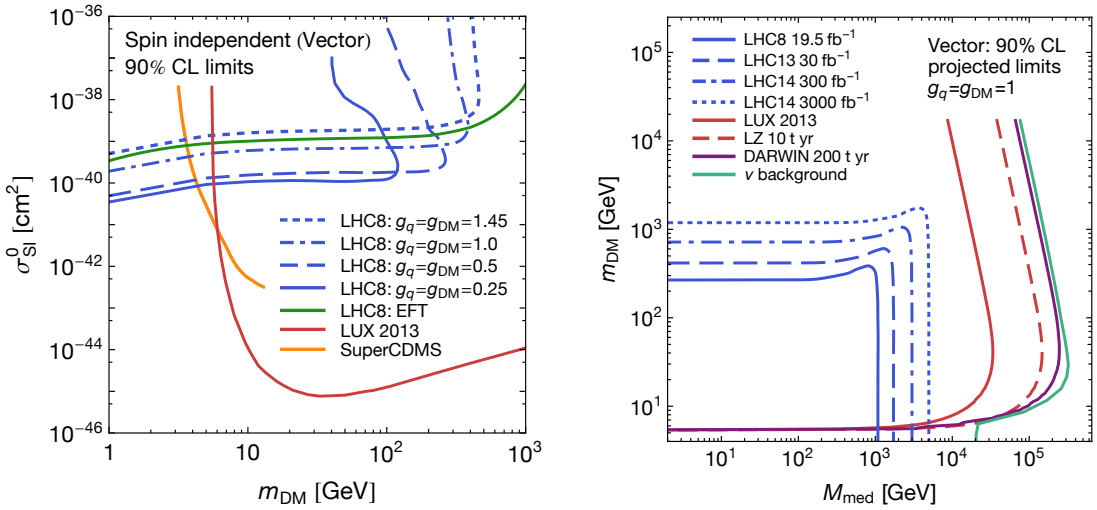

Figure 3.1: Comparison between the current limits from LUX and SuperCDMS and the mono-jet searches at the LHC. Left panel: Exclusion limits on the spin-independent DM-nucleon interaction cross-section. Right panel: Exclusion limits in the $m_{\rm DM}$ versus $M_{\rm med}$ plane. Both plots correspond to the simplified model with a vector mediator and different values for the interaction couplings. Figures taken from Ref. [279].

$\Gamma_{\rm med}$. The reason for coupling the mediator only to quarks in the SM is twofold. On the one hand, the initial states at the LHC consist of quarks and hence it is natural to include a coupling to them. On the other hand, this allows us to avoid di-lepton searches which already lead to strong constraints on new particles that couple to leptons.

In order to illustrate the complementarity between direct detection and LHC searches we present in Fig. 3.1 the exclusion limits for the simplified model with a vector mediator, as in Eq. (3.2.11). In the right panel we show the exclusion limits in the $m_{\rm DM}$ versus $M_{\rm med}$ plane. As can be seen, direct detection experiments give stronger constraints except when $m_{\rm DM}$ is below a few GeV, where these experiments lose sensitivity since the nucleon recoil energy is below the threshold needed for a detectable signal. In the left panel we show the exclusion limit on the spin-independent cross-section from LHC, in this plot it becomes evident that collider constraints are relevant for dark matter masses below a few GeV.

These simplified models do not come free of problems. The Lagrangian densities

presented in Eqs. (3.2.12)-(3.2.14) contain terms that break gauge invariance[1] [280]. Firstly, we shall examine the axial-vector case. The new U(1)′ gauge symmetry under which the SM quarks are charged is anomalous. The cancellation of these anomalies requires either a coupling to leptons or the addition of new fermions, some of which may not be singlets under the SM and will therefore lead to strong constraints from the LHC [281]. The mass term for the spin-1 mediator also breaks gauge invariance. Consequently, a dark Higgs boson providing the mass to V'_μ via spontaneous symmetry breaking must be introduced. Experimental constraints on these new states will further constrain the parameter space of the model.

Secondly, the scalar and pseudoscalar mediators are coupled to the terms $\bar{q}q$ and $\bar{q}\gamma^5 q$ respectively, neither of these terms is gauge invariant in the SM. One possible solution to this problem is to include portal interactions between the scalar mediator and the Higgs boson such that scalar mixing arises. For the pseudoscalar mediator this can also be done in the context of 2HDM plus a pseudoscalar singlet [282–284]. For these reasons there has been recent interest in moving towards more complete models that have a richer phenomenology [280, 285]. For a recent review on DM searches at the LHC we refer the reader to [286].

3.3 Tau-philic Dark Matter Coannihilation at the LHC

The non-observation of DM is starting to put some pressure on the so-called WIMP Miracle paradigm, which posits that the observed relic abundance can be explained by DM candidates which are weakly interacting massive particles (WIMPs) with masses in the 10s of GeV to a few TeV range (assuming simple $2 \to 2$ DM annihilation to SM particles and the standard thermal freeze-out mechanism). A growing number of such WIMP models of DM are being strongly constrained by, or at least show tension with the experimental limits, including supersymmetric DM realisations

[1] In the case of vector interactions, the Stueckelberg mechanism can be responsible for giving mass to the spin-1 mediator

discussed in [287–298] as well as other models considered in e.g. [299, 300].

Our ignorance of the dark sector structure and the negative experimental results for DM searches have motivated more model-independent studies which fall into two categories. The first is based on exploiting effective operators describing the low energy interactions between the DM and the SM particles [263–276]. This EFT approach manifestly does not depend on the UV structure of the (unknown) microscopic dark sector theory and works well when applied to the low energy experiments, such as the direct detection. However, the EFT approximation often breaks down when studying collider signatures since the cut-off of the effective field theory may not be larger than the LHC's energy scale or the dark sector often requires a new mediator particle other than the DM which may dramatically alter the collider signature itself [262, 277, 278].

The alternative framework is the simplified model approach, in which sets of phenomenological models are constructed with a minimal particle content to describe various experimental signatures. This approach turns out to be very useful and searches for dark matter at colliders are now commonly described in terms of simplified models with scalar, pseudo-scalar, vector and axial-vector mediators [301–304]. These simplified models have become the main vehicle for interpreting DM searches at the LHC [305, 306] and for projecting the DM reach of future hadron colliders [307–309].

These simplified models can be viewed as arising from integrating out the irrelevant particles and taking a certain limit of the more detailed microscopic theories. The dependence on specific details of any particular UV embedding in this case is by definition beyond the scope of the simplified models settings. An interesting question to ask is of course whether and which types of UV completions of specific simplified models are possible and if the additional degrees of freedom would affect the simplified model predictions at particular collider scales. For recent examples and studies of such 'next-to-simplified models' we refer the reader to Refs. [280,283,284,310–313].

The simplified models used by the LHC experiments and aggregated by the ATLAS-CMS DM Forum and the LHC DM Working Group [305, 306] are conven-

tionally classified based on the type of mediator particles that connect the DM to the SM particles. However, this classification may miss an effect of *coannihilation* that can be important to determine the DM relic density [314]. In the scenario where the coannihilation is operative, a charged (or coloured) particle is introduced in addition to the DM, which we call the *coannihilation partner*. Since the interaction between the coannihilation partner and the SM particles is unsuppressed, they annihilate efficiently into the SM particles in the early Universe. Due to the thermal transition between the DM and the coannihilation partner, the DM density is also reduced. This scenario does not require conventional interactions between the DM and the ordinary particles through a mediator, and otherwise severe experimental constraints, can easily be avoided. Simplified model studies addressing DM coannihilation and collider signatures so far have mostly focused on the coloured coannihilation partners [285, 314–319], with only few exceptions as in [320] (or in [177] including semi-annihilation effects between two different components of dark matter, e.g. Vector Vector $\to$ Vector Scalar).

The collider signature is also different in the coannihilation scenario from the usual DM simplified models. Since the coannihilation partner couples to the SM sector with an unsuppressed coupling, the production rate is much higher for the coannihilation partners than for DM particles. Moreover, the coannihilation partner can be long-lived at colliders because its mass difference from the DM mass is small and the decay rate incurs a significant phase space suppression. This may be the case in particular when the coannihilation partner has a contact interaction with the DM particle and a τ-lepton, since if the mass difference is smaller than m_τ, the coannihilation partner decays into multi-body final states via an off-shell τ, leading to a strong phase space suppression. This situation is familiar in supersymmetric (SUSY) theories with the stau coannihilation [321–327].

In this section, we introduce a class of simplified models that enables us to study the phenomenology of the dark sector containing a coannihilation partner. Inspired in part by the neutralino–stau coannihilation mechanism in SUSY theories, we want to recreate it in more general settings using a new class of simplified model. In Section **3.4.2**, we will define four types of simplified models with different parti-

cle spins and coupling structures and assume the existence of a contact interaction involving the DM particle, its coannihilation partner and the SM τ-lepton. Our simplified model choices include a fermionic DM with a scalar coannihilation partner, a scalar DM with a fermionic coannihilation partner and a vector DM with a fermionic coannihilation partner. Some of these models are manifestly gauge invariant and renormalisable, others are supposed to descend from a more detailed UV complete theory with or without supersymmetry, some may be realised as a certain limit of composite models, or descent from models with large extra dimensions.

The expressions for our Simplified Model Lagrangians and the definitions of the free parameters characterising the models can be found in Eqs. (3.3.19), (3.3.24) and (3.3.25). In Section **3.3.2**, we explain the coannihilation mechanism for computing the DM relic density in the context of our simplified models. This is followed by a general overview of experimental signatures for direct and indirect detection and collider searches in Section **3.3.3**. Our main results are presented and discussed in Sections **3.3.4 - 3.3.7**. In addition, we present in Section **3.3.8** the exclusion limits in the mass versus lifetime plane for the different models we have considered.

3.3.1 Simplified Models of Tau-philic Dark Matter

To implement the Dark Matter coannihilation mechanism we consider dark sectors which include two distinct degrees of freedom: the DM particle, χ, and the charged coannihilation partner (CAP), $\eta^{(\pm)}$. We assume that both of these dark sector particles have odd parity under a Z_2 symmetry to ensure the stability of the dark matter χ. Our simplified models are defined by the three-point interactions between χ, η and the τ-lepton of the Standard Model sector,

$$\mathcal{L} \supset g_{\rm DM}\, \chi\, \eta\, \tau + \text{h.c.} \ . \tag{3.3.15}$$

Here $g_{\rm DM}$ denotes the dark sector coupling constant which we take to be real and we also note that η has a non-vanishing τ-lepton number. In view that the DM candidate has tree-level interactions solely with the τ-lepton in the SM, we refer to this class of models as *tau-philic dark matter*. Restricting the particle content of our

Model-1a			
Component	Field	Charge	Interaction (3.3.19)
DM	Majorana fermion (χ)	$Y = 0$	$\phi^*(\chi\tau_R) + \text{h.c.}$
CAP	Complex scalar (ϕ)	$Y = -1$	

Model-1b			
Component	Field	Charge	Interaction (3.3.22)-(3.3.23)
DM	Majorana fermion (χ)	$Q = 0$	$\phi^*(\chi\tau_R) + \phi^*(\chi\tau_L) + \text{h.c.}$
CAP	Complex scalar (ϕ)	$Q = -1$	

Model-2			
Component	Field	Charge	Interaction (3.3.24)
DM	Real scalar (S)	$Y = 0$	$S(\overline{\Psi}P_R\tau) + \text{h.c.}$
CAP	Dirac fermion (Ψ)	$Y = -1$	

Model-3			
Component	Field	Charge	Interaction (3.3.25)
DM	Vector (V_μ)	$Y = 0$	$V_\mu(\overline{\Psi}\gamma^\mu P_R\tau) + \text{h.c.}$
CAP	Dirac fermion (Ψ)	$Y = -1$	

Table 3.1: Simplified Models of DM with a colourless coannihilation partner (CAP)

simplified models to spins not higher than 1, we consider three possible spin assignments [2] for the (χ, η) pair: ($\frac{1}{2}$, 0), (0, $\frac{1}{2}$) and (1, $\frac{1}{2}$). The corresponding simplified DM-coannihilation models we wish to consider are summarised in Table 3.1.

A note on notation: we use χ to denote the DM particle and η (or $\eta^\pm$) for the coannihilation particle in general. For the simplified models in Table 3.1 we have $\chi = \{\chi, S, V_\mu\}$ and $\eta = \{\phi, \Psi\}$ depending on the choice of the model.

For the ($\frac{1}{2}$, 0) spin assignment we consider the case where the dark matter is a Majorana fermion, χ, and the coannihilation partner is a complex scalar field, ϕ, bearing in mind the similarity of this case with the neutralino–stau coannihilation picture in SUSY models, where χ plays the role of the lightest neutralino, and the scalar ϕ is the stau. In the simplest realisation of this simplified model, which we refer to as the Model-1a in Table 3.1, the Yukawa interactions (3.4.27) between the dark sector particles χ, ϕ and the SM involve only the right-handed component of

[2] An additional potential assignment ($\frac{1}{2}$, 1) leads to η being an electrically charged vector boson which prevent us from finding an $\text{SU}(2)_L \times \text{U}(1)_Y$ invariant operator for Eq. (3.4.27). We therefore will not consider this option further.

the τ-lepton, τ_R, hence the coannihilation scalar ϕ is an $\mathrm{SU}(2)_L$-singlet. At the same time, the second realisation – the Model-1b – involves interactions with both left- and right-handed τ-leptons, and hence the stau-like scalar dark partner ϕ is charged under the $\mathrm{SU}(2)_L$. The Simplified Model-1a is a UV-consistent theory as it stands; on the other hand, the Model-1b should ultimately be embedded into a more fundamental microscopic theory in the UV to be consistent with the gauge invariance under $\mathrm{SU}(2)_L$. One such embedding can for example be a supersymmetric model with an operational neutralino–stau coannihilation mechanism.

We refer to the model corresponding to the $(0, \frac{1}{2})$ spin assignment as Model-2, in which we introduce a real scalar S as the dark matter and a Dirac fermion, Ψ, as the coannihilation partner, assuming they couple together with τ_R. Model-3 is constructed for the $(1, \frac{1}{2})$ spin assignment that introduces a real vector, V_μ, for the dark matter and a Dirac fermion, Ψ, for the coannihilation partner, assuming again the interaction with τ_R. These two simplified models can be realised in models of extra dimensions and/or composite models as we will outline in Sections **3.3.6** and **3.3.7** .

The simplified models 1a, 2 and 3 constructed above have the following free parameters: the dark matter mass, $m_{\mathrm{DM}} \equiv m_\chi$, the mass splitting, $\Delta M = M_\eta - m_\chi$, and the dark sector coupling, g_{DM}. In Model-1b we fix the dark sector coupling to be the $\mathrm{U}(1)_Y$ gauge coupling ($g_{\mathrm{DM}} = g'$). Instead, we introduce the L-R mixing angle, θ, which controls the relative strength of the coupling to τ_L and τ_R, as we will discuss later in more detail. The simplified model Lagrangians and the parameter definitions are given in Eq. (3.3.19) for Model 1a, Eqs. (3.3.22)-(3.3.23) for Model 1b, Eq. (3.3.24) for Model 2 and in (3.3.25) for Model 3.

3.3.2 Coannihilation

The effect of coannihilation can be understood qualitatively in the space of simplified model parameters. First of all, it is worth noting that χ couples to the SM sector only through the operator Eq. (3.4.27), whereas $\eta^\pm$ interacts with the SM particles also via the electromagnetic and weak gauge interactions. In our simplified models,

there is a unique channel for the DM pair annihilation: $\chi\,\chi \to \tau^+\tau^-$, as shown in the left diagram in Fig. 3.2. For small $g_{\rm DM}$, the DM pair annihilation is highly suppressed because the rate of this process is proportional to $g_{\rm DM}^4$. For our simplified models 1a,b and 2 where the dark matter is a Majorana fermion or a real scalar ($\chi = \{\chi,\, S\}$), there is another suppression factor. The initial state in both these cases forms a spin-0 state (due to the Pauli blocking in the Majorana case). To conserve the angular momentum, the $\tau^+\tau^-$ pair in the final state must have the opposite chiralities in the s-wave contribution, hence meaning that this contribution is suppressed by m_τ^2 (chiral suppression). The dominant contribution then comes from the p-wave for a Majorana DM and d-wave for a scalar DM, which are suppressed by the factor v^2 and v^4, respectively, where v is the average of the relative velocity of the annihilating DM particles.

Unlike the DM pair annihilation, the annihilation of the CAP particles, $\eta\,\eta \to$ SM particles, proceeds via the electromagnetic or weak gauge interactions, as indicated in the second diagram of Fig. 3.2. As such, the $\eta\,\eta$ annihilation can have much larger rates than the first process in Fig. 3.2 at small $g_{\rm DM}$. For a small but non-vanishing values of $g_{\rm DM}$, there are transition processes between η and χ: $\eta + \text{SM} \leftrightarrow \chi + \text{SM}$. These processes are in general much more efficient than annihilation processes, since the number density of light SM particles is not Boltzmann suppressed at the time of freeze-out. As long as the mass splitting, ΔM, is small, the transition process effectively equalises the number densities of χ and η, and the DM density (in the unit of the entropy density) freezes out when the annihilation of η is decoupled. We therefore find that in the region of small $g_{\rm DM}$, the DM relic density is not sensitive to $g_{\rm DM}$ and determined mainly by ΔM and $\sigma(\eta\,\eta \to \text{SM particles}) \times v$.

As $g_{\rm DM}$ approaches the $\mathrm{U}(1)_Y$ gauge coupling, g', the coannihilation process $\chi\,\eta \to \text{SM particles}$ becomes important (see, for example, the right diagram in Fig. 3.2). The rate of this process is proportional to $g_{\rm DM}^2$. As in the previous process, this process is only effective when ΔM is small as we will see below more explicitly.

For even higher values of $g_{\rm DM}$, the dark matter pair annihilation, $\chi\,\chi \to \tau^+\tau^-$, can become important, since the annihilation rate is proportional to $g_{\rm DM}^4$. However,

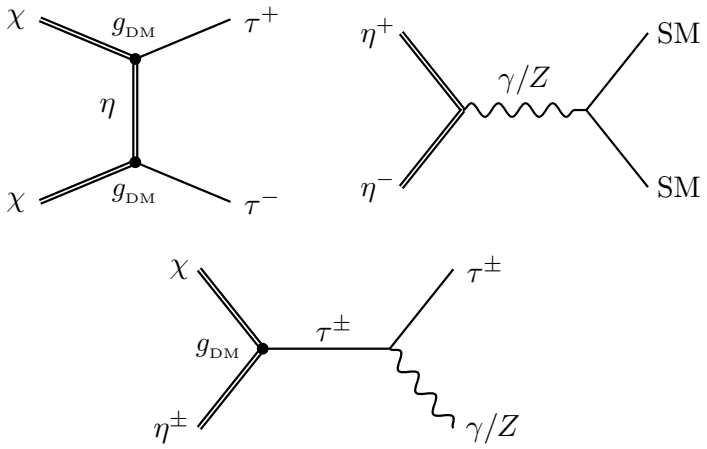

Figure 3.2: Feynman diagrams for the annihilation and coannihilation processes.

as we have discussed above, for $\chi = \{\chi, S\}$, this process can never become very large because it is velocity suppressed. However it can be dominant for the vector DM case $\chi = V_\mu$. Unlike the other channels, the contribution of this process is independent of ΔM.

As it is well known, the DM relic abundance scales as

$$\Omega_{\rm DM} h^2 \;\propto\; \langle \sigma_{\rm eff}\, v \rangle^{-1} \,, \tag{3.3.16}$$

where $\langle \sigma_{\rm eff}\, v \rangle$ is the thermal average of the effective annihilation cross-section that is given by [328]

$$\begin{aligned} \sigma_{\rm eff}\, v \;\; = \;\; & \frac{1}{(\mathsf{g}_\chi + \overline{\mathsf{g}}_\eta)^2} \Big[\, \mathsf{g}_\chi^2 \cdot \sigma(\chi\,\chi \to \tau^+\tau^-) + \\ & \qquad \mathsf{g}_\chi \overline{\mathsf{g}}_\eta \cdot \sigma(\chi\,\eta \to \text{SM particles}) + \\ & \qquad \overline{\mathsf{g}}_\eta^2 \cdot \sigma(\eta\,\eta \to \text{SM particles}) \, \Big] \, v \,, \end{aligned} \tag{3.3.17}$$

with

$$\overline{\mathsf{g}}_\eta = \mathsf{g}_\eta \Big(\frac{M_\eta}{m_\chi} \Big)^{3/2} \exp\Big(- \frac{\Delta M}{T} \Big) \,, \tag{3.3.18}$$

where g_χ and g_η denote the degrees of freedom of the fields χ and η, respectively,

and should not be confused with the dark sector coupling $g_{\rm DM}$. Their explicit values are given as $(\mathtt{g}_S, \mathtt{g}_\chi, \mathtt{g}_\phi, \mathtt{g}_{V_\mu}, \mathtt{g}_\Psi) = (1, 2, 2, 3, 4)$. Each line of Eq. (3.3.17) corresponds to the different contribution discussed above and depicted in Fig. 3.2. The dependence of these contributions on ΔM can be found through $\overline{\mathtt{g}}_\eta$. Since the freeze-out occurs around $T \sim m_{\rm DM}/25$, $\Delta M \lesssim m_{\rm DM}/25$ is required in order not to have large suppressions for the processes $\chi\,\eta \to$ SM particles and $\eta\,\eta \to$ SM particles. In this study we are interested in the regime where the coannihilation is operative, and we demand ΔM to be small. In our numerical study we compute $\Omega_{\rm DM}h^2$ using `MicrOMEGAs 4.1.5` [211] implementing the simplified models with help of `FeynRules 2.0` [329] and `LanHEP 3.2` [330].

3.3.3 Experimental Signatures

Direct detection

Since the DM couples to the SM sector only through the interaction term Eq. (3.4.27), the strength of experimental signatures is rather weak in general for the simplified models introduced in Section **3.4.2**. Direct detection experiments measure the nuclei recoil resulting from their interaction with dark matter, but such interactions involving DM with quarks and gluons are absent at tree-level in our simplified models. At one-loop level, the relevant operators may be generated. The Higgs mediating contributions are too small because the amplitude is suppressed by the product of the tau Yukawa coupling and the Yukawa coupling in the hadron sector. The relevant operators describing the interactions between the DM and the neutral gauge bosons are generated at dimension 6 at the lowest and suppressed by $1/M_\eta^2$. For example, for the Majorana DM case, such an operator is given by the anapole moment operator $\mathcal{A}\,\bar{\chi}\gamma_\mu\gamma_5\chi\partial^\nu F_{\mu\nu}$. For $m_{\rm DM} \simeq 500\,\text{GeV}$ and $\Delta M/m_\tau < 1$, the anapole moment is roughly given by $\mathcal{A}/g_{\rm DM}^2 \sim 8\cdot 10^{-7}\,[\mu_N\cdot\text{fm}]$ [331], which is more than one order of magnitude smaller than the current limit obtained by LUX [221] and also smaller than the projected sensitivity of LZ [79], even for $g_{\rm DM}^2 = 1$.[3] Although a dedicated

[3]The limits mentioned here assume the observed energy density of the DM. On the other hand, for $m_{\rm DM} \simeq 500\,\text{GeV}$ and $g_{\rm DM} \simeq 1$, all of our simplified models underproduce the χ particles. The actual constraints would therefore be even milder if this effect is taken into account.

study may shed some light on the future direct detection prospects for our simplified models, we shall postpone such a study to a future work.

Indirect detection

Indirect detection experiments are looking for high energy cosmic rays or neutrinos originated from the DM pair annihilation (or decay) in the present Universe. For the $2 \to 2$ topology, the only relevant process is $\chi\,\chi \to \tau^+\tau^-$ shown by the right diagram of Fig. 3.2. As mentioned in the previous section, for $\chi = \{\chi,\, S\}$ this process suffers from the chiral suppression, and the signal rate for the indirect detection goes below the experimental sensitivity. The chiral suppression is absent for $\chi = V_\mu$ (Model-3). In Section **3.3.7** we compare the annihilation rate of $V_\mu\, V_\mu \to \tau^+\tau^-$ with the current limit obtained by Fermi-LAT [332], taking into account the rescaling of the flux factor by the predicted relic abundance. We find that the annihilation rate in Model-3 is two orders of magnitude smaller than the current limit across the parameter region.

The $2 \to 3$ scattering, $\chi\,\chi \to \tau^+\tau^-\gamma$, may be more interesting in a small ΔM region. In this regime, the reaction rate of this process is enhanced in the following way. One of the DM particles can be converted into a slightly off-shell η radiating off a soft tau, $\chi \to \eta^\pm\tau^\mp$. This $\eta^\pm$ can then co-annihilate with the other χ particle via $\chi\,\eta^\pm \to \tau^\pm\gamma$ (see, for example, the third diagram in Fig. 3.2). Since the converted $\eta^\pm$ is only slightly off-shell, the propagator of $\eta^\pm$ is enhanced, and the energy distribution of the produced γ has a peak around $m_{\rm DM}/2$, which can be seen as a bump in a smoothly falling background. Although this signature is in principle promising, it has been shown that for $\Delta M \ll m_{\rm DM}$ the annihilation rate is nevertheless below the experimental sensitivities [331, 333–335]. For example, for the Majorana (scalar) DM with $m_{\rm DM} = 500\,\text{GeV}$ and $\Delta M/m_\tau < 1$, the annihilation rate is roughly given by $\langle v\sigma(\chi\chi \to \tau^+\tau^-\gamma)\rangle/g_{\rm DM}^2 \sim 5\cdot10^{-29}\,(5\cdot10^{-28})$ [cm^3/s], which is smaller than the current limits obtained by Fermi-LAT [332] and HESS [87], and also below the future sensitivity of CTA [336, 337] even for $g_{\rm DM} = 1$ and assuming $\Omega_\chi h^2 = \Omega_{\rm DM} h^2 \simeq 0.1197$. As in the direct detection case, we reserve the dedicated study on the prospects of the indirect detection sensitivity to our simplified models

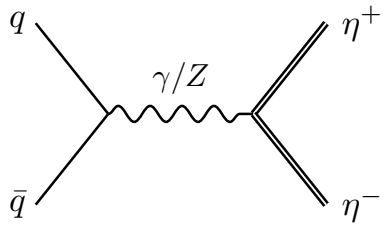

Figure 3.3: Coannihilation partner (CAP) pair-production process.

for a future work.

Collider searches

In general, DM particles can be produced in proton-proton collisions at the LHC and the experimental collaborations are looking for signatures of such DM production, usually involving mono- and multi-jets plus missing energy, or alternatively constraining a direct mediator production which could decay back into SM. In our simplified models of DM with colourless coannihilation partners, however, no direct DM production processes are possible at tree level since the DM couples to the SM sector only via the interactions (3.4.27).

Unlike the DM particle, the coannihilation η particle couples to the SM sector via electro-weak gauge interactions, and η can be pair-produced by exchanging off-shell neutral gauge bosons $q\bar{q} \to (\gamma/Z)^* \to \eta\eta$ as depicted in Fig. 3.3. The production rate is independent of $g_{\rm DM}$ and is well-defined once the mass and quantum numbers of η are specified. For our simplified models of DM with coannihilation partners η, the latter are either a complex scalar or Dirac fermions. The η production cross-sections $pp \to \eta\eta$ at the 8 TeV and 13 TeV LHC computed at leading order by `MadGraph 5` [338] for our range of simplified models are plotted in Fig. 3.18 as the function of the coannihilation partner mass. It can be seen that the production cross-section in the fermion case is one order of magnitude higher than in the scalar case. This is because the scalar production suffers from velocity suppression near the threshold; we will further comment on this effect in Section **5.3**.

In the region where the coannihilation is operative, ΔM is small and the decay

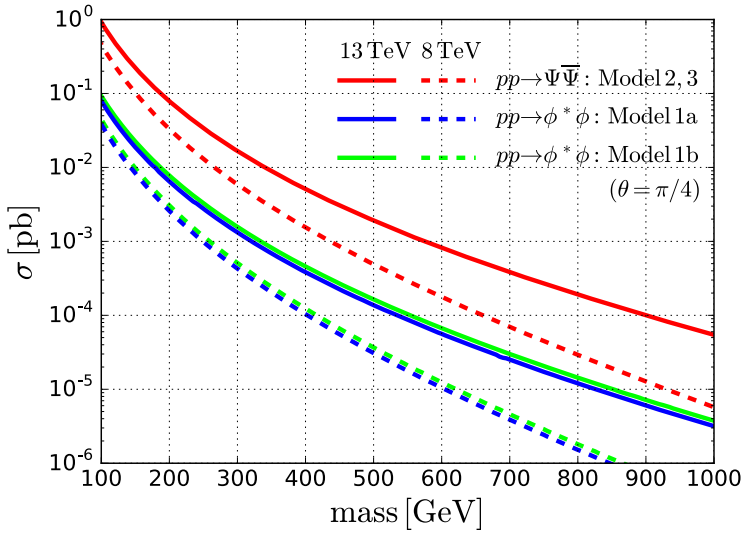

Figure 3.4: Collider cross-section $\sigma^{\rm LO}(pp \to \eta^+\eta^-)$ for the simplified models defined in Table 3.1.

products of η will be too soft to be reconstructed.[4] The standard strategy to trigger such events is to demand additional hard jet originated from the initial state QCD radiation. This leads to a distinct mono-jet plus large missing energy signature and the signal can (in favourable settings) be separated from the background. It is known that the mono-jet channel is powerful if η has a colour charge, but for our colour-neutral η this prospect is, as one would expect, quite pessimistic. For example, the study presented in [340] did not find any limit on the stau mass in the stau coannihilation region in SUSY models using a mono-jet channel even for a 100 TeV pp collider with a 3 ab^{-1} integrated luminosity. In this work we focus on the sensitivity at the LHC and aim to look for an alternative search channel.

As we have seen in Section **3.3.2**, the effective coannihilation mechanism in the dark sector imposes an upper bound on the mass splitting between the DM and the CAP particles, $\Delta M \lesssim m_{\rm DM}/25$. Furthermore, if ΔM becomes smaller than the τ-lepton mass, $m_\tau = 1.777$ GeV, the on-shell 2-body decay, $\eta^\pm \to \chi\tau^\pm$, is kinematically forbidden and the 3- and 4-body decay modes, $\eta^\pm \to \chi\,\nu_\tau\,\pi^\pm$ and $\eta^\pm \to \chi\,\nu_\tau\,\ell^\pm\,\nu_\ell$ ($\ell = e, \mu$) shown in Fig. 3.5, become dominant. Since these 3- and 4-body decays

[4]The LHC phenomenology of a similar model in the opposite limit ($\Delta M \sim m_{\rm DM}$) have been studied in [339].

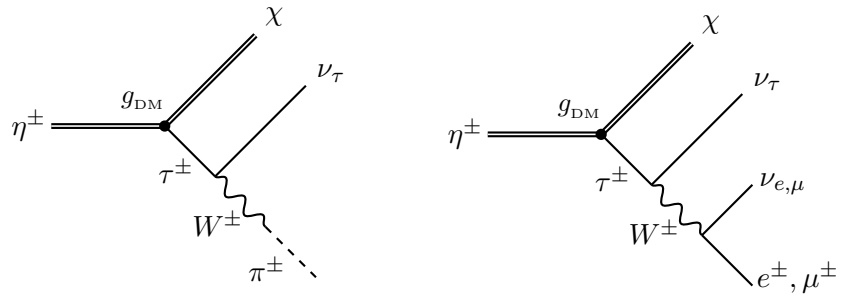

Figure 3.5: The 3-body and 4-body η-decays via an off-shell τ (and W).

are suppressed by the off-shell intermediate propagators and the multi-body phase space, the η decay rate becomes minuscule.

We show in Fig. 3.6 the lifetimes of $\eta^\pm$ computed with `CalcHEP` [341] as functions of ΔM for our simplified models of DM with a coannihilation partner. As can be seen, the lifetimes quickly increase once ΔM crosses m_τ from above and reach $\sim 1\mu s$ around $\Delta M \sim 1$ GeV, for all simplified models. If the lifetime is of the order of μs, η can reach the tracker and may leave anomalously highly ionizing tracks or slowly moving charged particle signature. Such exotic charged track signatures are intensively looked for by ATLAS [342, 343] and CMS [344, 345] and also can be investigated by the MoEDAL experiment [346]. We calculate the projected limits obtained from anomalous charged track searches for various simplified models and discuss an interplay with the dark matter relic abundance obtained by the coannihilation mechanism in the next section.

3.3.4 Model 1a: Majorana Fermion Dark Matter

The first simplified model we consider has a Majorana fermion singlet dark matter, $\chi = \chi^\dagger$, and a complex scalar coannihilation partner, $(\eta^+, \eta^-) = (\phi^*, \phi) = (\phi^+, \phi^-)$.

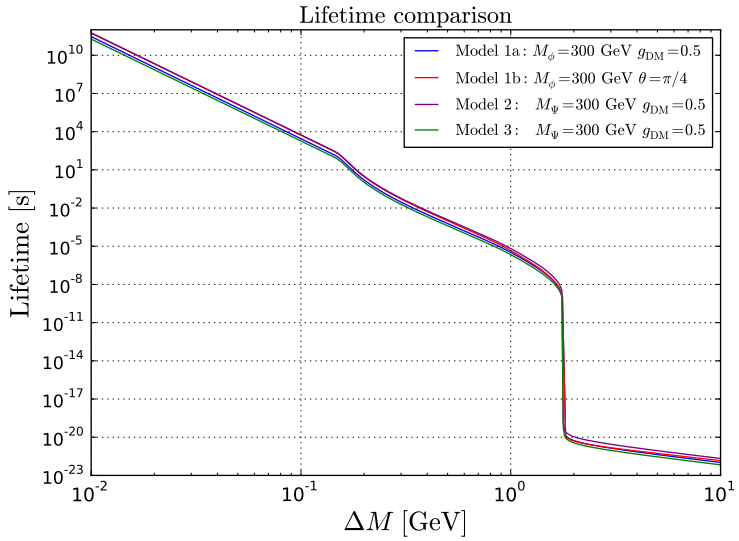

Figure 3.6: The lifetime of the coannihilation partner $\eta^\pm$ as a function of the mass splitting $\Delta M = M_\eta - m_\chi$. Model 1a (blue): $M_\phi = 300\,\text{GeV}$, $g_{\rm DM} = 0.5$, Model 1b (red): $M_\phi = 300\,\text{GeV}$, $\theta = \pi/4$, Model 2 (purple): $M_\Psi = 300\,\text{GeV}$, $g_{\rm DM} = 0.5$, Model 3 (green): $M_\Psi = 300\,\text{GeV}$, $g_{\rm DM} = 0.5$.

We extend the SM Lagrangian as:

$$\begin{aligned}
\mathcal{L} &= \mathcal{L}_{\rm SM} + \mathcal{L}_{\rm DM} + \mathcal{L}_{\rm CAP} + \mathcal{L}_{\rm int}\,, \\
\mathcal{L}_{\rm DM} &= \frac{1}{2}\chi(i\partial\!\!\!/ - m_{\rm DM})\chi\,, \\
\mathcal{L}_{\rm CAP} &= |D_\mu\phi|^2 - M_\phi^2\,|\phi|^2\,, \\
\mathcal{L}_{\rm int} &= g_{\rm DM}\,\phi^*\chi\tau_R + \text{h.c.}\,,
\end{aligned} \tag{3.3.19}$$

where $M_\phi = m_{\rm DM} + \Delta M$ and the covariant derivative D_μ contains the $\mathrm{U}(1)_Y$ gauge field. This simplified model has a particular interest since it can be realised in SUSY models by identifying χ as the Bino and ϕ as the right-handed stau. We, however, stress that the model is also interesting on its own right because it is gauge invariant and renormalisable. The searches at LEP have already excluded charged particles with mass below $\simeq 100$ GeV [347–349], and we focus on the region with $M_\phi \gtrsim 100$ GeV.

We show our numerical results for the Simplified Model 1a in Fig. 3.7. The three plots correspond to different values of the dark matter coupling: $g_{\rm DM} = 0.1$, 0.5 and 1.0 from left to right. The dark-blue region satisfies the correct dark matter

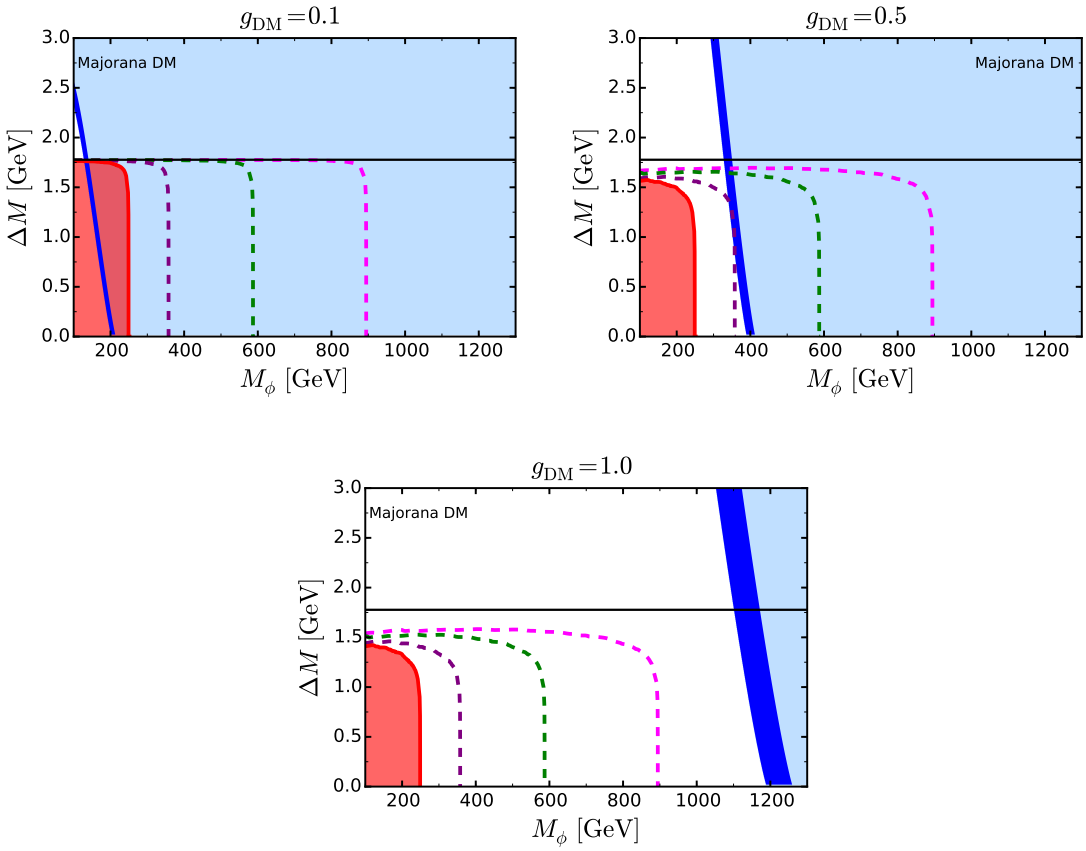

Figure 3.7: The DM coannihilation strip and collider searches for a long-lived charged scalar in the Simplified Model 1a. The dark-blue region satisfies the correct dark matter relic abundance within 3σ, the light-blue region overproduces the dark matter energy density. The horizontal black line indicates the mass of the τ lepton. The region coloured in red corresponds to current HSCP limits at the LHC for centre-of-mass energy of 8 TeV and 18.8 fb^{-1}. The three dashed lines (purple, green and magenta) correspond to our projections for centre-of-mass energy of 13 TeV and 30, 300 and 3000 fb^{-1} of integrated luminosity respectively.

relic abundance within 3σ, and the light-blue area to the right of it gives a relic abundance which exceeds the observed value and overcloses the Universe. The red region corresponds to the current 95% CL excluded region obtained by the heavy stable charged particle (HSCP) searches at the LHC using 8 TeV data with 18.8 fb^{-1} integrated luminosity [345]. The contours bounded by the purple, green and magenta dashed lines (from left to right) are projected limits assuming 13 TeV LHC with 30, 300 and 3000 fb^{-1} integrated luminosities, respectively. These projections are obtained by starting with the analysis conducted by CMS [345] of the 8 TeV data, and interpolating it to higher energies and luminosities following the Collider

Reach method [350].[5] We validated our computational approach by reproducing the 8 TeV limit on the long-lived stau calculated in [352]. The limit can also be presented as a function of the lifetime and mass of ϕ. Such limits are given in Section **3.3.8**.

In Fig. 3.7, the horizontal line represents $\Delta M = m_\tau$. One can see, as expected, that the limit from the HSCP searches is absent if $\Delta M > m_\tau$ since $\phi^\pm$ decays before reaching the tracker. Once ΔM gets smaller than m_τ, the propagation path of the ϕ charged scalar $c\tau_\phi$ reaches and then exceeds the detector scale, $\mathcal{O}(100)$ cm, although the exact ΔM needed for exclusion depends also on $g_{\rm DM}$ since the lifetime is inversely proportional to $g_{\rm DM}^2$. For $g_{\rm DM} = 0.1$, the HSCP searches can have strong sensitivities as far as $\Delta M < m_\tau$, whilst $\Delta M \lesssim 1.5$ GeV is required for $g_{\rm DM} = 0.5$ and 1. The model can be constrained at the LHC only when there is a large production cross-section for $pp \to \phi^+\phi^-$. The sensitivity of the HSCP search therefore has a strong dependence on M_ϕ. If $\Delta M < 1.3$ GeV, $M_\phi < 240$ GeV is already ruled out by the current data, and the 95% CL projected limits are estimated as $M_\phi < 330$, 580 and 870 GeV for 13 TeV LHC with 30, 300 and 3000 fb^{-1} integrated luminosities, respectively. These limits are almost independent of $g_{\rm DM}$ and ΔM as long as $\Delta M < 1.3$ GeV.

We have also shown the constraints from the DM relic density in the same plots. The dark-blue strip in Fig. 3.7 represents the region where the DM relic density, computed by `MicrOMEGAs 4.1.5` [211], is consistent with the latest Planck satellite measurement $\Omega_{\rm DM}h^2 = 0.1197 \pm 0.0022$ [37] within the 3-σ level. Note that the DM is overproduced on the right of the dark-blue strip, where this region is shaded with light-blue. Conversely, the DM is underproduced on the left of the dark-blue strip. This region may not be excluded phenomenologically since there may be another component for the DM, whose relic density makes up the remaining part of the $\Omega_{\rm DM}h^2$. We can therefore identify the white region as the currently allowed region by the LHC and the DM relic density constraints.

As we have discussed in Section **3.3.2**, the relic density depends on ΔM through

[5] A fast recasting method for a HSCP search has been proposed in [351]. We opt for the Collider Reach method, since our main focus is to extrapolate the existing limit to higher energies and luminosities.

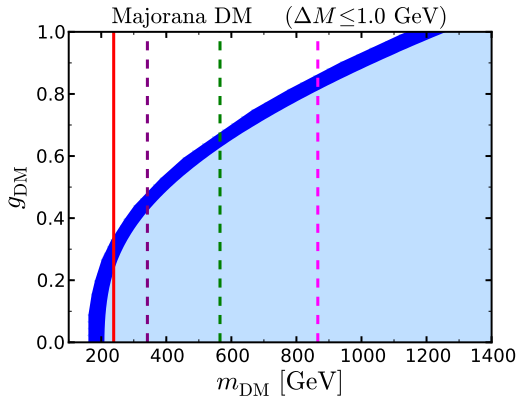

Figure 3.8: Model 1a: Plot of the coupling $g_{\rm DM}$ versus the dark matter mass $m_{\rm DM} = m_\chi$. We scan over $\Delta M \leq 1$ GeV, where $\Delta M = M_\phi - m_\chi$, this is the mass region where the HSCP limits are independent of the coupling $g_{\rm DM}$. The dark blue band satisfies the correct DM relic abundance within 3σ, the region in light blue overproduces the amount of DM. The colour-coding for the exclusion regions is the same as in the previous Figure.

the coannihilation mechanism, which can be seen clearly in Fig. 3.7. The mass and the dark sector coupling also affect the value of the relic density. To investigate this behaviour in more detail, in Fig. 3.8 we present a scan of the ($g_{\rm DM}$, $m_{\rm DM}$) plane in our Simplified Model 1a over the mass splittings in the region $0 \leq \Delta M \leq 1$ GeV. The dark-blue strip gives the correct relic density within 3σ. As previously discussed, the dependence on $g_{\rm DM}$ is weak if $g_{\rm DM} \ll 1$, since the $\langle \sigma_{\rm eff} v \rangle$ is almost entirely determined by the $\phi^+ \phi^- \to$ SM particles, which is independent of $g_{\rm DM}$. Once $g_{\rm DM}$ gets as large as the $\mathrm{U}(1)_Y$ gauge coupling, the second process, $\phi^\pm \chi \to$ SM particles, becomes important, and the dependence on $g_{\rm DM}$ enters into $\Omega_{\rm DM} h^2$. For very large $g_{\rm DM}$, the process $\phi^+ \phi^+ \to \tau^+ \tau^+$ (and its conjugate), exchanging χ in the t-channel, becomes dominant since it does not incur the chiral suppression and the cross-section is proportional to $g_{\rm DM}^4$. Because the DM relic density is inversely proportional to $\langle \sigma_{\rm eff} v \rangle$, the constraint of the DM overproduction excludes small $g_{\rm DM}$ regions depending on $m_{\rm DM}$. From this plot we conclude that the high luminosity LHC at 3000 fb^{-1} can explore almost the entire region with $g_{\rm DM} \lesssim 1$ except for a small segment around $g_{\rm DM} \sim 0.9$, $m_{\rm DM} \sim 1$ TeV.

3.3.5 Model 1b: Effect of L-R Mixing

In SUSY models we often encounter the situation where the DM and the lighter stau, $\widetilde{\tau}_1$ (coannihilation partner), interact with both left and right-handed τ-leptons via the L-R mixing in the stau sector. To study this case, we extend the previous simplified model such that the coannihilation partner ϕ can couple to both τ_L and τ_R. We will now construct our simplified model by starting with the $\mathrm{SU}(2)_L \times \mathrm{U}(1)_Y$ invariant formulation involving a minimal particle content required for the DM fermion, the coannihilation scalar(s), and the SM leptons. We thus introduce a scalar $\mathrm{SU}(2)_L$ doublet $\Phi_L^T = (\phi_\nu, \phi_L)$ and a singlet ϕ_R with the same hyper-charges as those of the SM doublet $l_3^T = (\nu_\tau, \tau_L)$ and the singlet τ_R, respectively. We then write down their Yukawa interactions with the DM Majorana fermion χ as follows,

$$\sqrt{2}\, g'\, Y_l\, \Phi_L^\dagger\, \chi\, l_3 \,+\, \sqrt{2}\, g'\, Y_e\, \phi_R^*\, \chi\, \tau_R \,+\, \text{h.c.}\,, \tag{3.3.20}$$

where $g' \simeq 0.36$ is the $\mathrm{U}(1)_Y$ gauge coupling and $Y_l = -\frac{1}{2}$ and $Y_e = 1$ are the corresponding hyper-charges. These terms are analogous to the bino–stau–tau interaction in SUSY models.

After the electroweak symmetry breaking, the scalars ϕ_L and ϕ_R will generically mix with each other forming two mass eigenstates, the lighter of which,

$$\phi \,=\, \cos\theta\; \phi_L \,+\, \sin\theta\; \phi_R\,, \tag{3.3.21}$$

we identify as the coannihilation particle of our simplified model. The mixing angle θ will be a free parameter in the simplified model. After integrating out the heavier scalar eigenstate, the interaction terms in Eq. (3.3.20) reduce to the simplified model interaction

$$\mathcal{L}_{\text{int}} \,=\, g_L\, \phi^* \chi \tau_L \,+\, g_R\, \phi^* \chi \tau_R \,+\, \text{h.c.}\,, \tag{3.3.22}$$

with the two couplings given by

$$g_L = \frac{1}{\sqrt{2}} g' \cos\theta, \quad g_R = -\sqrt{2} g' \sin\theta\,. \tag{3.3.23}$$

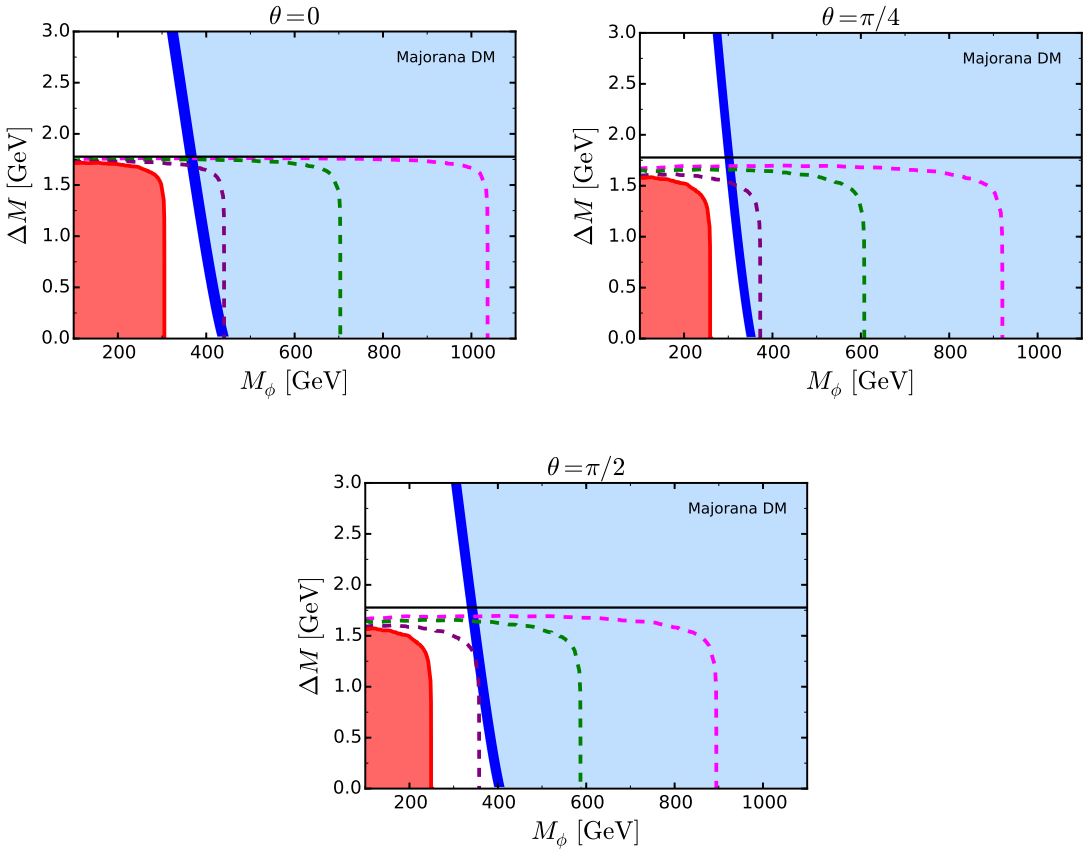

Figure 3.9: Model 1b: $\phi - \chi$ coannihilation strip and collider searches. The dark-blue region satisfies the correct dark matter relic abundance within 3σ, the light-blue region overproduces the dark matter energy density. The horizontal black line corresponds to the mass of the τ lepton. The region coloured in red corresponds to current HSCP limits for centre-of-mass energy of 8 TeV and 18.8 fb^{-1}. The three dashed lines (purple, green and magenta) correspond to our projections for centre-of-mass energy of 13 TeV and 30, 300 and 3000 fb^{-1} of integrated luminosity respectively.

In the same way, the interaction of ϕ with γ, Z and $W^{\pm}$ can be obtained by extracting ϕ from the kinetic terms $|D_\mu \Phi_L|^2 + |D_\mu \phi_R|^2$. This defines our Simplified Model 1b, which is determined in terms of three free parameters: θ, M_ϕ and $\Delta M = M_\phi - m_\chi$.

We show in Fig. 3.9 the constraints in the (M_ϕ, ΔM) plane for the Simplified Model 1b for the following parameter choices: $\theta = 0$ for $\phi = \phi_L$ (left plot), $\theta = \pi/4$ for $\phi = (\phi_L + \phi_R)/\sqrt{2}$ (central plot) and $\theta = \pi/2$ for $\phi = \phi_R$ (plot on the right). We note that $\theta = \pi/2$ corresponds to Model-1a with $|g_{\rm DM}| = \sqrt{2} g' \simeq 0.5$. Therefore, the right plot of Fig. 3.9 resembles the second plot of Fig. 3.7. One can see that turning on g_L makes the LHC constraint tighter. The current HSCP LHC-8 TeV limit on

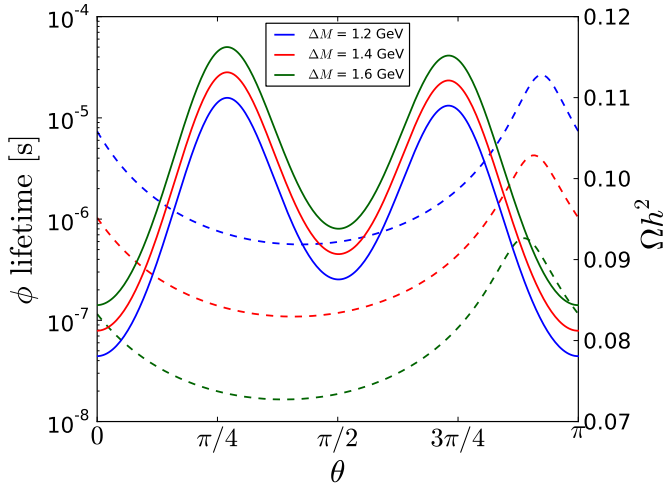

Figure 3.10: The lifetime of $\phi^{\pm}$ (dashed) and the DM relic density Ωh^2 (solid) as functions of the L-R mixing parameter θ. The DM mass is fixed at 300 GeV and ΔM is varied as 1.2 (blue), 1.4 (red) and 1.6 (green) GeV.

the coannihilation partner mass increases from 220 GeV to 300 GeV as θ changes from $\pi/2$ to 0. This is because the interaction strength of the $q\bar{q} \to (\gamma/Z)^* \to \phi^+\phi^-$ process increases due to inclusion of the $\mathrm{SU}(2)_L$ coupling found in $|D_\mu \Phi_L|^2$.

The dependences of the DM relic density and the lifetime of the coannihilation partner on θ are more complicated, and shown in Fig. 3.10. Here we plot $\Omega_{\mathrm{DM}}h^2$ (solid lines) and τ_ϕ (dashed lines) as functions of θ by fixing $m_\chi = 300$ GeV and varying $\Delta M = 1.2$, 1.4 and 1.6 GeV. We see that $\Omega_{\mathrm{DM}}h^2$ is globally minimized at $\theta = 0$ and π ($\phi = \phi_L$) due to the relatively large $\mathrm{SU}(2)_L$ coupling. Another local minimum is found at $\theta = \pi/2$ ($\phi = \phi_R$). The relic density has two local maxima implying that there is a cancellation in $\langle \sigma_{\mathrm{eff}} v \rangle$ among g_L and g_R terms in Eq. (3.3.22). The interference between g_L and g_R terms can also be observed in the lifetime of ϕ. Unlike $\Omega_{\mathrm{DM}}h^2$, τ_ϕ is minimized (maximized) at $\theta \simeq \frac{3\pi}{8}$ ($\frac{7\pi}{8}$).

3.3.6 Model 2: Scalar Dark Matter

In this section, we consider Simplified Model 2 where the DM particle is a real singlet scalar, $\chi = S$, and the coannihilation partner is a Dirac fermion, $(\eta^+, \eta^-) = (\overline{\Psi}, \Psi) = (\Psi^+, \Psi^-)$. We take Ψ to have the same quantum numbers as τ_R except for

the Z_2 (dark sector) charge. The Lagrangian is given as:

$$\begin{aligned}
\mathcal{L} &= \mathcal{L}_{\rm SM} + \mathcal{L}_{\rm DM} + \mathcal{L}_{\rm CAP} + \mathcal{L}_{\rm int}, \\
\mathcal{L}_{\rm DM} &= \frac{1}{2}(\partial_\mu S)^2 - \frac{1}{2} m_{\rm DM}^2 S^2 \,, \\
\mathcal{L}_{\rm CAP} &= \overline{\Psi}(i\not{\partial} - M_\Psi)\Psi \,, \\
\mathcal{L}_{\rm int} &= g_{\rm DM}\, S\, \overline{\Psi}\, P_R\, \tau + \text{h.c.}\,,
\end{aligned} \tag{3.3.24}$$

where $M_\Psi = m_{\rm DM} + \Delta M$ and $P_R = \frac{1+\gamma_5}{2}$ is the right-handed projection operator for Dirac spinors. This simplified model can be realised for example in models with extra dimensions by regarding Ψ as the first excited Kaluza-Klein (KK) mode of the τ and S as a heavy and stable singlet, such as the first KK-mode of the Higgs boson [353, 354] or a scalar photon in $D \geq 6$ theories [354, 355]. In such models, the approximate mass-degeneracy, or a compressed spectrum between m_χ and M_Ψ, resulting in $\Delta M \ll m_{\rm DM}$, which is assumed in this work, is justified because the mass of each of the KK modes for different particles is dominated by an universal contribution that is inversely proportional to the size of the extra dimension(s). As in the case of Simplified Model 1a, this model is manifestly gauge invariant and renormalisable.

We note that a term $|H|^2 S^2$ is also allowed by the symmetry. After the electroweak symmetry breaking, this term induces a 3-point interaction hSS that gives the contribution to the direct detection as well as $\Omega_{\rm DM}h^2$. A phenomenological implication of this term has been well studied in the literature [177, 356–360]. Since the aim of this work is to primarily study the effect of coannihilation, we simply assume that the coefficient of this term is small or otherwise exclude it from our simplified model.

Fig. 3.11 shows our numerical results of this simplified model for $g_{\rm DM} = 0.1$, 0.5 and 1.0 from left to right. Comparing it with Fig. 3.7, one can see that the LHC limits are tightened but also the preferred coannihilation partner mass by the relic density gets shifted to higher values. This is because the number of degrees freedom for Ψ is doubled compared to ϕ. Also, the production cross-section of the coannihilation partners is enhanced compared to Model-1a because $q\bar{q} \to \Psi^+\Psi^-$

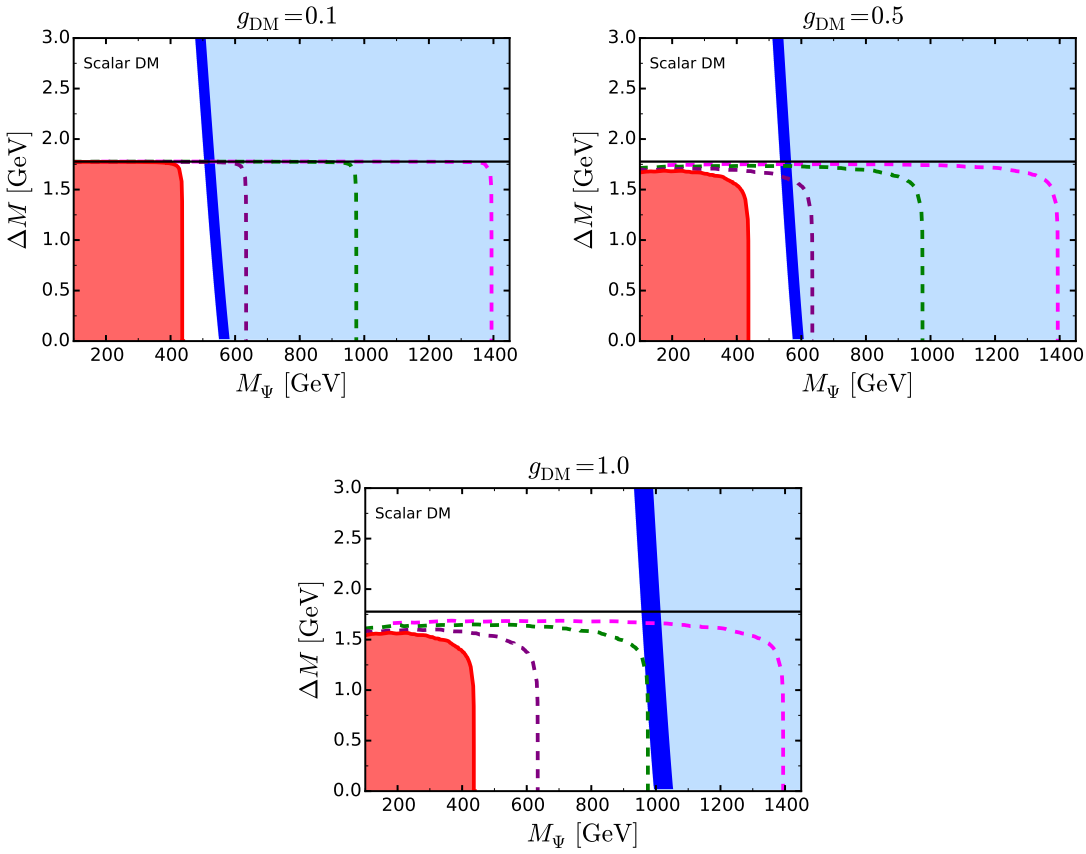

Figure 3.11: Model 2: The DM coannihilation strip and collider searches for a long-lived charged Dirac fermion Ψ. The dark-blue region satisfies the correct dark matter relic abundance within 3σ, the light-blue region overproduces the dark matter energy density. The horizontal black line corresponds to the mass of the τ lepton. The region coloured in red corresponds to current HSCP limits for centre-of-mass energy of 8 TeV and 18.8 fb^{-1}. The three dashed lines (purple, green and magenta) correspond to our projections for centre-of-mass energy of 13 TeV and 30, 300 and 3000 fb^{-1} of integrated luminosity respectively.

does not incur velocity suppression near the threshold. The current bound from the HSCP search excludes $M_\Psi \lesssim 410$ GeV and the projected sensitivity reaches 600, 950 and 1350 GeV for the 13 TeV LHC with 30, 300 and 3000 fb^{-1} integrated luminosity, respectively. These current and projected limits are independent of $g_{\rm DM}$ and ΔM as long as $\Delta M \lesssim 1.5$ GeV.

The preferred coannihilation partner mass required by the relic density (the dark-blue strip) is found around $M_\Psi \simeq 500-600$ GeV for $g_{\rm DM} = 0.1$ and 0.5, and $M_\Psi \simeq 950-1050$ GeV for $g_{\rm DM} = 1.0$. The impact of $g_{\rm DM}$ and $m_{\rm DM}$ on $\Omega_{\rm DM}h^2$ can be seen more clearly in Fig. 3.12, where limits from the LHC and $\Omega_{\rm DM}h^2$ are plotted in

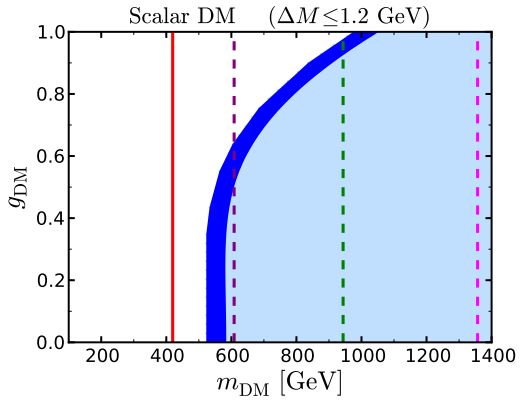

Figure 3.12: Model 2: Plot of the coupling $g_{\rm DM}$ versus the dark matter mass $m_{\rm DM} = m_S$. We scan over $\Delta M \in [0, 1.2\,\text{GeV}]$, where $\Delta M = M_\Psi - m_S$. The dark blue band satisfies the correct DM relic abundance within 3σ, the region in light blue overproduces the amount of DM. The colour-coding for the exclusion regions is the same as in the previous Figure.

the $(m_{\rm DM}, g_{\rm DM})$ plane scanning ΔM in the $[0, 1.2]$ GeV range. In this plot, one can see the DM relic density is not sensitive to $g_{\rm DM}$ until $g_{\rm DM} \lesssim 0.5$. This is because the $\langle \sigma_{\rm eff} v \rangle$ is determined by the process $\Psi^+\Psi^- \to$ SM particles, which is independent of $g_{\rm DM}$. For $g_{\rm DM} > 0.5$, the dependence enters through, i.e., $\Psi^\pm \chi \to$ SM particles ($\langle \sigma_{\rm eff} v \rangle \propto g_{\rm DM}^2$) and $\Psi^\pm\Psi^\pm \to \tau^\pm\tau^\pm$ exchanging S in the t-channel ($\langle \sigma_{\rm eff} v \rangle \propto g_{\rm DM}^4$). Considering the limit of the DM overproduction and the HSCP searches, one can see that the entire parameter region with $g_{\rm DM} \lesssim 1.0$ will be explored by the LHC Run-2 with 3000 fb^{-1} of integrated luminosity.

3.3.7 Model 3: Vector Dark Matter

We now study the case in which the coannihilation partner is a Dirac fermion, $(\eta^+, \eta^-) = (\overline{\Psi}, \Psi) = (\Psi^+, \Psi^-)$, as in Model-2 but the dark matter is a neutral vector boson, $\chi = V_\mu$. We modify the Lagrangian Eq. (3.3.24) with

$$\begin{aligned} \mathcal{L}_{\rm DM} &= \frac{1}{4}(\partial_\mu V_\nu - \partial_\nu V_\mu)^2 + \frac{1}{2} m_{\rm DM}^2 V_\mu V^\mu \,, \\ \mathcal{L}_{\rm int} &= g_{\rm DM} V^\mu \, \overline{\Psi} \gamma_\mu P_R \, \tau + \text{h.c.}\,. \end{aligned} \tag{3.3.25}$$

Similarly to Model-2, this simplified model can be realised in models with extra dimensions by identifying V_μ as the KK photon and Ψ as the KK τ. It may also be

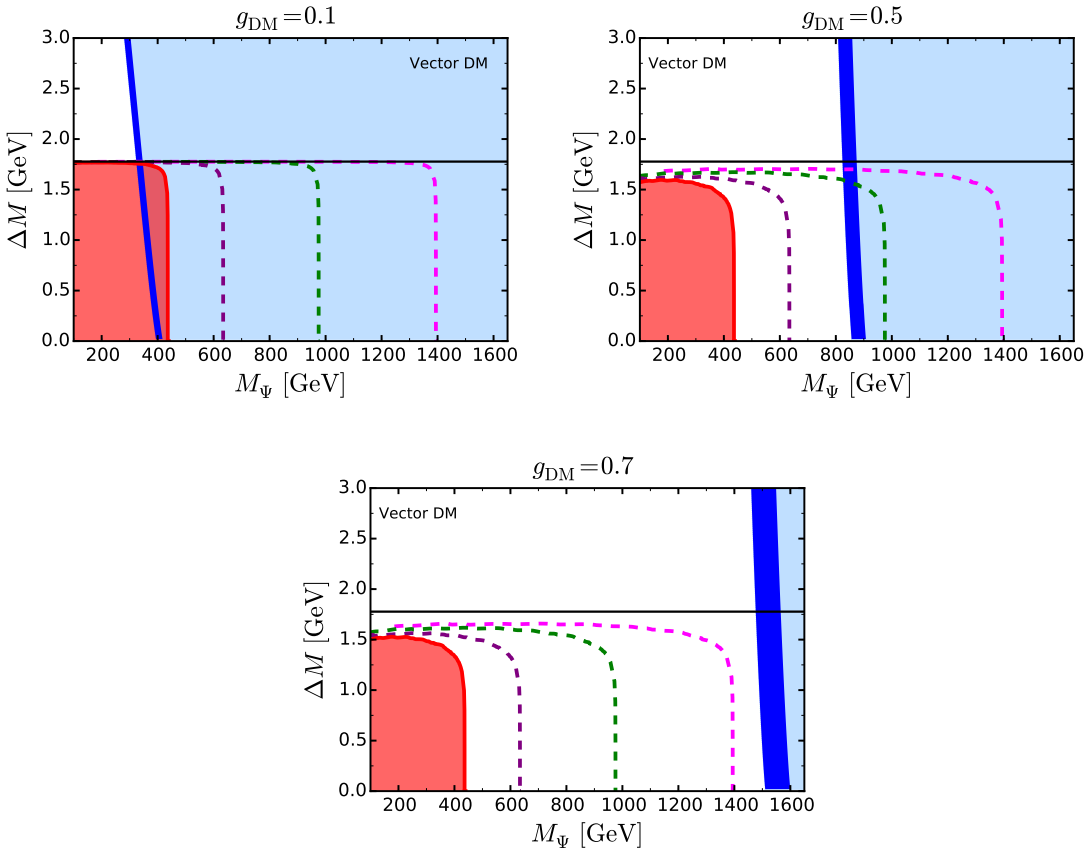

Figure 3.13: Model 3: The coannihilation strip and collider searches for vector DM and a long-lived charged Dirac fermion Ψ. The dark-blue region satisfies the correct dark matter relic abundance within 3σ, the light-blue region overproduces the dark matter energy density. The horizontal black line corresponds to the mass of the τ lepton. The region coloured in red corresponds to current HSCP limits for centre-of-mass energy of 8 TeV and 18.8 fb^{-1}. The three dashed lines (purple, green and magenta) correspond to our projections for centre-of-mass energy of 13 TeV and 30, 300 and 3000 fb^{-1} of integrated luminosity respectively.

possible to interpret V_μ as a ρ meson and Ψ as a baryon in a new strong sector in composite models.

We show our numerical results of this model in Fig. 3.13, where $g_{\rm DM} = 0.1$, 0.5 and 0.7 are examined from left to right. One can see that the current and projected LHC limits are almost identical to those found in Model-2, since those models have the same coannihilation partner Ψ, and the relevant production process $q\bar{q} \to (\gamma/Z)^* \to \Psi\overline{\Psi}$ is independent of the spin of the DM. On the other hand, the relic density constraint is quite different from the corresponding constraint in Model-

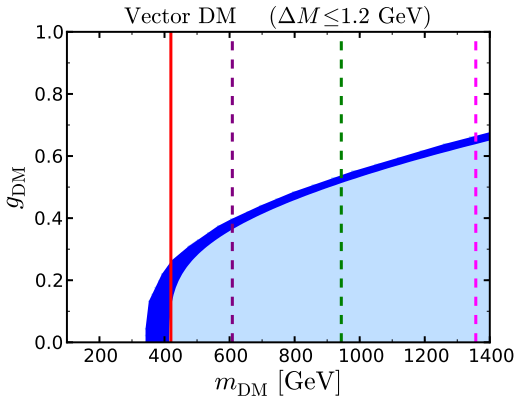

Figure 3.14: Model 3: Plot of the coupling $g_{\rm DM}$ versus the dark matter mass $m_{\rm DM} = m_V$. We scan over $\Delta M \in [0, 1.2\,\text{GeV}]$, where $\Delta M = M_\Psi - m_V$, this is the mass region where the HSCP limits are independent of the coupling $g_{\rm DM}$. The dark blue band satisfies the correct DM relic abundance within 3σ, the region in light blue overproduces the amount of DM. The colour-coding for the exclusion regions is the same as in the previous Figure.

2. Interestingly, this model has larger $\Omega_{\rm DM}h^2$ for $g_{\rm DM} = 0.1$ compared to Model-2. In the limit $g_{\rm DM} \ll 1$, Eq. (3.3.17) implies

$$\frac{\langle\sigma_{\rm eff}v\rangle|_{\rm Model\,2}}{\langle\sigma_{\rm eff}v\rangle|_{\rm Model\,3}} \simeq \frac{(\mathrm{g}_{V_\mu} + \mathrm{g}_\Psi)^2}{(\mathrm{g}_S + \mathrm{g}_\Psi)^2} = \frac{49}{25}\,. \tag{3.3.26}$$

On the other hand, for larger $g_{\rm DM}$ the DM relic rapidly decreases, as can be seen in Fig. 3.14. This is because the contribution of $V_\mu V_\mu \to \tau^+\tau^-$ process is not chiral or velocity suppressed in this model and it has a strong dependency on $g_{\rm DM}$: $\langle\sigma(V_\mu V_\mu \to \tau^+\tau^-)v\rangle \propto g_{\rm DM}^4$. One can see from Fig. 3.14 that a large region of the parameter space can be explored by the LHC and relic density constraints. Nevertheless, the region with $m_{\rm DM} \gtrsim 1.4$ TeV and $g_{\rm DM} \gtrsim 0.7$ may be left unconstrained even after the high luminosity LHC with 3000 fb^{-1}, although such large values of $g_{\rm DM}$ might bring sensitivities for direct detection experiments, which, however, is beyond the scope of this work.

Indirect detection

Unlike Model-1 and Model-2, Model-3 postulates a spin-1 dark matter particle, V_μ. The dark matter pair annihilation $V_\mu V_\mu \to \tau^+\tau^-$ in the present Universe is therefore

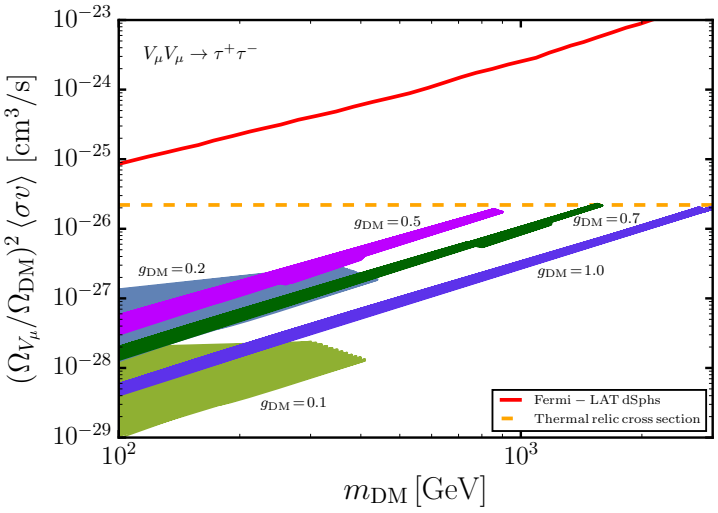

Figure 3.15: The rate of the dark matter annihilation $V_\mu V_\mu \to \tau^+\tau^-$ as a function of the dark matter mass. The red line corresponds to the current limit obtained by the gamma-ray observation of Milky Way dwarf spheroidal galaxies (dSphs) at the Fermi-LAT satellite [85]. The yellow dashed line corresponds to the thermal relic cross-section assuming the pure $V_\mu V_\mu \to \tau^+\tau^-$ process. The coloured regions correspond to different values of the coupling $g_{\rm DM}$ and ΔM is scanned over the $[0, 3]$ GeV range.

not chiral suppressed and may be sensitive to indirect detection experiments. We compare the annihilation cross-section computed by `MicrOMEGAs 4.1.5` with the upper limit derived from the gamma-ray observations of Milky Way dwarf spheroidal galaxies (dSphs) at the Fermi-LAT satellite [85].

We show our results in Fig. 3.15, where $\Delta M = M_\Psi - m_{\rm DM}$ is scanned over the $[0, 3]$ GeV range and the coloured regions correspond to different values of the coupling $g_{\rm DM}$, as explained in the figure. In order to confront these with the experimental limit assuming the nominal DM flux, these predictions are rescaled by the square ratio of the calculated relic abundance and the observed one, $(\Omega_{V_\mu}/\Omega_{\rm DM})^2$ with $\Omega_{\rm DM}h^2 = 0.1197$. We do not consider points that overproduce the relic abundance, i.e. all the points satisfy $\Omega_{V_\mu}h^2 \leq 0.1197$.

As can be seen, by increasing the dark sector coupling $g_{\rm DM}$ from 0.5 to 1.0, the annihilation rate decreases. This is because in this region, the abundance of V_μ is mainly determined by the same annihilation process $V_\mu V_\mu \to \tau^+\tau^-$ in the early Universe and $(\Omega_{V_\mu}/\Omega_{\rm DM})^2$ decreases more rapidly than the increase of the present time annihilation cross-section. The situation is different for smaller values of $g_{\rm DM}$,

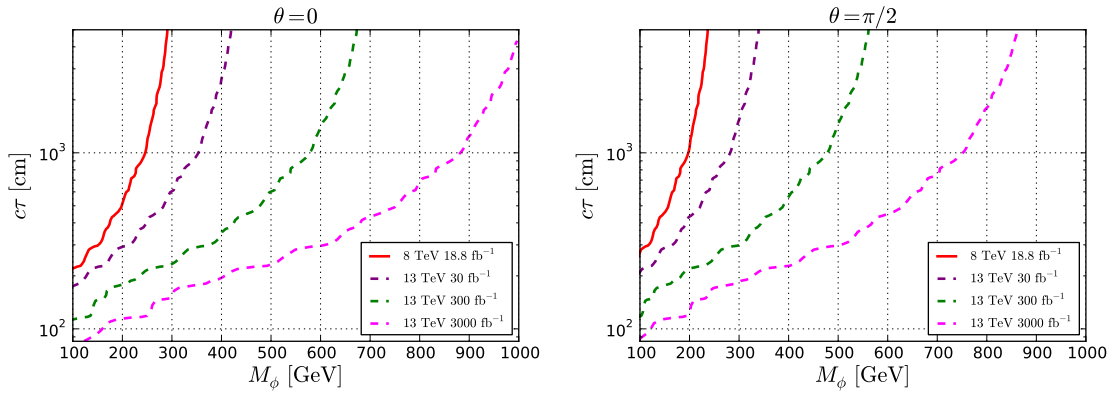

Figure 3.16: The 8 TeV (solid) and projected 13 TeV (dashed) limits from HSCP searches at the LHC for pair-production of the scalar coannihilation partner, $\phi^{\pm}$. The projected limits correspond to the 13 TeV LHC with 30, 300 and 3000 fb^{-1} integrated luminosities.

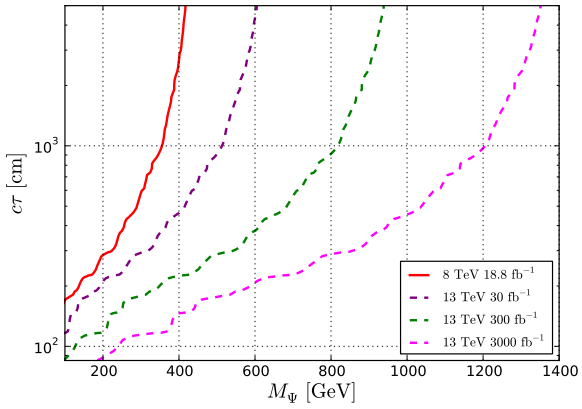

Figure 3.17: The 8 TeV (solid) and projected 13 TeV (dashed) limits from HSCP searches at the LHC for pair-production of the fermionic coannihilation partner, $\Psi^{\pm}$. The projected limits correspond to the 13 TeV LHC with 30, 300 and 3000 fb^{-1} integrated luminosities.

where $\Omega_{V_\mu} h^2$ is determined by the coannihilation mechanism and the annihilation rate of $\Psi^+\Psi^- \to$ SM particles, which does not depend on $g_{\rm DM}$, as discussed in Section **3.3.2**. One can therefore see that going from $g_{\rm DM} = 0.1$ to 0.5, the annihilation rate increases.

The red line in Fig. 3.15 shows the Fermi-LAT limit assuming dark matter annihilation into the $\tau^+\tau^-$ final state. As can be seen, the predicted rate is more than two order of magnitude smaller than the current limit across the parameter region.

3.3.8 Limits in the Mass vs Lifetime Plane

The current and projected limits obtained from the heavy stable charged particle searches shown in the previous sections can also be presented in a more model-independent fashion by plotting on the mass vs lifetime plane. The plots in Fig. 3.16 shows the 8 TeV (solid) and projected (dashed) limits for the pair-production of long-lived complex scalar field, ϕ, as a function of the mass, M_ϕ, and the lifetime times the speed of light, $c\tau$. The left plot assumes ϕ has the same quantum number as the right-handed τ corresponding to Simplified Model 1a. In the right plot, on the other hand, the interaction of ϕ is obtained by the procedure explained in Section **3.3.5** (Simplified Model 1b) and taking $\theta = 0$. The coannihilation partner ϕ in this case corresponds to the purely left-handed stau in SUSY theories. Fig. 3.17 shows the same limits for the fermionic coannihilation partner, Ψ. These limits are applicable for both Simplified Model 2 and 3 discussed in this work.

3.4 Tau-philic Dark Matter Coannihilation at CLIC

In this section, we study the sensitivity at future e^+e^- linear colliders for the simplified models of dark matter presented in Section **3.3**. There are current plans to construct the Compact Linear Collider (CLIC) at the CERN site located across the border between France and Switzerland. The first stage is planned to have centre-of-mass energy $\sqrt{s} = 380$ GeV, while future stages with higher centre-of-mass energies are planned to go up to 3 TeV [91]. Moreover, there are plans for the construction of the International Linear Collider (ILC) in Japan, its first stage is planned to have centre-of-mass energy $\sqrt{s} = 250$ GeV [90]. Considering that CLIC is planned to reach higher centre-of-mass energies, we will focus our study on the latter.

3.4.1 Motivation

The simplified models of dark matter with a mediator particle can be classified by its spin and quantum numbers, and they offer a rich phenomenology. However, not all features that may be present in more complete models are implemented within this framework. The primary example is the *coannihilation mechanism*, in which

the DM (χ) comes with an almost mass degenerate coannihilation partner (CAP, η) and the DM relic abundance is determined not by the χ-χ scattering but mainly by the η-η and η-χ scattering. This mechanism appears in various extensions of the SM, such as supersymmetric and extra dimensional models, and does not require a mediator particle. In particular, the stau-coannihilation ($\eta = \tilde{\tau}$) is often found in phenomenological scans of the MSSM parameter space [293, 361], since the lightest stau tends to be the next-to-the-lightest SUSY particle after the neutralino DM.

Phenomenology of the coannihilation mechanism is quite different from that in models with mediators. In the latter, the interaction dictating thermal freeze-out connects the DM and SM particles and severe constraints are placed from direct/indirect detection experiments. On the other hand, if the coannihilation mechanism is operative, the thermal freeze-out is controlled by the interaction between the CAP and SM particles, and the direct/indirect detection constraints can easily be avoided. LHC phenomenology is also very different. Unlike mediator particles, the coannihilation partner decays into the DM and SM particles very softly, and the signal is easily swamped by the overwhelming background. Therefore, the LHC can do very little on the coannihilation DM models in general. The only exception is the extreme case where the mass splitting between the CAP and DM is smaller than the tau-lepton mass, 1.777 GeV. In such a case, the coannihilation partner may have a detector-scale lifetime and its production can be constrained at the LHC by looking for highly ionizing and/or slowly moving anomalous tracks. We have studied this possibility in Section **3.3**.

In this section, we discuss DM simplified models with tau-philic coannihilation partners and study them in light of the future Compact Linear Collider (CLIC). We demonstrate that, unlike the LHC, CLIC and other future lepton colliders can resolve soft tau-lepton signature and offer the ideal opportunity to explore this class of models. Even though CLIC proves clean final states for signal, the soft tau background produced by bremsstrahlung photon collisions, $\gamma\gamma \to \tau^+\tau^-$, is significant. We take this effect into account and show how well CLIC can constrain the bulk of the model parameter space at each stage of the experiment.

Model-1			
Component	Field	Charge	Interaction
DM	Majorana fermion (χ)	$Y = 0$	$\phi^*(\chi\tau_R) + \text{h.c.}$
CAP	Complex scalar (ϕ)	$Y = -1$	

Model-2			
Component	Field	Charge	Interaction
DM	Real scalar (S)	$Y = 0$	$S(\overline{\Psi}P_R\tau) + \text{h.c.}$
CAP	Dirac fermion (Ψ)	$Y = -1$	

Model-3			
Component	Field	Charge	Interaction
DM	Vector (V_μ)	$Y = 0$	$V_\mu(\overline{\Psi}\gamma^\mu P_R\tau) + \text{h.c.}$
CAP	Dirac fermion (Ψ)	$Y = -1$	

Table 3.2: Simplified Models of DM with a colourless coannihilation partner (CAP)

3.4.2 Simplified Models for Tau-philic Dark Matter

Our simplified models consist of two new degrees of freedom: the gauge singlet DM particle, χ, and the charged coannihilation partner (CAP), $\eta^{(\pm)}$. We assign these particles the odd Z_2 charge to ensure the stability of the DM. The interaction term is given by

$$\mathcal{L} \supset g_{\text{DM}}\, \chi\, \eta\, \bar{\tau}_R + \text{h.c.} \ , \tag{3.4.27}$$

where g_{DM} is the dark sector coupling which we take to be real. The gauge invariance forces η to be singlet under $\text{SU}(3)_c$ and $\text{SU}(2)_L$ and have the hypercharge -1 as for the right-handed tau. Restricting the particles not to have spins higher than 1, we consider three possible spin assignments for the (χ, η) pair: ($\frac{1}{2}$, 0), (0, $\frac{1}{2}$) and (1, $\frac{1}{2}$). We refer to them as Model-1, 2 and 3, respectively. Those models together with our notation are summarised in Table 3.2.

The DM annihilation channel in our simplified models is unique, $\chi\chi \to \tau^+\tau^-$. In Model-1 (-2) where the DM is a Majorana fermion χ (a real scalar S), this channel is suppressed. The initial state in both cases forms a spin-0 state (due to the Pauli blocking in the Majorana case). To conserve the angular momentum, the $\tau^+\tau^-$ pair in the final state must have the opposite chiralities in s-wave, rendering the contri-

bution to be proportional to m_τ^2 (chiral suppression). The dominant contribution then comes from the p-wave for a Majorana DM and d-wave for a scalar DM, which are suppressed by the factor v^2 and v^4, respectively, where v is the average velocity of the annihilating DM particles.

3.4.3 Expected Sensitivity at CLIC

At particle colliders the possibility arises to study pair production of the charged coannihilation partners via an off-shell neutral gauge boson (γ/Z) exchange. The produced CAPs subsequently decay into the DM particle and a tau lepton. In the bulk of the viable parameter region, the mass splitting is small ($\Delta M \sim 20$ GeV) and the decay products of the CAP become very soft. In this region the LHC is hopeless to distinguish the signal from the overwhelming background.

The e^+e^- collider can create pairs of coannihilation partners (η) via a neutral gauge boson exchange. The produced CAPs then decay into the DM particle χ and a tau lepton:

$$e^+e^- \to \eta^+\eta^- \to \tau^+\tau^-\chi\,\chi\,. \tag{3.4.28}$$

We focus our study on the signal coming from prompt decays of $\eta^\pm$ and hence we study the region of parameter space with $\Delta M > m_\tau$. The opposite case ($\Delta M \leq m_\tau$) may be probed at the LHC by looking for anomalous charged track signatures since η can be long-lived in this region, cf. Section **3.3**.

The production cross-sections for scalar (ϕ) and fermionic (Ψ) CAPs with $Y=-1$ are given by [362–364]

$$\sigma(e^+e^- \to \phi^+\phi^-) = \alpha^2\pi s\cdot\mathcal{A}\cdot\frac{1}{6}\beta^3, \tag{3.4.29}$$

$$\sigma(e^+e^- \to \Psi^+\Psi^-) = \alpha^2\pi s\cdot\mathcal{A}\cdot\beta\left(1-\frac{1}{3}\beta^2\right), \tag{3.4.30}$$

with

$$\mathcal{A} = \frac{2}{s^2} + \frac{2}{s}\frac{(g_L+g_R)g_R}{(s-m_Z^2)} + \frac{(g_L^2+g_R^2)g_R^2}{(s-m_Z^2)^2}, \tag{3.4.31}$$

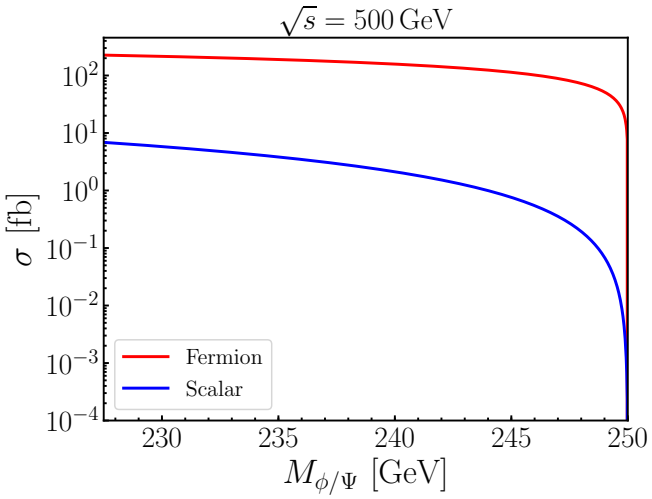

Figure 3.18: The cross-sections for pair production of coannihilation partners. The scenario with Dirac fermion (complex scalar) as the coannihilation partner correspond to red (blue) curves.

$$g_L = \frac{-\frac{1}{2} + s_W^2}{s_W c_W}, \qquad g_R = \frac{s_W^2}{s_W c_W}, \tag{3.4.32}$$

where α stands for the fine-structure constant, g_L and g_R correspond to the couplings between the Z boson and the electron, and β is the velocity of the outgoing ηs

$$\beta = \sqrt{1 - \frac{4M_{\phi/\Psi}^2}{s}}\,. \tag{3.4.33}$$

These simple formulae neglect the subleading effects of the Z boson width and the energy loss of incoming electrons due to bremsstrahlung photons.

In Fig. 3.18 we present the cross-sections of scalar (ϕ) and fermionic (Ψ) CAPs at the 500 GeV CLIC. In the formulae we can see that the cross-section is proportional to β for fermions, while it is proportional to β^3 for scalars as $\beta \to 0$; therefore, the scalar production is significantly reduced as the mass gets closer to half of the e^+e^- centre-of-mass energy. This feature is clearly seen in Fig. 3.18. Moreover, we note that the production rate is independent of g_{DM}.

We also comment on the vector boson (γ/Z) fusion (VBF) channel, $e^+e^- \to \eta^+\eta^- e^+e^-$.[6] Unlike the Drell-Yan process, the production rate of this channel is

[6]In our simplified models the W-boson fusion channel, $e^+e^- \to \eta^+\eta^-\nu\bar{\nu}$, is absent, since the

not proportional to $1/s$ and could potentially be important for large s. We have estimated the LO cross-section of this process with `MadGraph` [338] requiring that out-going electrons have $p_T > 0.01$ GeV and $|\eta| < 7$ to avoid the t-channel singularity in the forward region. For $m_\eta = 300$ GeV we find the cross-section of this process to be $\sigma_\phi^{\rm VBF} = 0.17$ fb and $\sigma_\psi^{\rm VBF} = 0.9$ fb, both of which are order of magnitude smaller than the Drell-Yan processes of the corresponding models. We therefore do not include this process in our study.

In the region where the coannihilation mechanism is effective, the final state taus are very soft due to a small mass splitting between the CAP and DM. This region suffers from a large soft tau background produced by collisions of forward photons emitted by the incoming electrons: $\gamma\gamma \to \tau^+\tau^-$. This background can be suppressed by demanding a high energy ISR photon in the event. If such a photon is produced, one of the beam-remnant electrons will be deflected and detected, and the event can be safely rejected [365]. The efficiency of the analysis based on this technique in the case of hadronic tau final state is studied in detail in Ref. [366]. The latter work provides the 95 % CL exclusion limit in the (M_η, m_χ) plane assuming 500 GeV e^+e^- collider with 500 fb^{-1}. We recast their result into our simplified models in the following way: along the exclusion contour, we calculate the required signal events, $N_{\rm max}(\Delta M)$, (before event selection) needed for exclusion for each value of ΔM. For different collider energies $\sqrt{s}$, integrated luminosities $\mathcal{L}$ and spins ϕ/Ψ, we demand the signal events before event selection not to exceed the corresponding upper limit:

$$\sigma_{\phi/\Psi}^{\sqrt{s}}(M_{\phi/\Psi}) \cdot \mathcal{L} \;\leq\; N_{\rm max}(\Delta M)\,. \tag{3.4.34}$$

This recasting method has been commonly used in the literature [3, 293, 350] and proved to work well empirically. The assumption behind this method is that in the future analysis, the signal efficiency over the square root of the background efficiency $(\epsilon^S/\sqrt{\epsilon^B})$ may be improved compared to the current value $(\epsilon_0^S/\sqrt{\epsilon_0^B})$, since more events are available due to the increase of the energy or luminosity, in such a way that $\epsilon^S/\sqrt{\epsilon^B} \sim (\sqrt{B/B_0})(\epsilon_0^S/\sqrt{\epsilon_0^B})$, where B and B_0 are the number of future and

coannihilation partner is $\mathrm{SU}(2)_L$ singlet and does not couple to the W-bosons.

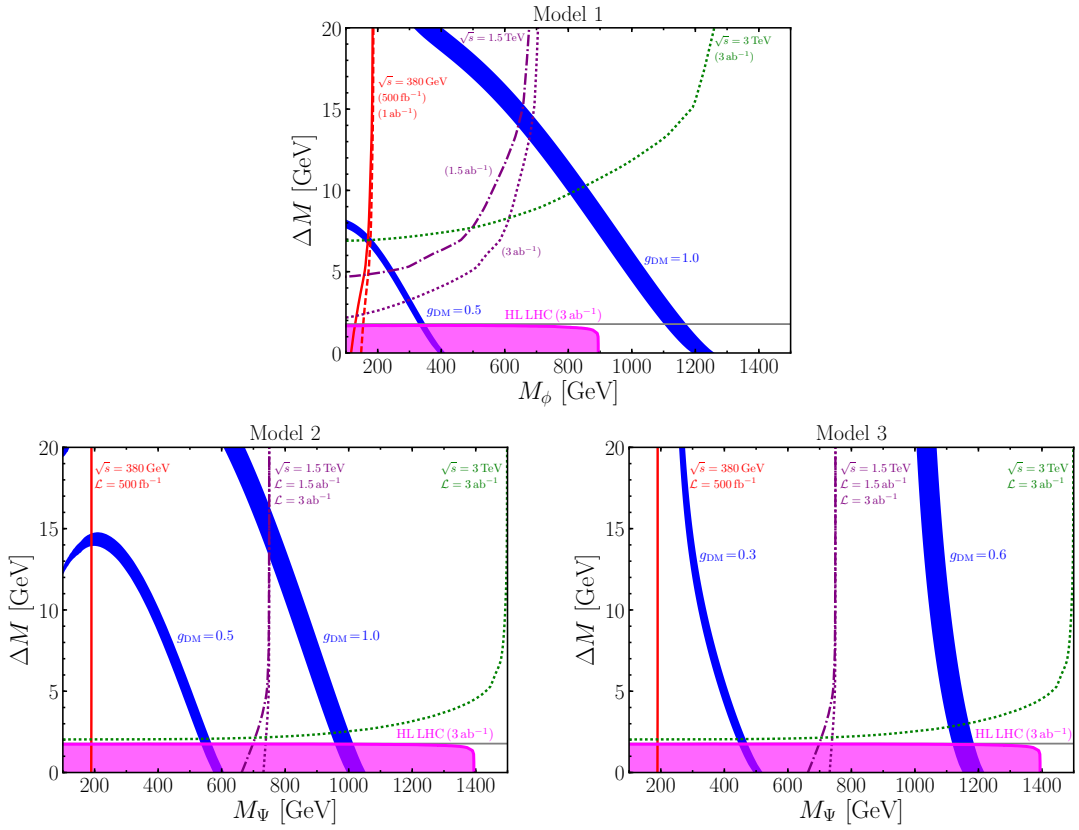

Figure 3.19: The DM coannihilation strip and the projected exclusion limits at CLIC for the three models presented in Table 3.2. Different colours correspond to different centre-of-mass energies $\sqrt{s}$ as shown in the plot. Solid, dashed, dot-dashed and dotted lines correspond to 500 fb^{-1}, 1 ab^{-1}, 1.5 ab^{-1} and 3 ab^{-1} for the integrated luminosities respectively. The region coloured in magenta corresponds to projected limits for long-lived charged particles searches at the high luminosity stage of the LHC; namely, centre-of-mass energy of 13 TeV and 3 ab^{-1} [3]. The horizontal grey line indicates the mass of the τ lepton. The blue regions satisfy the correct dark matter relic abundance within 3σ for different values of the coupling $g_{\rm DM}$.

present background events, respectively. We present our results in Fig. 3.19 where the projected sensitivity of 95 % CL are shown for various assumptions on the collider energy and luminosity. The blue bands show the region corresponding to the DM relic density observed by the Planck satellite mission [37], within $3\,\sigma$, for several values of $g_{\rm DM}$. The region above the blue band is excluded due to overproduction of DM, unless the thermal history of the Universe is modified. These plots illustrate the complementarity between the projected limits for CLIC and the ones corresponding to searches for long-lived charged particles at the LHC, the latter correspond to the

region coloured in magenta.

The upper panel shows the projected sensitivity for Model-1 in which DM is a Majorana fermion. In this scenario, the coannihilation partner is a complex scalar (ϕ) and the production cross-section Eq. (3.4.29) gets suppressed by β^3 at the vicinity of the kinematic threshold. Therefore, the exclusion limits on this scenario are weaker than those in the scenarios with a fermionic CAP (Ψ) (Model-2 and -3). Furthermore, the production rate gets smaller for larger $\sqrt{s}$ as can be seen in the expression of $\mathcal{A}$ in Eq. (3.4.31). Consequently, increasing the collider energy does not help to explore smaller ΔM region. In order to probe the coannihilation strip for $g_{\rm DM}=0.5$, increasing the luminosity from 1 to 3 ab^{-1} represents a better improvement than increasing the centre-of-mass energy from 1.5 to 3 TeV.

The lower panel shows the exclusion limits on Model-2 and -3 corresponding to a scalar and a vector DM, respectively. The coannihilation partner is a charged Dirac fermion (Ψ) in both scenarios. For $\sqrt{s}$ = 380 GeV with 500 fb^{-1}, the projected limits on these models are very close to the kinematic threshold (M_Ψ = 190 GeV). In Model-2, the DM overproduction constraint requires M_Ψ to be smaller than 1 TeV for $g_{\rm DM} \leq 1$. This region can be explored by 3 TeV CLIC apart from a compressed mass region $\Delta M < 2.5$ GeV. Unlike Model-1 and -2, the DM density in Model-2 can easily be brought down to the allowed value, without resorting to small ΔM, due to the absence of chiral suppression in the $\chi\chi \to \tau^+\tau^-$ mode. Thus, M_Ψ can go higher than as 1.5 TeV for $g_{\rm DM} \gtrsim 0.7$, which exceeds the kinematical threshold of 3 TeV CLIC. On the other hand, almost the entire region with $g_{\rm DM} \lesssim 0.7$ can be explored by CLIC, as can be seen in the lower right panel of Fig. 3.19.

3.4.4 Summary

We have studied the sensitivity of the future Compact Linear Collider to the tau-philic DM simplified models with a coannhilation partner. Three distinctive scenarios have been examined: **(i)** Majorana DM, **(ii)** Real scalar DM and **(iii)** Vector DM, where the CAP is a complex scalar in the first model, while it is a Dirac fermion in the latter two. We have found that CLIC has the excellent sensitivity to these

models. In particular, if the CAP is a Dirac fermion, almost entire region allowed by the DM relic constraint can be explored by 3 TeV CLIC. If it is a complex scalar, the region with small mass splitting $\Delta M < 10$ GeV may not be probed depending on the mass of the scalar. We found that larger luminosity helps greatly in exploring the small ΔM region even for low energy options ($\sqrt{s} = 380$ GeV and 1.5 TeV).

The models presented in this report are difficult to be probed by direct and indirect DM detection experiments as well as by the LHC. Therefore, lepton colliders such as CLIC, provide an almost unique opportunity to explore them. Consequently, a possible discovery of a new heavy electrically charged particle decaying into a τ-lepton plus missing energy can provide information about one of the most pressing questions in high-energy physics; the nature of dark matter. In addition, this would present motivation to develop new techniques to explore models with compressed mass spectra at CLIC.

3.5 Summary

The nature of dark matter remains one of nature's best kept secrets. For this reason, there is a considerable ongoing experimental and theoretical effort dedicated to the discovery of the dark matter particle. There has been a rapid development in the number and scope of direct and indirect detection experiments, and in LHC and future collider searches of DM. A standard signature to search for dark matter at colliders is the mono-X (or multi-jets) plus missing energy. These searches are being exploited and interpreted in terms of simplified dark matter models with mediators. A growing number of the analyses are also dedicated to the direct search of the mediator which can decay back to the SM degrees of freedom.

In this chapter we considered an alternative DM scenario characterised by simplified models without mediators. Instead, they include a coannihilation partner particle in the dark sector. In the scenarios with a relatively compressed mass spectrum between the DM and its charged coannihilation partner, the latter plays an important role in lowering the dark matter relic density. The signal we study at particle colliders is the pair-production of the coannihilation partners that then

ultimately decay into cosmologically stable dark matter.

Concerning searches at the LHC, we have focused on the case when the dark matter candidate and the coannihilation partner are nearly mass-degenerate, which makes the latter long-lived. Compared to other models of dark matter that rely on signals with missing energy at colliders, in these models the crucial collider signature to look for are tracks of long-lived electrically charged particles. For the region of parameter space with larger mass splitting, where the coannihilation partner promptly decays into dark matter (missing energy) and a τ-lepton, we studied the sensitivity at future linear e^+e^- colliders such as CLIC and ILC.

We considered three different scenarios for cosmological DM: a Majorana fermion, a real scalar and vector dark matter. The model with Majorana DM can be motivated by theories with supersymmetry, such as the bino–stau coannihilation strip in the MSSM. The model with vector DM can be motivated by Kaluza-Klein theories of extra dimensions, where the KK photon plays the role of dark matter, or by a new strong sector in composite models. Nevertheless, in this work we have advocated for a simple (and arguably more inclusive) purely phenomenological approach and we have considered the couplings and the masses as free parameters.

In the search for the dark matter particle, particle accelerators represent a complementary approach to direct and indirect detection experiments. Due to the large interaction energy, an effective field theory approach might not be the best framework to study dark matter pair production at particle colliders. In this chapter, we have presented a set of simplified models which are complementary to the standard mediator-based simplified DM models set. We have characterised these models in terms of three to four classes of simplified models with as little as three free parameters. We have demonstrated that a large region in the parameters space of these models will be probed at the LHC and future linear colliders to probe these models.

Chapter 4

New Observable for the Detection of Ultralight Axions

In this chapter we propose an observable that could serve for the detection of ultralight axions. A cloud of ultralight axions forms surrounding a Kerr black hole via the mechanism of superradiance. Due to its coupling to photons, an inhomogeneous pseudo-scalar (axion) field configuration behaves like an optically active medium. Consequently, if a light ray passes through the axion cloud, it may experience a polarisation-dependent bending. We explore the size and relevance of such effect considering both the QCD axion and a generic axion-like particle.

In Section **4.1**, we present a brief overview of the mechanism of black hole superradiance and the motivation for our work. In Section **4.2**, we discuss general aspects of black hole superradiance with a particular emphasis on the conditions that allow for an analytical approach. In Section **4.3**, we compute the polarisation-dependent bending that a ray of light experiences by travelling through an axion cloud. In Section **4.4**, we discuss the phenomenological relevance of our result, and in Section **4.5**, we provide further details of the calculations done in this work. Finally, we present a summary in Section **4.6**.

4.1 Motivation

Superradiance is a radiation enhancement process which occurs in the presence of a dissipative system. We refer the interested reader to [367] for an excellent and comprehensive review about the role of superradiance in astrophysics and particle physics. In the following, we highlight the main aspects that are relevant for our analysis.

In General Relativity, rotating black holes, also referred to as Kerr black holes, have an associated event horizon and ergoregion [145, 368–372]. It is the presence of these two regions that allows for the mechanism of superradiance to take place. The former is, for all intents and purposes, a one-way viscous membrane from which nothing, at least at the classical level, can escape. In other words, the presence of an event horizon makes black holes perfect absorbers. The latter is a region surrounding the event horizon where everything – literally, including light – is forced to co-rotate with the black hole. The presence of both the event horizon and the ergoregion creates the ideal conditions to make the Penrose process – that is the extraction of energy from a rotating black hole – possible [144]. Black hole superradiance can be thought of as the wave analogue of the Penrose process.

Superradiance has remarkable consequences in the presence of a confining mechanism, for instance provided by the presence of a perfectly reflecting mirror surrounding the black hole. In this case the amplified pulse bounces back and forth, exponentially increasing its amplitude, and eventually leading to an instability. This situation is naturally realized when the Kerr black hole is coupled to a massive boson since low-frequency radiation is confined due to a Yukawa-like suppression. In Fig. 4.1 we illustrate schematically the axion cloud that forms around a rotating black hole.

We now discuss these points in a more quantitative manner following the same line of reasoning presented in [367, 372]. We consider a massive wave-packet in the gravitational field of a black hole. The situation is remarkably similar to that of an electron in the Coulomb potential of an hydrogen atom, and the problem – after introducing the tortoise coordinate r^*, with $r^* \to -\infty$ as r approaches the

black hole horizon r_+ – reduces to the solution of a Schrödinger-like one-dimensional equation $d^2\Psi/dr^{*2} + V_{\rm eff}(r)\Psi = 0$ describing the radial motion under the influence of an effective potential. For a Schwarzschild black hole of mass M the effective potential takes the form

$$V_{\rm eff}^{\rm Schw}(r) = \omega^2 - \left(1 - \frac{2G_N M}{r}\right)\left[\frac{2G_N M}{r^3} + \frac{l(l+1)}{r^2} + \mu^2\right] \ , \tag{4.1.1}$$

where $G_N = (1/M_{\rm Pl})^2$ is the Newton's constant (with $M_{\rm Pl} \simeq 1.22 \times 10^{19}$ GeV the Planck mass), ω is the frequency of the wave-packet, μ the scalar field mass, and l the azimuthal quantum number. The structure of Eq. (4.1.1) remarks the analogy with the hydrogen atom mentioned before with a gravitational potential – instead of the usual Coulomb contribution – besides the centrifugal term. Asymptotically, considering both the horizon at $r \to r_+$ (equivalently, $r^* \to -\infty$) and spatially infinity at $r \to \infty$, the most general solution has the form

$$\Psi \sim \begin{cases} \mathcal{T}e^{-ik_+ r^*} + \mathcal{O}e^{ik_+ r^*} & r \to r_+ \ , \\ \mathcal{R}e^{ik_\infty r^*} + \mathcal{I}e^{-ik_\infty r^*} & r \to \infty \ , \end{cases} \tag{4.1.2}$$

with $k_+^2 \equiv V_{\rm eff}(r \to r_+)$, $k_\infty^2 \equiv V_{\rm eff}(r \to \infty)$, and generic transmitted ($\mathcal{T}$), reflected ($\mathcal{R}$), incident ($\mathcal{I}$), and outgoing ($\mathcal{O}$) flux. In the following simplified discussion we assume the potential to be real even if this is not true in general because ω is a complex number. Since under this assumption the Schrödinger equation is real, the complex conjugate of any solution is also a solution. We can, therefore, impose the Wronskian equality $\mathcal{W}(\Psi, \Psi^*)|_{r\to r_+} = \mathcal{W}(\Psi, \Psi^*)|_{r\to\infty}$, with $\mathcal{W}(\Psi, \Psi^*) \equiv \Psi(\Psi^*)' - \Psi^*(\Psi)'$, and we find the unitarity condition [367]

$$|\mathcal{R}|^2 = |\mathcal{I}|^2 - \frac{k_+}{k_\infty}\left(|\mathcal{T}|^2 - |\mathcal{O}|^2\right) \ . \tag{4.1.3}$$

Notice that for a black hole at the horizon the outgoing flux at the horizon is zero, $\mathcal{O} = 0$, at least at the classical level. The wave is superradiantly amplified, i.e. $|\mathcal{R}|^2 > |\mathcal{I}|^2$, if $k_+/k_\infty < 0$. For the Schwarzschild black hole in Eq. (4.1.1) one immediately finds that $k_+/k_\infty|_{\rm Schw} = \omega/\sqrt{\omega^2 - \mu^2}$, and the superradiant condition

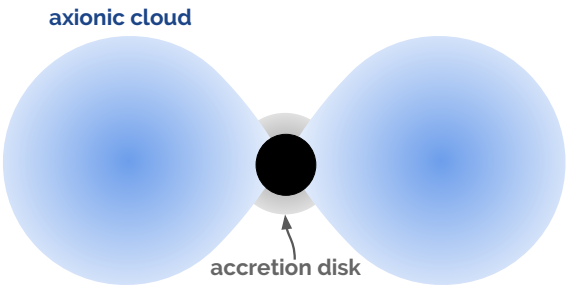

Figure 4.1: Schematic depiction of BH superradiance. The diagram shows the top view of the system. The blue shadow depicts the axion cloud surrounding the rotating black hole. The latter is shown in black at the centre of the image. The region coloured in grey represents the accretion disk.

never happens. On the contrary, since $\mathcal{O} = 0$, we find $|\mathcal{R}|^2 < |\mathcal{I}|^2$ that is the typical case of an absorber material. Let us now move to the case of a Kerr black hole with mass M and angular momentum $J = aM$. The effective potential is more complicated (see Eqs. (4.2.11, 4.2.12) below) but it is straightforward to find

$$\left.\frac{k_+}{k_\infty}\right|_{\text{Kerr}} = \left(\omega - \frac{am}{2G_N M r_+}\right) / \sqrt{\omega^2 - \mu^2} \,. \tag{4.1.4}$$

The superradiant condition is satisfied if $\omega < am/2G_N M r_+$, where $-l \leqslant m \leqslant l$ is the magnetic quantum number, and the reflected wave is superradiantly amplified.

This simple example makes clear the general features of black hole superradiance outlined at the beginning of the section. First of all, the importance of the horizon. In the absence of an horizon – consider for instance a generic star – it is necessary to impose a regularity condition at the centre. As a consequence of $d\Psi/dr|_{r\to 0} = 0$, the Wronskian at the centre vanishes. The Wronskian at infinity gives $\mathcal{W}(\Psi, \Psi^*)|_{r\to\infty} = -2ik_\infty(|\mathcal{R}|^2 - |\mathcal{I}|^2) = 0$, and there superradiance does not take place since $|\mathcal{R}|^2 = |\mathcal{I}|^2$. More generally, this is the typical condition that occurs in the absence of a dissipative mechanism because in this case conservation of energy implies that the outgoing flux equals the transmitted one, $|\mathcal{T}|^2 = |\mathcal{O}|^2$, and the condition $|\mathcal{R}|^2 = |\mathcal{I}|^2$ follows from Eq. (4.1.3).[1] Second, we see that the black hole spin $a \neq 0$ is crucial

[1] In the absence of an horizon, superradiance is possible only in the presence of an alternative

to fulfil the superradiant condition, and rotational energy powers the growth of the reflected wave in Eq. (4.1.3). The extraction is made possible because the rotational energy of a Kerr black hole is not located inside the event horizon but in the ergoregion. This is the crucial difference compared to the Schwarzschild case, in which there is no energy available outside the event horizon. Finally, the presence of a mass term μ naturally provides a confining mechanism for the low-frequency reflected waves since if $\omega < \mu$ from $e^{ik_\infty r}$ and $k_\infty = \sqrt{\omega^2 - \mu^2}$ one gets a Yukawa-like suppression.

The striking conclusion that follows from this discussion is that, under the specific conditions that trigger a superradiant instability, in the presence of a massive scalar field it should not be possible to observe fast-spinning black holes simply because the black hole must spin down as a consequence of energy extraction.[2] Black hole spin-measurements [377, 378] are therefore a valid experimental observable to constrain or discover new massive scalar particles [147]. As a rule of thumb, superradiance is relevant if the Compton wavelength of the massive particle $\lambda_{\rm Compton} = 1/\mu$ is of the same order compared with the black hole radius $R \approx 2G_N M$

$$M \approx 6.7 \left(\frac{10^{-12}\,\text{eV}}{\mu}\right) M_\odot \ . \tag{4.1.5}$$

Supermassive black hole with $M \sim 10^6\ M_\odot$ corresponds to ultralight scalar with $\mu \sim 10^{-18}$ eV while stellar-mass black holes are relevant if $\mu \sim 10^{-12}$ eV.

From a particle physics perspective, such light scalars are natural if protected by some underlying symmetry that makes the presence of a tiny mass term technically natural, and the most convincing case is that of a pseudo-Nambu–Goldstone boson, a light scalar field arising from the spontaneous breaking of a global symmetry. The QCD axion and, more generally, axion-like particles (ALPs) are typical examples. The former is theoretically motivated by the solution of the strong CP problem, the latter are ubiquitous in the low-energy limit of string constructions

dissipation mechanism. See [373] for an interesting recent example in the context of conducting rotating stars.

[2] Superradiance is also possible for a massive spin-1 [374, 375] and spin-2 field [376].

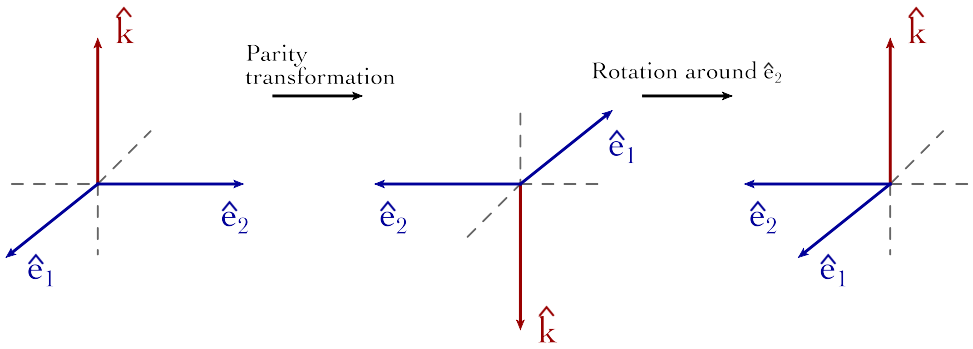

Figure 4.2: Parity transformation for a triad of vectors under a parity transformation (central panel). A further rotation by π around the $\hat{e}_2$ axis (right panel), made possible by isotropy of space, brings the vectors to the final configuration.

(the "axiverse" [146]). Black hole superradiance is, therefore, an extremely interesting discovery tool for this class of new physics particles.

However, the story told so far only relies on gravitational interactions. In other words, any boson with mass μ, irrespective of its particle physics origin, will display the same physics as far as the aforementioned picture of superradiance is concerned.

The goal of the present chapter is to present and discuss an observable consequence of black hole superradiance that is intimately connected to the axionic nature of the scalar cloud. To this end, we shall exploit the axion effective coupling to photons which is defined by the Lagrangian density

$$\mathcal{L}_{a\gamma\gamma} = \frac{g_{a\gamma\gamma}}{4}\Phi F_{\mu\nu}\tilde{F}^{\mu\nu} = -g_{a\gamma\gamma}\Phi\vec{E}\cdot\vec{B}\ . \tag{4.1.6}$$

In the case of the QCD axion this coupling – inherited from the mixing with light mesons (π_0, η, η', *et cetera*) as well as by the triangle anomaly of the Peccei-Quinn fermions – is in general non vanishing and it motivates a rich search strategy based on axion-photon conversion in external magnetic fields [379].

Our idea is very simple, and can be illustrated as follows. Consider an electromagnetic wave in the vacuum, defined by the wave vector $\hat{k} = \vec{k}/|\vec{k}|$ determining the direction of propagation, the angular frequency ω, and two basis polarisation vectors $\hat{e}_{i=1,2}$, both being perpendicular to $\hat{k}$. Under parity, we have the transformation property $(\hat{k}, \hat{e}_1, \hat{e}_2) \xrightarrow{P} (\hat{k}, \hat{e}_1, -\hat{e}_2)$. The situation is illustrated in two steps in Fig. 4.2. The wave vector $\hat{k}$ flips sign as a consequence of the Fourier space

identification $\vec{\nabla} \to i\vec{k}$. The two polarisation vectors also flip sign. This is evident in the Coulomb gauge, in which $\vec{E} = i\omega\vec{A}$. The vector potential $\vec{A}$ inherits the parity transformation property of the electric field, $\vec{E} \xrightarrow{P} -\vec{E}$. The Coulomb gauge is very useful because it exhibits the physical degrees of freedom: the 3 components of $\vec{A}$ satisfy the constraint $\vec{\nabla} \cdot \vec{A} = 0$, leaving behind the 2 degrees of freedom that can be identified with the polarisation states of the photon. This means that one can write (for some numbers $a_{i=1,2}$ left unspecified) $\vec{A} = \sum_{i=1,2} a_i \hat{e}_i$, and the parity transformation of $\hat{e}_{i=1,2}$ follows from $\vec{A} \xrightarrow{P} -\vec{A}$. Finally, because of isotropy of space, only the relative orientation between vectors really matters. We can therefore apply a π rotation around the $\hat{e}_2$ axis in order to get the final parity transformation quoted above, $(\hat{k}, \hat{e}_1, \hat{e}_2) \xrightarrow{P} (\hat{k}, \hat{e}_1, -\hat{e}_2)$. This specific choice suggests to use left- and right-handed circular polarisation vectors defined by $\hat{e}_{\mathrm{L,R}} \equiv (\hat{e}_1 \mp i\hat{e}_2)/\sqrt{2}$ since under parity $\hat{e}_{\mathrm{L,R}} \xrightarrow{P} \hat{e}_{\mathrm{R,L}}$. In the absence of parity violation, there should be no difference in the physical properties of a right- and a left-handed circularly polarised electromagnetic wave. This discussion is of course a trivial consequence of parity invariance of electromagnetism.

The photon coupling in Eq. (4.1.6) does not respect parity, since $\vec{E} \xrightarrow{P} -\vec{E}$ and $\vec{B} \xrightarrow{P} \vec{B}$. This implies that the left and right components of an electromagnetic wave travelling through an axion background should experience different physical effects. This is precisely what we shall explore in this work considering the axion cloud surrounding a Kerr black hole as an optically active medium.

4.2 Axion Clouds around Rotating Black Holes

The massive Klein-Gordon equation

$$\Box\Phi = \mu^2\Phi \tag{4.2.7}$$

in a Kerr background

$$ds^2_{\rm Kerr} = -\left(1-\frac{2Mr}{\Sigma}\right)dt^2 + \frac{\Sigma}{\Delta}dr^2 - \frac{4raM}{\Sigma}s^2_\theta d\phi dt + \Sigma d\theta^2 + \left[(r^2+a^2)s^2_\theta + \frac{2rMa^2}{\Sigma}s^4_\theta\right]d\phi^2 \ , \tag{4.2.8}$$

where $\Sigma = r^2 + a^2c^2_\theta$, $\Delta = (r-r_+)(r-r_-)$, $r_\pm = M(1\pm\sqrt{1-\tilde{a}^2})$, $a = J/M$, $\tilde{a} = a/M$, admits the existence of quasi-bound states, as we shall briefly review in the following.

We use the short-hand notation $s_\theta \equiv \sin\theta$, $c_\theta \equiv \cos\theta$, and (t, r, θ, ϕ) are the usual Boyer-Lindquist coordinates. We work in natural units in which Planck's constant $\hbar$, the speed of light c, and Newton's constant G_N are set to one. Occasionally, we will reintroduce G_N to make some equations more transparent.

The massive Klein-Gordon equation in the Kerr background allows separation of variables[3] with the following simple ansatz for the scalar field [372]

$$\Phi(t, r, \theta, \phi) = \sum_{l,m} e^{im\phi} S_{lm}(\theta) e^{-i\omega t} R_{nl}(r) \ . \tag{4.2.9}$$

The angular equation defines the spheroidal harmonics $S_{lm}(\theta)$ [383]. The angular eigenvalues λ_{lm} are approximated by

$$\lambda_{lm} \simeq l(l+1) + \frac{2c^2\left[m^2 - l(l+1) + 1/2\right]}{(2l-1)(2l+3)} \ , \tag{4.2.10}$$

where the so-called degree of spheroidicity c^2 is defined by $c^2 \equiv a^2(\omega^2 - \mu^2)$. The radial part, on the contrary, reduces to a Schrödinger-like problem. Defining the Regge-Wheeler tortoise coordinate $dr^* = [(r^2+a^2)/\Delta]dr$, and rescaling the radial function according to $u_{nl}(r^*) = (r^2+a^2)^{1/2}R_{nl}(r)$, the radial equation reads

$$\frac{d^2u}{dr^{*2}} + \left[\omega^2 - V(\omega)\right]u = 0 \ , \tag{4.2.11}$$

[3]This property follows from the fact that the Kerr metric admits – among its mysterious "miracles" [380] – the existence of a Killing-Yano tensor [381, 382].

where the potential is given by

$$V = \frac{\Delta\mu^2}{r^2+a^2} + \frac{4Mram\omega - a^2m^2 + \Delta\left[\lambda_{lm} + (\omega^2-\mu^2)a^2\right]}{(r^2+a^2)^2} + \frac{\Delta(3r^2-4Mr+a^2)}{(a^2+r^2)^3} - \frac{3r^2\Delta^2}{(r^2+a^2)^4} \ . \tag{4.2.12}$$

The relation between the tortoise coordinate r^* and the ordinary radial coordinate r is

$$r^* = r + \frac{2Mr_+}{(r_+-r_-)}\ln\left(\frac{r}{r_+}-1\right) - \frac{2Mr_-}{(r_+-r_-)}\ln\left(\frac{r}{r_-}-1\right) \ . \tag{4.2.13}$$

The radial equation must be solved with the following boundary conditions

$$R \underset{r^*\to-\infty}{\sim} e^{-ik_+r^*} \ , \qquad R \underset{r^*\to\infty}{\sim} \frac{1}{r}\, e^{i(\omega^2-\mu^2)^{1/2}r^*} \ , \tag{4.2.14}$$

with $k_+ \equiv \omega - m\Omega_H$, being $\Omega_H \equiv a/2Mr_+$ the angular velocity of the Kerr black hole. Notice that we have purely ingoing waves at the horizon ($r^* = -\infty$ in tortoise coordinate); towards spatial infinity, on the contrary, the solution tends to zero since we are interested in bound states.

The manipulations above reduced the problem to the motion of a particle subject to the one-dimensional effective potential in Eq. (4.2.12). We show the effective potential in the left panel of Fig. 4.3. The presence of the mass term in the Klein-Gordon equation generates a potential well in region III, allowing for the formation of bound states. Notice that in the massless limit, the potential well cannot be formed (dot-dashed red line in the left panel of Fig. 4.3). Gravitational and centrifugal effects create a potential barrier in region II, and the particle bounded in region III can tunnel in the black hole ergoregion, region I. If the phase velocity of the purely ingoing wave at the horizon is negative – that is if $\omega_R < m\Omega_H$ from the boundary condition in Eq. (4.2.14), with $\omega_R \equiv \mathrm{Re}\,(\omega)$ – the transmitted wave will carry negative energy into the black hole, and the reflected wave will return to infinity with greater amplitude and energy than the incident wave: The superradiance mechanism is triggered.

The growth of superradiant instability depends on the dimensionless product

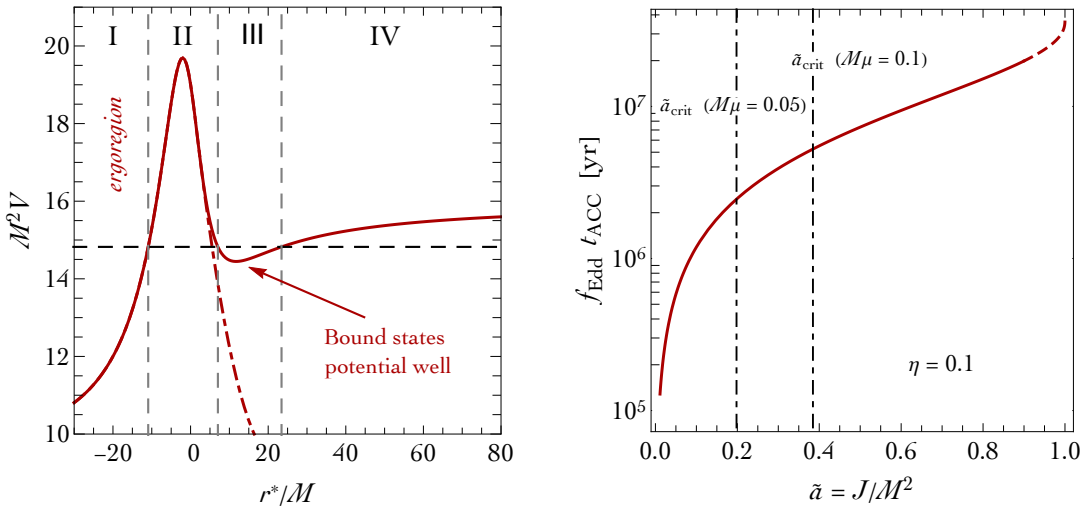

Figure 4.3: Left panel. Effective potential in Eq. (4.2.12) as a function of the tortoise coordinate r^*. Right panel. Evolution of the black hole angular momentum due to accretion starting from the Schwarzschild limit. Vertical lines mark two critical conditions in Eq. (4.2.22) for $m = 1$ and different values of $M\mu$. The solid red line becomes dashed where the inclusion of radiation is important.

$M\mu$. This product represents the ratio between the horizon size of the black hole and the Compton wavelength $\lambda_{\rm Compton}$ of the scalar field

$$M\mu \equiv \frac{G_N M\mu}{\hbar c} \sim \frac{r_+}{\lambda_{\rm Compton}} \ . \tag{4.2.15}$$

Two limits are commonly used, $M\mu \ll 1$ and $M\mu \gg 1$. The crucial difference is the growth rate of bound states. Parametrically, we have the following order-of-magnitude estimates [147, 371, 372]

$$\tau \underset{M\mu\ll 1}{\approx} \frac{M}{(M\mu)^9} \ , \qquad \tau \underset{M\mu\gg 1}{\approx} 10^7 e^{3.7(M\mu)} M \ . \tag{4.2.16}$$

In the limit $M\mu \ll 1$ the growth of superradiant instability can be as short as 10^2 s for stellar black holes

$$\tau \sim 10^2 \left(\frac{M}{10\,M_\odot}\right)\left(\frac{0.2}{M\mu}\right)^9 \ {\rm s} \ , \tag{4.2.17}$$

while in the opposite limit the presence of the e-folding makes the instability insignificant for astrophysical black holes.

In the following we assume the small $M\mu$ limit, with

$$M\mu = 7.5 \times 10^{-2} \times \left(\frac{M}{10\,M_\odot}\right) \times \left(\frac{\mu}{10^{-12}\,\mathrm{eV}}\right) \ . \tag{4.2.18}$$

The small $M\mu$ limit allows for a simple analytical understanding of superradiance.

In the small $M\mu$ limit, the eigenvalue problem for the radial equation admits an hydrogenic-like solution $\omega \equiv \omega_R + i\omega_I$ [372]

$$\omega_R \simeq \mu - \frac{\mu}{2}\left(\frac{M\mu}{l+n+1}\right)^2 \ , \tag{4.2.19}$$

$$\omega_I \simeq \mathcal{F}_{nl}\frac{(M\mu)^{4l+5}}{M}\left(\frac{am}{M} - 2\mu r_+\right)\prod_{j=1}^{l}\left[j^2\left(1-\frac{a^2}{M^2}\right) + \left(\frac{am}{M} - 2\mu r_+\right)^2\right] \ , \tag{4.2.20}$$

with

$$\mathcal{F}_{nl} \equiv \frac{2^{4l+2}(2l+1+n)!}{(l+n+1)^{2l+4}n!}\left[\frac{l!}{(2l)!(2l+1)!}\right]^2 \ . \tag{4.2.21}$$

The eigenfrequencies are, in general, complex, and the superradiance condition reads

$$a_{\mathrm{crit}} \sim \frac{2\mu r_+ M}{m} \ . \tag{4.2.22}$$

When $a > a_{\mathrm{crit}}$, the imaginary part of ω becomes positive: The corresponding modes increase in time, signaling an instability of the Kerr black hole in the presence of the massive scalar field.

In the small $M\mu$ limit, the radial eigenfunction reads [372, 384] (see also Section **4.5.1**)

$$R_{nl}(r) = A_{nl}g(\tilde{r}) \ , \qquad g(\tilde{r}) \equiv \tilde{r}^l e^{-\tilde{r}/2}\mathrm{L}_n^{2l+1}(\tilde{r}) \ , \qquad \tilde{r} \equiv \frac{2rM\mu^2}{l+n+1} \ , \tag{4.2.23}$$

with $\mathrm{L}_n^{2l+1}(\tilde{r})$ the Laguerre polynomials. In analogy with the hydrogen atom, the combination $\nu \equiv l+n+1$ defines the principal quantum number.

It is important to notice that the size of the cloud can be estimated as [147]

$$r_{\rm cloud} \sim \frac{(l+n+1)^2 M}{(M\mu)^2} \sim (l+n+1)^2 \times 1.5 \times 10^3 \left(\frac{M}{M_\odot}\right)\left(\frac{0.1}{M\mu}\right)^2 \text{ km} \,. \quad (4.2.24)$$

It implies that the cloud extends way beyond the horizon, where rotation effects can be neglected. In this limit the spheroidal harmonics $S_{lm}(\theta)$ reduce to the flat space spherical harmonics.

As clear from the previous discussion, superradiance is a dynamical process. It is therefore crucial to specify what are the assumption underlying our analysis. The physical setup we have in mind is the following.

1. Let us start considering a rotating black hole. In order to trigger the superradiant instability, the black hole must spin above the critical value in Eq. (4.2.22). We can not take this condition for granted, given in particular the lack of unambiguous experimental informations about black hole spins at birth. However, it is not difficult to imagine physical processes by means of which a black hole, even starting from a slowly-rotating configuration, increases its mass and spin, eventually fulfilling the superradiant condition. The simplest possibility is provided by accretion. Astrophysical black holes are generally surrounded by an accretion disk of matter in the form of gas and plasma, and the inner edge of this disk is located in the equatorial plane at the position of the innermost stable circular orbit, $r_{\rm ISCO}$. From $r_{\rm ISCO}$, because of the pull of gravitational attraction, particles are sucked into the black hole increasing its mass and angular momentum. We can, therefore, ask the following crude question. What is the typical time scale needed to increase, via accretion, the spin of a non-rotating Schwarzschild black hole with initial mass $M_{\rm in}$ to maximally-rotating values? The accretion of a certain amount of rest mass ΔM_0 results into a change of the black hole mass M and spin J given by $\Delta J = l(z, M)\Delta M_0$ and $\Delta M = e(z)\Delta M_0$ [385, 386],[4] where $z \equiv r_{\rm ISCO}/M$,

[4] In our simplified discussion we do not include the contribution from radiation, i.e. the torque produced by photons emitted from the surface of the accretion disk. As shown in [386], radiation limits the maximum spin to $\tilde{a} \lesssim 0.998$. The inclusion of radiation is, therefore, important to prevent violation of the cosmic censorship hypothesis but it is not crucial for our argument.

$e(z)$ is the energy per unit rest mass and $l(z, M)$ is the angular momentum per unit rest mass for a particle in the vicinity of the black hole. The explicit expressions can be found in [387]. A simple algebraic manipulation leads to a first-order differential equation that can be solved with the Schwarzschild initial condition $z_{\rm in} = 6$. All in all, we find [387]

$$\tilde{a}(M) = \left(\frac{2}{3}\right)^{1/2} \frac{M_{\rm in}}{M} \left\{ 4 - \left[18 \left(\frac{M_{\rm in}}{M} \right)^2 - 2 \right]^{1/2} \right\} . \tag{4.2.25}$$

To fix ideas, Eq. (4.2.25) implies, for instance, that $\tilde{a} = 0.6$ when $M/M_{\rm in} \simeq 1.25$. Having set the relation between mass and spin, we now need an expression for the mass accretion rate. Following [388], we assume the mass accretion rate to be proportional to the Eddington rate $\dot{M} = f_{\rm Edd}\dot{M}_{\rm Edd} = f_{\rm Edd}(4\pi G_N M m_p/\eta\sigma_T)$, where η is the efficiency, m_p the proton mass and $\sigma_T \approx 1.7 \times 10^3$ GeV^{-2} the Thomson cross-section. We take $\eta = 0.1$. The reader should keep in mind that this is a very conservative estimate. It is indeed possible to imagine values of $\dot{M}$ much greater than the ones inferred by using the Eddington formula by making the accretion disk physically thick, and with low density. By integrating the mass accretion formula we find the following expression for the accretion time $t_{\rm ACC}$

$$\ln \frac{M}{M_{\rm in}} = f_{\rm Edd} \left(\frac{4\pi G_N m_p}{\eta \sigma_T} \right) t_{\rm ACC} , \tag{4.2.26}$$

where in the left-hand side the ratio $M/M_{\rm in}$ can be obtained by inverting Eq. (4.2.25). In the right panel of Fig. 4.3 we show the product $f_{\rm Edd} t_{\rm ACC}$ in years (yr) as a function of the black hole spin. As mentioned above, the computation of $t_{\rm ACC}$ is subject to some astrophysical uncertainty, and the only intent of our plot is to show that, even starting from the borderline case of a Schwarzschild black hole, it is possible to reach critical values of spin in a finite amount of time. We refer the reader to [388] for a more detailed numerical study about the interplay between accretion and superradiance, and for the rest of the chapter we will assume that the scalar cloud is not directly coupled

to the disk.

2. When the condition $a > a_{\rm crit}$ is satisfied, the black hole rapidly loses its spin favouring the growth of the axion cloud. The cloud sprouts up from an initial seed that can be simply provided by a quantum fluctuation of the vacuum, as suggested in [389]. En route, we also note that Kerr black hole itself may naturally provide a source term for the axion field. This is because the Kerr metric in Eq. (4.2.8) has non-vanishing Hirzebruch signature density $R\tilde{R}$ [390]. By explicit computation, we find

$$\frac{1}{2}R\tilde{R} \equiv \frac{1}{2}\varepsilon^{\alpha\beta\mu\nu}R_{\rho\lambda\alpha\beta}R_{\mu\nu}{}^{\rho\lambda} = \frac{\epsilon^{\alpha\beta\mu\nu}}{2\sqrt{-g}}R_{\rho\lambda\alpha\beta}R_{\mu\nu}{}^{\rho\lambda} = \frac{288\,\tilde{a}M^3\cos\theta}{r^7} + \mathcal{O}(\tilde{a}^2)\ . \tag{4.2.27}$$

$R\tilde{R}$ is proportional to the spin, and vanishes for a Schwarzschild black hole. If the electromagnetic field is quantized in a gravitational background with such property, the pseudo-scalar combination $F_{\mu\nu}\tilde{F}^{\mu\nu}$ acquires a non-vanishing expectation value $F_{\mu\nu}\tilde{F}^{\mu\nu} = R\tilde{R}/48\pi^2$ [391] which, in turn, acts like a background source term for the axion field via the usual electromagnetic coupling. After this digression, let us now go back to the growth of the axion cloud. In the left panel of Fig. 4.4 we show the superradiance rates in Eq. (4.2.20) – in units of M^{-1} – for different levels. In the small $M\mu$ limit the fastest superradiant level is the $2p$ level with $n = 0$ and $l = m = 1$. The black hole loses its spin by populating the $2p$ shell while all the remaining ones can be neglected. As already noticed in Eq. (4.2.16), this process can be as short as 10^2 s for stellar black holes.

3. The spin-down of the black hole continues until it reaches the threshold value given by Eq. (4.2.22) with $m = 1$. The imaginary part in Eq. (4.2.20) vanishes, and the spin-down process terminates. The black hole remains in this state for a period of time that can be very long. Indeed, the next $3d$ level of the axion cloud does not start being populated until a large enough number of axions dissipate from the $2p$ level. In this respect, annihilation into gravitons and annihilation into unbounded axions due to self-interactions are the most efficient processes [147]. As soon as the cloud mass drops below a critical value,

superradiance becomes operative again, and the black hole rapidly travels to the next level. As discussed in [147], the time required for an axion cloud in the $2p$ level to dissipate such that the next superradiant level can start being populated can be extremely long – specially in the small $M\mu$ limit. To give a concrete idea, the annihilation time – considering the $2p \to 3d$ transition – can be computed as follows. We start writing in full generality the time evolution of the axion population in the $2p$ level due to axion annihilation into gravitons as $dN/dt = -\Gamma_{\rm ann} N^2$. The annihilation rate $\Gamma_{\rm ann}$ is given by

$$\Gamma_{\rm ann} = \frac{1}{2\omega N^2} \int d\Omega \frac{dP}{d\Omega} \ , \tag{4.2.28}$$

where N is the number of axions and $\int d\Omega \, dP/d\Omega \equiv dE_{\rm GW}/dt$ is the energy per unit of time emitted into gravitational radiation. When the superradiance condition is satisfied the imaginary part of ω vanishes, and in the small $M\mu$ limit we have $\omega_{\rm R} \approx \mu$. The computation of $dE_{\rm GW}/dt$ cannot be performed in flat space because the leading term in the small $M\mu$ expansion accidentally cancels. We therefore use the corresponding expression derived in the Schwarzschild background metric [388]

$$\frac{dE_{\rm GW}}{dt} = \frac{484 + 9\pi^2}{23040} \left(\frac{M_S^2}{M^2}\right) (M\mu)^{14} \ , \tag{4.2.29}$$

where M_S is the mass of the axion cloud. Furthermore, since axions are non-relativistic, we can write $M_S = N\mu$. Eq. (4.2.29) is in good agreement with the computation recently performed in [392, 393] using the Teukolsky formalism in the fully relativistic regime. We can now integrate $dN/dt = -\Gamma_{\rm ann} N^2$, and find

$$N(t) = \frac{N(0)}{1 + \Gamma_{\rm ann} N(0) t} \approx \frac{1}{\Gamma_{\rm ann} t} \ . \tag{4.2.30}$$

In order to proceed further, we use the condition according to which the $3d$ level starts being populated when the number of axions in the $2p$ level drops below the value [147]

$$N \lesssim \frac{16\pi f_a^2 M^2}{(M\mu)^3} \left|\frac{\Gamma_{\rm 3d}}{\Gamma_{\rm 1s}}\right|^{1/2} \ . \tag{4.2.31}$$

The presence in Eq. (4.2.31) of the damping rate related to the level $1s$ is due to the effect of axion non-linearities. These interactions are responsible for level mixing, and introduce a superposition of the $2p$ level with the non-superradiant $1s$ mode. In our example – remember that we are considering a black hole spin such that the superradiant condition in Eq. (4.2.22) vanishes for the $2p$ level – the frequency of the $1s$ mode has a negative imaginary part, and the level is damped. In the small $M\mu$ limit we compute the rate Γ_i using the imaginary frequencies in Eq. (4.2.20). The condition derived in Eq. (4.2.31) defines, plugged into Eq. (4.2.29), the critical time scale

$$t_{\rm cr} \simeq \left(\frac{720}{484+9\pi^2}\right) \frac{M}{\pi f_a^2 (M\mu)^{12}} \left|\frac{\Gamma_{1\rm s}}{\Gamma_{3\rm d}}\right|^{1/2} \ . \tag{4.2.32}$$

In Fig. 4.4 we show the time in years to depopulate the level $2p$ for two representative value of black hole mass, $M = 50\, M_\odot$ and $M = 10^6\, M_\odot$, as a function of the axion coupling f_a and the parameter $M\mu$. From this estimate it is clear that in the small $M\mu$ limit the axion cloud can remain stuck for a very long time in the $2p$ level. It is therefore reasonable to focus on the values $l = m = 1$, $n = 0$. Motivated by these arguments, we adopt this assumption in the rest of the chapter.

There are two scales in the problem, the oscillation time $\tau_S = 1/\omega_R$ and the instability growth time scale $\tau \equiv 1/\omega_I$. In the small $M\mu$ limit we have

$$\omega_R = \mu - \frac{\mu}{2}\left(\frac{M\mu}{2}\right)^2 \approx \mu \ , \tag{4.2.33}$$

$$\omega_I = \frac{1}{48M}\left(\frac{a}{M} - 2\mu r_+\right)(M\mu)^9 \approx \frac{(M\mu)^9}{M} \ . \tag{4.2.34}$$

As a consequence

$$\frac{\tau}{\tau_S} \approx \frac{1}{(M\mu)^8} \gg 1 \quad \Longrightarrow \quad \tau \gg \tau_S \ . \tag{4.2.35}$$

We can therefore assume a stationary cloud, and write

$$\Phi(t, r, \theta, \phi) = A_0 g(\tilde{r}) \cos\left(\phi - \omega_R t\right) \sin\theta \ , \qquad A_0 \equiv A_{01} \ . \tag{4.2.36}$$

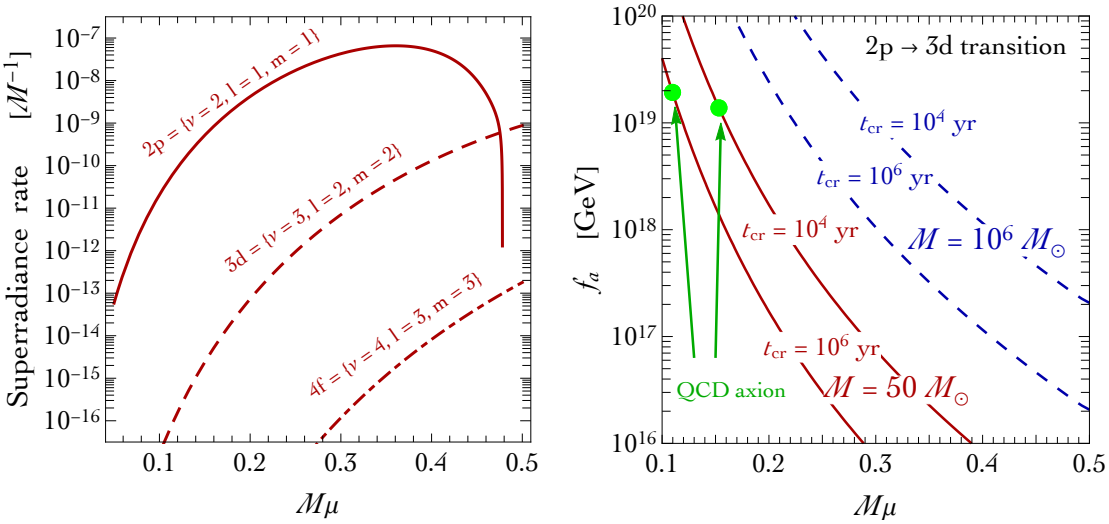

Figure 4.4: Left panel. Superradiant rates ω_I as a function of the dimensionless parameter $M\mu$ for different levels. Right panel. Time required for an axion cloud in the $2p$ level around a Kerr black hole with mass $M = 50\,M_\odot$ (red solid lines) and $M = 10^6\,M_\odot$ (blue dashed lines) to trigger a superradiant regime in the next $3d$ level as a function of the axion decay constant f_a and for different values of the parameter $M\mu$. For each $M\mu$, we compute the critical spin in Eq. (4.2.22) and the rates Γ_{1s} and Γ_{3d} using the frequencies in Eq. (4.2.20). The time scale of the transition is given by Eq. (4.2.32). For each of the two analysed black hole masses, the value of the parameter $M\mu$ fixes the axion mass μ. In the case of the QCD axion, the latter is related to a specific value of the axion decay constant f_a (see Eq. (4.3.51) below). For a stellar black hole with mass $M = 50\,M_\odot$, this correspondence is indicated in the plot with the green dots.

Notice that we focused on a real scalar cloud, since we have in mind the axions. The amplitude A_0 can be expressed in terms of the mass M_S of the scalar cloud [388]. In full generality, we write

$$M_S = \int \rho\, r^2 dr \sin\theta d\theta d\phi \ , \tag{4.2.37}$$

with $\rho = -T^0_0$. The energy density ρ can be directly computed from the definition of the stress-energy tensor

$$T^{\mu\nu}(\Phi) = (D^\mu\Phi)(D^\nu\Phi) - g^{\mu\nu}\left[\frac{g^{\rho\sigma}}{2}(D_\rho\Phi)(D_\sigma\Phi) + V(\Phi)\right] \ , \tag{4.2.38}$$

where $V(\Phi) = \mu^2\Phi^2/2$. Assuming flat space – see comment below Eq. (4.2.24) – we

find

$$\begin{aligned}\rho &= \frac{A_0^2}{2r^2}\left\{\mu^4 M^2 r^2 g'(\tilde{r})^2 \sin^2\theta\cos^2(\phi-\omega_R t)\right.\\ &+ \left. g(\tilde{r})^2\left[\cos^2(\phi-\omega_R t)\left(\cos^2\theta+\mu^2 r^2\sin^2\theta\right)+\sin^2(\phi-\omega_R t)\left(1+\omega_R^2 r^2\sin^2\theta\right)\right]\right\}\ .\end{aligned}$$

The integral in Eq. (4.2.37) can be straightforwardly computed, and we find

$$M_S = \frac{2\pi A_0^2}{3M\mu^2}\left[2\mathcal{I}_0+\mathcal{I}_2'+\frac{2\mathcal{I}_2}{M^2\mu^2}\right]\ ,\quad \mathcal{I}_n=\int_0^\infty dx\, x^n g(x)^2\ ,\quad \mathcal{I}_n'=\int_0^\infty dx\, x^n g'(x)^2\ . \tag{4.2.39}$$

In the small $M\mu$ limit we have

$$A_0^2 = \frac{3}{4\pi\mathcal{I}_2}\left(\frac{M_S}{M}\right)(M\mu)^4\ ,\quad \text{with}\quad \mathcal{I}_2=24\ . \tag{4.2.40}$$

The scalar cloud in Eq. (4.2.36) becomes

$$\Phi = \sqrt{\frac{3}{4\pi\mathcal{I}_2}\left(\frac{M_S}{M}\right)}(M\mu)^2 g(\tilde{r})\cos(\phi-\omega_R t)\sin\theta\ . \tag{4.2.41}$$

Considering for definiteness the value of the cloud at $r_{\rm cloud}$ in Eq. (4.2.24), we have

$$r_{\rm cloud}\sim\frac{4M}{(M\mu)^2}\ ,\quad \tilde{r}_{\rm cloud}\sim 4\qquad\Longrightarrow\qquad g(\tilde{r}_{\rm cloud})\sim 0.5\ . \tag{4.2.42}$$

Furthermore, notice that the function $g(\tilde{r})$ has a maximum (for $l=1$) at $\tilde{r}_{\rm max}=2$.

Before proceeding, let us comment about possible limiting factors for the size of the cloud, in particular the so-called "bosenova" collapse [147]. The physics of the bosenova collapse can be summarized as follows. In the first stage, the energy of the cloud grows by superradiant instability. As the ratio M_S/M increases, the field amplitude in Eq. (4.2.41) becomes larger – eventually saturating the condition $\Phi/f_a\sim 1$. At this point, the nonlinear self-interaction of the axion field becomes important, and causes a rapid collapse of the cloud. The analysis in [147] (see also [394] for a numerical analysis) implies the condition

$$\frac{M_S}{M}\lesssim\frac{2l^4 f_a^2}{(M\mu)^4 M_{\rm Pl}^2}\ . \tag{4.2.43}$$

In the situation where $M\mu$ is small and f_a is large, the right-hand side of Eq. (4.2.43) becomes large. In this case, the axion cloud spins down the black hole to reach the marginal superradiant condition, $\mu = m\tilde{a}/2r_+$, well before the nonlinear self-interaction becomes important. In this case, therefore, the main limiting factor is the initial rotation energy of the black hole.

Finally, we note that the typical axionic hair configurations generated by quantum effects [395–399] are usually suppressed, if compared with Eq. (4.2.41), by the factor

$$\left(\frac{M_{\rm Pl}}{M}\right)^2 \sim \frac{10^{-76}}{(M/M_\odot)^2} \ . \tag{4.2.44}$$

However, these quantum effects may act as a seed for the axion cloud (see discussion related to Eq. (4.2.27)).

4.3 Polarisation-dependent Bending of Light

The Maxwell field equations in the presence of a background axion field are

$$\vec{\nabla}\cdot\vec{E} = -g_{a\gamma\gamma}\vec{\nabla}\Phi\cdot\vec{B} \ , \tag{4.3.45}$$

$$\vec{\nabla}\times\vec{E} + \frac{\partial\vec{B}}{\partial t} = 0 \ , \tag{4.3.46}$$

$$\vec{\nabla}\times\vec{B} - \frac{\partial\vec{E}}{\partial t} = g_{a\gamma\gamma}\left(-\vec{E}\times\vec{\nabla}\Phi - \vec{B}\frac{\partial\Phi}{\partial t}\right) \ , \tag{4.3.47}$$

$$\vec{\nabla}\cdot\vec{B} = 0 \ , \tag{4.3.48}$$

where $g_{a\gamma\gamma}$ is the effective coupling defined by the Lagrangian density

$$\mathcal{L}_{a\gamma\gamma} = \frac{g_{a\gamma\gamma}}{4}\Phi F_{\mu\nu}\tilde{F}^{\mu\nu} = -\frac{g_{a\gamma\gamma}}{2}\left(\partial_\mu\Phi\right)A_\nu\tilde{F}^{\mu\nu} \ , \tag{4.3.49}$$

with $\tilde{F}^{\mu\nu} = \epsilon^{\mu\nu\rho\sigma}F_{\rho\sigma}/2$. The effective coupling $g_{a\gamma\gamma}$ can be related to the axion decay constant f_a [400]

$$g_{a\gamma\gamma} = \frac{\alpha_{\rm em}}{2\pi f_a}\left[\frac{E}{N} - \frac{2}{3}\left(\frac{4m_d + m_u}{m_d + m_u}\right)\right] = \frac{\alpha_{\rm em}}{2\pi f_a}\left(\frac{E}{N} - 1.92\right) \ , \tag{4.3.50}$$

where E/N is the model-dependent ratio of the electromagnetic and color anomaly while the second term is a model-independent contribution coming from the minimal coupling to QCD at the non-perturbative level. The typical axion window is defined by the interval $0.07 \leqslant |E/N - 1.92| \leqslant 7$ [36]. Of particular interest are the reference values $E/N = 8/3$ (as in DFSZ models [121, 122] or KSVZ [119, 120] models with heavy fermions in complete SU(5) representations) and $E/N = 0$ (as in KSVZ models with electrically neutral heavy fermions). Recently [401], the aforementioned axion window was redefined in light of precise phenomenological requirements – such as the absence of Landau poles up to the Planck scale or the need to avoid overclosure of the Universe – related to the representations of the new heavy quarks that are needed in KSVZ-type models to induce the anomalous coupling of the axion with ordinary quarks. As a result, the window $0.25 \leqslant |E/N - 1.92| \leqslant 12.25$ was singled out in the case of one single pair of new heavy fermions. Furthermore, with the inclusion of additional pairs of new heavy quarks values as large as $E/N = 170/3$ become accessible. Note that it is also possible to construct models with multiple scalars in which the value of $g_{a\gamma\gamma}$ in Eq. (4.3.50) can be made arbitrarily large. We shall further explore this possibility in Section **4.3.2**.

For the QCD axion, the axion mass and decay constant are related by [400]

$$\frac{10^{16}\,\mathrm{GeV}}{f_a} = \frac{\mu}{5.7 \times 10^{-10}\,\mathrm{eV}} \,. \tag{4.3.51}$$

Only space-time gradients of the axion field configuration alter the Maxwell equations, since for a constant axion field $\Phi F_{\mu\nu}\tilde{F}^{\mu\nu}$ becomes a perfect derivative and does not affect the equation of motion. We assume that the length scale over which Φ changes appreciably is much larger than the wavelength λ of the electromagnetic wave. Within this approximation we can neglect in Eqs. (4.3.45-4.3.48) terms containing second derivative (or first derivative squared) of Φ [402]. Let us briefly discuss the validity of this assumption. Considering the radial direction, the characteristic length scale of the cloud can be estimated using Eq. (4.2.24). The condition

on the wavelength λ reads

$$\lambda \ll r_{\rm cloud} \sim 2.6 \times 10^6 \left(\frac{10\,M_\odot}{M}\right)\left(\frac{10^{-12}\,{\rm eV}}{\mu}\right)^2\ {\rm m}\ . \tag{4.3.52}$$

From Eq. (4.2.41), the characteristic length scale of time variation is $\tau_S = 1/\omega_R$; since we are interested in the small $M\mu$ limit in which $\omega_R \simeq \mu$, we have the following condition on the wavelength λ

$$\lambda \ll \lambda_{\rm Compton} \sim 2 \times 10^5 \left(\frac{10^{-12}\,{\rm eV}}{\mu}\right)\ {\rm m}\ . \tag{4.3.53}$$

Clearly, the conditions $\lambda \ll r_{\rm cloud}$, $\lambda_{\rm Compton}$ are verified for wavelength λ of astrophysical interest. The field equations take the form [402]

$$\Box\left(\vec{E} - \frac{g_{a\gamma\gamma}}{2}\Phi\vec{B}\right) = -\frac{g_{a\gamma\gamma}}{2}\Phi\Box\vec{B}\ , \tag{4.3.54}$$

$$\Box\left(\vec{B} + \frac{g_{a\gamma\gamma}}{2}\Phi\vec{E}\right) = \frac{g_{a\gamma\gamma}}{2}\Phi\Box\vec{E}\ , \tag{4.3.55}$$

and reduce to the usual electromagnetic wave equations in the limit $g_{a\gamma\gamma} \to 0$. Photon propagation is described by the following dispersion relation [403]

$$k^4 + g_{a\gamma\gamma}^2(\partial_\mu\Phi)(\partial^\mu\Phi)k^2 = g_{a\gamma\gamma}^2\left[k_\mu(\partial^\mu\Phi)\right]^2\ , \tag{4.3.56}$$

where $k^\alpha = (E_\gamma, \vec{k})$ is the four-momentum of the propagating photon. We give a derivation of Eq. (4.3.56) in Section **4.5.2**. At the first order, we have

$$E_\gamma^2 - |\vec{k}|^2 \approx \pm g_{a\gamma\gamma}\left[E_\gamma\frac{\partial\Phi}{\partial t} - \vec{k}\cdot\vec{\nabla}\Phi\right]\ , \tag{4.3.57}$$

where the sign $\pm$ corresponds to right- and left-handed circularly polarised waves. In Eq. (4.3.57) we used a flat background metric. The gradient of the scalar field, in spherical coordinates, is

$$\vec{\nabla}\Phi = \left(\frac{\partial\Phi}{\partial r}, \frac{1}{r}\frac{\partial\Phi}{\partial\theta}, \frac{1}{r\sin\theta}\frac{\partial\Phi}{\partial\phi}\right) \stackrel{\theta=\pi/2}{\longrightarrow} \left(\frac{\partial\Phi}{\partial r}, 0, \frac{1}{r}\frac{\partial\Phi}{\partial\phi}\right)\ , \tag{4.3.58}$$

where in the last passage we restrict the analysis to the equatorial plane. Eq. (4.3.57)

reads

$$\left(\frac{dr}{d\xi}\right)^2 = E_\gamma^2 - \frac{L^2}{r^2} \mp g_{a\gamma\gamma}\left\{E_\gamma \frac{\partial\Phi}{\partial t} - \left[\left(\frac{dr}{d\xi}\right)\frac{\partial\Phi}{\partial r} + \frac{L}{r^2}\frac{\partial\Phi}{\partial\phi}\right]\right\} , \tag{4.3.59}$$

where ξ is the affine parameter while E_γ and L are, respectively, the conserved energy and angular momentum of the photon, with $k^r \equiv dr/d\xi$, $k^\theta \equiv d\theta/d\xi = 0$, $k^\phi \equiv d\phi/d\xi = L/r^2$. From Eq. (4.2.41), we have

$$\frac{\partial\Phi}{\partial t} = \sqrt{\frac{3}{4\pi\mathcal{I}_2}\left(\frac{M_S}{M}\right)}(M\mu)^2 g(\tilde{r})\omega_R \sin(\phi - \omega_R t) , \tag{4.3.60}$$

$$\frac{\partial\Phi}{\partial r} = \sqrt{\frac{3}{4\pi\mathcal{I}_2}\left(\frac{M_S}{M}\right)}(M\mu)^2 g'(\tilde{r})(M\mu)^2 \cos(\phi - \omega_R t) , \tag{4.3.61}$$

$$\frac{1}{r}\frac{\partial\Phi}{\partial\phi} = -\frac{1}{r}\sqrt{\frac{3}{4\pi\mathcal{I}_2}\left(\frac{M_S}{M}\right)}(M\mu)^2 g(\tilde{r}) \sin(\phi - \omega_R t) . \tag{4.3.62}$$

Notice that natural units can be recovered with the formal substitution $M \to G_N M$. Considering the radial distance at $\tilde{r}_{\rm max}$, we have

$$\frac{\partial\Phi}{\partial r}, \frac{1}{r}\frac{\partial\Phi}{\partial\phi} \sim (M\mu)\frac{\partial\Phi}{\partial t} \qquad \overset{M\mu\ll 1}{\Longrightarrow} \qquad \frac{\partial\Phi}{\partial t} \gg \frac{\partial\Phi}{\partial r}, \frac{1}{r}\frac{\partial\Phi}{\partial\phi} . \tag{4.3.63}$$

This relation simplifies the equation for the photon orbit in the presence of the axion background field. The differential equation for the photon orbit (see Section **4.5.3**) is

$$\frac{d\phi}{dx} = -\frac{1}{x^2\sqrt{\frac{1}{x_{\rm max}^2} - \frac{1}{x^2}}} \mp \frac{a(E_\gamma, x, \phi) - a(E_\gamma, x_{\rm max}, \frac{\pi}{2})}{2x^2 x_{\rm max}^2\left(\frac{1}{x_{\rm max}^2} - \frac{1}{x^2}\right)^{3/2}} , \quad \text{with } a(E_\gamma, r, \phi) \equiv \frac{g_{a\gamma\gamma}}{E_\gamma}\left.\frac{\partial\Phi}{\partial t}\right|_{r,\phi} , \tag{4.3.64}$$

with dimensionless variable $x \equiv r/M$ (which of course corresponds to $x \equiv r/G_N M$ in natural units), and must be integrated between $x_0 = \infty$ and $x_{\rm max} = 2/(M\mu)^2$. The choice $x_0 = \infty$ practically means that we are considering a source and an observer at distance much larger than the impact parameter (see Section **4.5.3** for a detailed discussion).

The outcome of this computation is the angular separation $|\Delta\phi_+ - \Delta\phi_-|$ between left- and right-handed circularly polarised waves that a ray of light experiences by

travelling through the axion cloud.

In the following we shall solve this equation for the QCD axion and for a generic ALP. In Section **4.4** we shall explain in more detail what is the phenomenological relevance of our computation.

4.3.1 The QCD Axion

Stellar black hole superradiance in the presence of an ultralight scalar field may produce in the next few years spectacular signatures – both direct and indirect – in gravitational wave detectors such as Advanced LIGO. Indirect signatures refer to the observation of gaps in the spin-mass distribution of final state black holes produced by binary black hole mergers. Direct signatures refer to monochromatic gravitational wave signals produced during the dissipation of the scalar condensate after the superradiant condition is saturated. In [389] it was shown that spin and mass measurements of stellar-size black holes exclude the QCD axion mass window $6 \times 10^{-13} \lesssim \mu\,[\mathrm{eV}] \lesssim 2 \times 10^{-11}$, corresponding to $3 \times 10^{17} \lesssim f_a\,[\mathrm{GeV}] \lesssim 10^{19}$. It is worth emphasizing that this bound is most likely only indicative since it is based on black hole spin measurements that are extracted indirectly from X-ray observations of accretion disks in X-ray binaries. We only have very few of such measurements at our disposal, and it is difficult to extract a bound with robust statistical confidence.

As far as direct signatures are concerned, a careful assess of the detection prospects in Advanced LIGO and LISA was recently proposed in [392, 393]. The outcome of the analysis is that, considering optimistic astrophysical models for black hole populations, the gravitational wave signal produced by superradiant clouds of scalar bosons with mass in the range

$$2 \times 10^{-13} \lesssim \mu\ [\mathrm{eV}] \lesssim 10^{-12}\ , \tag{4.3.65}$$

is observable – i.e. it is characterized by a signal-to-noise ratio larger than the experimental threshold – by Advanced LIGO. For the QCD axion the mass range in Eq. (4.3.65) corresponds to $5.7 \times 10^{18} \lesssim f_a\,[\mathrm{GeV}] \lesssim 2.8 \times 10^{19}$. In the following, we shall adopt the mass interval in Eq. (4.3.65) as benchmark for our analysis in

the case of the QCD axion. However, before proceeding, an important comment is in order. For large values of f_a non-perturbative gravitational instantons become important, as discussed in [404]. If computed in the context of General Relativity, these effects generate a gravitational correction to the axion mass that increases with f_a and, if $f_a \gtrsim 10^{16}$ GeV, overcomes the QCD term in Eq. (4.3.51). This effectively produces a lower limit on the QCD axion mass, $\mu \gtrsim 4.8 \times 10^{-10}$ eV [404]. From this perspective, the mass range in Eq. (4.3.65) is theoretically disfavoured. As discussed in [404] (see also [405] for the original formulation of the argument), the computation of non-perturbative gravitational effects – and as a consequence the validity of the lower limit on μ – can be invalidated if the UV completion of General Relativity is weakly coupled since in this case we expect new degrees of freedom to become dynamical even below $M_{\rm Pl}$. For this reason, it is important to keep investigating Planckian values of f_a since they may open an indirect window on quantum gravity effects.

The QCD axion with mass in the range given by Eq. (4.3.65) falls into the so-called "anthropic" window. The Peccei-Quinn symmetry is broken before the end of inflation, and the possibility to reproduce the observed dark matter relic density $\Omega_{\rm DM}h^2 \simeq 0.1$ relies on a fine-tuned choice of the initial misalignment angle $\theta_{\rm in}$. We find $1.19 \lesssim \theta_{\rm in} \times 10^5$ [rad] $\lesssim 3.98$ for the mass interval in Eq. (4.3.65).

We show our result in Fig. 4.5. We imagine a ray of light with energy E_γ travelling through the axion cloud, and in the left panel we plot (at fixed t) the angular splitting $|\Delta\phi_+ - \Delta\phi_-|$ as a function of E_γ and the axion mass μ. We fix $M\mu = M_S/M = 10^{-1}$, and we consider different values for the parameter E/N in Eq. (4.3.50). Since $M\mu$ is fixed, at each value of μ corresponds a black hole mass M (respectively, left and right y axis). As expected, the QCD axion is relevant in connection with stellar-mass black holes. For typical values $0 < E/N < 8/3$, we obtain an angular splitting between left and right polarisation of the order $10^{-7} < |\Delta\phi_+ - \Delta\phi_-|[\text{arcsec}] < 10^{-9}$. As we shall discuss in Section **4.4**, these values are probably too small for a detection since, even taking an optimistic view, it is not possible at present to reach angular resolutions below $\delta\theta \approx 10^{-6}$ arcsec. For the QCD axion $|\Delta\phi_+ - \Delta\phi_-| \simeq 10^{-6}$ arcsec can be obtained in the analysed parameter space for $E/N = 170/3$ (dot-dashed

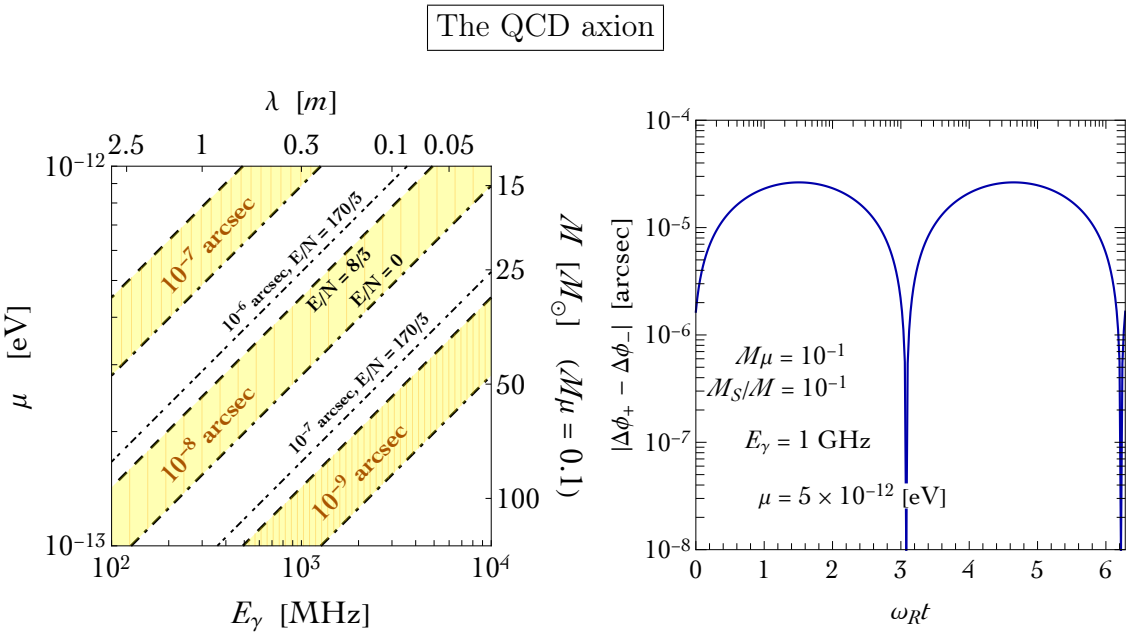

Figure 4.5: Left panel. Contours of constant angular splitting $|\Delta\phi_+ - \Delta\phi_-|$ (for fixed time t) as a function of the radio wave energy E_γ and the QCD axion mass μ. We fix $M\mu = M_S/M = 10^{-1}$, and we explore different possibilities for the electromagnetic-to-color anomaly ratio E/N in Eq. (4.3.50). Right panel. Time-dependence of the angular splitting $|\Delta\phi_+ - \Delta\phi_-|$ for fixed QCD axion mass and radio wave energy. The period of the signal is set by the inverse of $\omega_R \approx \mu$, and we have $1/\mu \approx 0.66 \times 10^{-3}\,(10^{-12}\,\text{eV}/\mu)$ s.

black lines in Fig. 4.5).

In the right panel of Fig. 4.5 we show the time-dependence of $|\Delta\phi_+ - \Delta\phi_-|$ due to the rotation of the cloud. We choose $\mu = 5 \times 10^{-12}$ eV and fixed energy $E_\gamma = 1$ GHz. The signal displays the expected periodicity set by $T = 2\pi/\omega_{\rm R} \simeq 2\pi/\mu$.

As far as the QCD axion is concerned, the relevance of the polarisation-dependent bending seems to be quite modest. The reason is that Eq. (4.3.50) and Eq. (4.3.51) imply a very strong relation between the mass of the QCD axion and its coupling to photons, and the range explored in Eq. (4.3.65) corresponds to a coupling $g_{a\gamma\gamma}$ that is too weak. However, this is not a lapidary conclusion. The way-out is that the relation between the axion mass and the axion-photon coupling can not be considered a solid prediction of QCD, in clear contrast with the relation between axion mass and axion decay constant. The latter is dictated by the minimization of the effective potential generated by the explicit breaking of the continuous global shift symmetry of the axion due to QCD instanton effects, and thus tightly linked to

the solution of the strong CP problem. The former has a degree of model-dependence – a fact already clear from the discussion about the possible values of E/N below Eq. (4.3.50) – that can be exploited. It is possible, therefore, to construct simple models in which the axion-photon coupling can be arbitrarily large without altering Eq. (4.3.51). In the next section, we shall illustrate one explicit realization of this idea.

4.3.2 The Photo-philic QCD Axion

The photo-philic ($\gamma_\heartsuit$ hereafter) QCD axion [406] is a specific realization of the clockwork mechanism proposed in [407, 408]. In its original incarnation, the clockwork is a renormalisable theory that consists in a chain of $\mathcal{N}+1$ complex scalar fields with a $\mathrm{U}(1)^{\mathcal{N}+1}$ global symmetry spontaneously broken at the scale f. The $\mathrm{U}(1)^{\mathcal{N}+1}$ global symmetry is also explicitly broken in such a way to preserve a single $\mathrm{U}(1)$ symmetry whose Nambu–Goldstone boson – eventually identified with the QCD axion in [406] – lives in a compact field space with a dimension that is set by the effective decay constant $f_a = 3^{\mathcal{N}} f \gg f$. The key idea of [406] is the following. New vector-like fermions which are responsible for the generation of the color anomaly are coupled to the last site $\mathcal{N}$ of the scalar chain. This guarantees the usual solution of the strong CP problem with the important difference that the scale $f_a = 3^{\mathcal{N}} f$ entering in Eq. (4.3.51) can be parametrically much larger than the fundamental symmetry breaking scale f. This feature has very important phenomenological consequences because the model predicts the presence of additional pseudo-scalar particles which can be light and accessible at the LHC while keeping f_a above the astrophysical bounds (roughly $f_a \gtrsim 10^9$ GeV). In the usual realization of the QCD axion presented in Section **4.3.1**, the same vector-like fermions mediating the QCD anomaly also contribute to the axion-photon coupling. In the $\gamma_\heartsuit$ QCD axion, on the contrary, there are additional electromagnetically charged vector-like fermions coupled to the site $\mathcal{M} < \mathcal{N}$ of the scalar chain. These fermions are responsible for the axion-photon coupling that is, by all accounts, disentangled from the solution of the strong CP problem. In the simplest realization proposed in [406], the $\gamma_\heartsuit$ QCD model requires the existence of a single pair of vector-like coloured fermions in the

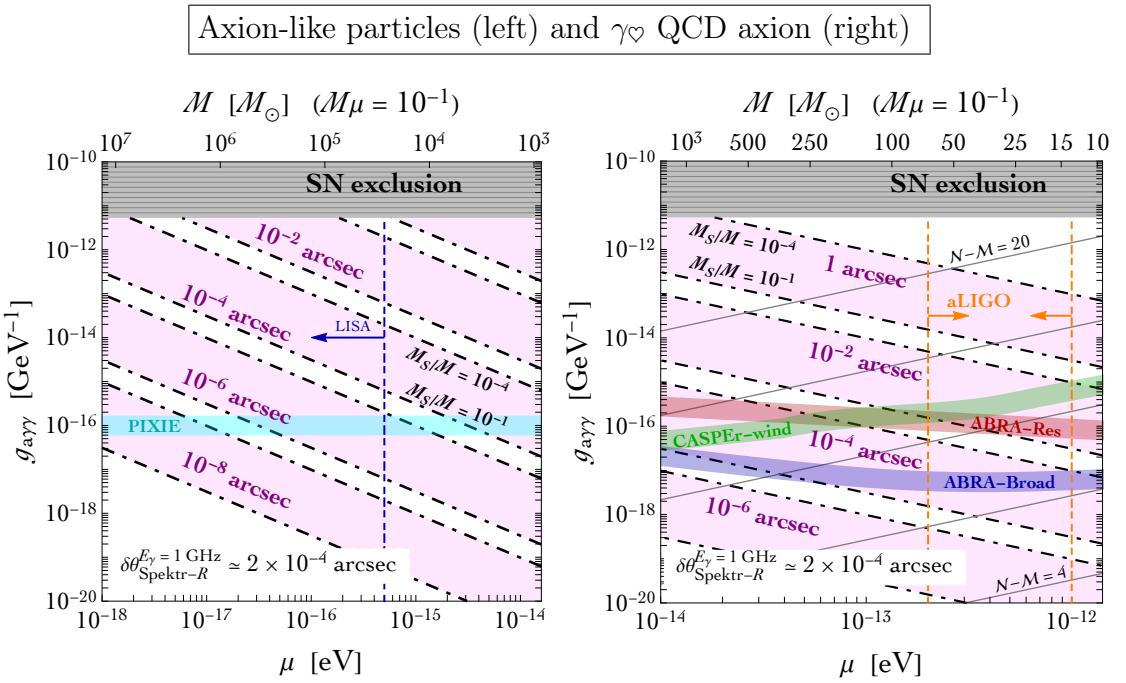

Figure 4.6: Left (right) panel. Contours of constant angular splitting for a generic ALP (the $\gamma_\heartsuit$ QCD axion) as a function of the axion mass μ and the axion-photon coupling $g_{a\gamma\gamma}$. In the case of the $\gamma_\heartsuit$ QCD axion we show the projected sensitivities of ABRACADABRA [130] and CASPEr-wind [409] together with the mass range that will be explored by the Advanced LIGO gravitational wave interferometer [392,393]. For a generic ALP, we show a projected limit for the PIXIE/PRISM experiment [410] (see text for details).

fundamental representation of $\mathrm{SU}(3)_C$ and a single pair of color neutral vector-like fermions with unit hypercharge and singlet under $\mathrm{SU}(2)_L$. Under these conditions the axion-photon coupling turns out to be [406]

$$g_{a\gamma\gamma} = \left(\frac{2}{3^{\mathcal{M}-\mathcal{N}}}\right) \frac{\alpha_{\mathrm{em}}}{2\pi f_a} \,, \tag{4.3.66}$$

and the free parameter $\mathcal{N}$, that is a fundamental parameter of the model, can be changed to make $g_{a\gamma\gamma}$, as promised, arbitrarily large.

In the right panel of Fig. 4.6 we show the result of our analysis for the $\gamma_\heartsuit$ QCD axion. We explore the parameter space (μ, $g_{a\gamma\gamma}$), and we fix $M\mu = 10^{-1}$. We enlarge the axion mass range to the interval $10^{-14} \leqslant \mu\,[\mathrm{eV}] \leqslant 10^{-12}$, and we bracket between two vertical dot-dashed orange lines the mass range covered by Advanced LIGO in Eq. (4.3.65). The above mass range corresponds to the axion decay constant $5.7 \times 10^{18} \lesssim f_a\,[\mathrm{GeV}] \lesssim 5.7 \times 10^{20}$, and in order to reproduce the observed value of

the dark matter relic abundance we need to tune the initial misalignment angle to the values $0.12 \lesssim \theta_{\rm in} \times 10^5$ [rad] $\lesssim 3.98$. We consider the axion-photon coupling in the range $10^{-20} \leqslant g_{a\gamma\gamma}$ [GeV^{-1}] $\leqslant 10^{-10}$, and the thin diagonal solid gray lines indicate – in steps of 4, from $\mathcal{N}-\mathcal{M}=4$ to $\mathcal{N}-\mathcal{M}=20$ – the values of $g_{a\gamma\gamma}$ as a function of the axion mass for different choices of $\mathcal{N}-\mathcal{M}$ in Eq. (4.3.66). Contours of constant angle $|\Delta\phi_+ - \Delta\phi_-|$ are shown with dot-dashed diagonal black lines, and the shaded area in magenta corresponds to $10^{-4} \leqslant M_S/M \leqslant 10^{-1}$. We fix $E_\gamma = 1$ GHz, and – to give an idea about the relevance of the effect – we quote the angular resolution of the Spektr-R radio telescope [411–413], $\delta\theta^{E_\gamma=1\,\rm GHz}_{\rm Spektr-R} \simeq 2\times 10^{-4}$ arcsec. We postpone to Section **4.4** a more detailed discussion about experimental prospects. The gray area is excluded by SN1987A gamma-ray limit on ultralight axion-like particles, and we use the results of the updated analysis presented in [414]. The plot shows that $|\Delta\phi_+ - \Delta\phi_-| > \delta\theta^{E_\gamma=1\,\rm GHz}_{\rm Spektr-R}$ in a wide range of the explored parameter space. We argue that the polarisation-dependent lensing computed in Section **4.3** can be relevant for the $\gamma_\heartsuit$ QCD axion. It is also important to keep in mind that the same region of parameter space is well within the sensitivity range of well-motivated proposals for future experiments. In the right panel of Fig. 4.6 we show the projected sensitivities of ABRACADABRA [130] (considering both the resonant and broadband approach) and CASPEr-wind [409]. ABRACADABRA exploits the fact that when axion dark matter encounters a static magnetic field, it sources an effective electric current that follows the magnetic field lines and oscillates at the axion Compton frequency. CASPEr-wind considers couplings of the background classical axion field which give rise to observable effects like nuclear electric dipole moment, and axial nucleon and electron moments.

4.3.3 Axion-like Particles

We now turn to discuss the more general case of ALPs. The crucial difference is that there is no *a priori* relationship between the ALP mass μ and the coupling $g_{a\gamma\gamma}$ while in the QCD axion case they are linearly related, and we can therefore treat them as independent parameters. As a result, ultralight values of μ below those explored in Section **4.3.1** and **4.3.2** are possible. We show our result in the left panel of

Fig. 4.6. In order to provide complementary information with respect to the case of the $\gamma_\heartsuit$ QCD axion, we consider the mass range $10^{-18} \leqslant \mu\ [\text{eV}] \leqslant 10^{-14}$. Since $M\mu = 10^{-1}$, this range covers from intermediate-mass to supermassive black holes. As far as the computation of $|\Delta\phi_+ - \Delta\phi_-|$ is concerned, the color code follows what already discussed in Section **4.3.2**. We delimit with a vertical dot-dashed blue line the mass range that will be explored by LISA according to the analysis proposed in [392, 393]. We find that $|\Delta\phi_+ - \Delta\phi_-| > \delta\theta^{E_\gamma=1\,\text{GHz}}_{\text{Spektr}-\text{R}}$ in a wide range of the explored parameter space, and we argue that the polarisation-dependent effect computed in Section **4.3** can be relevant also for a generic ALP. We also show a possible complementarity with future CMB tests of dark matter. The idea is that resonant conversions between CMB photons and light ALPs could result in observable CMB distortions. These resonant conversions depend on the strength of primordial magnetic fields B, and it was shown in [410] that the PIXIE/PRISM experiment [415], according to the expected sensitivity, has the capabilities to set the limit $g_{a\gamma\gamma}B \lesssim 10^{-16}$ GeV^{-1} nG for axion mass $\mu \lesssim 10^{-14}$ eV (see also [416] for a recent analysis using galaxy clusters). Assuming a strength of primordial magnetic fields close to the current upper limit $B \sim \mathcal{O}(1)$ nG [417], we show in cyan the expected limit on $g_{a\gamma\gamma}$ in Fig. 4.6.

4.4 Discussion and Outlook

The setup we have in mind is sketched in Fig. 4.7. We envisage the presence of a black hole surrounded by a scalar cloud in between an astrophysical source emitting linearly polarised light and a ground- or space-based radio telescope. An statistical analysis to quantify how likely is for this configuration to exist and the number of expected events is left for future work. Moreover, the angular splitting depends on the state of the cloud. For our study we assumed the axion cloud to be in the $2p$ level, this is because in the small $M\mu$ limit the cloud remains in that state for a long period of time.

A linearly polarised ray of light is a superposition of right- and left-handed circularly polarised waves (RCP and LCP in Fig. 4.7). By travelling trough the

scalar cloud, the two components experience a polarisation-dependent bending as discussed in the previous sections. In that event, a polarisation-dependent lensing effect would appear in the image captured by the radio telescope. Is this situation ever possible? In this section, we shall explore in more detail some of the necessary conditions needed to realize this idea.

4.4.1 General Remarks: Dual-polarisation Receiver and VLBI

Consider an electromagnetic wave travelling in the $\hat{z}$ direction. In general, light is elliptically polarised and can be described by means of the electric field

$$\vec{E}_{\rm EP} = E_x^{(0)} \cos(kz - \omega t)\hat{x} + E_y^{(0)} \cos(kz - \omega t + \delta)\hat{y} \equiv E_x\hat{x} + E_y\hat{y} \ . \tag{4.4.67}$$

The case $\delta = 0$ corresponds to linear polarisation whereas the conditions $\delta = \pm\pi/2$, $E_x^{(0)} = E_y^{(0)}$ describe, respectively, a right and left circularly polarised wave. The relevant observable in astrophysics is the light intensity rather than field amplitude. For this reason it is useful to introduce the four Stokes parameters [418]

$$\mathfrak{I} = \langle E_x^2 \rangle + \langle E_y^2 \rangle \ , \quad \mathfrak{Q} = \langle E_x^2 \rangle - \langle E_y^2 \rangle \ , \quad \mathfrak{U} = 2\langle E_x E_y \cos\delta \rangle \ , \quad \mathfrak{V} = 2\langle E_x E_y \sin\delta \rangle \ , \tag{4.4.68}$$

where $\langle \cdots \rangle$ denotes a time average over times much larger than $2\pi/\omega$. The parameter $\mathfrak{I}$ measures the intensity of the wave, $\mathfrak{Q}$ and $\mathfrak{U}$ fully describe linear polarisation, and $\mathfrak{V}$ corresponds to circularly polarised intensity. In particular, a net right (left) polarisation has a positive (negative) $\mathfrak{V}$.

The radio emission from most bright radio sources arises from synchrotron radiation, and it is linearly polarised. Qualitatively speaking, the reason is the following. The radiation from a single relativistic electron gyrating around a magnetic field is elliptically polarised. For an ensemble of electrons with a smooth distribution of pitch angles the opposite senses of elliptical polarisation will cancel out, resulting in linearly polarised radiation. This is in particular true in the case of synchrotron emission from Active Galactic Nuclei (AGN) observed at radio frequencies. This is, therefore, the class of astrophysical sources that might be well-suited for our

purposes.

Next, we need a radio telescope able to distinguish between left and right polarisations with sufficiently high angular resolution. Polarisation-dependent measurements are possible if the instrument is a dual-polarisation receiver. In a nutshell, such telescope can be thought of as a cross of two dipoles aligned along orthogonal directions. Each of the two dipoles measures the corresponding polarisation component and converts it into an electric signal. The signals are auto-correlated and cross-correlated, thus allowing for a reconstruction of the Stokes parameters. We would like to stress that all four Stokes parameters are actual intensities. This means that they can be used at the level of image analysis in order to reconstruct and visualize the polarisation of the observed source. This makes the detection of our effect, at least in principle, possible. Furthermore, we remind that the time average implied in the measurement of the Stokes parameters refers to a time interval Δt much larger than the typical wavelength λ of the observed light. If the condition $\lambda \ll \Delta t \ll \lambda_{\rm Compton}$ is satisfied, it could even be possible to detect the time variation of the signal.

Let us now comment on the angular resolution. The angular resolution $\delta\theta$ of a telescope can be calculated from the wavelength of observed radio waves λ and the diameter D of the telescope

$$\delta\theta \approx 2.5 \times 10^5 \, \frac{\lambda}{D} \text{ arcsec} \, . \tag{4.4.69}$$

To fix ideas, a radio telescope with $D = 65$ m observing radio wavelengths at $E_\gamma = 1$ GHz ($\lambda \approx 0.3$ m) has an angular resolution $\delta\theta \approx 10^3$ arcsec. The angular resolution of a typical radio telescope is, therefore, by far too low to detect the effect computed in Section **4.3**. However, it is possible to use multiple radio telescopes at the same time, a technique that is called interferometry. The angular resolution is greatly improved because – by synchronizing and combining observations from all the telescopes of the array, each one equipped by its own atomic clock – one effectively creates a single telescope as large as the distance between the two farthest telescopes. This simple principle lies at the heart of the very-long-baseline interfer-

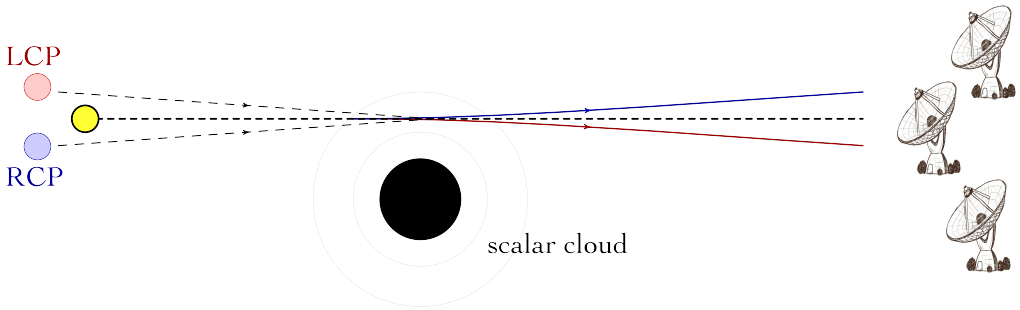

Figure 4.7: Sketch of the typical configuration needed to detect the polarisation-dependent bending discussed in Section **4.3**. Linearly polarised light is emitted from an astrophysical source, e.g. an active galactic nuclei. Travelling through the axion scalar cloud surrounding a Kerr black hole, the left and right circular components (LCP and RCP) experience different deflection angles thus creating a polarisation-dependent lensing that could be observed by an array of radio telescopes using the VLBI technique.

ometry (VLBI) technique, in which a signal from an astronomical radio source is collected from multiple radio telescopes on Earth. VLBI gives angular resolutions of the order of $\delta\theta \approx 10^{-3}$ arcsec or better, thus making our speculations about a possible detection more realistic.

A further improvement can be obtained by combining a VLBI array with an additional antenna placed on board of a satellite orbiting the Earth. As a benchmark reference, let us consider the case of the Russian project Spektr-R [411–413]. Spektr-R (formerly RadioAstron) is a dual-polarisation receiver space-based 10 meter radio telescope in a highly apogee orbit around the Earth, launched on July 2011. Spektr-R works in conjunction with some of the largest ground-based radio telescopes, and the system forms an interferometric baseline extending up to 3×10^5 km [411–413]. This configuration is able to reach an astonishing angular resolution up to a few millionths of an arcsecond. As a reference, in Fig. 4.6 we quote the typical angular resolution of Spektr-R at $E_\gamma = 1$ GHz, that is about $\delta\theta \approx 2 \times 10^{-4}$ arcsec.

In conclusion, we argue that radio astronomy techniques have the capabilities to detect the polarisation-dependent bending discussed in Section **4.3**, if realized in nature. Of course, for the aim of the present work our discussion is purely qualitative, and our intent is that of stimulating the interplay with the radio astronomy community to fully understand the validity of our conclusions.

4.4.2 Comparison with "Background" Effects

Scintillation is an optical effect arising when light rays emitted by a compact source pass through a turbulent ionized medium. As far as radio frequencies are concerned, scintillation theory can be applied to the turbulent interstellar medium (ISM) of the Galaxy through angular and pulse broadening of pulsars [419–421], and to the turbulent intergalactic medium (IGM) through quasar observations [422–424].

Interstellar scattering of an extragalactic source of radio waves results in angular broadening. It is, therefore, important to keep in mind the typical size of this effect since it acts as a sort of "background" for the polarisation-dependent effect discussed in Section **4.3**. If the angular broadening proves to be much larger than the angular splitting $|\Delta\phi_+ - \Delta\phi_-|$, we expect the latter to be clouded by the former.

The size of the broadening of an extragalactic source at redshift z_S due to the IGM – modelled as a thin-screen at redshift z_L with homogeneous Kolmogorov turbulence – is [425]

$$\theta_{\rm scat} \sim 19.75\ {\rm SM}^{3/5} \left(\frac{D_{\rm LS}}{D_{\rm S}}\right) \left(\frac{E_\gamma}{1\,{\rm GHz}}\right)^{-2.2} (1+z_L)^{-1.2}\, 10^{-3}\,{\rm arcsec}\ , \qquad (4.4.70)$$

where $D_{\rm LS}$ ($D_{\rm S}$) is the angular diameter distance between the scattering region and the source (between the observer and the source). The angular diameter distance at redshift z is given by the integral

$$D(z) = cH_0^{-1}(1+z)^{-1} \int_0^z \left[\Omega_\Lambda + (1-\Omega)(1+z')^2 + \Omega_m(1+z')^3 + \Omega_r(1+z')^4\right]^{-1/2} dz'\ , \qquad (4.4.71)$$

where H_0 is the Hubble constant, $\Omega = \Omega_\Lambda + \Omega_m + \Omega_r$, and Ω_Λ, Ω_m, Ω_r are, respectively, the ratios of the dark energy density, matter density and radiation density to the critical density of the Universe. We assume Standard Cosmology, with $\Omega = 1$, $\Omega_\Lambda = 0.7$, and $\Omega_r = 0$. In Eq. (4.4.70) we introduced the short-hand notation $D(z_i) \equiv D_i$. We use $H_0 = 67.8 \pm 0.9$ (km/s)/Mpc [37]. Notice that – defining the angular diameter distance between the observer and the scattering region as $D_{\rm L}$ – we have in general $D_{\rm LS} \neq D_{\rm S} - D_{\rm L}$. In Eq. (4.4.70), the scattering measure SM encodes the level of turbulence of the IGM, and can be defined as the line-of-sight

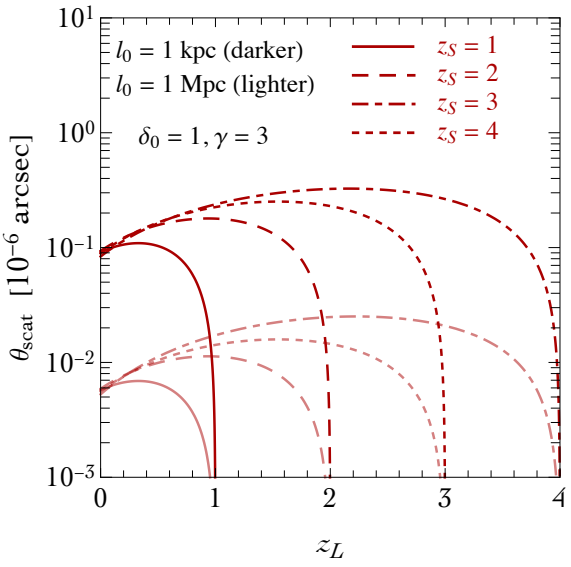

Figure 4.8: Angular broadening in the IGM at $E_\gamma = 1$ GHz for a screen at redshift z_L.

integral of the spectral coefficient characterizing the power spectrum of electron density fluctuations. Following [425], we have $\mathrm{SM} = C_{\rm SM}\, F\, n_e^2(z)\, D_S$. The constant $C_{\rm SM}$ takes the value $C_{\rm SM} = 1.8\,\mathrm{m}^{-20/3}\,\mathrm{cm}^6$, $n_e(z)$ is the electron density at redshift z, and the fluctuation parameter is $F = (\zeta\epsilon^2/\eta)(l_0/1\,\mathrm{pc})^{-2/3}$ [419] where l_0 is the outer scale of the turbulence, η is the filling factor of the turbulent medium, ϵ is the variance of the electron density fluctuations within a single cloud, and ζ is a measure of fluctuations in the mean density between clouds. We assume in our estimate $\epsilon \sim \zeta \sim \eta \sim 1$ for all redshifts. This choice implies that the turbulence is fully developed at all redshifts of interest. The outer scale length of turbulence l_0 defines an upper cut off in the size of turbulent structures, and we consider the two benchmark values $l_0 = 1$ kpc, $l_0 = 1$ Mpc. The mean free electron density as a function of the redshift is given by $n_e(z) = \delta_0\, x_e(z)\, n_e(0)\, (1+z)^\gamma$, where $x_e(z)$ is the ionization fraction, and $n_e(0) = 2.1 \times 10^{-7}$ cm^{-3} is the mean free electron density at $z = 0$. We assume a significant ionized fraction, $x_e(z) \sim 1$, for all redshifts of interest. The parameter δ_0 controls possible electron overdensity while $\gamma \sim 3$ for IGM components with constant comoving densities. For simplicity, we take $\delta_0 = 1$. The presence of possible electron overdensity results in a rescaling of Eq. (4.4.70) according to the factor $\delta_0^{6/5}$. In Fig. 4.8 we show the angular broadening predicted

by Eq. (4.4.70) at $E_\gamma = 1$ GHz for a screen of ionized medium at redshift z_L. We consider four different source locations, at $z_S = 1, 2, 3, 4$, and two possible choices for the outer scale of the turbulence l_0 (see caption for details). The scattering angle ranges between $10^{-9} \lesssim \theta_{\rm scat} \lesssim 10^{-7}$ arcsec for $1\,{\rm kpc} \lesssim l_0 \lesssim 1\,{\rm Mpc}$. We notice that the scattering broadening in the medium hosted by the background source (i.e. considering scattering screens located at $z_L \simeq z_S$) drops to negligible values. Finally, changing the spectral index γ results in a different z_L dependence of the scattering angle, but it does not alter the order of magnitude estimate of the broadening effect.

Given the model-dependence and the astrophysical uncertainties entering in the computation of the angular broadening, no firm conclusion can be established. Nevertheless, the order-of-magnitude estimate proposed in this section keeps alive the hope of detecting the polarisation-dependent bending due to a superradiant axion cloud.

4.4.3 Faraday Rotation

Finally, let us close this section with a short discussion about another important effect that is usually relevant in the presence of an optically active medium: Faraday rotation.

Consider a beam of light linearly polarised along the $\hat{x}$ axes

$$\vec{E}_{\rm LP} = E_0 \cos(kz - \omega t)\hat{x} \ , \qquad \text{with} \quad k = 2\pi/\lambda \ , \ \omega = 2\pi\nu \ . \tag{4.4.72}$$

A linearly-polarised wave can be decomposed into a sum of left- and right-circularly polarised waves at the same frequency

$$\vec{E}_{\rm LP} = \frac{\vec{E}_{\rm RCP} + \vec{E}_{\rm LCP}}{2} \ , \quad \text{with} \quad \vec{E}_{\rm RCP,LCP} = E_0 \left[\cos(kz - \omega t)\hat{x} \pm \sin(kz - \omega t)\hat{y}\right] \ . \tag{4.4.73}$$

Imagine this beam enters a region characterized by the presence of a medium which has slightly different propagation velocities for light with opposite circular polarisations. Upon exiting this region, the left- and right-circular polarisation modes have

picked up a net phase difference

$$\vec{E}_{\rm RCP,LCP} = E_0 \left[\cos(kz - \omega t + \delta_{\rm R,L})\hat{x} \pm \sin(kz - \omega t + \delta_{\rm R,L})\hat{y}\right] \tag{4.4.74}$$

which causes their sum to still be linearly-polarised, but along a different axis. Indeed the sum $\vec{E}_{\rm LP} = (\vec{E}_{\rm RCP} + \vec{E}_{\rm LCP})/2$

$$\vec{E}_{\rm LP} = E_0 \left[\cos\left(\frac{\delta_{\rm R} - \delta_{\rm L}}{2}\right)\hat{x} + \sin\left(\frac{\delta_{\rm R} - \delta_{\rm L}}{2}\right)\hat{y}\right] \cos\left(kz - \omega t + \frac{\delta_{\rm R} + \delta_{\rm L}}{2}\right) , \tag{4.4.75}$$

describes a plane polarised wave with the polarisation direction twisted by an angle $\Delta \equiv (\delta_{\rm R} - \delta_{\rm L})/2$ from the x-axis towards the y-axis. This is the Faraday rotation.

The parity violating interaction in Eq. (4.1.6) may induce Faraday rotation for a beam of light travelling through the axion cloud. We can estimate the size of such effect by considering a wave travelling a distance $L \sim r_{\rm cloud}$ in the equatorial plane at radial distance $r \sim r_{\rm max}$. The change in phase of a circularly polarised mode travelling a distance L is $\delta = L|\vec{k}|$. From Eq. (4.3.57), and considering the approximation discussed in Eq. (4.3.63), at the linear order in $g_{a\gamma\gamma}$ we have $|\vec{k}| \approx E_\gamma \mp (g_{a\gamma\gamma}/2)\partial\Phi/\partial t$. We therefore find the estimate $\Delta = L(g_{a\gamma\gamma}/2)\, \partial\Phi/\partial t|_{r=r_{\rm max}}$ where for simplicity we assumed a constant cloud (with value fixed at $r = r_{\rm max}$) along the distance L. We also neglected the trigonometric factor that is responsible for the rotation of the cloud. This estimate should be therefore considered as an order-of magnitude upper limit for the effect. For the QCD axion and for a generic ALP we find

$$\begin{aligned}
\Delta_{\rm QCD} &= 2 \times 10^{-5} \left(\frac{E}{N} - 1.92\right) \left(\frac{\mu}{10^{-12}\,{\rm eV}}\right) \left(\frac{M_S/M}{0.1}\right)^{1/2} \left(\frac{M\mu}{0.1}\right) \ {\rm rad} \ , \\
\Delta_{\rm ALP} &= 10 \left(\frac{g_{a\gamma\gamma}}{10^{-16}\,{\rm GeV}^{-1}}\right) \left(\frac{M_S/M}{0.1}\right)^{1/2} \left(\frac{M\mu}{0.1}\right) \ {\rm rad} \ .
\end{aligned} \tag{4.4.76}$$

Our Galaxy is full of ionized hot gas, and is simultaneously permeated by a large-scale magnetic field. The Faraday effect due to this plasma is observed in the polarised signal from radio pulsars within our Galaxy, and on all extragalactic radio sources. The subtlety is that we do not know the original plane of polarisation.

As a consequence, the effect is almost always studied as a function of frequency. In this case the Faraday rotation has the simple form $\Delta = \mathrm{RM}\,\lambda^2$, where λ is the wavelength of the observed light and RM is the rotation measure which in general depends on the interstellar magnetic field and the number density of electrons along the propagation path. In the idealized case, one can determine the RM by measuring Δ at different wavelengths, and then performing a linear fit. From the value of RM, one can in turn try to decrypt the physical conditions along the lines of sight.

The effect proposed in Eqs. (4.4.76) does not feature any energy dependence. Without knowing the original direction of polarisation, therefore, a possible detection of this effect seems hopeless. One possibility is to exploit the time-dependence of the signal, similar to the one discussed in the right panel of Fig. 4.5, that should give rise to a time-dependent oscillating effect with period set by $1/\mu$.

Another interesting aspect is to consider as a source of light the accretion disk surrounding the black hole (instead of a distant source as done in Section **4.4**). Gravitational and frictional forces compress and raise the temperature of the material in the disk, thus causing the emission of electromagnetic radiation that should travel through the axion cloud before escaping.

We do not explore further such possibilities, and we postpone a more detailed investigation to future work.

4.5 Details of the Calculation

4.5.1 Radial Eigenfunctions and Rotating Axion Cloud

The radial Eq. (4.2.11) admits two well-defined limits in the near- and far-horizon region. In the far-horizon region, defined by the condition $r \gg M$, $\Delta \simeq r^2(1 - 2M/r)$, the radial equation reduces to

$$\frac{d^2(\tilde{r}R_{\rm far})}{d\tilde{r}^2} + \left[-\frac{1}{4} + \frac{l+n+1}{\tilde{r}} - \frac{l(l+1)}{\tilde{r}^2}\right]\tilde{r}R_{\rm far} = 0\ , \tag{4.5.77}$$

with $R_{\rm far}$ function of $\tilde{r}$ defined accordingly to Eq. (4.2.23). This is the same equation describing an electron in the hydrogen atom, thus enforcing the analogy with Quantum Mechanics. Eq. (4.5.77) can be solved in terms of confluent hypergeometric function

$$R_{\rm far}(\tilde{r}) = \tilde{r}^l e^{-\tilde{r}/2} {}_1F_1(l+1-\nu;\, 2l+2;\, \tilde{r}) \ , \tag{4.5.78}$$

with $\nu = l + n + 1$ the principal quantum number. The confluent hypergeometric function is given in terms of the Laguerre polynomial by

$$\mathrm{L}_n^m(x) = \frac{(m+n)!}{m!n!} {}_1F_1(-n;\, m+1;\, x) \ , \tag{4.5.79}$$

and Eq. (4.5.78) reproduces the radial function used in Eq. (4.2.23) that is, therefore, strictly valid only in the far-horizon limit. In the near-horizon region, defined by $0 < r - r_+ \ll (l/M\mu)^2 M$, the radial equation is solved by [147]

$$R_{\rm near}(r) = \left(\frac{r-r_+}{r-r_-}\right)^{-iP} {}_2F_1\left(-l;\, l+1;\, 1+2iP;\, \frac{r-r_-}{r_+-r_-}\right) \ , \quad P \equiv 2r_+\left(\frac{\omega - m\Omega_+}{r_+-r_-}\right) \ , \tag{4.5.80}$$

where the angular velocity of the black hole horizon is $\Omega_H = \tilde{a}/2r_+$.

The eigenvalue problem for the radial equation can be solved by means of the continued fraction method championed in [426] (see also [427], and [428] for a pedagogical review about modern black hole perturbation theory). In a nutshell, we look for a radial solution of the form

$$R(r) = (r-r_+)^{-i\sigma}\,(r-r_-)^{i\sigma+\chi-1}\, e^{-r\sqrt{\mu^2-\omega^2}} \sum_{n=0}^{\infty} a_n \left(\frac{r-r_+}{r-r_-}\right)^n \ , \tag{4.5.81}$$

with

$$\sigma = \frac{2Mr_+}{r_+-r_-}(\omega - m\Omega_H) \ , \qquad \chi = \frac{M(2\omega^2-\mu^2)}{\sqrt{\mu^2-\omega^2}} \ . \tag{4.5.82}$$

Note that this ansatz correctly describes the characteristic asymptotic behaviour of bound states. Using this expression for $R(r)$, the radial equation returns a three-term recurrence relation for the coefficients a_n that can be solved only for particular values of $\omega = \omega_R + i\omega_I$. These are the eigenfrequencies describing bound states. We implement numerically the continued fraction method, and we show in Fig. 4.9

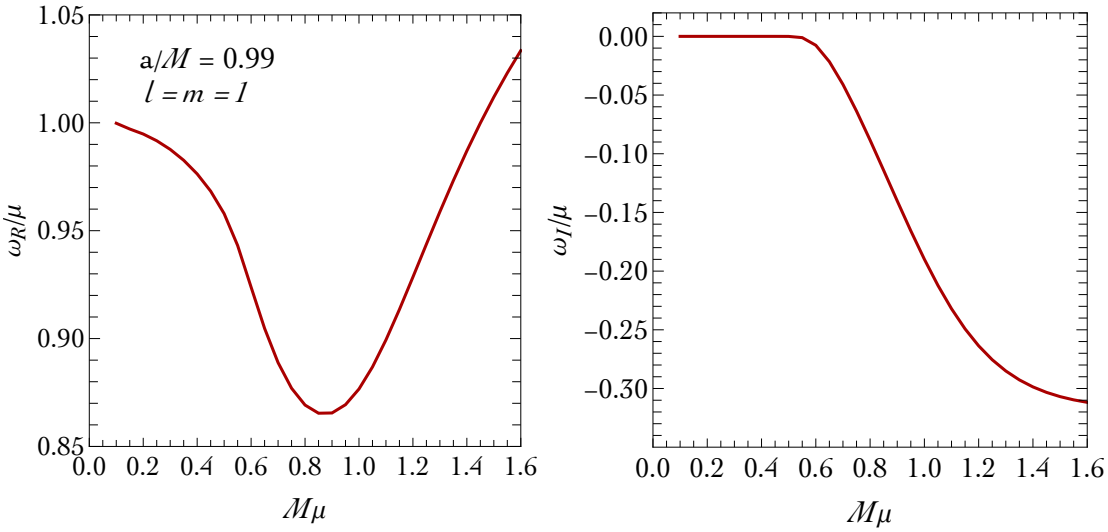

Figure 4.9: Real and imaginary part (left and right panel, respectively) of the bound state frequencies for a scalar field in a Kerr background, as a function of the dimensionless parameter $M\mu$. We fix the spin parameter $a/M = 0.99$, and we focus on the eigenmode with $l = m = 1$. We solved numerically Eq. (4.2.11), and we used the Leaver's method to obtain the bound state frequencies when $M\mu \sim 1$ [427].

the values of ω_R (left panel) and ω_I (right panel) obtained by solving the eigenvalue problem for the radial equation. In the small $M\mu$ limit, the agreement with the approximation used in Eqs. (4.2.19, 4.2.20) is evident. Having computed the bound state frequencies, the full radial eigenfunction can be obtained from Eq. (4.5.81). We show our numerical solution in Fig. 4.10, and we comment about the comparison with the far-horizon approximation (see caption for details).

Finally, it is possible to reconstruct the full solution of the Klein-Gordon equation in Eq. (4.2.9) by including the angular- and time-dependent part. For completeness, we show the full solution in the equatorial plane in Fig. 4.11 (see caption for details).

4.5.2 Modified Dispersion Relation

In this section we derive the dispersion relation in Eq. (4.3.56). From the Lagrangian density

$$\mathcal{L} = -\frac{1}{4} F_{\mu\nu} F^{\mu\nu} - \frac{g_{a\gamma\gamma}}{2} \left(\partial_\mu \Phi\right) A_\nu \tilde{F}^{\mu\nu} \ , \tag{4.5.83}$$

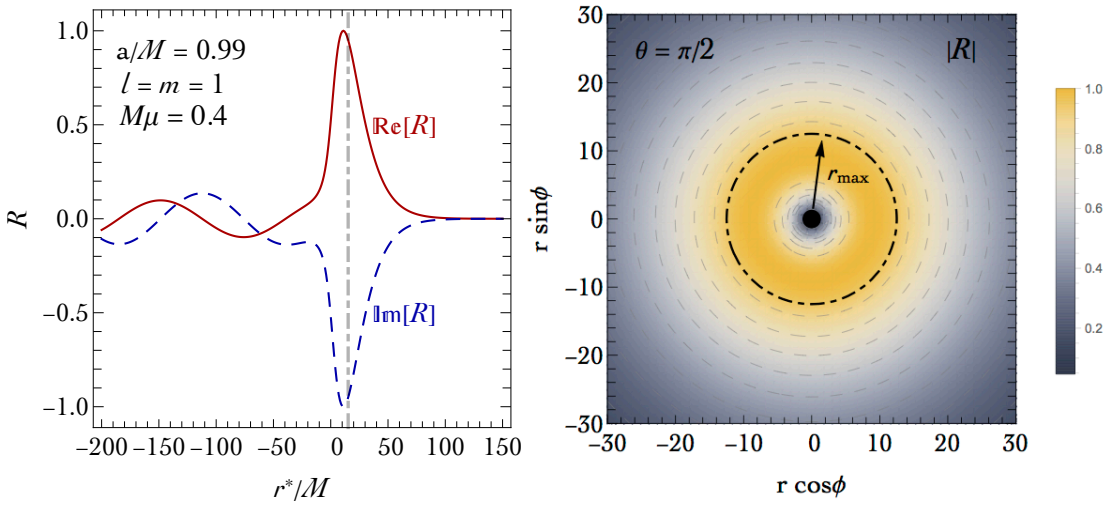

Figure 4.10: Left panel. Real (red, solid line) and imaginary (blue, dashed line) part of the radial eigenfunction R with $l = m = 1$ as a function of the tortoise coordinate r^* obtained numerically using the Leaver's method [427]. For comparison, the vertical gray dot-dashed line indicates at $r^*/M \simeq 15.2$ indicates the position of $\tilde{r}_{\rm max} = 2$ in terms of the tortoise coordinate. Right panel. Density plot of the absolute value $|R|$ (arbitrarily normalized to 1 at the maximum) in the equatorial plane $\theta = \pi/2$. The black dot-dashed circle indicates the location of $\tilde{r}_{\rm max} = 2$ obtained using the analytical approximation in Eq. (4.2.23).

we extract the Euler-Lagrange equations of motion

$$\left[g^{\mu\nu}\Box - g_{a\gamma\gamma}\epsilon^{\mu\nu\alpha\beta}(\partial_\alpha\Phi)\partial_\beta\right] A_\nu(x) = 0, \tag{4.5.84}$$

which, in Fourier space, give

$$\left[g^{\mu\nu}k^2 + ig_{a\gamma\gamma}\epsilon^{\mu\nu\alpha\beta}(\partial_\alpha\Phi)k_\beta\right] \tilde{A}_\nu(k) \equiv K^{\mu\nu}\tilde{A}_\nu(k) = 0\ . \tag{4.5.85}$$

In Eq. (4.5.85) we neglected the second derivative term proportional to $g_{a\gamma\gamma}(\partial_\mu\partial_\rho\Phi)A_\sigma\epsilon^{\rho\sigma\mu\nu}$, in analogy with the discussion in Section **4.3**. We introduce the short-hand notation $\eta_\alpha \equiv g_{a\gamma\gamma}(\partial_\alpha\Phi)$. In order to solve Eq. (4.5.85) we define the operator $S^\mu{}_\nu \equiv \epsilon^{\lambda\mu\alpha\beta}\eta_\alpha k_\beta \epsilon_{\lambda\nu\rho\sigma}\eta^\rho k^\sigma$. The Levi-Civita contraction property

$$\epsilon_{i_1,\ldots,i_k,i_{k+1},\ldots,i_n}\epsilon^{i_1,\ldots,i_k,j_{k+1},\ldots,j_n} = (-1)\,k!\,\delta^{j_{k+1},\ldots,j_n}_{i_{k+1},\ldots,i_n}\,, \qquad \text{with} \quad \delta^{\mu_1,\ldots,\mu_p}_{\nu_1,\ldots,\nu_p} \equiv \begin{vmatrix} \delta^{\mu_1}_{\nu_1} & \ldots & \delta^{\mu_1}_{\nu_p} \\ \vdots & \ddots & \vdots \\ \delta^{\mu_p}_{\nu_1} & \ldots & \delta^{\mu_p}_{\nu_p} \end{vmatrix}\,, \tag{4.5.86}$$

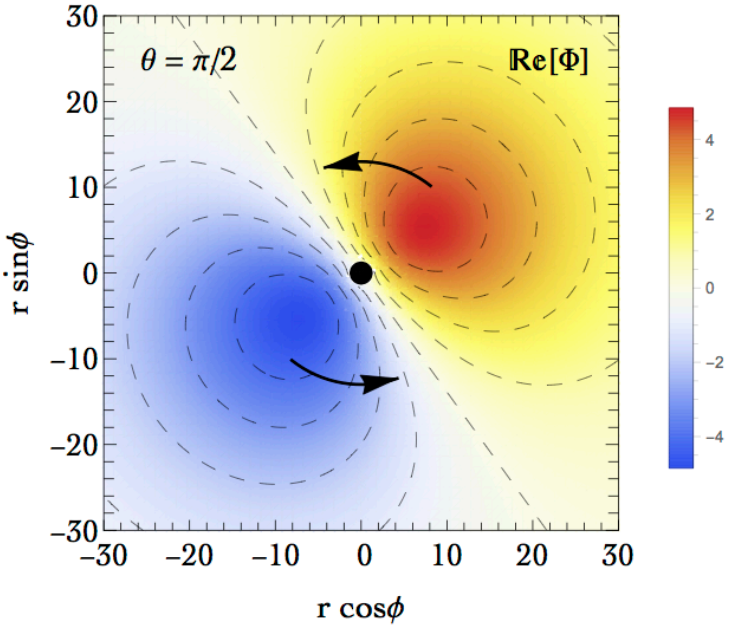

Figure 4.11: Density plot of the axion cloud $\mathrm{Re}\,[\Phi] = \mathrm{Re}\,\left[e^{im\phi}S_{lm}(\theta)e^{-i\omega t}R_{nl}(r)\right]$ with $n = 0$, $l = m = 1$ in the equatorial plane. We consider the explicit case with $a/M = 0.99$, $M\mu = 0.4$, and we take for reference $t = 0$. As time passes by, the axion cloud rotates anti-clockwise in the direction of the black arrows. The period is $T = 2\pi/\omega_R$.

gives the explicit expression

$$S^{\mu\nu} = g^{\mu\nu}\left[(\eta\cdot k)^2 - \eta^2 k^2\right] - \eta\cdot k\,(\eta^\mu k^\nu + \eta^\nu k^\mu) + k^2\eta^\mu\eta^\nu + \eta^2 k^\mu k^\nu\ , \qquad (4.5.87)$$

with the following properties

$$S^{\mu\nu}k_\nu = S^{\mu\nu}\eta_\nu = 0\ , \quad S \equiv S^\mu{}_\mu = 2\left[(\eta\cdot k)^2 - \eta^2 k^2\right]\ , \quad S^{\mu\nu}S_{\nu\lambda} = \frac{S}{2}S^\mu{}_\lambda\ . \qquad (4.5.88)$$

We can define the two projectors

$$\mathcal{P}^{\mu\nu}_{\pm} \equiv \frac{S^{\mu\nu}}{S} \mp \frac{i}{\sqrt{2S}}\epsilon^{\mu\nu\alpha\beta}\eta_\alpha k_\beta\ . \qquad (4.5.89)$$

This is a good definition, since we have the following properties

$$\mathcal{P}^{\mu\lambda}_{\pm}\mathcal{P}_{\pm\,\lambda\nu} = \mathcal{P}_{\pm\,\nu}^{\ \ \mu}\ , \quad \mathcal{P}^{\mu\lambda}_{\pm}\mathcal{P}_{\mp\,\lambda\nu} = 0\ . \qquad (4.5.90)$$

Furthermore, $\mathcal{P}^{\mu\nu}_{\pm} k_\nu = \mathcal{P}^{\mu\nu}_{\pm} \eta_\nu = 0$, $g_{\mu\nu}\mathcal{P}^{\mu\nu}_{\pm} = 1$, and $\mathcal{P}^{\mu\nu}_{+} + \mathcal{P}^{\mu\nu}_{-} = 2S^{\mu\nu}/S$. The operator in Eq. (4.5.85) becomes

$$K^{\mu\nu} = g^{\mu\nu}k^2 + \sqrt{\frac{S}{2}}\left(\mathcal{P}^{\mu\nu}_{-} - \mathcal{P}^{\mu\nu}_{+}\right) \ . \tag{4.5.91}$$

We now have all the ingredients to derive a dispersion relation from Eq. (4.5.85). We start from a space-like unit vector, for example $\varepsilon = (0, i, 1, 0)/\sqrt{2}$. We then define the two projections $\tilde{\varepsilon}^{\mu}_{\pm} \equiv \mathcal{P}^{\mu\nu}_{\pm}\varepsilon_\nu$. From the properties of the projectors it follows that

$$K^{\mu\nu}\tilde{\varepsilon}_{\pm\,\nu} = \left[k^2 \mp \sqrt{\frac{S}{2}}\right]\tilde{\varepsilon}^{\mu}_{\pm} \ . \tag{4.5.92}$$

Therefore, $\tilde{A}^\mu = \tilde{\varepsilon}^{\mu}_{\pm}$ is a solution of Eq. (4.5.85) if and only if $k^2 = \pm\sqrt{S/2}$, or

$$k^4 + \eta^2 k^2 = (\eta \cdot k)^2 \ , \tag{4.5.93}$$

that is the modified dispersion relation presented in Eq. (4.3.56). Since the limit $g_{a\gamma\gamma} \to 0$ should recover the standard parity-invariant propagation in which there is no difference in the physical properties of a right- and a left-handed circularly polarised electromagnetic wave, it is natural to identify the two distinct solutions arising in the case $g_{a\gamma\gamma} \neq 0$ as the two different circular polarisations.

4.5.3 Equation for the Photon Orbit

Let us start from Eq. (4.3.59) in Schwarzschild background

$$\left(\frac{dr}{d\xi}\right)^2 = E_\gamma^2 - \frac{L^2}{r^2}\left(1 - \frac{2M}{r}\right) \mp g_{a\gamma\gamma}E_\gamma\frac{\partial\Phi}{\partial t} \ . \tag{4.5.94}$$

The equation for the photon orbit is given by

$$\frac{d\phi}{dr} = \frac{d\phi}{d\xi}\frac{d\xi}{dr} = \pm\frac{1}{r^2\sqrt{\frac{E_\gamma^2}{L^2}\left(1 \mp \frac{g_{a\gamma\gamma}}{E_\gamma}\frac{\partial\Phi}{\partial t}\right) - \frac{1}{r^2}\left(1 - \frac{2M}{r}\right)}} \ , \tag{4.5.95}$$

where the minus (plus) sign corresponds to incoming (outgoing) light rays.

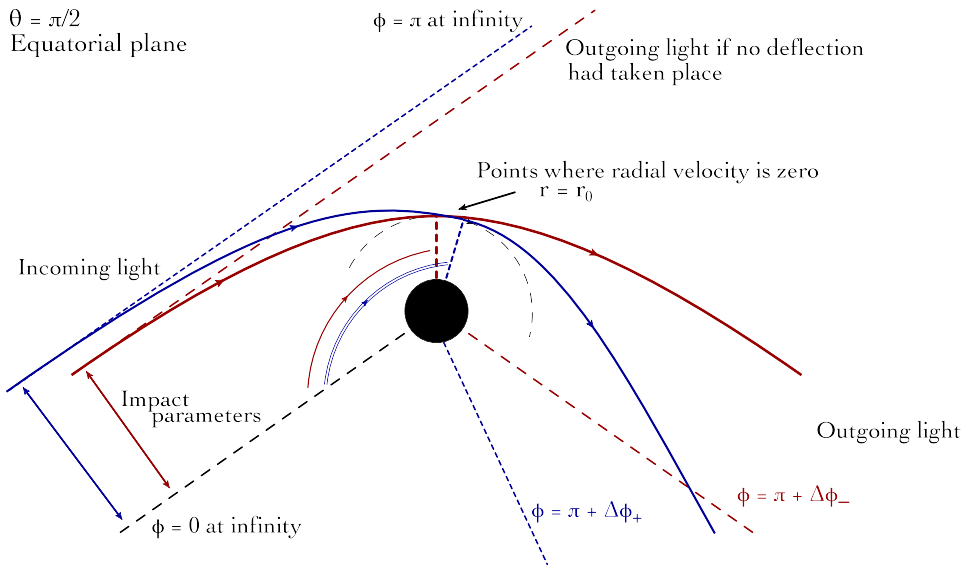

Figure 4.12: Deflection of a ray of light in the gravitational field of a black hole with mass M. The dashed arc of circumference represents the points at distance $r = r_0$ from the black hole centre.

The angle ϕ is defined to be $\phi = 0$ for incoming light at infinite distance from the black hole. Light travelling in straight line will have $\phi = \pi$ in the opposite outgoing limit. In order to compute the deflection angle we consider the setup illustrated in Fig. 4.12. We follow the standard computation of gravitational lensing. The distance of closest approach r_0 of the light ray is defined by means of the condition $dr/d\xi = 0$. From Eq. (4.5.94) we find

$$\frac{E_\gamma^2}{L^2} = \frac{1 - 2M/r_0}{r_0^2\left[1 \mp a(E_\gamma, r_0, \frac{\pi+\Delta\phi_\mp}{2})\right]} , \qquad \text{with} \quad a(E_\gamma, r, \phi) \equiv \frac{g_{a\gamma\gamma}}{E_\gamma}\left.\frac{\partial\Phi}{\partial t}\right|_{r,\phi} . \quad (4.5.96)$$

The distance of closest approach defines the angles $\Delta\phi_\pm$ as one can see from Fig. 4.12. Note that $E_\gamma^2/L^2 = 1/b^2$ defines the impact parameter b. If we fix r_0 to be the same for both left- and right-handed circularly polarised waves we have two different values for the impact parameter, as illustrated in Fig. 4.12. Alternatively, one can fix the impact parameter but in this case the distance of closest approach will differ between the two polarisations. We can now use the condition in Eq. (4.5.96) into

Eq. (4.5.95). For incoming light rays, we find

$$\frac{d\phi}{dr} = -\frac{1}{r^2\sqrt{\frac{1}{r_0^2}\frac{[1\mp a(E_\gamma,r,\phi)]}{\left[1\mp a(E_\gamma,r_0,\frac{\pi+\Delta\phi_\mp}{2})\right]}\left(1-\frac{2M}{r_0}\right)-\frac{1}{r^2}\left(1-\frac{2M}{r}\right)}} \,. \tag{4.5.97}$$

This equation must be integrated between $r = \infty$ and $r = r_0$ in order to obtain the deflection angle for incoming light rays. The final deflection angle, $\pi + \Delta\phi_\pm$, is obtained by adding the corresponding integration – in the interval between $r = r_0$ and $r = \infty$ – for outgoing light rays, as illustrated in Fig. 4.12.

We can use the following approximation in Eq. (4.5.97). In our computation we take the distance of closest approach to be $r_0 = r_{\rm max}$. Furthermore, we introduce the dimensionless variable $x \equiv r/M$, and we find

$$\frac{d\phi}{dx} = -\frac{1}{x^2\sqrt{\frac{1}{x_{\rm max}^2}\frac{[1\mp a(E_\gamma,x,\phi)]}{\left[1\mp a(E_\gamma,x_{\rm max},\frac{\pi+\Delta\phi_\mp}{2})\right]}\left(1-\frac{2}{x_{\rm max}}\right)-\frac{1}{x^2}\left(1-\frac{2}{x}\right)}} \,. \tag{4.5.98}$$

The flat space limit is

$$\frac{d\phi}{dx} = -\frac{1}{x^2\sqrt{\frac{1}{x_{\rm max}^2}\frac{[1\mp a(E_\gamma,x,\phi)]}{\left[1\mp a(E_\gamma,x_{\rm max},\frac{\pi+\Delta\phi_\mp}{2})\right]}-\frac{1}{x^2}}} \,. \tag{4.5.99}$$

Let us now expand the right-hand side for small a. We find

$$\frac{d\phi}{dx} = -\frac{1}{x^2\sqrt{\frac{1}{x_{\rm max}^2}-\frac{1}{x^2}}} \mp \frac{a(E_\gamma,x,\phi)-a(E_\gamma,x_{\rm max},\frac{\pi+\Delta\phi_\mp}{2})}{2x^2x_{\rm max}^2\left(\frac{1}{x_{\rm max}^2}-\frac{1}{x^2}\right)^{3/2}} \,. \tag{4.5.100}$$

The first term reproduces the trivial flat space limit, and the integration between $x = \infty$ and $x = x_{\rm max}$ gives the angle $\phi = \pi/2$ corresponding to outgoing light with no deflection, as illustrated in Fig. 4.12. Since by definition $\Delta\phi_\pm \sim \mathcal{O}(g_{a\gamma\gamma})$, at the first order in the coupling $g_{a\gamma\gamma}$ we can write

$$\frac{d\phi}{dx} = -\frac{1}{x^2\sqrt{\frac{1}{x_{\rm max}^2}-\frac{1}{x^2}}} \mp \frac{a(E_\gamma,x,\phi)-a(E_\gamma,x_{\rm max},\frac{\pi}{2})}{2x^2x_{\rm max}^2\left(\frac{1}{x_{\rm max}^2}-\frac{1}{x^2}\right)^{3/2}} \,, \tag{4.5.101}$$

that is the equation for the photon orbit that we solved in Section **4.3**.

4.6 Summary

Black holes were long considered a mathematical curiosity rather than a true prediction of General Relativity realized in nature. After the first direct detection of gravitational waves and the first observation of a binary black hole merger [429], the possibility to turn black holes from theoretical laboratories to real "particle detectors" has never been nearer than today. However paradoxical this may seem, black holes could help us in finding one of the most theoretically motivated, but experimentally elusive, particle: The axion. This is because a rotating black hole can host an axion cloud – fed by superradiant instability at the expense of the black hole rotational energy – surrounding it. Until present, the properties of such system were studied only considering gravitational interactions. This is a limitation since any boson with the same mass, irrespective of its particle physics origin, displays the same superradiant physics as long as gravitational interactions are concerned.

In this chapter we investigated the possible consequences of the parity-violating coupling of the axion with an electromagnetic field in the context of black hole superradiance. The key idea is that the axion cloud surrounding a Kerr black hole behaves like an optically active medium, and a ray of light experiences a polarisation-dependent bending travelling through it. Motivated by this picture, we computed the polarisation-dependent lensing caused by this phenomenon considering the QCD axion, the photo-philic QCD axion, and a generic ALP.

We discussed the experimental setup that is needed to detect such effect, focusing on the radio observation of a linearly polarised astrophysical source like an AGN. We argued that a VLBI array of radio telescopes has the capability to detect the polarisation-dependent bending effect caused by the axion cloud surrounding a Kerr black hole, and we delimited the parameter space in which this is relevant in conjunction with other experimental axion searches. Although, to properly assess the number of expected events of this observable, we would need to quantify the probability of having the required system configuration, e.g. an AGN and the black

hole being aligned to the line-of-sight of the telescope. We leave that study for future work.

Chapter 5

Conclusions

The Standard Model of particle physics has been one of the most successful theories in physics. However, there are observations that require new physics beyond the SM to find an explanation. In this thesis we discussed different directions in the construction of models beyond the SM that address some of its problems and studied their phenomenological implications at different types of experiments.

Lacking experimental evidence for new fundamental physics to support the most studied solutions to the naturalness problem of the Higgs mass, such as supersymmetry, composite Higgs scenarios and extra-dimensions, it is timely to discuss alternative theoretical guiding principles for models beyond the SM. In Chapter **2**, we discussed the concept of classical scale invariance, in this approach all energy scales in the theory are generated through quantum corrections.

We applied this approach to the inert doublet model, a minimal extension of the SM where a second $\mathrm{SU}(2)_L$ doublet is added and its lightest neutral component (scalar or pseudoscalar) is a good dark matter candidate. Even though new parameters (and particles) are introduced to the inert doublet model, the Coleman-Weinberg relation imposes a constraint among them. We found that, when compared to the inert doublet model, the classically scale invariant extension has a reduced parameter space compatible with low-scale physics and dark matter experimental constraints. In addition, we characterised the regions in the parameter space of the model that can be extrapolated up to the Planck scale.

In addition, we discussed a minimal classically scale invariant extension of the SM which explains dark matter, neutrino masses and the baryon asymmetry of the Universe. In order to achieve this, the following states are added to the SM, a dark non-Abelian sector SU(2), a scalar doublet charged under the latter, three right-handed neutrinos and a singlet scalar. Active neutrinos acquire their masses via the type-I seesaw mechanism. The gauge bosons in the dark sector are mass-degenerate and stable due to a remnant global SO(3) symmetry, and therefore, represent good candidates for dark matter. The baryon asymmetry is generated in the early Universe via CP-violating oscillations of the GeV right-handed neutrinos.

From dark matter considerations, the scale connected to dark matter is required to be around the TeV, and due to the common origin of all the vacuum expectation values in the model, the one giving mass to the right-handed neutrinos cannot be too large. We showed that the right-handed neutrinos should have masses around the GeV scale in order for leptogenesis to work without severe tuning of their mass splittings. Under some mild assumptions, we also found a connection among the two scales in order to explain the observed ration $\Omega_{\rm DM}h^2/\Omega_b h^2 = 5$.

We studied the dark matter phenomenology in both models previously discussed. We computed the relic abundance and presented cross-sections for direct detection experiments, demonstrating that a large region of parameter space will be probed in the near future. Moreover, both of these models contain a Coleman-Weinberg scalar that mixes with the SM Higgs and its phenomenology at the LHC has been discussed. The framework of classical scale invariance also provides relations between originally free parameters in a theory and if embedded in a theory with exact scale invariance in the UV could potentially solve the Higgs mass naturalness problem.

In Chapter **3**, we discussed a set of simplified models of dark matter in which a dark matter candidate and a coannihilation partner are introduced to the SM. At tree-level the DM particle interacts with the SM only via the heaviest lepton; namely, the τ-lepton. Some of these models are gauge-invariant and renormalisable, others would ultimately require a UV completion. In the region of parameter space where the mass splitting between the dark matter particle and the coannihilation partner is smaller or equal to the mass of the tau, $\Delta M \leq m_\tau$, two-body decays

of the coannhilation partner are forbidden, and therefore, its lifetime is larger than 10^{-8} seconds leading to highly ionised charged tracks. We demonstrated how ongoing searches for long-lived charged particles at ATLAS and CMS can probe these models.

In the scenario where the mass splitting is larger than the mass of the τ-lepton, $\Delta M > m_\tau$, the coannihilation partner decays promptly into a tau and the dark matter candidate, the latter as missing energy in the detector. In view that the reconstruction of soft τ-leptons is a hard task at the LHC and the overwhelming background, the prospects to detect this decay at the LHC are hopeless. However, there exist current plans for the construction of a electron-positron linear collider, where owing to the clean environment the soft decay products can be detected. We studied the expected sensitivity to the pair-production of the coannihilation partner for different centre-of-mass energies and integrated luminosities. We found the prospects to be very promising, leaving only a small window around $\Delta M \approx m_\tau$ untested, once the sensitivity of the LHC and electron-positron colliders are combined. The models discussed are difficult to probe by direct and indirect DM detection experiments. Therefore, the LHC and future lepton colliders provide an almost unique opportunity to explore them.

In the Introduction, we discussed the motivation for the QCD axion. A very light pseudoscalar particle that solves the strong CP problem and due to its very weak interactions and its long lifetime, it also represents a good candidate for dark matter. Moreover, observational evidence for the existence of dark matter and string theory constructions motivate axion like particles independently of the strong CP problem. In the presence of an ultralight axion, a cloud of these particles forms surrounding a Kerr black hole through superradiance, this effect relies solely on the gravitational interaction. In Chapter **4**, we discussed the effect of polarisation-dependent bending as light passes through the axionic cloud, the latter arises due to the effective coupling between axions and photons.

In view that right- and left-handed circularly polarised waves propagate differently in the presence of an inhomogeneous scalar background, the deflection angle for right-handed circular polarisation differs from the one with left-handed circular polarisation. Therefore, the image of a source that emits light with linear polarisa-

tion, such as an AGN, will be split into two as its light reaches the telescope. We calculated the angular splitting of the images as a function of the coupling $g_{a\gamma\gamma}$ and showed that a VLBI array of radio telescopes has the potential to detect this effect.

A possible astrophysical mechanism that could affect the signal is angular broadening. If the angular broadening proves to be much larger than the angular splitting, we expect the latter to be clouded by the former. Angular broadening can arise as radio waves scatter with the intergalactic medium. We computed this effect and find it to be subleading to the one coming from the axionic cloud in a large region of the parameter space. Therefore, there is hope of detecting the polarisation-dependent bending due to a superradiant axion cloud.

In this thesis, we have discussed different models beyond the SM that address some of its shortcomings and studied their phenomenological implications. The SM cannot be a complete theory and the quest for new physics continues.

Bibliography

[1] A. D. Plascencia, *Classical scale invariance in the inert doublet model*, *JHEP* **09** (2015) 026, [arXiv:1507.04996].

[2] V. V. Khoze and A. D. Plascencia, *Dark Matter and Leptogenesis Linked by Classical Scale Invariance*, *JHEP* **11** (2016) 025, [arXiv:1605.06834].

[3] V. V. Khoze, A. D. Plascencia, and K. Sakurai, *Simplified models of dark matter with a long-lived co-annihilation partner*, *JHEP* **06** (2017) 041, [arXiv:1702.00750].

[4] A. D. Plascencia and A. Urbano, *Black hole superradiance and polarization-dependent bending of light*, *JCAP* **1804** (2018), no. 04 059, [arXiv:1711.08298].

[5] C.-N. Yang and R. L. Mills, *Conservation of Isotopic Spin and Isotopic Gauge Invariance*, *Phys. Rev.* **96** (1954) 191–195. [,150(1954)].

[6] S. L. Glashow, *Partial Symmetries of Weak Interactions*, *Nucl. Phys.* **22** (1961) 579–588.

[7] S. Weinberg, *A Model of Leptons*, *Phys. Rev. Lett.* **19** (1967) 1264–1266.

[8] A. Salam, *Weak and Electromagnetic Interactions*, *Conf. Proc.* **C680519** (1968) 367–377.

[9] G. 't Hooft, *Renormalizable Lagrangians for Massive Yang-Mills Fields*, *Nucl. Phys.* **B35** (1971) 167–188. [,201(1971)].

[10] G. 't Hooft and M. J. G. Veltman, *Regularization and Renormalization of Gauge Fields*, *Nucl. Phys.* **B44** (1972) 189–213.

[11] **Gargamelle Neutrino** Collaboration, F. J. Hasert et al., *Observation of Neutrino Like Interactions Without Muon Or Electron in the Gargamelle Neutrino Experiment*, *Phys. Lett.* **B46** (1973) 138–140. [,5.15(1973)].

[12] **E598** Collaboration, J. J. Aubert et al., *Experimental Observation of a Heavy Particle J*, *Phys. Rev. Lett.* **33** (1974) 1404–1406.

[13] **SLAC-SP-017** Collaboration, J. E. Augustin et al., *Discovery of a Narrow Resonance in e^+e^- Annihilation*, *Phys. Rev. Lett.* **33** (1974) 1406–1408. [Adv. Exp. Phys.5,141(1976)].

[14] **UA1** Collaboration, G. Arnison et al., *Experimental Observation of Isolated Large Transverse Energy Electrons with Associated Missing Energy at s**(1/2) = 540-GeV*, *Phys. Lett.* **B122** (1983) 103–116. [,611(1983)].

[15] **UA2** Collaboration, M. Banner et al., *Observation of Single Isolated Electrons of High Transverse Momentum in Events with Missing Transverse Energy at the CERN anti-p p Collider*, *Phys. Lett.* **B122** (1983) 476–485. [,7.45(1983)].

[16] **UA1** Collaboration, G. Arnison et al., *Experimental Observation of Lepton Pairs of Invariant Mass Around 95-GeV/c**2 at the CERN SPS Collider*, *Phys. Lett.* **B126** (1983) 398–410. [,7.55(1983)].

[17] **UA2** Collaboration, P. Bagnaia et al., *Evidence for Z0 —> e+ e- at the CERN anti-p p Collider*, *Phys. Lett.* **B129** (1983) 130–140. [,7.69(1983)].

[18] P. W. Higgs, *Broken symmetries, massless particles and gauge fields*, *Phys. Lett.* **12** (1964) 132–133.

[19] F. Englert and R. Brout, *Broken Symmetry and the Mass of Gauge Vector Mesons*, *Phys. Rev. Lett.* **13** (1964) 321–323. [,157(1964)].

[20] G. S. Guralnik, C. R. Hagen, and T. W. B. Kibble, *Global Conservation Laws and Massless Particles*, *Phys. Rev. Lett.* **13** (1964) 585–587. [,162(1964)].

[21] **ATLAS** Collaboration, G. Aad et al., *Observation of a new particle in the search for the Standard Model Higgs boson with the ATLAS detector at the LHC*, *Phys. Lett.* **B716** (2012) 1–29, [arXiv:1207.7214].

[22] **CMS** Collaboration, S. Chatrchyan et al., *Observation of a new boson at a mass of 125 GeV with the CMS experiment at the LHC*, *Phys. Lett.* **B716** (2012) 30–61, [arXiv:1207.7235].

[23] **CMS** Collaboration, S. Chatrchyan et al., *Summaries of CMS cross section measurements*, 2018.

[24] R. Davis, *Solar neutrinos. II: Experimental*, *Phys. Rev. Lett.* **12** (1964) 303–305. [,107(1964)].

[25] R. Davis, Jr., D. S. Harmer, and K. C. Hoffman, *Search for neutrinos from the sun*, *Phys. Rev. Lett.* **20** (1968) 1205–1209.

[26] **Super-Kamiokande** Collaboration, Y. Fukuda et al., *Evidence for oscillation of atmospheric neutrinos*, *Phys. Rev. Lett.* **81** (1998) 1562–1567, [hep-ex/9807003].

[27] **SNO** Collaboration, Q. R. Ahmad et al., *Direct evidence for neutrino flavor transformation from neutral current interactions in the Sudbury Neutrino Observatory*, *Phys. Rev. Lett.* **89** (2002) 011301, [nucl-ex/0204008].

[28] B. Pontecorvo, *Mesonium and anti-mesonium*, *Sov. Phys. JETP* **6** (1957) 429. [Zh. Eksp. Teor. Fiz.33,549(1957)].

[29] Z. Maki, M. Nakagawa, and S. Sakata, *Remarks on the unified model of elementary particles*, *Prog. Theor. Phys.* **28** (1962) 870–880. [,34(1962)].

[30] I. Esteban, M. C. Gonzalez-Garcia, M. Maltoni, I. Martinez-Soler, and T. Schwetz, *Updated fit to three neutrino mixing: exploring the accelerator-reactor complementarity*, *JHEP* **01** (2017) 087, [arXiv:1611.01514].

[31] P. Minkowski, $\mu \to e\gamma$ *at a Rate of One Out of* 10^9 *Muon Decays?*, *Phys. Lett.* **67B** (1977) 421–428.

[32] T. Yanagida, *Horizontal Symmetry and Masses of Neutrinos*, *Conf. Proc.* **C7902131** (1979) 95–99.

[33] M. Gell-Mann, P. Ramond, and R. Slansky, *Complex Spinors and Unified Theories*, *Conf. Proc.* **C790927** (1979) 315–321, [arXiv:1306.4669].

[34] R. N. Mohapatra and G. Senjanovic, *Neutrino Mass and Spontaneous Parity Violation*, *Phys. Rev. Lett.* **44** (1980) 912. [,231(1979)].

[35] R. Cooke, M. Pettini, R. A. Jorgenson, M. T. Murphy, and C. C. Steidel, *Precision measures of the primordial abundance of deuterium*, *Astrophys. J.* **781** (2014), no. 1 31, [arXiv:1308.3240].

[36] **Particle Data Group** Collaboration, C. Patrignani et al., *Review of Particle Physics*, *Chin. Phys.* **C40** (2016), no. 10 100001.

[37] **Planck** Collaboration, P. A. R. Ade et al., *Planck 2015 results. XIII. Cosmological parameters*, *Astron. Astrophys.* **594** (2016) A13, [arXiv:1502.01589].

[38] A. D. Sakharov, *Violation of CP Invariance, C asymmetry, and baryon asymmetry of the universe*, *Pisma Zh. Eksp. Teor. Fiz.* **5** (1967) 32–35. [Usp. Fiz. Nauk161,no.5,61(1991)].

[39] J. M. Cline, *Baryogenesis*, in *Les Houches Summer School - Session 86: Particle Physics and Cosmology: The Fabric of Spacetime Les Houches, France, July 31-August 25, 2006*, 2006. hep-ph/0609145.

[40] D. E. Morrissey and M. J. Ramsey-Musolf, *Electroweak baryogenesis*, *New J. Phys.* **14** (2012) 125003, [arXiv:1206.2942].

[41] M. Fukugita and T. Yanagida, *Baryogenesis Without Grand Unification*, *Phys. Lett.* **B174** (1986) 45–47.

[42] E. K. Akhmedov, V. A. Rubakov, and A. Yu. Smirnov, *Baryogenesis via neutrino oscillations*, *Phys. Rev. Lett.* **81** (1998) 1359–1362, [hep-ph/9803255].

[43] L. Canetti and M. Shaposhnikov, *Baryon Asymmetry of the Universe in the NuMSM*, *JCAP* **1009** (2010) 001, [arXiv:1006.0133].

[44] M. Drewes, B. Garbrecht, D. Gueter, and J. Klaric, *Leptogenesis from Oscillations of Heavy Neutrinos with Large Mixing Angles*, *JHEP* **12** (2016) 150, [arXiv:1606.06690].

[45] P. Hernández, M. Kekic, J. López-Pavón, J. Racker, and J. Salvado, *Testable Baryogenesis in Seesaw Models*, *JHEP* **08** (2016) 157, [arXiv:1606.06719].

[46] S. Alekhin et al., *A facility to Search for Hidden Particles at the CERN SPS: the SHiP physics case*, *Rept. Prog. Phys.* **79** (2016), no. 12 124201, [arXiv:1504.04855].

[47] A. Pilaftsis and T. E. J. Underwood, *Resonant leptogenesis*, *Nucl. Phys.* **B692** (2004) 303–345, [hep-ph/0309342].

[48] F. Zwicky, *Die Rotverschiebung von extragalaktischen Nebeln*, *Helv. Phys. Acta* **6** (1933) 110–127. [Gen. Rel. Grav.41,207(2009)].

[49] K. C. Freeman, *On the disks of spiral and SO Galaxies*, *Astrophys. J.* **160** (1970) 811.

[50] V. C. Rubin and W. K. Ford, Jr., *Rotation of the Andromeda Nebula from a Spectroscopic Survey of Emission Regions*, *Astrophys. J.* **159** (1970) 379–403.

[51] G. Bertone and D. Hooper, *A History of Dark Matter*, *Submitted to: Rev. Mod. Phys.* (2016) [arXiv:1605.04909].

[52] P. J. E. Peebles, *Growth of the nonbaryonic dark matter theory*, *Nat. Astron.* **1** (2017), no. 3 0057.

[53] J. de Swart, G. Bertone, and J. van Dongen, *How Dark Matter Came to Matter*, arXiv:1703.00013. [Nature Astron.1,0059(2017)].

[54] G. Bertone, D. Hooper, and J. Silk, *Particle dark matter: Evidence, candidates and constraints*, *Phys. Rept.* **405** (2005) 279–390, [hep-ph/0404175].

[55] K. G. Begeman, A. H. Broeils, and R. H. Sanders, *Extended rotation curves of spiral galaxies: Dark haloes and modified dynamics*, *Mon. Not. Roy. Astron. Soc.* **249** (1991) 523.

[56] R. Massey, T. Kitching, and J. Richard, *The dark matter of gravitational lensing*, *Rept. Prog. Phys.* **73** (2010) 086901, [arXiv:1001.1739].

[57] R. S. Ellis, *Gravitational lensing: a unique probe of dark matter and dark energy*, *Philosophical Transactions of the Royal Society of London Series A* **368** (Feb., 2010) 967–987.

[58] D. Clowe, M. Bradac, A. H. Gonzalez, M. Markevitch, S. W. Randall, C. Jones, and D. Zaritsky, *A direct empirical proof of the existence of dark matter*, *Astrophys. J.* **648** (2006) L109–L113, [astro-ph/0608407].

[59] B. Holdom, *Two U(1)'s and Epsilon Charge Shifts*, *Phys. Lett.* **166B** (1986) 196–198.

[60] S. Davidson, S. Hannestad, and G. Raffelt, *Updated bounds on millicharged particles*, *JHEP* **05** (2000) 003, [hep-ph/0001179].

[61] S. A. Abel, J. Jaeckel, V. V. Khoze, and A. Ringwald, *Illuminating the Hidden Sector of String Theory by Shining Light through a Magnetic Field*, *Phys. Lett.* **B666** (2008) 66–70, [hep-ph/0608248].

[62] L. D. Duffy and K. van Bibber, *Axions as Dark Matter Particles*, *New J. Phys.* **11** (2009) 105008, [arXiv:0904.3346].

[63] D. J. E. Marsh, *Axion Cosmology*, *Phys. Rept.* **643** (2016) 1–79, [arXiv:1510.07633].

[64] K. M. Zurek, *Asymmetric Dark Matter: Theories, Signatures, and Constraints*, *Phys. Rept.* **537** (2014) 91–121, [arXiv:1308.0338].

[65] A. E. Nelson and J. Scholtz, *Dark Light, Dark Matter and the Misalignment Mechanism*, *Phys. Rev.* **D84** (2011) 103501, [arXiv:1105.2812].

[66] P. Arias, D. Cadamuro, M. Goodsell, J. Jaeckel, J. Redondo, and A. Ringwald, *WISPy Cold Dark Matter*, *JCAP* **1206** (2012) 013, [arXiv:1201.5902].

[67] T. Hambye, *Hidden vector dark matter*, *JHEP* **01** (2009) 028, [arXiv:0811.0172].

[68] J. McDonald, *Thermally generated gauge singlet scalars as selfinteracting dark matter*, *Phys. Rev. Lett.* **88** (2002) 091304, [hep-ph/0106249].

[69] L. J. Hall, K. Jedamzik, J. March-Russell, and S. M. West, *Freeze-In Production of FIMP Dark Matter*, *JHEP* **03** (2010) 080, [arXiv:0911.1120].

[70] B. Carr, F. Kuhnel, and M. Sandstad, *Primordial Black Holes as Dark Matter*, *Phys. Rev.* **D94** (2016), no. 8 083504, [arXiv:1607.06077].

[71] E. D. Carlson, M. E. Machacek, and L. J. Hall, *Self-interacting dark matter*, *Astrophys. J.* **398** (1992) 43–52.

[72] Y. Hochberg, E. Kuflik, T. Volansky, and J. G. Wacker, *Mechanism for Thermal Relic Dark Matter of Strongly Interacting Massive Particles*, *Phys. Rev. Lett.* **113** (2014) 171301, [arXiv:1402.5143].

[73] J. L. Feng, A. Rajaraman, and F. Takayama, *Superweakly interacting massive particles*, *Phys. Rev. Lett.* **91** (2003) 011302, [hep-ph/0302215].

[74] A. Kusenko, *Sterile neutrinos: The Dark side of the light fermions*, *Phys. Rept.* **481** (2009) 1–28, [arXiv:0906.2968].

[75] M. Drewes et al., *A White Paper on keV Sterile Neutrino Dark Matter*, *JCAP* **1701** (2017), no. 01 025, [arXiv:1602.04816].

[76] G. Arcadi, M. Dutra, P. Ghosh, M. Lindner, Y. Mambrini, M. Pierre, S. Profumo, and F. S. Queiroz, *The waning of the WIMP? A review of models, searches, and constraints*, *Eur. Phys. J.* **C78** (2018), no. 3 203, [arXiv:1703.07364].

[77] E. W. Kolb, D. J. H. Chung, and A. Riotto, *WIMPzillas!*, *AIP Conf. Proc.* **484** (1999), no. 1 91–105, [hep-ph/9810361]. [,592(1999)].

[78] **CRESST** Collaboration, G. Angloher et al., *Results on light dark matter particles with a low-threshold CRESST-II detector*, *Eur. Phys. J.* **C76** (2016), no. 1 25, [arXiv:1509.01515].

[79] D. C. Malling et al., *After LUX: The LZ Program*, arXiv:1110.0103.

[80] **PandaX-II** Collaboration, A. Tan et al., *Dark Matter Results from First 98.7 Days of Data from the PandaX-II Experiment*, *Phys. Rev. Lett.* **117** (2016), no. 12 121303, [arXiv:1607.07400].

[81] **SuperCDMS** Collaboration, R. Agnese et al., *Low-mass dark matter search with CDMSlite*, *Phys. Rev.* **D97** (2018), no. 2 022002, [arXiv:1707.01632].

[82] **XENON** Collaboration, E. Aprile et al., *Physics reach of the XENON1T dark matter experiment*, *JCAP* **1604** (2016), no. 04 027, [arXiv:1512.07501].

[83] **AMS** Collaboration, M. Aguilar et al., *Precision Measurement of the Boron to Carbon Flux Ratio in Cosmic Rays from 1.9 GV to 2.6 TV with the Alpha Magnetic Spectrometer on the International Space Station*, *Phys. Rev. Lett.* **117** (2016), no. 23 231102.

[84] **CTA Consortium** Collaboration, M. Doro et al., *Dark Matter and Fundamental Physics with the Cherenkov Telescope Array*, *Astropart. Phys.* **43** (2013) 189–214, [arXiv:1208.5356].

[85] **Fermi-LAT** Collaboration, M. Ackermann et al., *Searching for Dark Matter Annihilation from Milky Way Dwarf Spheroidal Galaxies with Six Years of Fermi Large Area Telescope Data*, *Phys. Rev. Lett.* **115** (2015), no. 23 231301, [arXiv:1503.02641].

[86] **HAWC** Collaboration, A. U. Abeysekara et al., *Sensitivity of HAWC to high-mass dark matter annihilations*, *Phys. Rev.* **D90** (2014), no. 12 122002, [arXiv:1405.1730].

[87] **H.E.S.S.** Collaboration, A. Abramowski et al., *Search for Photon-Linelike Signatures from Dark Matter Annihilations with H.E.S.S.*, *Phys. Rev. Lett.* **110** (2013) 041301, [arXiv:1301.1173].

[88] **IceCube** Collaboration, M. G. Aartsen et al., *Search for Neutrinos from Dark Matter Self-Annihilations in the center of the Milky Way with 3 years of IceCube/DeepCore*, *Eur. Phys. J.* **C77** (2017), no. 9 627, [arXiv:1705.08103].

[89] **PAMELA** Collaboration, O. Adriani et al., *Cosmic-Ray Positron Energy Spectrum Measured by PAMELA*, *Phys. Rev. Lett.* **111** (2013) 081102, [arXiv:1308.0133].

[90] T. Behnke, J. E. Brau, B. Foster, J. Fuster, M. Harrison, J. M. Paterson, M. Peskin, M. Stanitzki, N. Walker, and H. Yamamoto, *The International Linear Collider Technical Design Report - Volume 1: Executive Summary*, arXiv:1306.6327.

[91] L. Linssen, A. Miyamoto, M. Stanitzki, and H. Weerts, *Physics and Detectors at CLIC: CLIC Conceptual Design Report*, arXiv:1202.5940.

[92] M. Mangano, *Physics at the FCC-hh, a 100 TeV pp collider*, arXiv:1710.06353.

[93] J. L. Feng, *Dark Matter Candidates from Particle Physics and Methods of Detection*, *Ann. Rev. Astron. Astrophys.* **48** (2010) 495–545, [arXiv:1003.0904].

[94] M. Lisanti, *Lectures on Dark Matter Physics*, in *Proceedings, Theoretical Advanced Study Institute in Elementary Particle Physics: New Frontiers in Fields and Strings (TASI 2015): Boulder, CO, USA, June 1-26, 2015*, pp. 399–446, 2017. arXiv:1603.03797.

[95] J. A. Casas, J. R. Espinosa, and M. Quiros, *Improved Higgs mass stability bound in the standard model and implications for supersymmetry*, *Phys. Lett.* **B342** (1995) 171–179, [hep-ph/9409458].

[96] D. Buttazzo, G. Degrassi, P. P. Giardino, G. F. Giudice, F. Sala, A. Salvio, and A. Strumia, *Investigating the near-criticality of the Higgs boson*, *JHEP* **12** (2013) 089, [arXiv:1307.3536].

[97] G. Degrassi, S. Di Vita, J. Elias-Miro, J. R. Espinosa, G. F. Giudice, G. Isidori, and A. Strumia, *Higgs mass and vacuum stability in the Standard Model at NNLO*, *JHEP* **08** (2012) 098, [arXiv:1205.6497].

[98] M. Lindner, *Implications of Triviality for the Standard Model*, *Z. Phys.* **C31** (1986) 295.

[99] M. Sher, *Electroweak Higgs Potentials and Vacuum Stability*, *Phys. Rept.* **179** (1989) 273–418.

[100] **ATLAS** Collaboration, T. A. collaboration, *Measurement of the top quark mass in the $t\bar{t} \to$ lepton+jets channel from $\sqrt{s}$=8 TeV ATLAS data*, .

[101] S. Menke, *Measurements of the top quark mass using the cms and atlas detectors at the lhc*, *Moriond-Electroweak* (2018).

[102] N. K. Nielsen, *On the Gauge Dependence of Spontaneous Symmetry Breaking in Gauge Theories*, *Nucl. Phys.* **B101** (1975) 173–188.

[103] A. D. Plascencia and C. Tamarit, *Convexity, gauge-dependence and tunneling rates*, *JHEP* **10** (2016) 099, [arXiv:1510.07613].

[104] H. H. Patel and M. J. Ramsey-Musolf, *Baryon Washout, Electroweak Phase Transition, and Perturbation Theory*, *JHEP* **07** (2011) 029, [arXiv:1101.4665].

[105] L. Di Luzio and L. Mihaila, *On the gauge dependence of the Standard Model vacuum instability scale*, *JHEP* **06** (2014) 079, [arXiv:1404.7450].

[106] Z. Lalak, M. Lewicki, and P. Olszewski, *Gauge fixing and renormalization scale independence of tunneling rate in Abelian Higgs model and in the standard model*, *Phys. Rev.* **D94** (2016), no. 8 085028, [arXiv:1605.06713].

[107] A. Andreassen, W. Frost, and M. D. Schwartz, *Scale Invariant Instantons and the Complete Lifetime of the Standard Model*, *Phys. Rev.* **D97** (2018), no. 5 056006, [arXiv:1707.08124].

[108] S. Chigusa, T. Moroi, and Y. Shoji, *State-of-the-Art Calculation of the Decay Rate of Electroweak Vacuum in the Standard Model*, *Phys. Rev. Lett.* **119** (2017), no. 21 211801, [arXiv:1707.09301].

[109] R. J. Crewther, P. Di Vecchia, G. Veneziano, and E. Witten, *Chiral Estimate of the Electric Dipole Moment of the Neutron in Quantum Chromodynamics*, *Phys. Lett.* **88B** (1979) 123. [Erratum: Phys. Lett.91B,487(1980)].

[110] C. A. Baker et al., *An Improved experimental limit on the electric dipole moment of the neutron*, *Phys. Rev. Lett.* **97** (2006) 131801, [hep-ex/0602020].

[111] R. D. Peccei and H. R. Quinn, *CP Conservation in the Presence of Instantons*, *Phys. Rev. Lett.* **38** (1977) 1440–1443. [,328(1977)].

[112] **MILC** Collaboration, A. Bazavov et al., *Nonperturbative QCD Simulations with 2+1 Flavors of Improved Staggered Quarks*, *Rev. Mod. Phys.* **82** (2010) 1349–1417, [arXiv:0903.3598].

[113] **European Twisted Mass** Collaboration, N. Carrasco et al., *Up, down, strange and charm quark masses with $N_f = 2+1+1$ twisted mass lattice QCD*, *Nucl. Phys.* **B887** (2014) 19–68, [arXiv:1403.4504].

[114] **MILC** Collaboration, S. Basak et al., *Electromagnetic effects on the light hadron spectrum*, *J. Phys. Conf. Ser.* **640** (2015), no. 1 012052, [arXiv:1510.04997].

[115] S. Weinberg, *A New Light Boson?*, *Phys. Rev. Lett.* **40** (1978) 223–226.

[116] F. Wilczek, *Problem of Strong p and t Invariance in the Presence of Instantons*, *Phys. Rev. Lett.* **40** (1978) 279–282.

[117] R. D. Peccei, *The Strong CP problem and axions*, *Lect. Notes Phys.* **741** (2008) 3–17, [hep-ph/0607268]. [,3(2006)].

[118] A. Ringwald, *Exploring the Role of Axions and Other WISPs in the Dark Universe*, *Phys. Dark Univ.* **1** (2012) 116–135, [arXiv:1210.5081].

[119] J. E. Kim, *Weak Interaction Singlet and Strong CP Invariance*, *Phys. Rev. Lett.* **43** (1979) 103.

[120] M. A. Shifman, A. I. Vainshtein, and V. I. Zakharov, *Can Confinement Ensure Natural CP Invariance of Strong Interactions?*, *Nucl. Phys.* **B166** (1980) 493–506.

[121] M. Dine, W. Fischler, and M. Srednicki, *A Simple Solution to the Strong CP Problem with a Harmless Axion*, *Phys. Lett.* **104B** (1981) 199–202.

[122] A. R. Zhitnitsky, *On Possible Suppression of the Axion Hadron Interactions. (In Russian)*, *Sov. J. Nucl. Phys.* **31** (1980) 260. [Yad. Fiz.31,497(1980)].

[123] G. G. Raffelt, *Astrophysical axion bounds*, *Lect. Notes Phys.* **741** (2008) 51–71, [hep-ph/0611350]. [,51(2006)].

[124] H. M. Lee, M. Park, and W.-I. Park, *Fermi Gamma Ray Line at 130 GeV from Axion-Mediated Dark Matter*, *Phys. Rev.* **D86** (2012) 103502, [arXiv:1205.4675].

[125] M. Dine and W. Fischler, *The Not So Harmless Axion*, *Phys. Lett.* **B120** (1983) 137–141. [,URL(1982)].

[126] L. F. Abbott and P. Sikivie, *A Cosmological Bound on the Invisible Axion*, *Phys. Lett.* **B120** (1983) 133–136. [,URL(1982)].

[127] O. Wantz and E. P. S. Shellard, *Axion Cosmology Revisited*, *Phys. Rev.* **D82** (2010) 123508, [arXiv:0910.1066].

[128] P. Svrcek and E. Witten, *Axions In String Theory*, *JHEP* **06** (2006) 051, [hep-th/0605206].

[129] A. G. Dias, A. C. B. Machado, C. C. Nishi, A. Ringwald, and P. Vaudrevange, *The Quest for an Intermediate-Scale Accidental Axion and Further ALPs*, *JHEP* **06** (2014) 037, [arXiv:1403.5760].

[130] Y. Kahn, B. R. Safdi, and J. Thaler, *Broadband and Resonant Approaches to Axion Dark Matter Detection*, *Phys. Rev. Lett.* **117** (2016), no. 14 141801, [arXiv:1602.01086].

[131] **ADMX** Collaboration, N. Du et al., *A Search for Invisible Axion Dark Matter with the Axion Dark Matter Experiment*, *Phys. Rev. Lett.* **120** (2018), no. 15 151301, [arXiv:1804.05750].

[132] **ALPS** Collaboration, K. Ehret et al., *Resonant laser power build-up in ALPS: A 'Light-shining-through-walls' experiment*, *Nucl. Instrum. Meth.* **A612** (2009) 83–96, [arXiv:0905.4159].

[133] **ALPS-II** Collaboration, B. Döbrich, *What's new in ALPS-II*, in *Proceedings, 9th Patras Workshop on Axions, WIMPs and WISPs (AXION-WIMP 2013): Mainz, Germany, June 24-28, 2013*, 2013. arXiv:1309.3965.

[134] D. Budker, P. W. Graham, M. Ledbetter, S. Rajendran, and A. Sushkov, *Proposal for a Cosmic Axion Spin Precession Experiment (CASPEr)*, *Phys. Rev.* **X4** (2014), no. 2 021030, [arXiv:1306.6089].

[135] D. F. Jackson Kimball et al., *Overview of the Cosmic Axion Spin Precession Experiment (CASPEr)*, arXiv:1711.08999.

[136] **CAST** Collaboration, S. Aune et al., *CAST search for sub-eV mass solar axions with 3He buffer gas*, *Phys. Rev. Lett.* **107** (2011) 261302, [arXiv:1106.3919].

[137] **CAST** Collaboration, S. Andriamonje et al., *An Improved limit on the axion-photon coupling from the CAST experiment*, *JCAP* **0704** (2007) 010, [hep-ex/0702006].

[138] J. K. Vogel et al., *IAXO - The International Axion Observatory*, in *8th Patras Workshop on Axions, WIMPs and WISPs (AXION-WIMP 2012) Chicago, Illinois, July 18-22, 2012*, 2013. arXiv:1302.3273.

[139] E. Armengaud et al., *Conceptual Design of the International Axion Observatory (IAXO)*, *JINST* **9** (2014) T05002, [arXiv:1401.3233].

[140] **MADMAX Working Group** Collaboration, A. Caldwell, G. Dvali, B. Majorovits, A. Millar, G. Raffelt, J. Redondo, O. Reimann, F. Simon, and F. Steffen, *Dielectric Haloscopes: A New Way to Detect Axion Dark Matter*, *Phys. Rev. Lett.* **118** (2017), no. 9 091801, [arXiv:1611.05865].

[141] K. Mimasu and V. Sanz, *ALPs at Colliders*, *JHEP* **06** (2015) 173, [arXiv:1409.4792].

[142] B. Döbrich, J. Jaeckel, F. Kahlhoefer, A. Ringwald, and K. Schmidt-Hoberg, *ALPtraum: ALP production in proton beam dump experiments*, *JHEP* **02** (2016) 018, [arXiv:1512.03069]. [JHEP02,018(2016)].

[143] A. Ayala, I. Domínguez, M. Giannotti, A. Mirizzi, and O. Straniero, *Revisiting the bound on axion-photon coupling from Globular Clusters*, *Phys. Rev. Lett.* **113** (2014), no. 19 191302, [arXiv:1406.6053].

[144] R. Penrose and R. M. Floyd, *Extraction of rotational energy from a black hole*, *Nature* **229** (1971) 177–179.

[145] W. H. Press and S. A. Teukolsky, *Floating Orbits, Superradiant Scattering and the Black-hole Bomb*, *Nature* **238** (1972) 211–212.

[146] A. Arvanitaki, S. Dimopoulos, S. Dubovsky, N. Kaloper, and J. March-Russell, *String Axiverse*, *Phys. Rev.* **D81** (2010) 123530, [arXiv:0905.4720].

[147] A. Arvanitaki and S. Dubovsky, *Exploring the String Axiverse with Precision Black Hole Physics*, *Phys. Rev.* **D83** (2011) 044026, [arXiv:1004.3558].

[148] A. de Gouvea, D. Hernandez, and T. M. P. Tait, *Criteria for Natural Hierarchies*, *Phys. Rev.* **D89** (2014), no. 11 115005, [arXiv:1402.2658].

[149] C. Csáki and P. Tanedo, *Beyond the Standard Model*, in *Proceedings, 2013 European School of High-Energy Physics (ESHEP 2013): Paradfurdo, Hungary, June 5-18, 2013*, pp. 169–268, 2015. arXiv:1602.04228.

[150] S. R. Coleman and E. J. Weinberg, *Radiative Corrections as the Origin of Spontaneous Symmetry Breaking*, *Phys.Rev.* **D7** (1973) 1888–1910.

[151] W. A. Bardeen, *On naturalness in the standard model*, *FERMILAB-CONF-95-391* (1995).

[152] C. Englert, J. Jaeckel, V. Khoze, and M. Spannowsky, *Emergence of the Electroweak Scale through the Higgs Portal*, *JHEP* **1304** (2013) 060, [arXiv:1301.4224].

[153] D. F. Litim and F. Sannino, *Asymptotic safety guaranteed*, *JHEP* **12** (2014) 178, [arXiv:1406.2337].

[154] A. D. Bond, G. Hiller, K. Kowalska, and D. F. Litim, *Directions for model building from asymptotic safety*, *JHEP* **08** (2017) 004, [arXiv:1702.01727].

[155] G. M. Pelaggi, A. D. Plascencia, A. Salvio, F. Sannino, J. Smirnov, and A. Strumia, *Asymptotically Safe Standard Model Extensions?*, *Phys. Rev.* **D97** (2018), no. 9 095013, [arXiv:1708.00437].

[156] F. Vissani, *Do experiments suggest a hierarchy problem?*, *Phys. Rev.* **D57** (1998) 7027–7030, [hep-ph/9709409].

[157] M. Farina, D. Pappadopulo, and A. Strumia, *A modified naturalness principle and its experimental tests*, *JHEP* **08** (2013) 022, [arXiv:1303.7244].

[158] N. G. Deshpande and E. Ma, *Pattern of Symmetry Breaking with Two Higgs Doublets*, *Phys.Rev.* **D18** (1978) 2574.

[159] R. Barbieri, L. J. Hall, and V. S. Rychkov, *Improved naturalness with a heavy Higgs: An Alternative road to LHC physics*, *Phys.Rev.* **D74** (2006) 015007, [hep-ph/0603188].

[160] R. Hempfling, *The Next-to-minimal Coleman-Weinberg model*, *Phys.Lett.* **B379** (1996) 153–158, [hep-ph/9604278].

[161] C. T. Hill, *Conjecture on the physical implications of the scale anomaly*, hep-th/0510177.

[162] K. A. Meissner and H. Nicolai, *Conformal Symmetry and the Standard Model*, *Phys.Lett.* **B648** (2007) 312–317, [hep-th/0612165].

[163] R. Foot, A. Kobakhidze, K. McDonald, and R. Volkas, *Neutrino mass in radiatively-broken scale-invariant models*, *Phys.Rev.* **D76** (2007) 075014, [arXiv:0706.1829].

[164] R. Foot, A. Kobakhidze, K. L. McDonald, and R. R. Volkas, *A Solution to the hierarchy problem from an almost decoupled hidden sector within a classically scale invariant theory*, *Phys.Rev.* **D77** (2008) 035006, [arXiv:0709.2750].

[165] S. Iso, N. Okada, and Y. Orikasa, *Classically conformal B^- L extended Standard Model*, *Phys.Lett.* **B676** (2009) 81–87, [arXiv:0902.4050].

[166] M. Holthausen, M. Lindner, and M. A. Schmidt, *Radiative Symmetry Breaking of the Minimal Left-Right Symmetric Model*, *Phys.Rev.* **D82** (2010) 055002, [arXiv:0911.0710].

[167] L. Alexander-Nunneley and A. Pilaftsis, *The Minimal Scale Invariant Extension of the Standard Model*, *JHEP* **1009** (2010) 021, [arXiv:1006.5916].

[168] J. S. Lee and A. Pilaftsis, *Radiative Corrections to Scalar Masses and Mixing in a Scale Invariant Two Higgs Doublet Model*, *Phys.Rev.* **D86** (2012) 035004, [arXiv:1201.4891].

[169] M. Heikinheimo, A. Racioppi, M. Raidal, C. Spethmann, and K. Tuominen, *Physical Naturalness and Dynamical Breaking of Classical Scale Invariance*, *Mod.Phys.Lett.* **A29** (2014) 1450077, [arXiv:1304.7006].

[170] T. Hambye and A. Strumia, *Dynamical generation of the weak and Dark Matter scale*, *Phys. Rev.* **D88** (2013) 055022, [arXiv:1306.2329].

[171] A. Farzinnia, H.-J. He, and J. Ren, *Natural Electroweak Symmetry Breaking from Scale Invariant Higgs Mechanism*, *Phys.Lett.* **B727** (2013) 141–150, [arXiv:1308.0295].

[172] V. V. Khoze, *Inflation and Dark Matter in the Higgs Portal of Classically Scale Invariant Standard Model*, *JHEP* **1311** (2013) 215, [arXiv:1308.6338].

[173] C. Tamarit, *Running couplings with a vanishing scale anomaly*, *JHEP* **1312** (2013) 098, [arXiv:1309.0913].

[174] E. Gabrielli, M. Heikinheimo, K. Kannike, A. Racioppi, M. Raidal, and C. Spethmann, *Towards Completing the Standard Model: Vacuum Stability, EWSB and Dark Matter*, *Phys. Rev.* **D89** (2014), no. 1 015017, [arXiv:1309.6632].

[175] O. Antipin, M. Mojaza, and F. Sannino, *Conformal Extensions of the Standard Model with Veltman Conditions*, *Phys. Rev.* **D89** (2014), no. 8 085015, [arXiv:1310.0957].

[176] S. Benic and B. Radovcic, *Electroweak breaking and Dark Matter from the common scale*, *Phys. Lett.* **B732** (2014) 91–94, [arXiv:1401.8183].

[177] V. V. Khoze, C. McCabe, and G. Ro, *Higgs vacuum stability from the dark matter portal*, *JHEP* **08** (2014) 026, [arXiv:1403.4953].

[178] K. Allison, C. T. Hill, and G. G. Ross, *Ultra-weak sector, Higgs boson mass, and the dilaton*, *Phys.Lett.* **B738** (2014) 191–195, [arXiv:1404.6268].

[179] S. Benic and B. Radovcic, *Majorana dark matter in a classically scale invariant model*, *JHEP* **01** (2015) 143, [arXiv:1409.5776].

[180] S. Di Chiara and K. Tuominen, *A minimal model for SU(N) vector dark matter*, *JHEP* **11** (2015) 188, [arXiv:1506.03285].

[181] T. Lee, *A Theory of Spontaneous T Violation*, *Phys.Rev.* **D8** (1973) 1226–1239.

[182] E. Ma, *Verifiable radiative seesaw mechanism of neutrino mass and dark matter*, *Phys.Rev.* **D73** (2006) 077301, [hep-ph/0601225].

[183] M. E. Peskin and D. V. Schroeder, *An Introduction to quantum field theory*. Addison-Wesley, Reading, USA, 1995.

[184] S. L. Adler, J. C. Collins, and A. Duncan, *Energy-Momentum-Tensor Trace Anomaly in Spin 1/2 Quantum Electrodynamics*, *Phys. Rev.* **D15** (1977) 1712. [,318(1976)].

[185] J. C. Collins, A. Duncan, and S. D. Joglekar, *Trace and Dilatation Anomalies in Gauge Theories*, *Phys. Rev.* **D16** (1977) 438–449.

[186] N. K. Nielsen, *The Energy Momentum Tensor in a Nonabelian Quark Gluon Theory*, *Nucl. Phys.* **B120** (1977) 212–220.

[187] S. Coleman, *Aspects of Symmetry*. Cambridge University Press, Cambridge, U.K., 1985.

[188] E. Gildener and S. Weinberg, *Symmetry Breaking and Scalar Bosons*, *Phys. Rev.* **D13** (1976) 3333.

[189] J. K. Esbensen, T. A. Ryttov, and F. Sannino, *Quantum critical behavior of semisimple gauge theories*, *Phys. Rev.* **D93** (2016), no. 4 045009, [arXiv:1512.04402].

[190] E. Mølgaard and F. Sannino, *Asymptotically safe and free chiral theories with and without scalars*, *Phys. Rev.* **D96** (2017), no. 5 056004, [arXiv:1610.03130].

[191] G. M. Pelaggi, F. Sannino, A. Strumia, and E. Vigiani, *Naturalness of asymptotically safe Higgs*, *Front.in Phys.* **5** (2017) 49, [arXiv:1701.01453].

[192] S. Abel and F. Sannino, *Radiative symmetry breaking from interacting UV fixed points*, *Phys. Rev.* **D96** (2017), no. 5 056028, [arXiv:1704.00700].

[193] A. D. Bond and D. F. Litim, *More asymptotic safety guaranteed*, *Phys. Rev.* **D97** (2018), no. 8 085008, [arXiv:1707.04217].

[194] S. Abel and F. Sannino, *Framework for an asymptotically safe Standard Model via dynamical breaking*, *Phys. Rev.* **D96** (2017), no. 5 055021, [arXiv:1707.06638].

[195] A. D. Bond and D. F. Litim, *Asymptotic safety guaranteed in supersymmetry*, *Phys. Rev. Lett.* **119** (2017), no. 21 211601, [arXiv:1709.06953].

[196] A. D. Bond, D. F. Litim, G. Medina Vazquez, and T. Steudtner, *UV conformal window for asymptotic safety*, *Phys. Rev.* **D97** (2018), no. 3 036019, [arXiv:1710.07615].

[197] A. D. Bond and D. F. Litim, *Theorems for Asymptotic Safety of Gauge Theories*, *Eur. Phys. J.* **C77** (2017), no. 6 429, [arXiv:1608.00519]. [Erratum: Eur. Phys. J.C77,no.8,525(2017)].

[198] A. D. Bond and D. F. Litim, *Price of Asymptotic Safety*, arXiv:1801.08527.

[199] A. Palanques-Mestre and P. Pascual, *The $1/N^- f$ Expansion of the γ and Beta Functions in QED*, *Commun. Math. Phys.* **95** (1984) 277.

[200] J. A. Gracey, *The QCD Beta function at O(1/N(f))*, *Phys. Lett.* **B373** (1996) 178–184, [hep-ph/9602214].

[201] B. Holdom, *Large N flavor beta-functions: a recap*, *Phys. Lett.* **B694** (2011) 74–79, [arXiv:1006.2119].

[202] V. V. Khoze and M. Spannowsky, *Higgsploding universe*, *Phys. Rev.* **D96** (2017), no. 7 075042, [arXiv:1707.01531].

[203] O. Antipin, N. A. Dondi, F. Sannino, A. E. Thomsen, and Z.-W. Wang, *Gauge-Yukawa theories: Beta functions at large N_f*, *Phys. Rev.* **D98** (2018), no. 1 016003, [arXiv:1803.09770].

[204] R. Mann, J. Meffe, F. Sannino, T. Steele, Z.-W. Wang, and C. Zhang, *Asymptotically Safe Standard Model via Vectorlike Fermions*, *Phys. Rev. Lett.* **119** (2017), no. 26 261802, [arXiv:1707.02942].

[205] K. Kowalska and E. M. Sessolo, *Gauge contribution to the $1/N_F$ expansion of the Yukawa coupling beta function*, *JHEP* **04** (2018) 027, [arXiv:1712.06859].

[206] T. Hambye and M. H. Tytgat, *Electroweak symmetry breaking induced by dark matter*, *Phys.Lett.* **B659** (2008) 651–655, [arXiv:0707.0633].

[207] H. Davoudiasl and I. M. Lewis, *Right-Handed Neutrinos as the Origin of the Electroweak Scale*, *Phys.Rev.* **D90** (2014), no. 3 033003, [arXiv:1404.6260].

[208] V. Martín Lozano, J. M. Moreno, and C. B. Park, *Resonant Higgs boson pair production in the $hh \to b\bar{b}\, WW \to b\bar{b}\ell^+\nu\ell^-\overline{\nu}$ decay channel*, *JHEP* **08** (2015) 004, [arXiv:1501.03799].

[209] T. Robens and T. Stefaniak, *Status of the Higgs Singlet Extension of the Standard Model after LHC Run 1*, *Eur. Phys. J.* **C75** (2015) 104, [arXiv:1501.02234].

[210] A. Falkowski, C. Gross, and O. Lebedev, *A second Higgs from the Higgs portal*, *JHEP* **05** (2015) 057, [arXiv:1502.01361].

[211] G. Belanger, F. Boudjema, A. Pukhov, and A. Semenov, *MicrOMEGAs: A Program for calculating the relic density in the MSSM*, *Comput. Phys. Commun.* **149** (2002) 103–120, [hep-ph/0112278].

[212] L. Lopez Honorez, E. Nezri, J. F. Oliver, and M. H. Tytgat, *The Inert Doublet Model: An Archetype for Dark Matter*, *JCAP* **0702** (2007) 028, [hep-ph/0612275].

[213] A. Goudelis, B. Herrmann, and O. Stål, *Dark matter in the Inert Doublet Model after the discovery of a Higgs-like boson at the LHC*, *JHEP* **1309** (2013) 106, [arXiv:1303.3010].

[214] L. Lopez Honorez and C. E. Yaguna, *A new viable region of the inert doublet model*, *JCAP* **1101** (2011) 002, [arXiv:1011.1411].

[215] **XENON100** Collaboration, E. Aprile et al., *Limits on spin-dependent WIMP-nucleon cross sections from 225 live days of XENON100 data*, *Phys.Rev.Lett.* **111** (2013), no. 2 021301, [arXiv:1301.6620].

[216] G. Belanger, B. Dumont, A. Goudelis, B. Herrmann, S. Kraml, et al., *Dilepton constraints in the Inert Doublet Model from Run 1 of the LHC*, *Phys.Rev.* **D91** (2015), no. 11 115011, [arXiv:1503.07367].

[217] A. Arhrib, Y.-L. S. Tsai, Q. Yuan, and T.-C. Yuan, *An Updated Analysis of Inert Higgs Doublet Model in light of the Recent Results from LUX, PLANCK, AMS-02 and LHC*, *JCAP* **1406** (2014) 030, [arXiv:1310.0358].

[218] T. Hambye, F.-S. Ling, L. Lopez Honorez, and J. Rocher, *Scalar Multiplet Dark Matter*, *JHEP* **0907** (2009) 090, [arXiv:0903.4010].

[219] M. Gustafsson, *The Inert Doublet Model and Its Phenomenology*, *PoS (CHARGED 2010)* (2010) 030, [arXiv:1106.1719].

[220] A. Dutta Banik and D. Majumdar, *Inert doublet dark matter with an additional scalar singlet and 125 GeV Higgs boson*, *Eur.Phys.J.* **C74** (2014), no. 11 3142, [arXiv:1404.5840].

[221] **LUX** Collaboration, D. S. Akerib et al., *First results from the LUX dark matter experiment at the Sanford Underground Research Facility*, *Phys. Rev. Lett.* **112** (2014) 091303, [arXiv:1310.8214].

[222] J. Billard, L. Strigari, and E. Figueroa-Feliciano, *Implication of neutrino backgrounds on the reach of next generation dark matter direct detection experiments*, *Phys.Rev.* **D89** (2014), no. 2 023524, [arXiv:1307.5458].

[223] **CDMS-II** Collaboration, P. L. Brink et al., *Beyond the CDMS-II dark matter search: SuperCDMS*, *eConf* **C041213** (2004) 2529, [astro-ph/0503583].

[224] **XENON1T** Collaboration, E. Aprile, *The XENON1T Dark Matter Search Experiment*, *Springer Proc.Phys.* **C12-02-22** (2013) 93–96, [arXiv:1206.6288].

[225] M. Klasen, C. E. Yaguna, and J. D. Ruiz-Alvarez, *Electroweak corrections to the direct detection cross section of inert higgs dark matter*, *Phys.Rev.* **D87** (2013) 075025, [arXiv:1302.1657].

[226] T. Abe and R. Sato, *Quantum corrections to the spin-independent cross section of the inert doublet dark matter*, *JHEP* **1503** (2015) 109, [arXiv:1501.04161].

[227] N. Khan and S. Rakshit, *Constraints on inert dark matter from metastability of electroweak vacuum*, arXiv:1503.03085.

[228] F. Staub, *SARAH 4: A tool for (not only SUSY) model builders*, *Comput.Phys.Commun.* **185** (2014) 1773–1790, [arXiv:1309.7223].

[229] S. Kanemura, T. Kubota, and E. Takasugi, *Lee-Quigg-Thacker bounds for Higgs boson masses in a two doublet model*, *Phys.Lett.* **B313** (1993) 155–160, [hep-ph/9303263].

[230] I. Ginzburg and I. Ivanov, *Tree-level unitarity constraints in the most general 2HDM*, *Phys.Rev.* **D72** (2005) 115010, [hep-ph/0508020].

[231] B. Swiezewska, *Yukawa independent constraints for two-Higgs-doublet models with a 125 GeV Higgs boson*, *Phys. Rev.* **D88** (2013), no. 5 055027, [arXiv:1209.5725]. [Erratum: Phys. Rev.D88,no.11,119903(2013)].

[232] **ATLAS, CDF, CMS, D0** Collaboration, *First combination of Tevatron and LHC measurements of the top-quark mass*, arXiv:1403.4427.

[233] V. V. Khoze and G. Ro, *Leptogenesis and Neutrino Oscillations in the Classically Conformal Standard Model with the Higgs Portal*, *JHEP* **10** (2013) 075, [arXiv:1307.3764].

[234] W.-F. Chang, J. N. Ng, and J. M. S. Wu, *Shadow Higgs from a scale-invariant hidden U(1)(s) model*, *Phys. Rev.* **D75** (2007) 115016, [hep-ph/0701254].

[235] C. D. Carone and R. Ramos, *Classical scale-invariance, the electroweak scale and vector dark matter*, *Phys. Rev.* **D88** (2013) 055020, [arXiv:1307.8428].

[236] A. Karam and K. Tamvakis, *Dark matter and neutrino masses from a scale-invariant multi-Higgs portal*, *Phys. Rev.* **D92** (2015), no. 7 075010, [arXiv:1508.03031].

[237] M. Drewes and B. Garbrecht, *Leptogenesis from a GeV Seesaw without Mass Degeneracy*, *JHEP* **03** (2013) 096, [arXiv:1206.5537].

[238] S. Abel and A. Mariotti, *Novel Higgs Potentials from Gauge Mediation of Exact Scale Breaking*, *Phys. Rev.* **D89** (2014), no. 12 125018, [arXiv:1312.5335].

[239] K. Ghorbani and H. Ghorbani, *Scalar Dark Matter in Scale Invariant Standard Model*, *JHEP* **04** (2016) 024, [arXiv:1511.08432].

[240] A. Ahriche, A. Manning, K. L. McDonald, and S. Nasri, *Scale-Invariant Models with One-Loop Neutrino Mass and Dark Matter Candidates*, *Phys. Rev.* **D94** (2016), no. 5 053005, [arXiv:1604.05995].

[241] C. Gross, O. Lebedev, and Y. Mambrini, *Non-Abelian gauge fields as dark matter*, *JHEP* **08** (2015) 158, [arXiv:1505.07480].

[242] V. V. Khoze and G. Ro, *Dark matter monopoles, vectors and photons*, *JHEP* **10** (2014) 061, [arXiv:1406.2291].

[243] S. P. Martin, *Two loop effective potential for a general renormalizable theory and softly broken supersymmetry*, *Phys. Rev.* **D65** (2002) 116003, [hep-ph/0111209].

[244] J. A. Casas and A. Ibarra, *Oscillating neutrinos and muon —> e, gamma*, *Nucl. Phys.* **B618** (2001) 171–204, [hep-ph/0103065].

[245] C. Boehm, M. J. Dolan, and C. McCabe, *A weighty interpretation of the Galactic Centre excess*, *Phys. Rev.* **D90** (2014), no. 2 023531, [arXiv:1404.4977].

[246] J. Billard, L. Strigari, and E. Figueroa-Feliciano, *Implication of neutrino backgrounds on the reach of next generation dark matter direct detection experiments*, *Phys. Rev.* **D89** (2014), no. 2 023524, [arXiv:1307.5458].

[247] S. Baek, P. Ko, W.-I. Park, and E. Senaha, *Higgs Portal Vector Dark Matter : Revisited*, *JHEP* **05** (2013) 036, [arXiv:1212.2131].

[248] C. Arina, T. Hambye, A. Ibarra, and C. Weniger, *Intense Gamma-Ray Lines from Hidden Vector Dark Matter Decay*, *JCAP* **1003** (2010) 024, [arXiv:0912.4496].

[249] S. Davidson and A. Ibarra, *A Lower bound on the right-handed neutrino mass from leptogenesis*, *Phys. Lett.* **B535** (2002) 25–32, [hep-ph/0202239].

[250] B. Shuve and I. Yavin, *Baryogenesis through Neutrino Oscillations: A Unified Perspective*, *Phys. Rev.* **D89** (2014), no. 7 075014, [arXiv:1401.2459].

[251] D. Besak and D. Bodeker, *Thermal production of ultrarelativistic right-handed neutrinos: Complete leading-order results*, *JCAP* **1203** (2012) 029, [arXiv:1202.1288].

[252] M. C. Gonzalez-Garcia, M. Maltoni, and T. Schwetz, *Updated fit to three neutrino mixing: status of leptonic CP violation*, *JHEP* **11** (2014) 052, [arXiv:1409.5439].

[253] C. Bonilla, D. Sokolowska, N. Darvishi, J. L. Diaz-Cruz, and M. Krawczyk, *IDMS: Inert Dark Matter Model with a complex singlet*, *J. Phys.* **G43** (2016), no. 6 065001, [arXiv:1412.8730].

[254] M. Hindmarsh, R. Kirk, J. M. No, and S. M. West, *Dark Matter with Topological Defects in the Inert Doublet Model*, *JCAP* **1505** (2015), no. 05 048, [arXiv:1412.4821].

[255] P. Ko, Y. Omura, and C. Yu, *Dark matter and dark force in the type-I inert 2HDM with local U(1)$_H$ gauge symmetry*, *JHEP* **1411** (2014) 054, [arXiv:1405.2138].

[256] J. Guo, Z. Kang, P. Ko, and Y. Orikasa, *Accidental dark matter: Case in the scale invariant local B-L model*, *Phys.Rev.* **D91** (2015), no. 11 115017, [arXiv:1502.00508].

[257] E. Lundstrom, M. Gustafsson, and J. Edsjo, *The Inert Doublet Model and LEP II Limits*, *Phys.Rev.* **D79** (2009) 035013, [arXiv:0810.3924].

[258] E. Dolle, X. Miao, S. Su, and B. Thomas, *Dilepton Signals in the Inert Doublet Model*, *Phys.Rev.* **D81** (2010) 035003, [arXiv:0909.3094].

[259] M. Aoki, S. Kanemura, and H. Yokoya, *Reconstruction of Inert Doublet Scalars at the International Linear Collider*, *Phys.Lett.* **B725** (2013) 302–309, [arXiv:1303.6191].

[260] M. Krawczyk, D. Sokolowska, P. Swaczyna, and B. Swiezewska, *Constraining Inert Dark Matter by $R_{\gamma\gamma}$ and WMAP data*, *JHEP* **09** (2013) 055, [arXiv:1305.6266].

[261] E. W. Kolb and M. S. Turner, *The Early Universe*, *Front. Phys.* **69** (1990) 1–547.

[262] O. Buchmueller, M. J. Dolan, and C. McCabe, *Beyond Effective Field Theory for Dark Matter Searches at the LHC*, *JHEP* **01** (2014) 025, [arXiv:1308.6799].

[263] M. Beltran, D. Hooper, E. W. Kolb, and Z. C. Krusberg, *Deducing the nature of dark matter from direct and indirect detection experiments in the absence of collider signatures of new physics*, *Phys. Rev.* **D80** (2009) 043509, [arXiv:0808.3384].

[264] Q.-H. Cao, C.-R. Chen, C. S. Li, and H. Zhang, *Effective Dark Matter Model: Relic density, CDMS II, Fermi LAT and LHC*, *JHEP* **08** (2011) 018, [arXiv:0912.4511].

[265] J. Goodman, M. Ibe, A. Rajaraman, W. Shepherd, T. M. P. Tait, and H.-B. Yu, *Constraints on Light Majorana dark Matter from Colliders*, *Phys. Lett.* **B695** (2011) 185–188, [arXiv:1005.1286].

[266] Y. Bai, P. J. Fox, and R. Harnik, *The Tevatron at the Frontier of Dark Matter Direct Detection*, *JHEP* **12** (2010) 048, [arXiv:1005.3797].

[267] J. Fan, M. Reece, and L.-T. Wang, *Non-relativistic effective theory of dark matter direct detection*, *JCAP* **1011** (2010) 042, [arXiv:1008.1591].

[268] J. Goodman, M. Ibe, A. Rajaraman, W. Shepherd, T. M. P. Tait, and H.-B. Yu, *Constraints on Dark Matter from Colliders*, *Phys. Rev.* **D82** (2010) 116010, [arXiv:1008.1783].

[269] J.-M. Zheng, Z.-H. Yu, J.-W. Shao, X.-J. Bi, Z. Li, and H.-H. Zhang, *Constraining the interaction strength between dark matter and visible matter: I. fermionic dark matter*, *Nucl. Phys.* **B854** (2012) 350–374, [arXiv:1012.2022].

[270] M. R. Buckley, *Asymmetric Dark Matter and Effective Operators*, *Phys. Rev.* **D84** (2011) 043510, [arXiv:1104.1429].

[271] Z.-H. Yu, J.-M. Zheng, X.-J. Bi, Z. Li, D.-X. Yao, and H.-H. Zhang, *Constraining the interaction strength between dark matter and visible matter: II. scalar, vector and spin-3/2 dark matter*, *Nucl. Phys.* **B860** (2012) 115–151, [arXiv:1112.6052].

[272] A. Rajaraman, W. Shepherd, T. M. P. Tait, and A. M. Wijangco, *LHC Bounds on Interactions of Dark Matter*, *Phys. Rev.* **D84** (2011) 095013, [arXiv:1108.1196].

[273] K. Cheung, P.-Y. Tseng, Y.-L. S. Tsai, and T.-C. Yuan, *Global Constraints on Effective Dark Matter Interactions: Relic Density, Direct Detection, Indirect Detection, and Collider*, *JCAP* **1205** (2012) 001, [arXiv:1201.3402].

[274] R. C. Cotta, J. L. Hewett, M. P. Le, and T. G. Rizzo, *Bounds on Dark Matter Interactions with Electroweak Gauge Bosons*, *Phys. Rev.* **D88** (2013) 116009, [arXiv:1210.0525].

[275] H. Dreiner, D. Schmeier, and J. Tattersall, *Contact Interactions Probe Effective Dark Matter Models at the LHC*, *EPL* **102** (2013), no. 5 51001, [arXiv:1303.3348].

[276] U. Haisch, A. Hibbs, and E. Re, *Determining the structure of dark-matter couplings at the LHC*, *Phys. Rev.* **D89** (2014) 034009, [arXiv:1311.7131].

[277] G. Busoni, A. De Simone, E. Morgante, and A. Riotto, *On the Validity of the Effective Field Theory for Dark Matter Searches at the LHC*, *Phys. Lett.* **B728** (2014) 412–421, [arXiv:1307.2253].

[278] G. Busoni, A. De Simone, J. Gramling, E. Morgante, and A. Riotto, *On the Validity of the Effective Field Theory for Dark Matter Searches at the LHC, Part II: Complete Analysis for the s-channel*, *JCAP* **1406** (2014) 060, [arXiv:1402.1275].

[279] S. A. Malik et al., *Interplay and Characterization of Dark Matter Searches at Colliders and in Direct Detection Experiments*, *Phys. Dark Univ.* **9-10** (2015) 51–58, [arXiv:1409.4075].

[280] F. Kahlhoefer, K. Schmidt-Hoberg, T. Schwetz, and S. Vogl, *Implications of unitarity and gauge invariance for simplified dark matter models*, *JHEP* **02** (2016) 016, [arXiv:1510.02110].

[281] J. Ellis, M. Fairbairn, and P. Tunney, *Anomaly-Free Dark Matter Models are not so Simple*, *JHEP* **08** (2017) 053, [arXiv:1704.03850].

[282] S. Ipek, D. McKeen, and A. E. Nelson, *A Renormalizable Model for the Galactic Center Gamma Ray Excess from Dark Matter Annihilation*, *Phys. Rev.* **D90** (2014), no. 5 055021, [arXiv:1404.3716].

[283] D. Goncalves, P. A. N. Machado, and J. M. No, *Simplified Models for Dark Matter Face their Consistent Completions*, *Phys. Rev.* **D95** (2017), no. 5 055027, [arXiv:1611.04593].

[284] M. Bauer, U. Haisch, and F. Kahlhoefer, *Simplified dark matter models with two Higgs doublets: I. Pseudoscalar mediators*, *JHEP* **05** (2017) 138, [arXiv:1701.07427].

[285] A. Albert et al., *Towards the next generation of simplified Dark Matter models*, *Phys. Dark Univ.* **16** (2017) 49–70, [arXiv:1607.06680].

[286] F. Kahlhoefer, *Review of LHC Dark Matter Searches*, *Int. J. Mod. Phys.* **A32** (2017), no. 13 1730006, [arXiv:1702.02430].

[287] C. Cheung, L. J. Hall, D. Pinner, and J. T. Ruderman, *Prospects and Blind Spots for Neutralino Dark Matter*, *JHEP* **05** (2013) 100, [arXiv:1211.4873].

[288] H. Baer, V. Barger, and D. Mickelson, *Direct and indirect detection of higgsino-like WIMPs: concluding the story of electroweak naturalness*, *Phys. Lett.* **B726** (2013) 330–336, [arXiv:1303.3816].

[289] D. Barducci, A. Belyaev, A. K. M. Bharucha, W. Porod, and V. Sanz, *Uncovering Natural Supersymmetry via the interplay between the LHC and Direct Dark Matter Detection*, *JHEP* **07** (2015) 066, [arXiv:1504.02472].

[290] M. Badziak, A. Delgado, M. Olechowski, S. Pokorski, and K. Sakurai, *Detecting underabundant neutralinos*, *JHEP* **11** (2015) 053, [arXiv:1506.07177].

[291] P. Huang, R. A. Roglans, D. D. Spiegel, Y. Sun, and C. E. M. Wagner, *Constraints on Supersymmetric Dark Matter for Heavy Scalar Superpartners*, *Phys. Rev.* **D95** (2017), no. 9 095021, [arXiv:1701.02737].

[292] M. Badziak, M. Olechowski, and P. Szczerbiak, *Is well-tempered neutralino in MSSM still alive after 2016 LUX results?*, *Phys. Lett.* **B770** (2017) 226–235, [arXiv:1701.05869].

[293] E. A. Bagnaschi et al., *Supersymmetric Dark Matter after LHC Run 1*, *Eur. Phys. J.* **C75** (2015) 500, [arXiv:1508.01173].

[294] K. J. de Vries et al., *The pMSSM10 after LHC Run 1*, *Eur. Phys. J.* **C75** (2015), no. 9 422, [arXiv:1504.03260].

[295] E. Bagnaschi et al., *Likelihood Analysis of Supersymmetric SU(5) GUTs*, *Eur. Phys. J.* **C77** (2017), no. 2 104, [arXiv:1610.10084].

[296] T. Cohen, M. Lisanti, A. Pierce, and T. R. Slatyer, *Wino Dark Matter Under Siege*, *JCAP* **1310** (2013) 061, [arXiv:1307.4082].

[297] J. Fan and M. Reece, *In Wino Veritas? Indirect Searches Shed Light on Neutralino Dark Matter*, *JHEP* **10** (2013) 124, [arXiv:1307.4400].

[298] M. Beneke, A. Bharucha, A. Hryczuk, S. Recksiegel, and P. Ruiz-Femenia, *The last refuge of mixed wino-Higgsino dark matter*, *JHEP* **01** (2017) 002, [arXiv:1611.00804].

[299] T. Cohen, J. Kearney, A. Pierce, and D. Tucker-Smith, *Singlet-Doublet Dark Matter*, *Phys. Rev.* **D85** (2012) 075003, [arXiv:1109.2604].

[300] M. Chala, F. Kahlhoefer, M. McCullough, G. Nardini, and K. Schmidt-Hoberg, *Constraining Dark Sectors with Monojets and Dijets*, *JHEP* **07** (2015) 089, [arXiv:1503.05916].

[301] M. R. Buckley, D. Feld, and D. Goncalves, *Scalar Simplified Models for Dark Matter*, *Phys. Rev.* **D91** (2015) 015017, [arXiv:1410.6497].

[302] P. Harris, V. V. Khoze, M. Spannowsky, and C. Williams, *Constraining Dark Sectors at Colliders: Beyond the Effective Theory Approach*, *Phys. Rev.* **D91** (2015) 055009, [arXiv:1411.0535].

[303] U. Haisch and E. Re, *Simplified dark matter top-quark interactions at the LHC*, *JHEP* **06** (2015) 078, [arXiv:1503.00691].

[304] O. Buchmueller, M. J. Dolan, S. A. Malik, and C. McCabe, *Characterising dark matter searches at colliders and direct detection experiments: Vector mediators*, *JHEP* **01** (2015) 037, [arXiv:1407.8257].

[305] D. Abercrombie et al., *Dark Matter Benchmark Models for Early LHC Run-2 Searches: Report of the ATLAS/CMS Dark Matter Forum*, arXiv:1507.00966.

[306] G. Busoni et al., *Recommendations on presenting LHC searches for missing transverse energy signals using simplified s-channel models of dark matter*, arXiv:1603.04156.

[307] T. Golling et al., *Physics at a 100 TeV pp collider: beyond the Standard Model phenomena*, *CERN Yellow Report* (2017), no. 3 441–634, [arXiv:1606.00947].

[308] P. Harris, V. V. Khoze, M. Spannowsky, and C. Williams, *Closing up on Dark Sectors at Colliders: from 1/4 to 100 TeV*, *Phys. Rev.* **D93** (2016), no. 5 054030, [arXiv:1509.02904].

[309] V. V. Khoze, G. Ro, and M. Spannowsky, *Spectroscopy of scalar mediators to dark matter at the LHC and at 100 TeV*, *Phys. Rev.* **D92** (2015), no. 7 075006, [arXiv:1505.03019].

[310] A. Berlin, S. Gori, T. Lin, and L.-T. Wang, *Pseudoscalar Portal Dark Matter*, *Phys. Rev.* **D92** (2015) 015005, [arXiv:1502.06000].

[311] S. Baek, P. Ko, M. Park, W.-I. Park, and C. Yu, *Beyond the Dark matter effective field theory and a simplified model approach at colliders*, *Phys. Lett.* **B756** (2016) 289–294, [arXiv:1506.06556].

[312] C. Englert, M. McCullough, and M. Spannowsky, *S-Channel Dark Matter Simplified Models and Unitarity*, *Phys. Dark Univ.* **14** (2016) 48–56, [arXiv:1604.07975].

[313] S. Baek, P. Ko, and J. Li, *Minimal renormalizable simplified dark matter model with a pseudoscalar mediator*, *Phys. Rev.* **D95** (2017), no. 7 075011, [arXiv:1701.04131].

[314] M. J. Baker et al., *The Coannihilation Codex*, *JHEP* **12** (2015) 120, [arXiv:1510.03434].

[315] M. Garny, A. Ibarra, M. Pato, and S. Vogl, *Closing in on mass-degenerate dark matter scenarios with antiprotons and direct detection*, *JCAP* **1211** (2012) 017, [arXiv:1207.1431].

[316] C. Kelso, J. Kumar, P. Sandick, and P. Stengel, *Charged mediators in dark matter scattering with nuclei and the strangeness content of nucleons*, *Phys. Rev.* **D91** (2015) 055028, [arXiv:1411.2634].

[317] A. Ibarra, A. Pierce, N. R. Shah, and S. Vogl, *Anatomy of Coannihilation with a Scalar Top Partner*, *Phys. Rev.* **D91** (2015), no. 9 095018, [arXiv:1501.03164].

[318] J. Ellis, F. Luo, and K. A. Olive, *Gluino Coannihilation Revisited*, *JHEP* **09** (2015) 127, [arXiv:1503.07142].

[319] M. Buschmann, S. El Hedri, A. Kaminska, J. Liu, M. de Vries, X.-P. Wang, F. Yu, and J. Zurita, *Hunting for dark matter coannihilation by mixing dijet resonances and missing transverse energy*, *JHEP* **09** (2016) 033, [arXiv:1605.08056].

[320] M. Cirelli, N. Fornengo, and A. Strumia, *Minimal dark matter*, *Nucl. Phys.* **B753** (2006) 178–194, [hep-ph/0512090].

[321] J. R. Ellis, T. Falk, and K. A. Olive, *Neutralino - Stau coannihilation and the cosmological upper limit on the mass of the lightest supersymmetric particle*, *Phys. Lett.* **B444** (1998) 367–372, [hep-ph/9810360].

[322] T. Jittoh, J. Sato, T. Shimomura, and M. Yamanaka, *Long life stau in the minimal supersymmetric standard model*, *Phys. Rev.* **D73** (2006) 055009, [hep-ph/0512197]. [Erratum: Phys. Rev.D87,no.1,019901(2013)].

[323] S. Kaneko, J. Sato, T. Shimomura, O. Vives, and M. Yamanaka, *Measuring lepton flavor violation at LHC with a long-lived slepton in the coannihilation region*, *Phys. Rev.* **D87** (2013), no. 3 039904, [arXiv:0811.0703]. [Phys. Rev.D78,no.11,116013(2008)].

[324] T. Jittoh, K. Kohri, M. Koike, J. Sato, T. Shimomura, and M. Yamanaka, *Stau relic density at the Big-Bang nucleosynthesis era consistent with the abundance of the light element nuclei in the coannihilation scenario*, *Phys. Rev.* **D82** (2010) 115030, [arXiv:1001.1217].

[325] M. Citron, J. Ellis, F. Luo, J. Marrouche, K. A. Olive, and K. J. de Vries, *End of the CMSSM coannihilation strip is nigh*, *Phys. Rev.* **D87** (2013), no. 3 036012, [arXiv:1212.2886].

[326] Y. Konishi, S. Ohta, J. Sato, T. Shimomura, K. Sugai, and M. Yamanaka, *First evidence of the constrained minimal supersymmetric standard model is appearing soon*, *Phys. Rev.* **D89** (2014), no. 7 075006, [arXiv:1309.2067].

[327] N. Desai, J. Ellis, F. Luo, and J. Marrouche, *Closing in on the Tip of the CMSSM Stau Coannihilation Strip*, *Phys. Rev.* **D90** (2014), no. 5 055031, [arXiv:1404.5061].

[328] K. Griest and D. Seckel, *Three exceptions in the calculation of relic abundances*, *Phys. Rev.* **D43** (1991) 3191–3203.

[329] A. Alloul, N. D. Christensen, C. Degrande, C. Duhr, and B. Fuks, *FeynRules 2.0 - A complete toolbox for tree-level phenomenology*, *Comput. Phys. Commun.* **185** (2014) 2250–2300, [arXiv:1310.1921].

[330] A. Semenov, *LanHEP — A package for automatic generation of Feynman rules from the Lagrangian. Version 3.2*, *Comput. Phys. Commun.* **201** (2016) 167–170, [arXiv:1412.5016].

[331] J. Kopp, L. Michaels, and J. Smirnov, *Loopy Constraints on Leptophilic Dark Matter and Internal Bremsstrahlung*, *JCAP* **1404** (2014) 022, [arXiv:1401.6457].

[332] **Fermi-LAT** Collaboration, M. Ackermann et al., *Search for Gamma-ray Spectral Lines with the Fermi Large Area Telescope and Dark Matter Implications*, *Phys. Rev.* **D88** (2013) 082002, [arXiv:1305.5597].

[333] T. Toma, *Internal Bremsstrahlung Signature of Real Scalar Dark Matter and Consistency with Thermal Relic Density*, *Phys. Rev. Lett.* **111** (2013) 091301, [arXiv:1307.6181].

[334] F. Giacchino, L. Lopez-Honorez, and M. H. G. Tytgat, *Scalar Dark Matter Models with Significant Internal Bremsstrahlung*, *JCAP* **1310** (2013) 025, [arXiv:1307.6480].

[335] J. Kumar, P. Sandick, F. Teng, and T. Yamamoto, *Gamma-ray Signals from Dark Matter Annihilation Via Charged Mediators*, *Phys. Rev.* **D94** (2016), no. 1 015022, [arXiv:1605.03224].

[336] **CTA Consortium** Collaboration, M. Actis et al., *Design concepts for the Cherenkov Telescope Array CTA: An advanced facility for ground-based high-energy gamma-ray astronomy*, *Exper. Astron.* **32** (2011) 193–316, [arXiv:1008.3703].

[337] M. Garny, A. Ibarra, M. Pato, and S. Vogl, *Internal bremsstrahlung signatures in light of direct dark matter searches*, *JCAP* **1312** (2013) 046, [arXiv:1306.6342].

[338] J. Alwall, R. Frederix, S. Frixione, V. Hirschi, F. Maltoni, O. Mattelaer, H. S. Shao, T. Stelzer, P. Torrielli, and M. Zaro, *The automated computation of tree-level and next-to-leading order differential cross sections, and their matching to parton shower simulations*, *JHEP* **07** (2014) 079, [arXiv:1405.0301].

[339] Z.-H. Yu, X.-J. Bi, Q.-S. Yan, and P.-F. Yin, *Tau Portal Dark Matter models at the LHC*, *Phys. Rev.* **D91** (2015), no. 3 035008, [arXiv:1410.3347].

[340] M. Low and L.-T. Wang, *Neutralino dark matter at 14 TeV and 100 TeV*, *JHEP* **08** (2014) 161, [arXiv:1404.0682].

[341] A. Belyaev, N. D. Christensen, and A. Pukhov, *CalcHEP 3.4 for collider physics within and beyond the Standard Model*, *Comput. Phys. Commun.* **184** (2013) 1729–1769, [arXiv:1207.6082].

[342] **ATLAS** Collaboration, M. Aaboud et al., *Search for metastable heavy charged particles with large ionization energy loss in pp collisions at $\sqrt{s} = 13$ TeV using the ATLAS experiment*, *Phys. Rev.* **D93** (2016), no. 11 112015, [arXiv:1604.04520].

[343] **ATLAS** Collaboration, M. Aaboud et al., *Search for heavy long-lived charged R-hadrons with the ATLAS detector in 3.2 fb^{-1} of proton–proton collision data at $\sqrt{s} = 13$ TeV*, *Phys. Lett.* **B760** (2016) 647–665, [arXiv:1606.05129].

[344] **CMS** Collaboration, V. Khachatryan et al., *Search for long-lived charged particles in proton-proton collisions at $\sqrt{s} = 13$ TeV*, *Phys. Rev.* **D94** (2016), no. 11 112004, [arXiv:1609.08382].

[345] **CMS** Collaboration, V. Khachatryan et al., *Constraints on the pMSSM, AMSB model and on other models from the search for long-lived charged particles in proton-proton collisions at sqrt(s) = 8 TeV*, *Eur. Phys. J.* **C75** (2015), no. 7 325, [arXiv:1502.02522].

[346] **MoEDAL** Collaboration, B. Acharya et al., *The Physics Programme Of The MoEDAL Experiment At The LHC*, *Int. J. Mod. Phys.* **A29** (2014) 1430050, [arXiv:1405.7662].

[347] **ALEPH** Collaboration, A. Heister et al., *Absolute lower limits on the masses of selectrons and sneutrinos in the MSSM*, *Phys. Lett.* **B544** (2002) 73–88, [hep-ex/0207056].

[348] **L3** Collaboration, P. Achard et al., *Search for scalar leptons and scalar quarks at LEP*, *Phys. Lett.* **B580** (2004) 37–49, [hep-ex/0310007].

[349] **DELPHI** Collaboration, J. Abdallah et al., *Searches for supersymmetric particles in e+ e- collisions up to 208-GeV and interpretation of the results within the MSSM*, *Eur. Phys. J.* **C31** (2003) 421–479, [hep-ex/0311019].

[350] G. Salam and A. Weiler, "Collider reach." http://collider-reach.web.cern.ch/.

[351] J. Heisig, A. Lessa, and L. Quertenmont, *Simplified Models for Exotic BSM Searches*, *JHEP* **12** (2015) 087, [arXiv:1509.00473].

[352] J. A. Evans and J. Shelton, *Long-Lived Staus and Displaced Leptons at the LHC*, *JHEP* **04** (2016) 056, [arXiv:1601.01326].

[353] T. Flacke, A. Menon, and D. J. Phalen, *Non-minimal universal extra dimensions*, *Phys. Rev.* **D79** (2009) 056009, [arXiv:0811.1598].

[354] S. Arrenberg, L. Baudis, K. Kong, K. T. Matchev, and J. Yoo, *Kaluza-Klein Dark Matter: Direct Detection vis-a-vis LHC*, *Phys. Rev.* **D78** (2008) 056002, [arXiv:0805.4210].

[355] B. A. Dobrescu, D. Hooper, K. Kong, and R. Mahbubani, *Spinless photon dark matter from two universal extra dimensions*, *JCAP* **0710** (2007) 012, [arXiv:0706.3409].

[356] A. Djouadi, O. Lebedev, Y. Mambrini, and J. Quevillon, *Implications of LHC searches for Higgs–portal dark matter*, *Phys. Lett.* **B709** (2012) 65–69, [arXiv:1112.3299].

[357] L. Lopez-Honorez, T. Schwetz, and J. Zupan, *Higgs portal, fermionic dark matter, and a Standard Model like Higgs at 125 GeV*, *Phys. Lett.* **B716** (2012) 179–185, [arXiv:1203.2064].

[358] A. Djouadi, A. Falkowski, Y. Mambrini, and J. Quevillon, *Direct Detection of Higgs-Portal Dark Matter at the LHC*, *Eur. Phys. J.* **C73** (2013), no. 6 2455, [arXiv:1205.3169].

[359] A. Freitas, S. Westhoff, and J. Zupan, *Integrating in the Higgs Portal to Fermion Dark Matter*, *JHEP* **09** (2015) 015, [arXiv:1506.04149].

[360] J. Brooke, M. R. Buckley, P. Dunne, B. Penning, J. Tamanas, and M. Zgubic, *Vector Boson Fusion Searches for Dark Matter at the LHC*, *Phys. Rev.* **D93** (2016), no. 11 113013, [arXiv:1603.07739].

[361] **GAMBIT** Collaboration, P. Athron et al., *Global fits of GUT-scale SUSY models with GAMBIT*, *Eur. Phys. J.* **C77** (2017), no. 12 824, [arXiv:1705.07935].

[362] S. Moretti, K. Odagiri, P. Richardson, M. H. Seymour, and B. R. Webber, *Implementation of supersymmetric processes in the HERWIG event generator*, *JHEP* **04** (2002) 028, [hep-ph/0204123].

[363] H. K. Dreiner, H. E. Haber, and S. P. Martin, *Two-component spinor techniques and Feynman rules for quantum field theory and supersymmetry*, *Phys. Rept.* **494** (2010) 1–196, [arXiv:0812.1594].

[364] K. Kong and S. C. Park, *Phenomenology of Top partners at the ILC*, *JHEP* **08** (2007) 038, [hep-ph/0703057].

[365] M. Berggren, F. Brümmer, J. List, G. Moortgat-Pick, T. Robens, K. Rolbiecki, and H. Sert, *Tackling light higgsinos at the ILC*, *Eur. Phys. J.* **C73** (2013), no. 12 2660, [arXiv:1307.3566].

[366] M. Berggren, *Simplified SUSY at the ILC*, in *Proceedings, 2013 Community Summer Study on the Future of U.S. Particle Physics: Snowmass on the Mississippi (CSS2013): Minneapolis, MN, USA, July 29-August 6, 2013*, 2013. arXiv:1308.1461.

[367] R. Brito, V. Cardoso, and P. Pani, *Superradiance*, *Lect. Notes Phys.* **906** (2015) pp.1–237, [arXiv:1501.06570].

[368] W. H. Press and S. A. Teukolsky, *Perturbations of a Rotating Black Hole. II. Dynamical Stability of the Kerr Metric*, *Astrophys. J.* **185** (1973) 649–674.

[369] S. A. Teukolsky and W. H. Press, *Perturbations of a rotating black hole. III - Interaction of the hole with gravitational and electromagnet ic radiation*, *Astrophys. J.* **193** (1974) 443–461.

[370] T. Damour, N. Deruelle, and R. Ruffini, *On Quantum Resonances in Stationary Geometries*, *Lett. Nuovo Cim.* **15** (1976) 257–262.

[371] T. J. M. Zouros and D. M. Eardley, *Instabilities of massive scalar perturbations of a rotating black hole*, *Annals Phys.* **118** (1979) 139–155.

[372] S. L. Detweiler, *Klein-Gordon equation and rotating black holes*, *Phys. Rev.* **D22** (1980) 2323–2326.

[373] V. Cardoso, P. Pani, and T.-T. Yu, *Superradiance in rotating stars and pulsar-timing constraints on dark photons*, *Phys. Rev.* **D95** (2017), no. 12 124056, [arXiv:1704.06151].

[374] P. Pani, V. Cardoso, L. Gualtieri, E. Berti, and A. Ishibashi, *Black hole bombs and photon mass bounds*, *Phys. Rev. Lett.* **109** (2012) 131102, [arXiv:1209.0465].

[375] M. Baryakhtar, R. Lasenby, and M. Teo, *Black Hole Superradiance Signatures of Ultralight Vectors*, *Phys. Rev.* **D96** (2017), no. 3 035019, [arXiv:1704.05081].

[376] R. Brito, V. Cardoso, and P. Pani, *Massive spin-2 fields on black hole spacetimes: Instability of the Schwarzschild and Kerr solutions and bounds on the graviton mass*, *Phys. Rev.* **D88** (2013), no. 2 023514, [arXiv:1304.6725].

[377] J. E. McClintock, R. Narayan, and J. F. Steiner, *Black Hole Spin via Continuum Fitting and the Role of Spin in Powering Transient Jets*, *Space Sci. Rev.* **183** (2014) 295–322, [arXiv:1303.1583].

[378] C. S. Reynolds, *Measuring Black Hole Spin using X-ray Reflection Spectroscopy*, *Space Sci. Rev.* **183** (2014), no. 1-4 277–294, [arXiv:1302.3260].

[379] G. Carosi, A. Friedland, M. Giannotti, M. J. Pivovaroff, J. Ruz, and J. K. Vogel, *Probing the axion-photon coupling: phenomenological and experimental perspectives. A snowmass white paper*, in *Proceedings, 2013 Community Summer Study on the Future of U.S. Particle Physics: Snowmass on the Mississippi (CSS2013): Minneapolis, MN, USA, July 29-August 6, 2013*, 2013. arXiv:1309.7035.

[380] S. Chandrasekhar, *General Relativity: An introductory survey.* Cambridge University Press, 1979. "Kerr's solution has also surpassing theoretical interest: it has many properties that have the aura of the miraculous about them".

[381] B. Carter, *Global structure of the Kerr family of gravitational fields*, *Phys. Rev.* **174** (1968) 1559–1571.

[382] M. Walker and R. Penrose, *On quadratic first integrals of the geodesic equations for type [22] spacetimes*, *Commun. Math. Phys.* **18** (1970) 265–274.

[383] E. Berti, V. Cardoso, and M. Casals, *Eigenvalues and eigenfunctions of spin-weighted spheroidal harmonics in four and higher dimensions*, *Phys. Rev.* **D73** (2006) 024013, [gr-qc/0511111]. [Erratum: Phys. Rev.D73,109902(2006)].

[384] H. Yoshino and H. Kodama, *Gravitational radiation from an axion cloud around a black hole: Superradiant phase*, *PTEP* **2014** (2014) 043E02, [arXiv:1312.2326].

[385] D. N. Page and K. S. Thorne, *Disk-Accretion onto a Black Hole. Time-Averaged Structure of Accretion Disk*, *Astrophys. J.* **191** (1974) 499–506.

[386] K. S. Thorne, *Disk accretion onto a black hole. 2. Evolution of the hole.*, *Astrophys. J.* **191** (1974) 507–520.

[387] J. M. Bardeen, *Kerr Metric Black Holes*, *Nature* **226** (1970) 64–65.

[388] R. Brito, V. Cardoso, and P. Pani, *Black holes as particle detectors: evolution of superradiant instabilities*, *Class. Quant. Grav.* **32** (2015), no. 13 134001, [arXiv:1411.0686].

[389] A. Arvanitaki, M. Baryakhtar, and X. Huang, *Discovering the QCD Axion with Black Holes and Gravitational Waves*, *Phys. Rev.* **D91** (2015), no. 8 084011, [arXiv:1411.2263].

[390] V. P. Frolov and I. D. Novikov, eds., *Black hole physics: Basic concepts and new developments*, vol. 96. 1998.

[391] A. D. Dolgov, I. B. Khriplovich, and V. I. Zakharov, *Chiral Boson Anomaly in a Gravitational Field*, *JETP Lett.* **45** (1987) 651–653. [Pisma Zh. Eksp. Teor. Fiz.45,511(1987)].

[392] R. Brito, S. Ghosh, E. Barausse, E. Berti, V. Cardoso, I. Dvorkin, A. Klein, and P. Pani, *Stochastic and resolvable gravitational waves from ultralight bosons*, *Phys. Rev. Lett.* **119** (2017), no. 13 131101, [arXiv:1706.05097].

[393] R. Brito, S. Ghosh, E. Barausse, E. Berti, V. Cardoso, I. Dvorkin, A. Klein, and P. Pani, *Gravitational wave searches for ultralight bosons with LIGO and LISA*, *Phys. Rev.* **D96** (2017), no. 6 064050, [arXiv:1706.06311].

[394] H. Yoshino and H. Kodama, *Bosenova collapse of axion cloud around a rotating black hole*, *Prog. Theor. Phys.* **128** (2012) 153–190, [arXiv:1203.5070].

[395] M. J. Bowick, S. B. Giddings, J. A. Harvey, G. T. Horowitz, and A. Strominger, *Axionic Black Holes and a Bohm-Aharonov Effect for Strings*, *Phys. Rev. Lett.* **61** (1988) 2823.

[396] K.-M. Lee and E. J. Weinberg, *Charge black holes with scalar hair*, *Phys. Rev.* **D44** (1991) 3159–3163.

[397] B. A. Campbell, N. Kaloper, and K. A. Olive, *Axion hair for dyon black holes*, *Phys. Lett.* **B263** (1991) 364–370.

[398] B. A. Campbell, N. Kaloper, and K. A. Olive, *Classical hair for Kerr-Newman black holes in string gravity*, *Phys. Lett.* **B285** (1992) 199–205.

[399] M. Reuter, *A Mechanism generating axion hair for Kerr black holes*, *Class. Quant. Grav.* **9** (1992) 751–756.

[400] G. Grilli di Cortona, E. Hardy, J. Pardo Vega, and G. Villadoro, *The QCD axion, precisely*, *JHEP* **01** (2016) 034, [arXiv:1511.02867].

[401] L. Di Luzio, F. Mescia, and E. Nardi, *Redefining the Axion Window*, *Phys. Rev. Lett.* **118** (2017), no. 3 031801, [arXiv:1610.07593].

[402] D. Harari and P. Sikivie, *Effects of a Nambu-Goldstone boson on the polarization of radio galaxies and the cosmic microwave background*, *Phys. Lett.* **B289** (1992) 67–72.

[403] S. M. Carroll, G. B. Field, and R. Jackiw, *Limits on a Lorentz and Parity Violating Modification of Electrodynamics*, *Phys. Rev.* **D41** (1990) 1231.

[404] R. Alonso and A. Urbano, *Wormholes and masses for Goldstone bosons*, arXiv:1706.07415.

[405] R. Kallosh, A. D. Linde, D. A. Linde, and L. Susskind, *Gravity and global symmetries*, *Phys. Rev.* **D52** (1995) 912–935, [hep-th/9502069].

[406] M. Farina, D. Pappadopulo, F. Rompineve, and A. Tesi, *The photo-philic QCD axion*, *JHEP* **01** (2017) 095, [arXiv:1611.09855].

[407] K. Choi and S. H. Im, *Realizing the relaxion from multiple axions and its UV completion with high scale supersymmetry*, *JHEP* **01** (2016) 149, [arXiv:1511.00132].

[408] D. E. Kaplan and R. Rattazzi, *Large field excursions and approximate discrete symmetries from a clockwork axion*, *Phys. Rev.* **D93** (2016), no. 8 085007, [arXiv:1511.01827].

[409] P. W. Graham and S. Rajendran, *New Observables for Direct Detection of Axion Dark Matter*, *Phys. Rev.* **D88** (2013) 035023, [arXiv:1306.6088].

[410] H. Tashiro, J. Silk, and D. J. E. Marsh, *Constraints on primordial magnetic fields from CMB distortions in the axiverse*, *Phys. Rev.* **D88** (2013), no. 12 125024, [arXiv:1308.0314].

[411] **RadioAstron** Collaboration, N. S. Kardashev and V. V. Khartov, *RadioAstron – a Telescope with a Size of 300 000 km: Main Parameters and First Observational Results*, *Astronomy Reports* **57** (2013) 153–194, [arXiv:1303.5013].

[412] "Radioastron website." http://www.asc.rssi.ru/radioastron/.

[413] A. P. Lobanov, J. L. Gómez, G. Bruni, Y. Y. Kovalev, J. Anderson, U. Bach, A. Kraus, J. A. Zensus, M. M. Lisakov, K. V. Sokolovsky, and P. A. Voytsik, *RadioAstron space VLBI imaging of polarized radio emission in the high-redshift quasar 0642+449 at 1.6 GHz*, *Astronomy and Astrophysics* **583** (2015) A100, [arXiv:1504.04273].

[414] A. Payez, C. Evoli, T. Fischer, M. Giannotti, A. Mirizzi, and A. Ringwald, *Revisiting the SN1987A gamma-ray limit on ultralight axion-like particles*, *JCAP* **1502** (2015), no. 02 006, [arXiv:1410.3747].

[415] **PRISM** Collaboration, P. Andre et al., *PRISM (Polarized Radiation Imaging and Spectroscopy Mission): A White Paper on the Ultimate Polarimetric Spectro-Imaging of the Microwave and Far-Infrared Sky*, arXiv:1306.2259.

[416] M. Schlederer and G. Sigl, *Constraining ALP-photon coupling using galaxy clusters*, *JCAP* **1601** (2016), no. 01 038, [arXiv:1507.02855].

[417] **Planck** Collaboration, P. A. R. Ade et al., *Planck 2015 results. XIX. Constraints on primordial magnetic fields*, *Astron. Astrophys.* **594** (2016) A19, [arXiv:1502.01594].

[418] B. Burke and F. Graham-Smith, *An Introduction to Radio Astronomy*. Cambridge University Press, 2010.

[419] J. H. Taylor and J. M. Cordes, *Pulsar distances and the galactic distribution of free electrons*, *Astrophys. J.* **411** (1993) 674.

[420] J. W. Armstrong, B. J. Rickett, and S. R. Spangler, *Electron density power spectrum in the local interstellar medium*, *Astrophys. J.* **443** (1995) 209–221.

[421] J. M. Cordes and T. J. W. Lazio, *NE2001. 1. A New model for the galactic distribution of free electrons and its fluctuations*, astro-ph/0207156.

[422] A. N. Hall and D. W. Sciama, *The angular broadening of compact radio sources observed through ionized gas in a rich cluster of galaxies*, *Astrophysical Journal, Part 2 - Letters to the Editor* **228** (1979) L15–L18.

[423] A. Ferrara and R. Perna, *Scintillation as a probe of the intergalactic medium*, *Mon. Not. Roy. Astron. Soc.* **325** (2001) 1643, [astro-ph/0104189].

[424] A. Pallottini, A. Ferrara, and C. Evoli, *Simulating intergalactic quasar scintillation*, *Mon. Not. Roy. Astron. Soc.* **434** (2013) 3293, [arXiv:1307.2573].

[425] J.-P. Macquart and J.-Y. Koay, *Temporal Smearing of Transient Radio Sources by the Intergalactic Medium*, *Astrophys. J.* **776** (2013) 125, [arXiv:1308.4459].

[426] E. W. Leaver, *An Analytic representation for the quasi normal modes of Kerr black holes*, *Proc. Roy. Soc. Lond.* **A402** (1985) 285–298.

[427] S. R. Dolan, *Instability of the massive Klein-Gordon field on the Kerr spacetime*, *Phys. Rev.* **D76** (2007) 084001, [arXiv:0705.2880].

[428] P. Pani, *Advanced Methods in Black-Hole Perturbation Theory*, *Int. J. Mod. Phys.* **A28** (2013) 1340018, [arXiv:1305.6759].

[429] **Virgo, LIGO Scientific** Collaboration, B. P. Abbott et al., *Observation of Gravitational Waves from a Binary Black Hole Merger*, *Phys. Rev. Lett.* **116** (2016), no. 6 061102, [arXiv:1602.03837].